DISSERTATION

submitted to the
Combined Faculty of Natural Sciences and Mathematics
of the Ruperto Carola University Heidelberg, Germany
for the degree of
Doctor of Natural Sciences

Presented by
Master of Science, Biology
Nadine Gillich
Born in Karlsruhe, Germany
Oral examination: 18.11.2021

Role of LGP2 in the Innate Immune System upon Viral Infections

Referees:
Prof. Dr. Ralf Bartenschlager
Prof. Dr. Alexander Dalpke

The applicant, Nadine Gillich, declares that she is the sole author of the submitted dissertation and no other sources or help from those specifically referred to have been used. Additionally, the applicant declares that she has not applied for permission to enter an examination procedure at any other institution and that this dissertation has not been presented to any other faculty and has not been used in its current or in any other form in another examination.

…….. …….

Date Signature

ACKNOWLEDGMENT

First, I would like to thank my supervisor Prof. Dr. Ralf Bartenschlager who gave me the possibility to perform this thesis in his laboratory. I am thankful for all discussions and input I got in our meetings and seminars.

I thank my second reviewer Prof. Dr. Alexander Dalpke, my additional TAC members Dr. Marco Binder and Dr. Steeve Boulant and my defense committee apl. Prof. Dr. Martin Müller and Prof. Dr. Nina Papavasiliou for their help, scientific input and willingness to be part of my committee.

I am very grateful to all people who helped me in this work, especially Dr. Zhenfeng Zhang and Prof. Dr. Stephan Urban with whom I enjoyed working on our collaborative HDV-LGP2 project. Moreover, I thank the DKFZ core facilities in the analysis of my samples: the MS-Based Protein Analysis Core Facility (at that time headed by Dr. Bernd Heßling) and the Genomics and Proteomics Core Facility. I thank Dr. Pietro Scaturro for the phospho-MS analysis of my LGP2 pulldowns and the evaluation of potential LGP2 interactors. And I especially thank Agnieszka and Zhenfeng for their proofreading of my thesis as well as Vladimir and Anna-Clara. I am happy about all the discussions and talks I had with people working at the DKFZ, Uniklinik Heidelberg and/or people founded by the TRR179.

Moreover, I am really happy that I had all my recent and former colleagues in the ATV building to talk to – Agnieszka, Firat, Antje, Julita, Eva-Maria, Pascal, Anna-Clara, Michael, Vladimir and all the rest! Additionally, I enjoyed all personal and scientific talks at our MolVirol, Schauinsland, TRR179 and ATV retreat, and at GfV and Cytokines congresses, I got the chance to join.

At last, I want to thank my family and friends, especially my parents and Christoph, who constantly support me and with whom I always spent great times.

ABSTRACT

RIG-I-like receptors (RLRs) are a family of pattern recognition receptors that play an important role in the induction of cellular antiviral responses. RLRs comprise LGP2, RIG-I and MDA5. The latter two initiate antiviral signaling upon binding of viral cytoplasmic double-stranded (ds) RNA, resulting in the expression of interferons (IFNs) and IFN stimulated genes. LGP2 enhances MDA5- and represses RIG-I-mediated signaling even though in the latter case the physiological implication is less clear. Whether posttranslational modifications of LGP2 are involved in its diverse functions remains obscure.

Hepatitis delta virus (HDV), a small RNA virus with a circular genome, is an important human pathogen responsible for the most severe form of viral hepatitis. HDV was shown to be sensed by MDA5 but the contribution of LGP2 to induction of the IFN response has not been explored. Hence, the aim of my thesis work was (i) to gain a deeper understanding of the role of LGP2 in regulating RLR signaling and (ii) to determine the contribution of LGP2 and its natural polymorphisms (encoding Q425R, N461S, R523Q) to sensing of HDV and other human viral pathogens. Using knockout and overexpression systems, immunocompetent lung A549 and hepatic HepaRG^{NTCP} cells were measured for their IFN response upon viral infection and synthetic dsRNA stimulation. Mass spectrometry (MS) was performed to elucidate the impact of phosphorylation on the regulatory function of LGP2.

Studies in A549 cells indicated faster RIG-I and delayed MDA5 signaling. LGP2 inhibited RIG-I and strongly enhanced MDA5 signaling. RNA binding but not ATP hydrolysis was important for both LGP2 functions upon synthetic dsRNA stimulation. In HDV infected HepaRG^{NTCP} cells LGP2 was shown to directly bind HDV RNA. Moreover, LGP2 RNA binding and ATP hydrolysis function were essential to fully activate an IFN response that impaired HDV replication.

MS identified S169, S365 and S464 as differentially regulated LGP2 phosphorylation sites. Follow-up functional assays revealed enhanced RIG-I inhibition by the phosphoablative S169A substitution in LGP2. Preliminary data with an S365A/S464D LGP2 double mutation, mimicking steady-state phosphorylation at those sites, indicated delayed responsiveness of this LGP2 mutant towards HDV sensing.

Investigation of the Q425R, N461S and R523Q LGP2 variants identified Q425R LGP2, which predominates in the African population, as a gain-of-function version. Q425R LGP2 enhanced basal and accelerated HDV-induced IFN signaling, thus lowering viral replication. This variant also enhanced MDA5-mediated antiviral signaling upon severe acute respiratory syndrome coronavirus type 2 infection. Mechanistically, Q425R LGP2 enhanced MDA5-RNA binding compared to wild-type LGP2.

In conclusion, the results obtained during my thesis work broaden our understanding of the regulation of RLR signaling by LGP2. In the future, the gained knowledge might facilitate the development of new antiviral interventions by targeting RLRs for disease control.

ZUSAMMENFASSUNG

RIG-I ähnliche Rezeptoren (RLRs) sind eine Familie von Mustererkennungs-Rezeptoren, die eine wichtige Rolle bei der Induktion zellulärer antiviraler Antworten spielen. RLRs umfassen LGP2, RIG und MDA5. Nach Bindung viraler zytoplasmatischer doppelsträngiger (ds) RNA leiten die letzteren beiden antivirale Signalwege ein, woraus die Expression von Interferonen (IFNs) und von IFN-stimulierten Genen resultiert. LGP2 verstärkt MDA5 und unterdrückt RIG-I vermittelte Signalübertragung, wenn auch in letzterem Falle die physiologische Bedeutung weniger klar ist. Ob posttranslationale Modifikationen von LGP2 an seinen unterschiedlichen Funktionen beteiligt sind, bleibt unklar.

Hepatitis Delta Virus (HDV), ein kleines RNA Virus mit zirkulärem Genom, stellt ein bedeutendes Humanpathogen dar, welches für die schlimmste Form der viralen Hepatitis verantwortlich ist. Es wurde gezeigt, dass HDV über MDA5 erkannt wird, allerdings wurde der Beitrag von LGP2 an der Induktion der IFN Antwort nicht erforscht.

Daher war das Ziel meiner Dissertationsarbeit (i) ein tieferes Verständnis für die Rolle von LGP2 in der Regulation des RLR-Signalwegs zu erlangen und (ii) den Beitrag von LGP2 und seiner natürlichen Polymorphismen (die Q425R, N461S, R523Q codieren) bei der Erkennung von HDV und anderen humanpathogenen Viren zu ermitteln. Unter Verwendung von Knockout- und Überexpressionssystemen wurden immunkompetente A549 Lungenzellen und HepaRG^{NTCP} Leberzellen auf ihre IFN Antwort nach Virusinfektion und Stimulation mit synthetischer dsRNA gemessen. Massenspektrometrie (MS) wurde durchgeführt um den Einfluss von Phosphorylierung auf die regulatorische Funktion von LGP2 aufzuklären.

Untersuchungen in A549 Zellen haben schnellere RIG-I und langsamere MDA5 Signalübertragung gezeigt. LGP2 hemmte den RIG-I und steigerte stark den MDA5 Signalweg. RNA Bindung nicht aber ATP Hydrolyse war wichtig für beide LGP2 Funktionen nach Stimulation mit synthetischer dsRNA. In HDV infizierten HepaRG^{NTCP} Zellen wurde gezeigt, dass LGP2 direkt HDV RNA bindet. Darüber hinaus waren LGP2 RNA Bindung und ATP Hydrolysefunktion essentiell für eine vollständige Aktivierung der IFN Antwort, was die HDV Replikation beeinträchtigte.

Die MS identifizierte S169, S365 und S464 als unterschiedlich regulierte LGP2 Phosphorylierungsstellen. Nachfolgende funktionale Untersuchungen zeigten eine gesteigerte RIG-I Hemmung mit der phospho-ablativen S169A Substitution in LGP2 auf. Vorläufige Daten zu der S365A/S464D LGP2 Doppelmutante, welche den unstimulierten Phosphorylierungszustand dieser Stellen nachahmt, hat auf eine verspätete Reaktivität dieser LGP2 Mutante gegenüber der HDV Erkennung hingewiesen.

Untersuchungen der LGP2 Q425R, N461S und R523Q Varianten zeigten, dass Q425R LGP2, welches in der afrikanischen Bevölkerung dominiert, eine Version mit Funktionszugewinn ist. Q425R LGP2 erhöhte die basale und beschleunigte die HDV-induzierte IFN Antwort, welches

folglich die virale Replikation reduzierte. Diese Variante verstärkte auch die MDA5-vermittelte antivirale Signalübertragung nach Infektion mit dem schweren akuten Atemwegssyndrom Coronavirus Typ 2. Mechanistisch steigerte Q425R LGP2 im Vergleich zum Wildtyp die MDA5-RNA Bindung.

Zusammenfassend erweitern die in meiner Dissertationsarbeit gewonnen Ergebnisse unser Verständnis zur Regulation des RLR Signalweges durch LGP2. In Zukunft könnten die gewonnenen Erkenntnisse die Entwicklung neuer antiviraler Medikamente durch das Ansteuern von RLRs für die Bekämpfung von Krankheiten erleichtern.

CONTENT

FIGURES

SUPPLEMENT FIGURES

TABLES

SUPPLEMENT TABLES

ABBREVIATIONS

µ	micro
A	alanine
ACE2	angiotensin-converting enzyme 2
ADAR1	adenosine deaminase acting on RNA
AGO2	argonaute RISC catalytic component 2
AIM2	absent in melanoma 2
AMP	adenosine monophosphate
APS	ammonium peroxydisulfate
ATP	adenosine triphosphate
BGP	β-glycerophosphate
BHQ	black hole quencher
bp	base pair
BSA	bovine serum albumin
CARD	caspase activation and recruitment domain
cGAS	cyclic GMP–AMP synthase
CIP	calf intestine phosphatase
CLR	C-type lectin receptor
COVID19	coronavirus disease 2019
CRISPR	clustered regularly interspaced short palindromic repeats
CTD	C-terminal domain
CXCL10	C-X-C motif chemokine 10
d	day
D	aspartic acid
DAPI	4′,6-Diamidin-2-phenylindol
DC	dendritic cell
ddhCTP	3′-deoxy-3′, 4′-didehydro-cytidine triphosphate
DHX30	DExH-box helicase 30
DI	defective interfering
DMEM	Dulbecco’s Modified Minimal Essential Medium
DMSO	dimethyl sulfoxide
DNA	desoxyribonucleic acid
ds	double-stranded
DTT	Dithiothreitol
E	glutamic acid
EDTA	ethylenediaminetetraacetic acid
eIF2α	eukaryotic translation initiation factor 2, alpha subunit
EIF6	eukaryotic translation initiation factor 6
ELISA	enzyme-linked immunosorbent assay
EMCV	encephalomyocarditis virus
ER	endoplasmic reticulum
FAM	6-carboxyfluorescein
FCS	fetal calf serum
G	glycine
GAS	IFN-gamma-activated sequence
GMP	guanosine monophosphate

GTP	guanosine triphosphate
h	hour
HA	hemagglutinin
HBsAg (L-, M-, S-)	hepatitis B virus surface antigen (large, medium, small)
HBV	hepatitis B virus
HCoV	human coronavirus
HCV	hepatitis C virus
HDAg (L-, S-)	hepatitis delta antigen (large, small)
HDV	hepatitis delta virus
HEX	6-carboxy-2,4,4,5,7,7-hexachlorofluorescein
HMW	high molecular weight
HRP	horseradish peroxidase
iBAQ	intensity Based Absolute Quantification
IF	immunofluorescence
IFI44	interferon-induced protein 44
IFIT	interferon-induced protein with tetratricopeptide repeats
IFN	interferon
IL	interleukin
IL22RA1	interleukin-22 receptor subunit alpha-1
IP	immunoprecipitation
ISG	interferon stimulated gene
ISGF3	interferon stimulated gene factor 3
ISRE	interferon stimulated response elements
IU	international units
JAK	Janus kinase
K	lysine
kDa	Kilodaltons
KH_2PO_4	potassium dihydrogen phosphate
KO	Knockout
KOH	potassium hydroxide
L	leucine
LGP2	laboratory of genetics and physiology
L-HDAg	large hepatitis delta antigen
lncRNA	long non-coding RNA
LOD	limit of detection
LRRC25	leucine-rich repeat containing protein 25
MAVS	mitochondrial antiviral-signaling
MDA5	melanoma differentiation-associated protein 5
miRNA	microRNA
MOA	mode of action
MOI	multiplicity of infection
MOPS	morpholino propane sulfonic acid
MS	mass spectrometry
MVBR	minimal V protein binding region
Mx1	myxovirus resistance 1
N	asparagine
Na_3VO_4	sodium orthovanadate

NaCl	sodium chloride
NaF	sodium fluoride
NEM	N-ethylenamide
NEMO	NF-κB essential modulator
NF-kB	nuclear factor κB
NLR	NOD-like receptor
NOD	nucleotide-binding and oligomerization domain
NP40	nonidet P-40
NT	non-targeting
NTCP	sodium taurocholate co-transporting polypeptide
OAS	2′-5′ oligoadenylate synthases
ORF	open reading frame
p	phospho
PACT	protein kinase activator A
PAMP	pathogen-associated molecular pattern
PBS	phosphate buffered saline
PCR	polymerase chain reaction
PEG	polyethylene glycol
PFA	paraformaldehyde
pi	post-infection
PIAS	protein inhibitor of activated STAT
PKR	protein kinase R
pNPP	para-nitrophenylphosphate
poly(I:C)	polyinosinic:polycytidylic acid
ppp	triphosphate
PRR	pattern recognition receptor
PTM	posttranslational modification
PUM1	Pumilio protein 1
Q	glutamine
qRT-PCR	quantitative real-time PCR
R	arginine
RB	RNA binding
RD	repressor domain
RIG-I	retinoic acid inducible gene I
RLR	RIG-I like receptor
RNA	ribonucleic acid
RNAi	RNA interference
RNP	ribonucleoprotein
RSAD2	radical S-adenosyl methionine domain-containing protein 2
RT	room temperature
RVFV	Rift Valley fever virus
S	serine
SARS-CoV-2	severe acute respiratory syndrome coronavirus type 2
SDS	sodium dodecyl sulfate
SDS-PAGE	sodium dodecyl sulfate polyacrylamide gel electrophoresis
SeV	Sendai virus
SF2	superfamily 2

S-HDAg	small hepatitis delta antigen
shRNA	short hairpin RNA
SNP	single nucleotide polymorphism
SOCS	suppressor of cytokine signaling
ss	single-stranded
STAT	signal transducer and activator of transcription
SUMO	small ubiquitin-like modifier
T	threonine
TAM	6-carboxytetramethylrhodamine
TBS	TRIS-buffered saline
$TCID_{50}$	median tissue culture infectious dose
TEMED	tetramethylethylenediamine
TGS	TRIS-glycine-SDS
TLR	Toll-like receptor
TMPRSS2	transmembrane protease serine subtype 2
TRAF	tumor necrosis factor receptor-associated factor
TRBP	TAR RNA-binding protein
TRIS	Tris-(hydroxymethyl)-aminomethane
TRIS-HCl	TRIS hydrochloride
U	unit
UT	untagged
VSV	vesicular stomatitis virus
WB	Western blotting
WT	wild-type
XRN2	5'-3' exoribonuclease 2
Y	tyrosine
ZIKV	Zika virus

1 INTRODUCTION

1.1 Innate immune system

Innate immunity constitutes a conserved and unspecific first line of defense against invading pathogens. As such, it can respond within minutes to hours to an infection but typically does not memorize a previous infection. Many different components are part of this system. For example, natural barriers represented by epithelial surfaces like skin and mucous membranes help to avoid the entry of pathogens [1]. Moreover, there exist specialized innate immune cells with a variety of functions shortly highlighted in 1.1.1. The complement system and secreted cytokines of activated cells are also part of this immune system. Both enable the induction of direct defense mechanisms and attraction of immune cells to the site of infection. In vertebrates, the innate immune system is also needed to activate the adaptive immune system which results in a pathogen-specific immune response mainly mediated by B and T cells allowing long-lasting protection [2].

The cellular production of cytokines is mediated by specific host pattern recognition receptors (PRRs). These receptors sense evolutionarily conserved structures present in pathogens called pathogen-associated molecular patterns (PAMPs). Recognition of PAMPs through PRRs leads to the activation of intracellular signaling cascades and thus the expression of cytokines [3]. Different PRRs with diverse specificity exist being present on immune and/or non-immune cells – further explained in 1.1.2. The innate immune activation by RIG-I-like receptors (RLRs), a subgroup of PRRs, is of special interest in this study. Their impact was investigated in hepatic and lung epithelial cells. The liver and lung constitute direct contact sites to blood and air, respectively, and are exposed to pathogens entering through those milieus [4, 5]. Thus, PRR signaling mediates an important defense mechanism at those sites. A short overview of the PRR families including their specificity and expression is provided in 1.1.2.

1.1.1 Innate immune cells

White-blood cells (leukocytes) arise from hematopoietic stem cells in the bone marrow. These stem cells give rise to myeloid and lymphoid lineages of innate immune cells. Neutrophils, basophils, eosinophils, mast cells, monocytes and macrophages are derived from the myeloid lineage while natural killer cells belong to the group of innate lymphoid cells [6]. Main dendritic cell (DC) subgroups are comprised of the conventional DCs and most potent interferon (IFN) producing plasmacytoid DCs (pDCs) [7]. They can develop from both myeloid or lymphoid progenitor cells [8].

Granulocytes are named after their large cytoplasmic granules and can be subdivided into basophils, eosinophils, neutrophils and mast cells with different specialized functions. They can migrate to the site of infection and release several effector molecules, including cytokines, chemokines and histamines, thereby contributing to inflammation. Macrophages play a critical role in immune surveillance as they can phagocytize pathogens, present their antigens to other immune cells and secrete inflammatory cytokines. Antigen presentation is also a hallmark of DCs acting as a bridge between the innate and adaptive immune systems [9]. Natural killer cells even share characteristics similar to cells of the adaptive immune system [10]. They are cytotoxic lymphocytes that kill infected cells or cancer cells and can produce cytokines and chemokines.

1.1.2 Pattern recognition receptors

Toll-like receptors (TLRs) can be found at the cell surface (bound to the cell membrane) or intracellularly bound to the endoplasmic reticulum (ER), endosomes, or lysosomes. All innate immune cells express TLRs as do T and B lymphocytes or non-immune cells like epithelial and endothelial cells or fibroblasts. Dependent on the subtype of TLR, they sense viral RNA, viral and bacterial DNA species, and different bacterial PAMPs, as cell-surface lipopolysaccharides or lipoproteins. In particular, TLR3 senses double-stranded (ds) RNA, while TLR7 and TLR8 sense single-stranded (ss) RNA of viruses [11]. Viral RNA is not only sensed by membrane-bound TLRs but also cytosolic RLRs (see 1.1.3).

C-type lectin receptors (CLRs) represent a large membrane-bound receptor family. They are primarily expressed on myeloid cells and harbor a C-type lectin-like domain with which they usually sense carbohydrates. Dependent on their integral motif they can have activating or inhibiting functions [12]. Moreover, CLRs can also be secreted in a soluble form thereby being essential for the opsonization of pathogens [13].

Absent in melanoma 2 (AIM2) and cyclic GMP–AMP synthase (cGAS) sense cytosolic DNA [14]. AIM2 regulates inflammasome formation and caspase-1 activation thereby triggering proinflammatory cytokine secretion and pyroptosis [15]. In the cGAS-STING pathway, cGAS is the initiator of DNA sensing while the adaptor molecule stimulatory of IFN genes (STING) is propagating the signal. cGAS is a nucleotidyl transferase converting GTP and ATP into cyclic GMP–AMP (cGAMP), a second messenger that can activate STING. Downstream signaling leads then to the induction of an IFN response via nuclear factor κB (NF-κB) and IFN regulatory factor 3 (IRF3) [16].

Cytosolic nucleotide-binding and oligomerization domain (NOD)-like receptors (NLRs) are another family of PRRs that are both important for the recognition of PAMPs and damage-associated molecular patterns, inflammasome formation and cell death regulation [17].

1.1.3 RIG-I like receptors

RIG-I-like receptors (RLRs) are cytoplasmic sensors of dsRNA derived from viruses and are ubiquitously expressed. The family consists of three members: Retinoic acid-inducible gene I (RIG-I), melanoma differentiation-associated gene 5 (MDA5) and laboratory of genetics and physiology 2 (LGP2). RLRs share conserved domains and significant sequence homology acting together as a viral monitoring system conserved within vertebrates.

1.1.3.1 Structure

RLRs are a subgroup of superfamily 2 (SF2) helicases [18]. They all consist of an RNA helicase domain necessary for dsRNA binding and ATP hydrolysis, and a C-terminal domain (CTD) which mediates the recognition of specific RNAs [19]. The DECH box helicase domain consists of two Rec A domains, called Hel1 and Hel2 including a specific insertion termed Hel2i (Figure 1A). The two Hel1 and Hel2 domains together create a surface for RNA binding, ATPase binding and hydrolysis [20]. They harbor highly conserved helicase motifs I-VI. Motif I, II and III lay within Hel1, while motif IV, V and VI lay in Hel2. These motifs are important for ATP hydrolysis and RNA binding. For example, motif I and II, also known as Walker A and B motifs, are essential for ATP binding and hydrolysis [21, 22]. Motif III was suggested to be involved in the formation of intramolecular interactions [22, 23], enabling the coordination between motifs [24] and thus RNA binding and ATP hydrolysis [25]. Studies with mutants of this motif in RIG-I or MDA5 rendered the proteins constitutively active. In the case of LGP2, mutants of motif III and IV impaired RNA binding [22]. The so-called pincer domain, a V-shaped bridging domain, connects the Hel2 domain with the CTD (Figure 1A). There is a difference in RNA substrate recognition between the CTDs of the different RLRs (see 1.1.3.2). Structural analysis of RLRs identified amino acids in the CTD to be important for RNA interaction. In the case of crystal structures of the LGP2 CTD electrostatic interactions to RNA were shown for lysine (K) 634 and K651 and their exchange to glutamic acid (E) abolished RNA binding, respectively [26, 27]. An exchange of K605 to E slightly reduced LGP2 RNA binding [27].

In addition to helicase and CTD, MDA5 and RIG-I harbor N-terminal tandem caspase activation and recruitment domains (CARDs), protein interaction domains that are necessary for the initiation of downstream signaling events. As LGP2 is lacking the tandem CARDs its role in RLR sensing is regulatory, influencing the strength of the innate response [28] (Figure 1A).

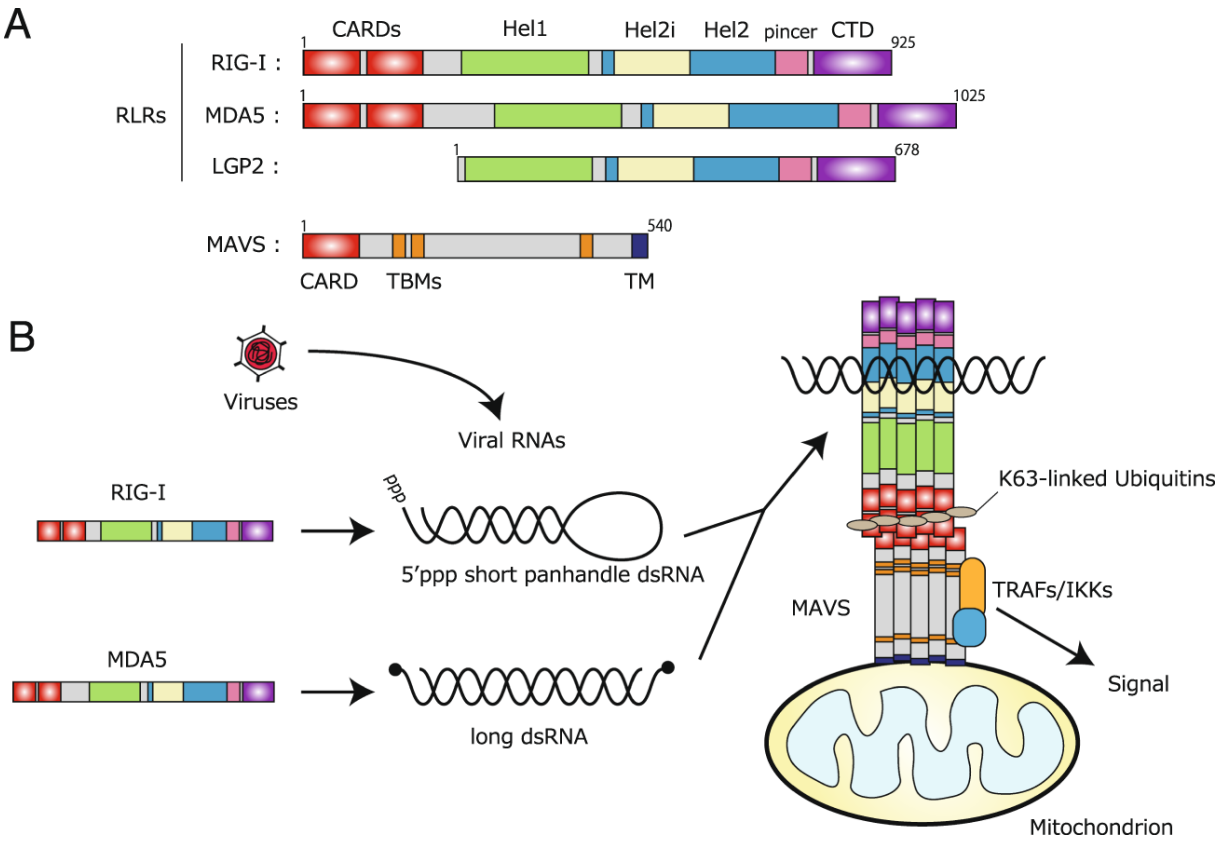

Figure 1: Domain structure of RLRs and their signaling activation.
(A) The RLR family consists of RIG-I, MDA5 and LGP2. All RLRs harbors a helicase domain (Hel1, Hel2i and Hel2) and CTD connected by the pincer motif. Additional tandem CARDs are found at the N-terminus of RIG-I and MDA5 needed for induction of downstream signaling via the adaptor molecule MAVS which also possesses a CARD region. MAVS additionally harbors TRAF-binding motifs (TBMs) needed for signaling transduction and a transmembrane anchor (TM) tethering MAVS to mitochondrial and other intracellular membranes. **(B)** RIG-I and MDA5 CTDs bind several dsRNA substrates, with MDA5 binding rather long dsRNAs while RIG-I is important for the recognition of 5′-triphosphate RNAs. RNA binding induces MDA5 and RIG-I oligomerization. The K63-linked polyubiquitination of RIG-I CARDs is important for their tetramer formation. The signaling competent RIG-I and MDA5 oligomers interact with the MAVS CARD. MAVS oligomerization recruits downstream signaling components such as TRAFs. From [28]

In the ligand-free, steady-state RIG-I CARD2 binds to the Hel2i, therefore, being unavailable for signal transduction [29, 30]. It was assumed that MDA5 is auto-repressed in the steady-state, too, probably with less robustness than for RIG-I [30].

1.1.3.2 Substrates

RIG-I binds dsRNA ends [31] and mainly recognizes short RNAs with a 5′-triphosphate (5′ppp) moiety or a 5’-diphosphate (5’pp) group [32-36] (Figure 1B). Negative-sensed RNA viruses often contain unmethylated 5’-ends with a triphosphate group, thus, studies identified RIG-I to be the main sensor of Sendai virus (SeV), vesicular stomatitis virus (VSV), influenza A virus and Rift Valley fever virus (RVFV) [37-40] (Table 1). Moreover, also some positive-sensed RNA viruses are recognized by RIG-I for example two members of the Flaviviridae family Zika virus (ZIKV) and dengue virus [41].

In contrast to RIG-I, MDA5 CTD binds the stem of the RNA [31]. MDA5 is activated by longer and higher-order dsRNAs (> 1 kb) (Figure 1B), especially those of replicative intermediates of positive-sensed, ssRNA viruses [34, 42-44]. MDA5 is in general of significance for sensing of picornaviruses [44-46]. Early *in vivo* studies already claimed that MDA5 is important for the type I IFN response after infection with encephalomyocarditis virus (EMCV) (Table 1). MDA5 was shown to recognize the replicative RNA form of hepatitis C virus (HCV), a Flavivirus with a positive-sensed ssRNA genome [47]. Hepatitis delta virus (HDV) [48] and severe acute respiratory syndrome (SARS) coronavirus type 2 (CoV-2) [49] are detected by MDA5, too (Table 1).

Table 1: RNA viruses used in this study.
RNA viruses used in this study and their taxonomy is depicted. The main RLR important for sensing and innate signaling is shown as is the respective cell system used. MEFs: mouse embryonic fibroblasts. (-): negative-sensed. (+): positive-sensed.

Species	Virus family	Genome	Sensor	Cellular system	Reference
SeV	Paramyxoviridae	(-) ssRNA	RIG-I	MEFs	[50]
VSV	Rhabdoviridae	(-) ssRNA	RIG-I	MEFs	[50]
ZIKV	Flaviviridae	(+) ssRNA	RIG-I	A549	[51, 52]
RVFV	Bunyaviridae	(-) ssRNA	RIG-I	HEK 293T	[40]
HDV	Kolmioviridae	(-) ssRNA	MDA5	HepaRG^{NTCP}, HepG2^{NTCP}	[48]
SARS-CoV-2	Coronaviridae	(+) ssRNA	MDA5	Calu-3	[49]
EMCV	Picornaviridae	(+) ssRNA	MDA5	murine DCs and macrophages	[46]

Analysis with chicken LGP2 suggests it combines characteristics of the other two RLRs. It binds both blunt-ended dsRNA termini and RNA stems [26, 53]. Moreover, in comparison to MDA5 and RIG-I, it probably can bind more diverse RNA substrates and imperfect dsRNAs, including 5'ppp-ssRNA, short blunt-ended dsRNA, small hairpin RNA [26, 54-56]. Among RLRs, LGP2 is supposed to have the strongest affinity to RNA and MDA5 the weakest [22, 57]. LGP2 catalyzes MDA5 filament assembly to improve MDA5's signaling capability [58, 59]. It was therefore identified as an important cofactor of MDA5, for example in sensing of HCV [60] or SARS-CoV-2 [49].

Several viruses block RLR signaling at multiple steps. Paramyxoviruses interfere with MDA5 and LGP2 [61-64] and picornaviruses cleave RIG-I [65]. Thus, the specificity of RLR recognition is further influenced by viral countermeasures [66]. To avoid such counteraction when investigating RLR signaling, synthetic dsRNA stimuli can be used, for example polyinosinic:polycytidylic acid (poly(I:C)), simulating viral infections [67]. dsRNAs of different lengths activate RLRs to different extents [34]. Low molecular weight poly(I:C) can be used to

activate RIG-I signaling, while high molecular weight (HMW) poly(I:C) is used to stimulate MDA5 signaling. Synthetic 5'ppp-dsRNA can also be used to activate RIG-I, which was applied in this study by using a length of 200 bp [68].

1.1.3.3 Signaling activation

Upon dsRNA binding, RLRs undergo conformational changes resulting in MDA5 and RIG-I oligomerization [31, 69, 70] and freeing of their CARDs. The activation includes several posttranslational modifications (PTMs) (see 1.1.3.4). Interaction of the RLR CARDs with the membrane-bound adaptor protein mitochondrial antiviral-signaling (MAVS) triggers MAVS aggregation, a prerequisite for activation of the downstream signaling cascade (Figure 1B). RIG-I promotes the formation of prion-like MAVS aggregates in the presence of lysine 63 (K63)-linked polyubiquitination and binding of viral RNA [71] (Figure 1B, Figure 2). RIG-I filament- and ubiquitin-dependent mechanisms of activation are thought to work in concert to induce downstream activation [72]. Analysis with MDA5 CARDs revealed that they rather form oligomers than tetramers (as is the case with RIG-I) and tend to self-associate into larger oligomers in a concentration-dependent manner. This suggests possibly different processes in RIG-I and MDA5 CARD assembly [73].

MAVS aggregates recruit tumor necrosis factor receptor-associated factor (TRAF) adaptor proteins (TRAF2, 3, 5, 6), ubiquitin ligases, that furthermore attract and activate the kinases IκB kinase (IKK) complex, TBK1 and IKKε [74, 75] (Figure 1B, Figure 2). The IKK kinase complex consists of IKKα and IKKβ and a regulatory subunit, NF-κB essential modulator (NEMO). The kinases activate the transcription factors IRF3, IRF7 and nuclear factor κB (NF-κB) [76] resulting in the transcription of type I and III IFNs and proinflammatory cytokines [77-79] (Figure 2). IRFs recognize a specific motif, called the IRF element, a core sequence of the ISRE (see 1.1.4.2), that is located in the promoters of IFN-α/β and ISGs [80]. IRF3 and IRF7 form homo- and heterodimers that bind target sequences to drive gene transcription. Some ISGs can also be directly activated by IRF3 signaling [81, 82]; for example, Viperin [83] and IFIT1 [84]. NF-κB is activated by the phosphorylation of its inhibitory subunit of NF-κBα (IκBα) which is polyubiquitinated by lysine 48 (K48)-linked polyubiquitin and degraded by the proteasome. This results in the release of NF-kB dimers to activate target gene transcription. NF-kB signaling is of importance for the induction of proinflammatory cytokines [85] (Figure 2). However, it was postulated that there is an interconnection of NF-kB and IRF signaling pathways as many genes show both NF-kB- and IRF-binding sites [86].

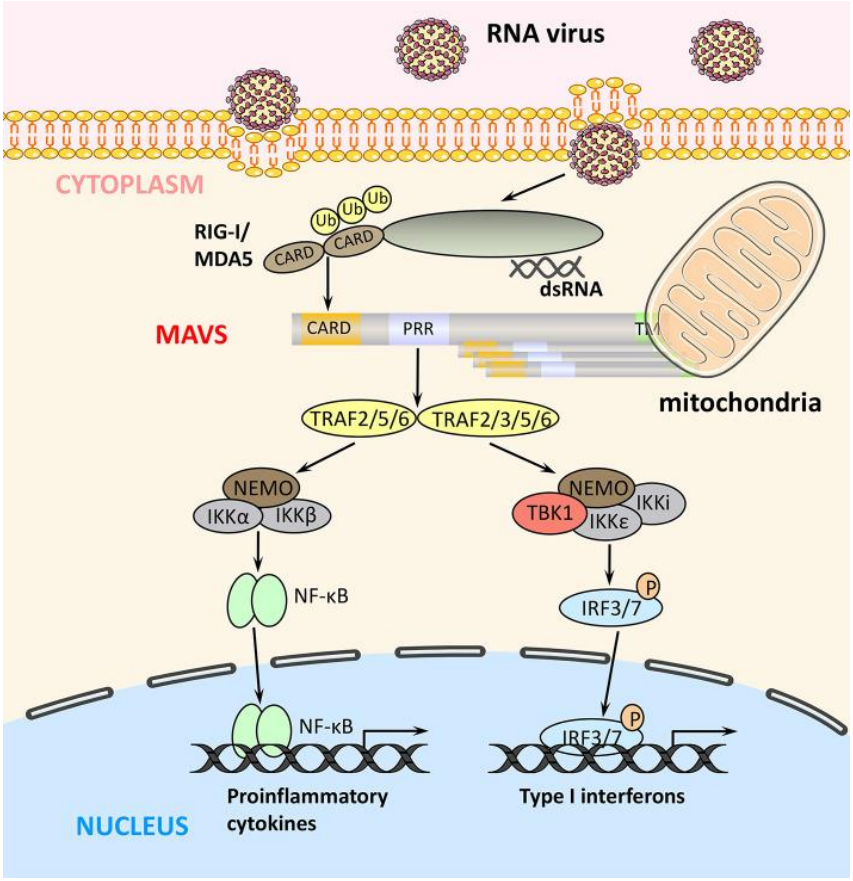

Figure 2: Overview of RLR signaling.
Cytoplasmic viral RNA is sensed by RIG-I, MDA5 and LGP2. Their binding to RNA induces conformational changes. CARD interaction between MAVS and RIG-I/MDA5 leads to oligomerization and activation of MAVS. Recruitment of TRAF E3 ligases leads to the activation of the IKK complex and TBK1/IKKε. The IKK complex activates NF-kB. TBK1/IKKε phosphorylates IRF3/7. Both NF-kB and IRF3/7 transcription factors then translocate into the nucleus where they induce the expression of proinflammatory cytokines and type I and III IFNs. From [87].

1.1.3.4 Regulation by posttranslational modifications

As mentioned above, the RLR signaling cascade is mediated by several steps of posttranslational modifications (PTMs). PTMs and their corresponding enzymes add a level of complexity to the regulation of RLRs and enable a tight control and quick reaction upon viral infection.

In the resting state, RIG-I and MDA5 reside in the cytoplasm being inactivated, amongst others, by phosphorylation. Serine/threonine phosphorylation of the RIG-I CARDs keeps the receptor in an inactive state suppressing CARD ubiquitination [88-90]. More recently CARD phosphorylation was also found for MDA5 [91]. In addition, RIG-I and MDA5 CTDs were also shown to be phosphorylated by casein kinase II in the case of RIG-I and by RIO kinase 3 (RIOK3) in the case of MDA5 further blocking activation [92, 93]. Similarly, acetylation of RIG-I was shown to block RIG-I signaling [94] (Figure 3).

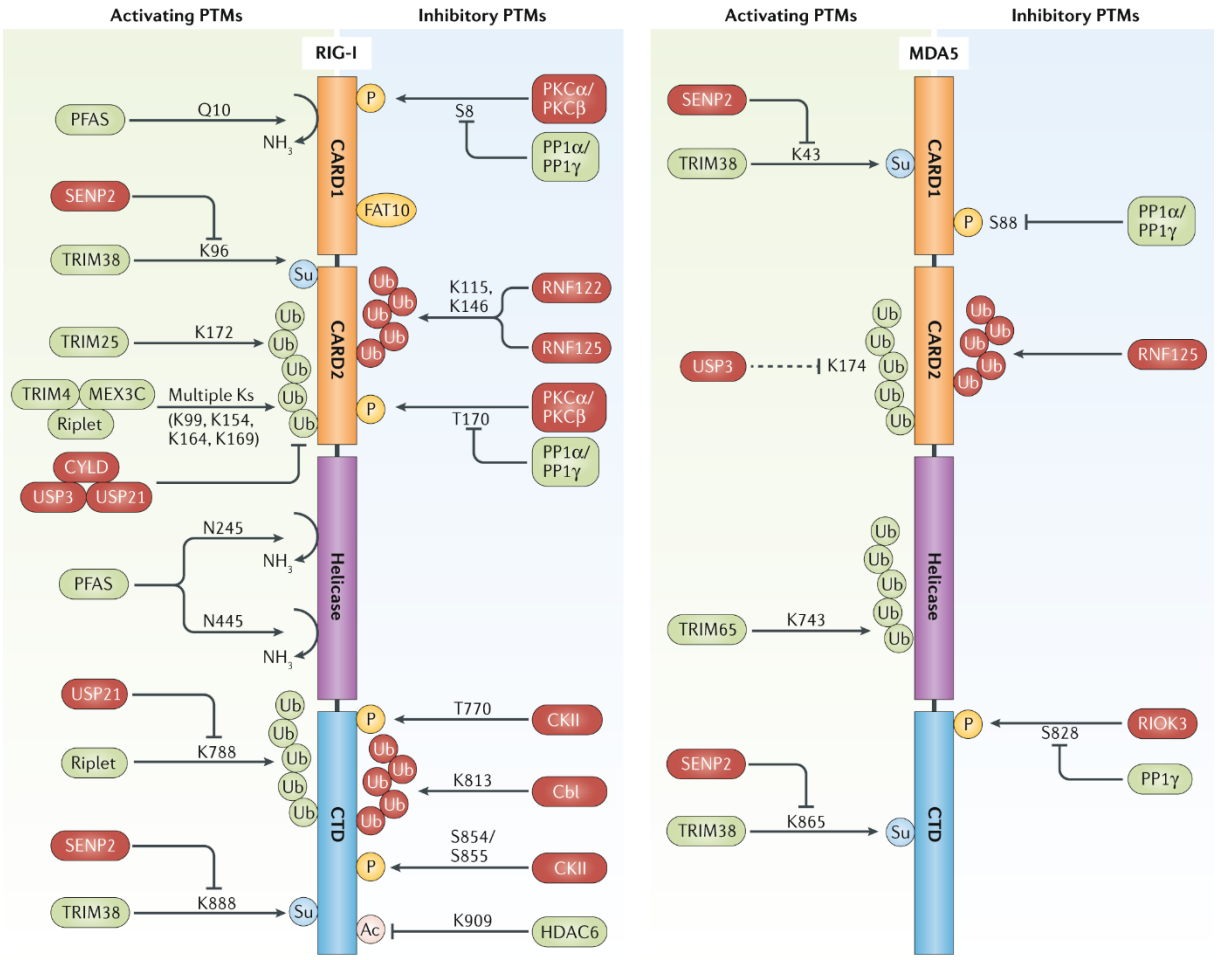

Figure 3: RIG-I and MDA5 posttranslational modifications and regulating enzymes.
RIG-I and MDA5 are posttranslationally modified by several enzymes either repressing (depicted in red) or activating (depicted in green) them. PTMs include acetylation (Ac), phosphorylation (P), SUMOylation (Su), modification with FAT10, K63-linked (depicted in green) and K48-linked (depicted in red) polyubiquitination. The modified amino acid positions are shown. From [18].

Upon viral infection, MDA5 and RIG-I CARDs are dephosphorylated by phosphoprotein phosphatase 1-α (PP1α) and PP1γ leading to signaling activation [91]. Moreover, histone deacetylase 6 (HDAC6) deacetylates RIG-I which is critical for its detection of RNA [94]. RIG-I CARDs and CTD become ubiquitinated by the E3 ligase Riplet and by tripartite motif-containing 25 (TRIM25) at the CARDs, activating RIG-I signaling [95-97] (Figure 3). In the case of MDA5, however, the role of K63-polyubiquitin is rather controversial [98].

Sumoylation has emerged as a critical PTM for the activation of MDA5 and RIG-I both at their CARDs and CTDs. TRIM38 was shown to sumoylate RIG-I and MDA5 in the steady-state and early after infection thereby inhibiting K48-polyubiquitination and protein degradation. At the late phase of infection, SENP2 desumoylates MDA5 and RIG-I, resulting in K48-polyubiquitination and degradation [99] (Figure 3).

ISGylation and non-covalently bound FAT10 were shown to be further negative RIG-I modulations [100-102]. These modifications occur as negative feedback upon infection. For

example, leucine-rich repeat-containing protein 25 (LRRC25) binds to ISG-15-associated RIG-I promoting RIG-I degradation [101] (Figure 3).

Although there are a variety of PTMs and their modifying enzymes identified which modulate the activation and inhibition of RIG-I and MDA5, the role of specific LGP2 PTMs still has to be analyzed.

Protein interactions, e.g. with cofactors, cellular non-coding RNAs (long non-coding (lnc) RNAs, micro (mi) RNAs), or autophagy further regulate RLR activity [18]. lncRNAs and miRNAs, with both enhancing and inhibiting functions, regulate gene expression or modulate protein activity by direct interaction. Autophagy-dependent degradation of RLRs and downstream proteins act as negative regulation [103].

1.1.3.5 Human polymorphisms

Single nucleotide polymorphisms (SNPs) within the RLR coding region can lead to non-synonymous nucleotide substitutions and thus single amino acid exchanges of the expressed protein. Such naturally occurring, genetic mutations in RLRs can be accompanied by changed signaling behavior. This leads to dysregulated signaling, either being reduced or enhanced [18].

RIG-I and MDA5 SNPs can result in partial or total loss-of-function mutations and can protect from autoimmune diseases [104, 105]. However, they might be problematic upon viral infections. A homozygous missense mutation in the gene coding for MDA5 was shown to be associated with life-threatening and recurring viral infections of the respiratory tract [106]. In contrast, gain-of-function mutations can lead to enhanced signaling. Those mutations can over-sensitize the detection of RNAs and can trigger constitute signaling in the absence of an infection. Natural RIG-I and especially MDA5 SNPs causing aberrant RLR signaling were shown to be associated with several autoimmune and autoinflammatory disorders, for example, systemic lupus erythematosus, type-1 diabetes and Singleton-Merten syndrome [107-109].

Besides increasing the risk for autoimmune diseases [110], such gain-of-function variants may also lead to beneficial outcomes. For example, a common MDA5 variant (A946T), associated with higher susceptibility for several autoimmune diseases [111], better limits viral infections, e.g. HCV [109, 112]. This reveals that the MDA5 genetics can influence the outcome of infection. Some MDA5 SNPs have even been proposed to be positively selected [113, 114] indicating advantageous features. Moreover, Vasseur et al. not only reported positively selected signatures in MDA5 (R460H and R843H) but also in LGP2 (Q425R, SNP 6748, rs2074158) [114]. In their sequencing analysis of healthy African, Asian and European

individuals they identified several SNPs in MDA5, RIG-I and LGP2 within these populations with different frequencies [114]. More frequent amino acid exchanges were detected in human MDA5/LGP2 than RIG-I indicating stronger evolutionary limitations for RIG-I. Besides the high frequency of Q425R LGP2 in the African population, two further non-synonymous SNPs were found in high frequency (SNP 6856, N461S, rs34016093 and SNP 8099, R523Q, rs2074160). The three LGP2 SNPs are listed in the dbSNP, a public-domain archive for human single nucleotide variations, with unknown clinical relevance [115-117].

1.1.3.6 Diverse roles of LGP2

LGP2 is still the least understood RLR. Besides its regulation of RLR signaling, data suggests its importance in further diverse cellular functions.

1.1.3.6.1 Regulatory role in RLR signaling

LGP2 itself is unable to induce RLR signaling, due to its lack of CARD domains. In the early days, it was assumed that (corroborated by its upregulation as an ISG) LGP2 represents a negative regulator by shutting down MDA5 and RIG-I responses at later stages to prevent aberrant signaling [57, 118]. However, studies with LGP2 knockout (KO) mice revealed a normal feedback mechanism, suggesting that LGP2 is not the primary responsible factor [119]. Mice challenged with VSV (RIG-I activating virus) and EMCV (MDA5 activating virus), respectively, revealed differential roles of LGP2 on RIG-I and MDA5 [119]. Loss of LGP2 upon VSV infection enhanced IFN production and viral resistance. Contrary, EMCV-induced IFN signaling was impaired in $LGP2^{KO}$ mice which were less resistant to lethal EMCV infection compared to wild-type (WT) mice. Another early study with cells derived from $LGP2^{KO}$ mice claimed a positive role of LGP2 in both RIG-I and MDA5 signaling contradicting the observed negative regulation of RIG-I [120].

The exact role of LGP2 in RIG-I signaling is thus not fully understood. Several *in vitro* studies confirmed the negative effect of LGP2 on RIG-I-induced IFN induction and hypothesized several scenarios for its mode of action (MOA). (i) LGP2's strong RNA binding affinity might separate the target dsRNAs from RIG-I [57, 118]. (ii) Direct LGP2 and RIG-I interaction could selectively inhibit RIG-I [121]. (iii) LGP2 could indirectly inhibit RIG-I by interaction with TRIM25 and abrogation of its ubiquitin ligase activity and thus circumventing RIG-I ubiquitination needed for activation [54]. (iv) LGP2 could form a complex with MAVS [122] or TRAF 2/3/5/6 [123], key signaling molecules in various cellular events, blocking downstream signaling. Studies with LGP2 mutants suggested that the inhibitory effect of LGP2 is independent of its RNA binding and ATP hydrolysis [22, 26, 124, 125].

The positive role of LGP2 on MDA5 signaling is consistent in the literature. The mechanism of MDA5 enhancement by LGP2 was revealed in *in vitro* studies. LGP2 was shown to assist MDA5-RNA interaction and regulates MDA5 filament assembly needed for downstream activation [58, 59]. ATPase function and RNA binding, at least by using non-synthetic viral substrates, are needed for MDA5 enhancement by LGP2 [53, 60, 120, 125].

Titration of RLRs suggested the negative regulation of LGP2 to be dose-dependent. Transfection of LGP2 and RIG-I expression plasmids in a 1:1 molar ratio reduced RIG-I activity in reporter assays to 50% whereas a 5:1 ratio showed lost activation [126]. Moreover, under similar conditions using reporter assays, higher LGP2 expression levels even inhibited MDA5-mediated signaling [56, 58]. Therefore, LGP2 was suggested to act as a concentration-dependent biphasic switch between the MDA5-specific enhancement mediated by low levels in acute infection and MDA5 and RIG-I inhibition by high LGP2 levels at later stages [56, 127-129].

1.1.3.6.2 Other interactions and potential functions

Via a mass spectrometry (MS) approach Li et al. identified several interactions of LGP2 [130]. These include components of the RNA silencing pathway, more precisely the endoribonuclease DICER1, argonaute RISC catalytic component 2 (AGO2) and TAR RNA-binding protein (TRBP). Additionally, some RNA binding proteins interacted with LGP2: the Staufen double-stranded RNA binding protein 1 (STAU1), the 5'-3' exoribonuclease 2 (XRN2), the DExH-box helicase 30 (DHX30) and the eukaryotic translation initiation factor 6 (EIF6) [130]. An overview of LGP2 interaction partners published by several studies can be found in Figure S 32. Several of those interactions are not functionally investigated yet.

LGP2 was shown to block RNA interference (RNAi), an ancient RNA silencing pathway for antiviral defense, in mammalian cells by inhibiting the DICER1-dependent cleavage of dsRNA into small-interfering RNA [94]. This might not only inhibit the RNAi mechanism but also could redirect RNAi components to alternative functions in IFN induction [131]. In line with this, LGP2 was shown to interact with two RNAi-related proteins TRBP and protein kinase activator A (PACT) to regulate RLR signaling [132-134].

Additionally, the binding of LGP2 to TRBP inhibited its pre-miRNA binding and recruitment [135]. This reveals the involvement of LGP2 in the regulation of endogenous miRNA-mediated gene expression. The same group further identified an LGP2-mediated induction of apoptosis regulatory genes upon viral infection with Sendai virus through repression of miR-106b, a TRBP-bound miRNA [136].

Protein kinase R (PKR), an important kinase involved in the regulation of cellular stress response and induction of apoptosis, was shown to interact with LGP2, too [130, 132]. The LGP2 binding partners TRBP and PACT have already been shown to contrary influence PKR activity [137, 138]. Several shared PKR/LGP2 interactors have been identified (Figure S 32C).

The RNA binding protein Pumilio protein 1 (PUM1) was postulated to downregulate the expression of LGP2 in the absence of infection [139]. In PUM1-depleted cells, LGP2 was needed for further upregulation of antiviral genes, for example, CXCL10 or IL6. Thus, LGP2 played a key role in the induction of some immune genes [139]. This hints at an additional function of LGP2 in innate signaling regulation at the transcriptional level.

LGP2 was shown to be important in specialized immune cells. It provided an essential prosurvival signal in cytotoxic CD8 T cells upon antigen stimulation [140] and was also required for optimal antitumor control after radiotherapy of patients with breast cancer by enabling IFN-β induction in and priming of DCs [141].

1.1.4 Interferon system

IFNs are the first family of cytokines discovered. It was found that virus infected cells secrete host factors that interfere with viral replication, therefore, calling the substance IFN [142, 143]. Around twenty years later scientists identified the location of IFNs on different sites of the human chromosome [144-146]. IFNs are poorly expressed under steady-state conditions and rapidly induce upon RLR sensing of viral pathogens.

1.1.4.1 Different types of interferons

Based on their related receptors human IFNs are classified into type I, type II and type III IFNs with partly multiple members. In humans, type I IFNs include 13 IFN-α subtypes, IFN-β, IFN-ε, IFN-κ and IFN-ω [147, 148]. Moreover, this class of IFNs includes some distantly related genes and pseudogenes found in other species. IFN-γ is the only member of type II IFNs. IFN-λ subgroups 1 to 4 represent type III IFNs [147]. Type I and type III IFNs are of special importance for the antiviral effects induced by innate immune responses. Their expression is inducible by virtually every cell type. Upon viral infection, IFN-λ1-3 seem to be the dominant IFNs induced in airway epithelial cells and high levels are observed in the lung and liver [149].

In contrast, type II IFN expression is restricted to specialized immune cells for example NK and T cells where IFN-γ production can be induced by IL-12 [150]. Therefore, this IFN subtype is not of relevance for this study. IFN-γ has immunostimulatory effects by inducing macrophage activation, priming proinflammatory cytokine production, or controlling the differentiation of naïve CD4 T cells [151].

Not only the expression of IFNs differs from cell-type to cell-type but also the expression of the receptors through which they induce signaling.

1.1.4.2 Downstream signaling

Secreted IFNs of infected cells interact with their specific cell surface receptors in an endocrine and paracrine manner which activates the so-called JAK-STAT pathway. This allows direct communication from the transmembrane-bound receptor to the nucleus. IFN receptors penetrate the cell membrane and are intracellularly associated with a Janus kinase (JAK), a family of tyrosine kinases. Receptor binding of IFNs results in conformational changes which induce autophosphorylation of JAKs and phosphorylation of the intracellular tail of their receptor. This establishes a latent docking site for signal transducer and activator of transcription (STAT) proteins which become phosphorylated by JAKs. STATs are then released from the receptor allowing their dimerization and nuclear translocation. They directly

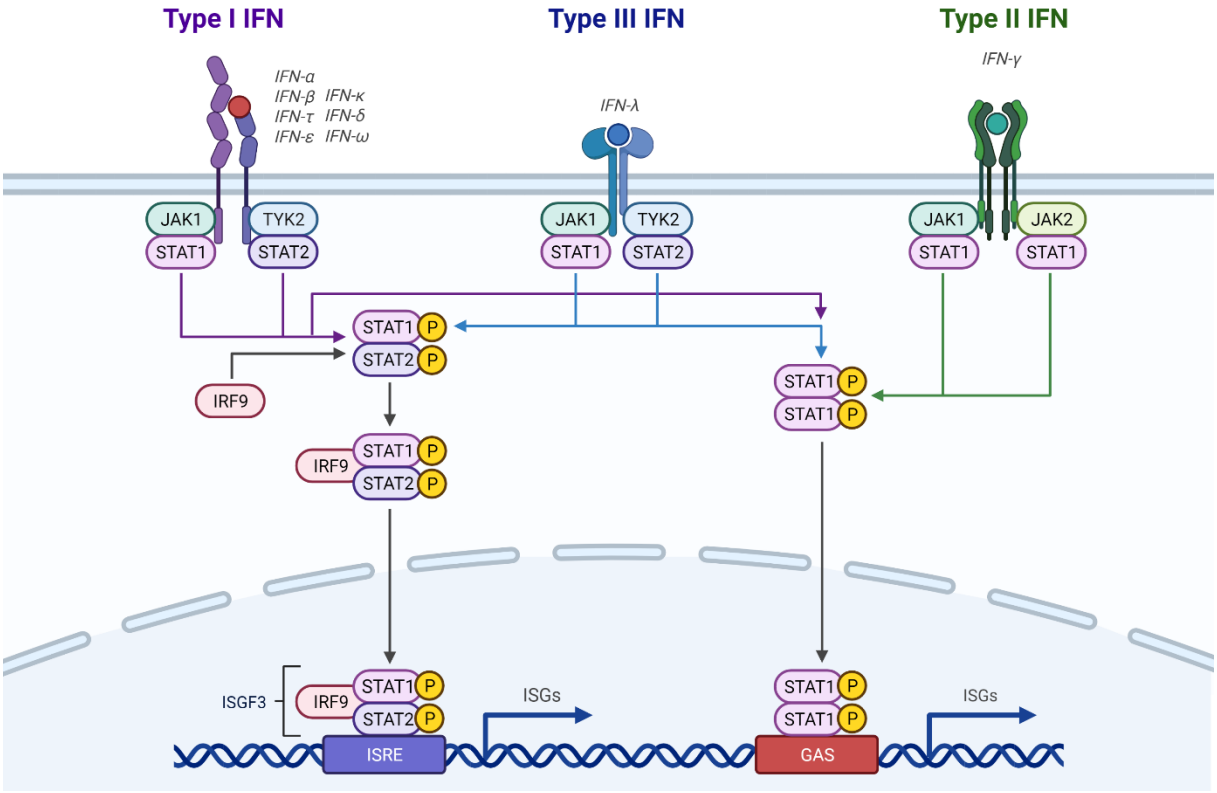

Figure 4: JAK-STAT signaling cascades of type I-III IFNs.
Type I, type II and type III IFNs signal via specific cell surface receptors, called IFNAR, IFNLR and IFNGR, respectively. They consist of two subunits associated with a specific kinase at their cytoplasmic tail. Upon IFN binding the activated kinases phosphorylate specific tyrosines in the intracellular receptor domain which recruits STAT1 and STAT2 transcription factors. This induces STAT1 and STAT2 phosphorylation and complex formation. In the case of canonical type I and type III IFN signaling, STAT1 and STAT2 heterodimers form a complex with IRF9 (called ISGF3) which binds to the IFN-stimulated response element (ISRE) in the promoter region of ISGs enabling the induction of an antiviral response. In the case of type II IFN signaling, STAT1 homodimers are formed binding to IFN-gamma-activated sequence (GAS) in the promoter of ISGs leading to the induction of proinflammatory genes. Reprinted from “Interferon Pathway”, by BioRender.com (2021). Retrieved from https://app.biorender.com/biorender-templates.

bind DNA and induce the expression of target genes [152], a plethora of IFN stimulatory genes (ISGs) (Figure 4) which serve as antivirals to fight the infection. ISGs block viral replication at several levels [153] – for some examples see 1.1.4.3.

The receptor for type I IFNs consists of two subunits, IFN-α/β receptor (IFNAR) 1 and 2, which are ubiquitously expressed. Receptor binding (on either the infected cell itself or on surrounding non-infected cells) activates the JAK tyrosine kinase 2 (Tyk2) and Jak1 that are associated with the cytoplasmic domains of IFNAR1 and 2, respectively. After activation of STAT1 and 2 and the formation of IFN-stimulated gene factor 3 (ISGF3), ISGs are transcribed (Figure 4). Type I IFNs differ in their affinity to IFNAR with the strongest affinity of IFN-β [154, 155]. By using the same receptor pathway, they can modulate the strength of the ISG induction.

In the case of type III IFNs, which are also activated in response to viral infections, the receptor, called IFNLR, comprises two subunits, IFNLR1 (also termed IL28Rα) and IL10Rβ. IFN-λ binds IFNLR1 with higher affinity which recruits low-affinity IL10Rβ resulting in a signaling competent complex. Although type I and type III IFNs use different receptors, their downstream signaling and transcriptional activity (ISG induction) are highly overlapping. However, they differ concerning their receptor distribution, as IFNLR1 is restricted by its preferential expression on epithelial cells, whereas IFNAR subunits are expressed ubiquitously [156]. There are probably differences in the intrinsic properties of both receptor pathways, as ISGs induced by type I IFNs peak early and then decline while ISG expression stays more sustained when induced by type III IFNs [157].

The family of STAT transcription factors includes seven members in mammals which can act as homo- or heterodimers after activation. STATs have conserved Src homology 2 (SH2) domains specifying STATs in recognizing different phosphorylated motifs. STATs can make contact with one another by the interaction between the SH2 domain of one STAT molecule with the phosphorylated tyrosine of another. This enables specific homo- and heterodimer formation. STAT1 homodimers (also called IFN-gamma activation factor (GAF)) are involved in type II IFN signaling. They bind the IFN-gamma activated sequence (GAS) promoter to induce the expression of ISGs (Figure 4). STAT1 and STAT2 heterodimers in combination with IRF9 are important for type I IFN signaling. The resulting complex called IFN-stimulated gene factor 3 (ISGF3) binds to the IFN-stimulated response element (ISRE) promoter region thereby also able to induce expression of ISGs [158] (Figure 4). It was suggested that different ISG subgroups exist, some of them which are only inducible by GAF (e.g. IRF1, ICAM1), others only by ISGF3 (e.g. ISG15, Mx1) or some that can be induced by both transcription factors (e.g. STAT1, STAT2 and IRF9) [80]. There exists evidence for unphosphorylated versions of

GAF and ISGF3 (or rather STAT2/IRF9 [159]) inducing basal expression of some specific ISGs that correlates with antiviral activity [80, 160].

Positive regulation to maintain the IFN signaling cascade is available but often cell-type specific. However, IRF7 is thought to be a shared positive regulator across different tissues being upregulated upon ISGF3 activation [147]. In many cell types, except for pDCs, its expression is low in resting cells in contrast to the constitutive expression of IRF3 [161, 162]. Therefore, IRF3 functions in immediate-early response while IRF7 acts predominantly as positive feedback [163].

Several mechanisms can lead to the turn-off of STATs and the IFN response. Dephosphorylation can be used to inhibit dimerization and DNA activation, as shown for STAT1 [164]. Protein degradation or alternative splice versions resulting in dominant-negative splice forms are other possibilities for negative regulation [165-167]. Furthermore, suppressors of cytokine signaling (SOCS) family members were shown to be negative regulators of the JAK-STAT pathway. They block JAK-STAT singling by binding to the cytokine receptors or JAKs [168-172]. Moreover, STATs can also be inhibited by protein inhibitors of activated STAT (PIAS) proteins [173-175].

1.1.4.3 IFN stimulated genes

It is estimated that around 10% of all human genes have the potential to be IFN regulated [176]. The encoded protein products induce a strong antiviral state to eliminate invading pathogens [177] targeting almost every step in the viral life cycle [176]. Moreover, they can stimulate the adaptive immune system and reveal antiproliferative functions. ISGs include PKR, 2′-5′ oligoadenylate synthases (OAS), IFN-induced transmembrane (IFITM) family members, Myxovirus resistance (Mx) proteins and IFN-inducible cytokines, as CXCL10 and CCL5, that are important for chemotaxis. The specific function of some well-known ISGs will shortly be presented below.

PKR is one of the best-studied ISGs [178]. It binds dsRNA and phosphorylates eukaryotic translation initiation factor 2 alpha subunit (eIF2α) which results in inhibition of translation initiation. PKR is involved in the control of cell proliferation and NF-kB signaling [179]. More recent studies indicate it contributes to the activation of type I IFN independent of the activity to phosphorylate eIF2α [180].

OAS regulates the early steps of viral infection by catalyzing the production of 2′-5′-linked oligoadenylate [181] upon dsRNA binding. This is needed to activate RNAse L which degrades viral and cellular RNA. The short cellular RNA products were shown to induce RIG-I signaling [182].

Both the PKR and OAS systems in addition to RLR signaling were shown to be blocked by adenosine deaminase acting on RNA (ADAR1). ADAR1 was shown to edit endogenous dsRNA and some viral RNA duplexes, thus preventing their detection by the cytoplasmic antiviral signaling pathways. ADAR1 editing circumvents endogenous RNA recognition by MDA5 [183]. Editing deficient ADAR1 mice were lethal and revealed activated IFN signature, however could be rescued by additional $MDA5^{KO}$ [183]. ADAR1 blocks autoimmunity against self RNA and can have both pro- and antiviral outcomes upon viral infection [180, 184]. Recently it was shown that especially the p150 IFN-inducible form of ADAR1 is responsible for most of the editing sites [185].

In the case of Mx proteins, an evolutionarily conserved group of GTPases, their antiviral activity is amazingly diverse. Their discovery started with the mouse Mx1, which made mice highly resistant to influenza virus infections [186]. The family is involved in the inhibition of several viruses by blockage of early viral replication steps [187].

Radical S-adenosyl methionine domain-containing protein 2 (RSAD2) inhibits the replication of a broad range of both RNA and DNA viruses [188]. Some viruses that replicate in ER-derived replication complexes are sensitive to RSAD2, for example, Flaviviridae family members. Viral secretion is inhibited by the binding of RSAD2 to the ER membrane and lipid droplets [189]. RSAD2 interacts with viral and host proteins important for viral replication [188]. It facilitates proteasomal degradation of some of its binding partners or downregulates proviral metabolic pathways [189]. RSAD2 was demonstrated to convert cytidine triphosphate (CTP) to 3′-deoxy-3′, 4′-didehydro-CTP (ddhCTP) [190]. When incorporated into the viral genome while replication, ddhCTP functions as a chain terminator of viral RNA-dependent RNA polymerase, thus directly counteracting viral replication [191].

The IFN-induced proteins with tetratricopeptide repeats (IFITs) consist of four proteins in humans without any known enzymatic activity known so far [192]. Many functions are accomplished through protein-protein interactions via their tetratricopeptide repeats [192-194]. IFIT1 binds to non-self RNA thus blocking translation and replication [195, 196]. It was also shown that IFIT proteins can form functional hetero-complexes among each other with an enhanced mode of action. For example, IFIT3 enhanced the RNA binding of IFIT1 [195].

1.2 RNA viruses involved in this study

1.2.1 Hepatitis delta virus

In 1977 Rizzetto et al. discovered hepatitis delta virus (HDV) in patients chronically infected with hepatitis B virus (HBV) [197] as a novel human pathogen. The genome consists of a circular RNA which was at that time found in plant viruses only [198]. With its size of around 1,700 nucleotides, HDV is the smallest virus known to infect mammals. Moreover, humans are the only natural host of HDV. HDV does not fulfill the criteria of a virus. To enable new infections and assembly, it depends on the envelope protein of its helper virus HBV which explains its clinical association with HBV. Thus, HDV is called a satellite virus of HBV.

HDV does not share any similarities to other animal pathogens [199] however shows some characteristics of plant viroids, as genome structure and replication. It was reclassified into the new virus family Kolmioviridae, genus Deltavirus [200, 201]. Recently, new HDV-like agents had been identified in birds [202], snakes [203], rats [204], fishes, amphibians and invertebrates [204]. Most of them lack hepadnaviruses as helpers which might indicate that the unique association of human HDV with HBV is not evolutionarily conserved [205].

1.2.1.1 Structure and genome organization

HDV can be subdivided into eight subtypes that share highly conserved motifs of nucleotides and amino acids indicating their structural and functional importance [206]. Genotype 5 to 8 (HDV-5 to HDV-8) and subgenotype HDV-1a and -1b were found around central Africa suggesting that this area might be the origin of HDV diversification [206]. In general, the HDV genome contains a negative-sensed, ssRNA, which encodes only one viral protein, hepatitis delta antigen (HDAg). HDAg exists in two isoforms: small (S-HDAg) and large (L-HDAg).

Due to 70% of sequence complementarity and 60% GC-content [207] the genome is folded into a stable rod-like structure accompanied by HDAg forming the ribonucleoprotein (RNP). The RNP is surrounded by the HBV envelope or so-called HBV surface antigen (HBsAg), which exists in the three isoforms small (S-HBsAg), medium (M-HBsAg) and large (L-HBsAg) (Figure 5A). They are embedded in the HDV envelope and equal to HBV, L-HBsAg myristoylation at its N-terminus is needed for cell entry [208]. Genomic and antigenomic HDV RNA contain ribozyme functions (Figure 5B) enabling self-cleavage [209, 210] and self-ligation [211]. Because the genome is circular, multimeric RNAs can be transcribed by a rolling-circle mechanism. Genome and antigenome can be exactly cleaved by their ribozyme functions. The ribozyme forms five helical regions that are connected by a pseudoknot [212] and can act in

cis and trans [213]. Thus, replication is strongly dependent on the structural feature of HDV RNA and host factors [214].

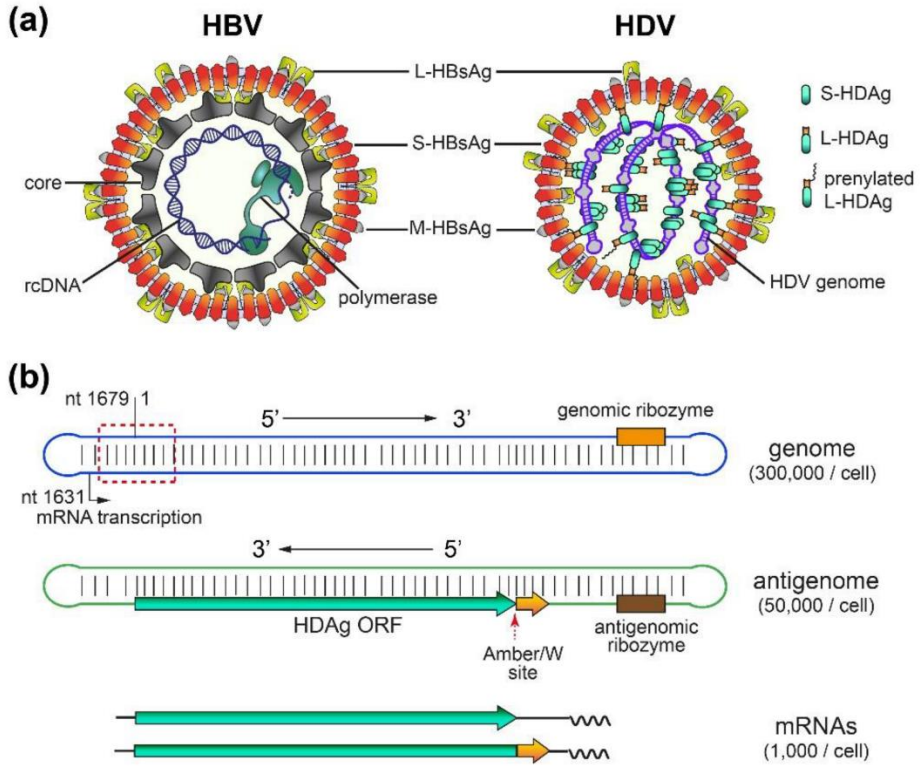

Figure 5: Hepatitis delta virion and RNA structure.
(A) Scheme of the viral structure of HBV and HDV. HDV is a small RNA virus enveloped with HBV surface (S) antigens (HBsAgs). HBsAgs are expressed in a large (L), medium (M) and small (S) form, dependent on the usage of different initiation codons in the S ORF. The HDV genome is surrounded by small (S) and large (L) isoforms of the hepatitis delta antigen (HDAg). Part of the L-HDAg is prenylated enabling the association with S-HBsAg. **(B)** Illustration of HDV genome, antigenome and mRNAs. The small, negative-sensed, circular ssRNA genome reveals strong intramolecular base-pairing forming a rod-like structure. mRNAs encoding for S- and L-HDAg are transcribed from the genome. The complementary antigenome can be edited at the Amber/W site by ADAR1 leading to modified genomes in the next replication round and subsequently an enlarged mRNA encoding for L-HDAg. From [215].

1.2.1.2 Life cycle

Intracellular HDV replication is HBV independent but it needs HBV envelope proteins to secrete infectious particles. In patients both HBV and HDV only infect hepatocytes [216]. As both viruses use HBV envelope proteins for entry, they attach to sodium taurocholate co-transporting polypeptide (NTCP), the entry receptor at the basolateral membrane of hepatocytes [217]. New viral particles are released into the bloodstream, thus new infections mainly occur via contaminated blood and blood products.

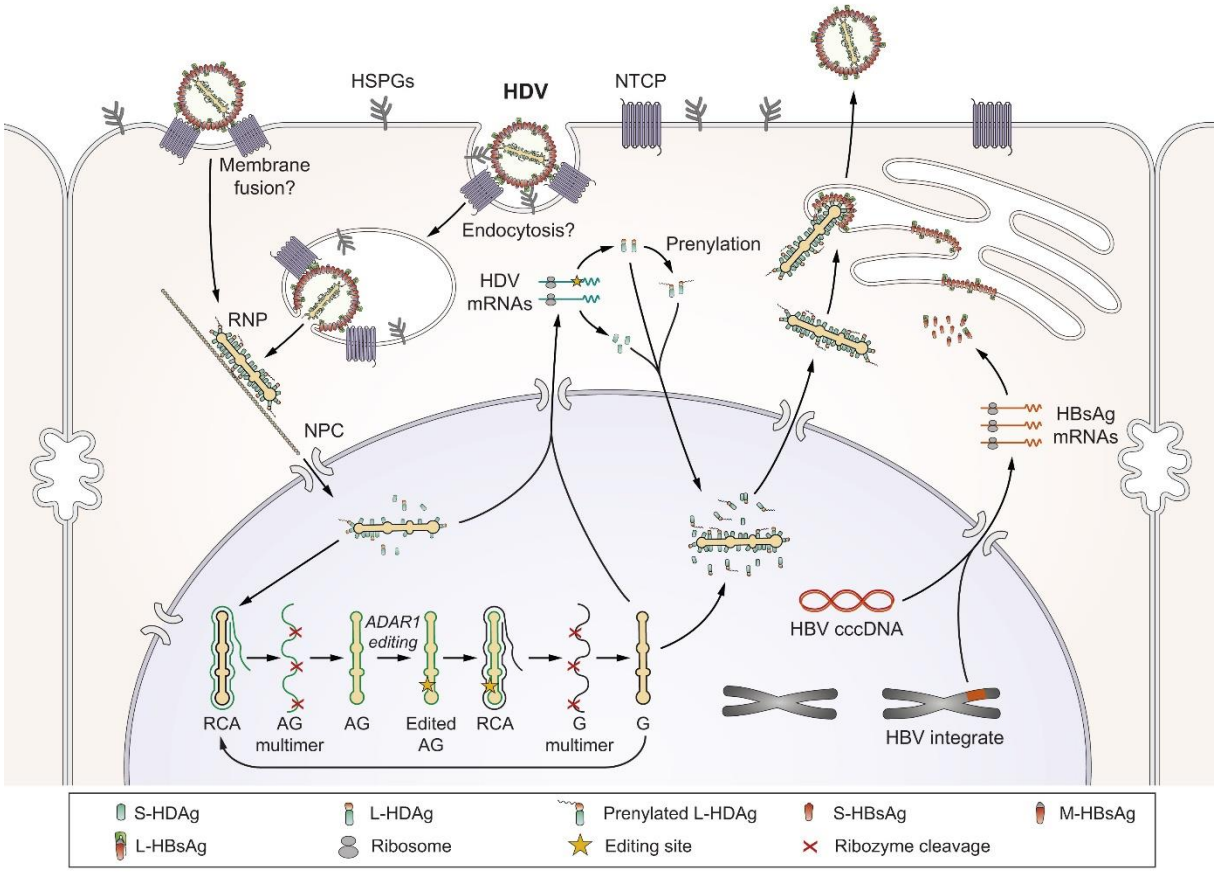

Figure 6: HDV life cycle.
HDV enters the cell via the binding of HBsAg to the hepatic sodium taurocholate co-transporting polypeptide (NTCP) receptor. Upon internalization, the HDV RNP is released into the nucleus where replication takes place using a rolling circle amplification (RCA) mechanism. Antigenomic (AG) and genomic (G) multimeric linear RNAs are produced. They are cleaved into monomers by internal ribozymes and ligated into circular forms. Unedited and edited genomic RNA give rise to S-HDAg and L-HDAg mRNAs, respectively. Over time edited genomes are produced from ADAR1 modified antigenomes. New RNPs are assembled and bud from the endoplasmic reticulum together with HBV envelope proteins. Prenylated L-HDAg enables the interaction with S-HBsAg essential for viral envelopment resulting in the release of progeny virions. From [218].

After membrane fusion, HDV RNP is released into the cytoplasm and further translocated to the nucleus with the help of HDAg containing a nuclear localization signal [219, 220] (Figure 6). HDV does not encode its own RNA-dependent RNA polymerase, however, the host RNA polymerase II transcribes the RNA genome although it is a DNA-directed RNA polymerase. It was assumed that the rod shape of HDV RNA is recognized as dsDNA by RNA polymerase II [221, 222], thus enabling its transcription. The genome serves as the template for the generation of antigenome multimers, produced by rolling circle amplification (Figure 6). They are cleaved through intrinsic ribozyme function and ligated into circular antigenome monomers [215] resulting in replication intermediates complementary to the genome. A second rolling circle with antigenome as template produces genome multimers that are cleaved by ribozyme function and ligated. Throughout HDV infection S-HDAg is translated from a sub-antigenome to maintain replication [223] (Figure 5B). However, editing events at the antigenome can occur

at the amber/W site, exchanging the amber stop codon (UAG) [224]. The adenosine deaminase acting on RNA (ADAR)1, primarily its constitutive and most abundant form in the liver [214], converts the adenosine to inosine in the amber/W site (resulting in UIG), that is recognized as guanosine by the cellular machinery resulting in a tryptophan codon (UGG) [225]. The resulting mRNA contains an extended open reading frame (ORF) encoding for L-HDAg (Figure 5B). L-HDAg inhibits replication [226] and is needed for viral assembly [227-229], thus being responsible to switch from the early to late phase of infection. Together both L-HDAg and S-HDAg interact with genomes and antigenomes to form RNPs [225], mainly detected in the nucleus [230]. However, RNPs can also shuttle to the cytoplasm and this export is probably mediated by HDV RNA [230] and a nuclear export signal present in L-HDAg [231, 232]. Moreover, it was reported that specifically genomic but not antigenomic HDV RNA was exported, conceivably analog to the export of cellular mRNAs [233]. The L-HDAg is further prenylated [229] by the cellular farnesyl transferase which is needed for its interaction with HBsAg and particle assembly. HDV RNPs are enveloped in the ER with HBsAg and particles are then released through the ER-Golgi secretory pathway [215] (Figure 6).

1.2.1.3 Immune recognition

With HBV envelope proteins, HDV can enter and replicate in hepatocytes independent of an HBV co-infection of the same cell. Experimentally, HDV can also occur as mono-infection for at least 6 weeks in humanized mice [234] and cell culture [235]. Thus, importantly, latent HDV infection can convert into a productive HBV/HDV co-infection which might contribute to HDV persistence [234].

HDV was shown to spread via two distinct mechanisms, extracellularly when enveloped by HBsAg, or via cell division, a mechanism that is independent of HBV [218].

In contrast to the stealth HBV [236], HDV replication is sensed by MDA5 which induces an IFN-β/λ response [48]. Moreover, MAVS was already shown beforehand to be a key component in sensing HDV resulting in amplification of innate responses by the adaptive immune system in mice [237]. Cell-division-mediated spread is IFN sensitive, whereas IFN only marginally affects an already established HDV infection in resting cells [218]. Thus far, it is not clear how MDA5 senses HDV RNA and what type of RNA is sensed. HDV replication occurs in the nucleus however MDA5 probably senses progeny RNP complexes in the cytoplasm – although nucleic sensing cannot be fully excluded [218]. Further specialized innate immune cells, macrophages and DCs, might also respond to an HDV infection [218]. As they cannot be infected with HDV, they might uptake replication intermediates via secreted extracellular vesicles of infected cells [218].

Moreover, as discussed above, ADAR1 editing of HDV antigenomes is important for the expression of L-HDAg, however has to be tightly controlled. Too frequent editing will cause the over-production of L-HDAg which was shown to inhibit replication. Already an L-HDAg to S-HDAg ratio of 1 to 10 reduced replication eightfold [226]. Moreover increased editing produces new virus particles that contain genomes encoding for HDAg-L and thus are not replication competent [214]. Type I IFN is known to induce a larger 150 kDa ADAR1 isoform (p150) that is also known to possess editing activity and is also expressed in the liver [238]. However its localization is mainly cytoplasmic, thus its role in counteraction of HDV replication needs further research [214]. Moreover, if IFN-inducible ADAR1 is upregulated upon HDV infection and contributes to enhanced editing with potentially antiviral effects or might be restricted by HDV is also not fully understood [214, 239-241].

1.2.1.4 Pathogenesis and treatment

An HBV mono-infection can already become chronic, estimating to date that over 296 million people globally are affected [242]. HDV infection can occur on top of an already established HBV infection, termed superinfection. Apart from that, a new HDV infection can occur simultaneously with HBV as co-infection without any preexposure [216]. Both co-infection and superinfection can have similar outcomes. The probability of severe outcomes is yet more likely in superinfections as there is already a chronic HBV infection [216]. The risk to develop virus-induced liver cirrhosis [243] is the highest with chronic HDV where it also progresses most rapidly [244]: within two years 10% to 15% of patients [245] and within 5 to 10 years 70% to 80% of patients are thought to develop cirrhosis [246]. Depending on the source, current estimations suggest that worldwide 5% to 13% of chronic HBV infected individuals are co-infected with HDV [244, 247-249]. The number is substantially higher in intravenous drug users and men who have sex with men [246].

HBV and HDV infections can be prevented by vaccination, while treatment of chronic HDV proves difficult [216]. So far, pegylated IFN-α (Peg-IFN-α) was the only treatment option for HDV infected patients with limited success rates [250-252] and side effects [248]. Thus, new drug therapies are urgently needed [251]. A Peg-IFN-λ application could be an alternative to Peg-IFN-α, with higher liver specificity (due to limited receptor expression) and better tolerability/less severe side effects [253]. Several new antiviral drugs are already in clinical trials. Extracellular HDV spread can be blocked by entry inhibitors like Hepcludex®/bulevirtide, formerly called Myrcludex B [254], which is already authorized for use by the European Medicines Agency since July 2020 [218, 255]. Therefore, bulevirtide is the first specific treatment option against HDV at the moment. Moreover, the spread can be blocked by HDV assembly inhibitors as lonafarnib [256]. However, after drug removal HDV rebound was

observed suggesting that an HDV reservoir might be kept independent of *de novo* infection [218]. Thus combination therapies with IFN are promising treatment options that showed synergistic effects when applied with lonafarnib or bulevirtide probably enabling inhibition of both *de novo* independent HDV maintenance and extracellular spread, respectively [218].

1.2.2 Severe acute respiratory syndrome coronavirus type 2

Severe acute respiratory syndrome (SARS) coronavirus type 2 (CoV-2) is a new member of the family of Coronaviridae, genus Betacoronavirus, consisting of a positive-sensed, ssRNA genome. Coronaviruses harbor the biggest genome of known RNA viruses (~30 kb) [257] and have the ability to expand their host range by homologous recombination [258]. To date there exist seven human coronaviruses (HCoVs) with four common cold-causing viruses that are worldwide endemic (HCoV-229E, HCoV-OC43, HCoV-NL63, HCoV-HKU1) [259]. They induce rather mild coughs and sneezes however in immune-suppressed, elderly and young patients they can cause severe lung disease. SARS-CoV and middle east respiratory syndrome (MERS)-CoV arose as zoonotic viruses from an animal reservoir (bats and camels) [260] and can cause severe disease and high death rates. The current SARS-CoV-2, another zoonotic virus that was first identified in 2019 in Wuhan, China, is responsible for the current pandemic and the respiratory coronavirus disease 2019 (COVID19). COVID19 manifests in a very broad spectrum of disease severity ranging from asymptomatic causes to death. In the majority of cases, the symptoms are rather mild to asymptomatic [261, 262]. It becomes apparent that asymptomatic patients can still develop a post-acute COVID19 syndrome often associated with fatigue [263]. Males and older patients are at higher risk to develop severe disease [264], however, younger people are also affected. In cell culture, SARS-CoV-2 was found to be sensitive to both type I and III IFNs [265-267]. Genetics within the IFN system was discussed as a risk of severe COVID19. Inborn errors of or auto-antibodies against the type I IFN response were mainly found in severe COVID19 patients [268, 269].

In general, the coronavirus family is thought to be sensed by MDA5 [270]. Recent studies with SARS-CoV-2 identified MDA5 and LGP2 to play major roles in fighting the virus in the infected lung epithelial cells [49, 271] with further data claiming an additional influence of RIG-I [272, 273]. A diversity of viral antagonists has already been identified to inhibit RLR and IFN signaling [274-279] – a strategy also known for other coronaviruses [280]. Vaccines are currently available [281]. The rising of escape mutants worldwide and the lack of herd immunity might delay the end of the current pandemic, yet.

1.2.3 Zika virus

Zika virus (ZIKV) is a member of the Flaviviridae family, harboring a positive-sensed, ssRNA genome. It is an arthropod-borne virus transmitted by *Aedes* mosquitoes [282], however sexual [283] and neonatal [284] transmission or infection via blood transfusion [285] were further described. In 1947 ZIKV was first discovered in rhesus macaques in Uganda's Zika forest [286, 287]. Until the 1980s several African and Asian countries described its circulation, however without signs of serious symptoms in the affected humans [288]. The first report of an outbreak outside Africa and Asia was observed in 2007 on the Yap Island, Micronesia [289]. In 2013 another outbreak occurred in French Polynesia [290] from where ZIKV spread rapidly into the Pacific area [291]. Subsequently, the first cases of severe clinical outcomes were documented in those areas, including Guillain-Barre syndrome, an autoimmune disease that leads to paralysis [291]. During pregnancy congenital Zika syndrome was found, characterized by developmental abnormalities in the brain as microcephaly and calcifications [292]. Hence nowadays two main ZIKV lineages (African and Asian) are circulating, each consisting of several strains. It was suggested that African and Asian lineage-derived ZIKV strains differ in their pathogenicity and virulence [293]. While MR-766 depicts the Ugandan prototype strain from the African lineage, H/PF/2013 derived from the French Polynesia outbreak in 2013 belongs to the Asian lineage. MR-766 strain was used for infection experiments in this study.

ZIKV strongly antagonizes the IFN system at several levels, by the expression of many viral antagonists [294-296]. For example, the non-structural proteins NS2A and NS4A were just recently shown to antagonize MDA5/RIG-I-induced NF-κB activity [297] and IRF3 [298]. However, not only the production of type I and III IFNs but also downstream signaling pathways were counteracted by ZIKV [299-301]. ZIKV pathogenesis was demonstrated in IFNAR1^{KO} mice [302], thus ZIKV countermeasures against the innate immune system might account for the pathogenicity. IFN signaling seems to play a dominant role in the disease outcome of ZIKV infection. IFN-λ showed antiviral functions against ZIKV, revealing a protective role against infection even in the placenta [303-305].

1.2.4 Other viruses used in this study

1.2.4.1 Encephalomyocarditis virus

Encephalomyocarditis virus (EMCV) is a non-enveloped positive-sensed, ssRNA virus of the family of Picornaviridae (pico: small, RNA: ribonucleic acid), genus Cardiovirus. The 5′-end of the viral RNA is not capped therefore starts translation with the help of an internal ribosomal entry site.

Although isolated in many parts of the world, EMCV consists mainly of one serotype. It is a pathogen especially found in pigs, however can infect non-human primates and a variety of domestic and wild animals. Fatal outbreaks had been described in Australian and American zoos [306, 307]. Rodents, especially mice and rats, are thought to be the natural hosts. The virus can be transmitted through feces- and urine-contaminated water and food or by direct ingestion of carcasses [308]. EMCV can have several disease outcomes - myocarditis, encephalitis, neurological diseases, diabetes and reproductive disorders in many mammalian species [309]. It was shown to infect humans however with rare frequency [308, 310].

The L and 2A proteins are virulence factors [309]. 2A induces shut-off of host protein synthesis whereas L protein is counteracting host immunity. EMCV is thought to be specifically recognized by MDA5 [39, 44] with the help of LGP2 [119, 120, 311]. EMCV encoded protease and caspase are supposed to cleave RIG-I [312]. In innate immunity, EMCV is widely used as a model virus to trigger PRRs [309]. To abrogate L protein function as IFN antagonist Mengovirus, a strain of EMCV was mutated in the L protein zinc-finger region, called Zn mutant. Cells and mice infected with Mengovirus Zn mutant produce and secrete IFNs, show lower viral load with less virulence than for the WT [313]. Mengovirus Zn thereby enables the study of RLR-induced IFN response upon infection and was used in this work.

1.2.4.2 Sendai virus

Sendai virus (SeV) belongs to the family of Paramyxoviridae, which includes some of the most significant human and livestock viruses [314]. Paramyxoviruses are enveloped, negative-sensed, ssRNA viruses. Several members are important pathogens in humans and animals causing high morbidity and variable mortality [315]. They are at risk of transmission events, as humans and domestic animals are susceptible [316]. For example, Nipah and Hendra viruses are highly lethal zoonotic paramyxoviruses [317] that are circulating in bats [318]. Several other paramyxoviruses are present in bats and other reservoirs that have unknown potential to transmit into humans [316].

The murine respirovirus SeV, also called murine parainfluenza virus type 1, is a prototype of paramyxoviruses, infecting mice and is closely related to human parainfluenza virus 1 and 3 [319]. It belongs to the genus Respirovirus and is not pathogenic for humans [320, 321]. It is widely used in research as a model pathogen and is also used in this study. SeV has a wide range of host tropism and infects many cell types as it uses ubiquitously expressed sialic acid for cell entry [320].

Paramyxoviruses encode accessory proteins that act as IFN antagonists [322]. They can directly block RLRs via their V and C proteins [323] and have many several mechanisms to

counteract IFN response [324]. V proteins were shown to interact with both MDA5 and LGP2 thereby blocking their activation [62, 64]. Some V proteins can also block RLR downstream kinases TBK1 and IKK-ε [325] or cause degradation of STAT1/2 proteins [326, 327]. Some of these V protein interactions may be cell-type-specific as the inhibition of RIG-I or TBK1 had not been observed in some tested cell lines [328]. Truncated forms of viral genomes are produced during the replication of RNA viruses, called defective interfering (DI) RNA [329]. Paramyxovirus DI particles were shown to be detected by RLRs [330-332] with RIG-I preferably binding to DI RNAs of SeV rather than the full-length counterpart [330].

1.2.4.3 Rift valley fever virus

Rift Valley fever virus (RVFV) has a tri-segmented, ssRNA genome and belongs to the family of Bunyaviridae, genus Phlebovirus. It is a zoonotic pathogen mainly transmitted by mosquitoes [333]. It primarily affects ruminants but can also be lethal to humans [334]. Rift Valley fever is characterized by increased abortions, fetal malformations, or high death rates in newborn lambs [335]. In humans, the disease is often self-limiting accompanied by fever [335]. No human-to-human transmission of the virus is documented [336]. RVFV mainly infects hepatocytes and monocytes thus its major replication site is the liver from which it can spread through the bloodstream to other tissues [336]. The virus encodes for a non-structural protein, NSs, a major virulence factor inhibiting both IFN production [337, 338] and PKR activation [339, 340]. Therefore, viruses lacking the NSs gene are attenuated and they induce IFN expression [339]. A naturally occurring isolate, called clone 13, with a deletion in the NSs region enables IFN-α/β production and is strongly attenuated and immunogenic in mice [338]. In this study, an attenuated IFN sensitive reporter RVFV was used.

1.2.4.4 Vesicular stomatitis virus

Vesicular stomatitis virus (VSV) belongs to the family of Rhabdoviridae containing a negative-sensed, ssRNA genome. Mammals, e.g., horses, cattle and pigs, and their insect vectors are natural hosts of VSV. The VSV-induced disease is normally non-lethal [341] and symptoms are blisters in the mouths or feet of infected animals resembling foot and mouth disease [342]. In humans, the infection is normally asymptomatic or mild and especially occurs in laboratory and agricultural workers when in contact with infected material/animals [341, 343]. VSV uses ubiquitously expressed cell-surface molecules such as phosphatidylserine and sialoglycolipids for cell attachment [343]. Nowadays, VSV is used as an attractive platform tool for vaccine and oncolytic vectors due to its broad host range and missing immunity in humans [344]. The IFN sensitive VSV preferentially replicates in cancer cells as many tumors have a deficiency in IFN signaling. VSV G, the glycoprotein needed for attachment and cell entry, is largely used for pseudotyping of other viruses or lentiviral vectors [345].

1.3 Aim of this study

Even though RIG-I and MDA5 were identified as type I IFN inducers for almost two decades [18, 63, 346] many open questions concerning the RLR pathway still exist. Earlier research focused on MDA5 and especially RIG-I; thus, the role of LGP2 is still most enigmatic. The mode-of-action of LGP2 in RLR signaling is not completely understood especially with regards to its regulatory switch (enhancing MDA5 and inhibiting RIG-I signaling). LGP2's synergy with MDA5 constitutes the most comprehensive analysis so far. Posttranslational modifications of LGP2 are still underexplored, although quite extensively investigated in the case of RIG-I and MDA5. Naturally occurring polymorphisms of LGP2 correlated to disease are unknown, although RIG-I and MDA5 gain- and loss-of-functions were described. HDV was discovered to be sensed by MDA5 [48], yet the role of LGP2 is not understood. Recently, LGP2 was shown to be important for the immune response upon SARS-CoV-2 infection [49] however was not investigated in depth.

Thus, the overall objective of this study was a deeper characterization of LGP2 in both RIG-I- and MDA5-mediated signaling. The following specific sub-aims were as follows:

- Investigation of the importance of LGP2 RNA binding and ATP hydrolysis in different stimulation contexts
- Investigation of the role of LGP2 in MDA5-mediated immune response and viral repression upon HDV infection
- Investigation of the impact of natural LGP2 polymorphisms on RLR regulation and viral replication upon infections including SARS-CoV-2, HDV, SeV, ZIKV
- Investigation of posttranslational regulation of LGP2 on the level of phosphorylation and its functional relevance

To achieve these goals, RIG-I- and MDA5-specific read-out systems were established using two different, IFN competent cell culture systems in the context of several viral infections and synthetic dsRNA stimulation. The role of LGP2 functional domains and LGP2 phosphorylation and the impact of three frequent variants was analyzed in RIG-I and MDA5 signaling. The experiments were performed in immunocompetent HepaRG^{NCTP} and A549 cells, two cell lines with different endogenous levels of LGP2.

In a first step, experiments were performed in easy to manipulate A549 cells with specific KO and overexpression to investigate selective responses upon stimulation with (i) reporter viruses and (ii) synthetic dsRNA to exclude viral counteractions.

The role of LGP2, its ATP hydrolysis and RNA binding function, and the contribution of naturally occurring LGP2 variants were further studied in an authentic HDV infection system using HepaRG^{NTCP} cells. IFN response and HDV replication were measured. Moreover, the mechanism of LGP2-MDA5 synergy was further analyzed in HepaRG^{NTCP} cells. To investigate the broader role of LGP2 polymorphisms in the IFN response activation and viral repression further infections with MDA5 and RIG-I activating viruses were performed in both A549 and HepaRG^{NTCP} cells.

To provide insights into the regulation mechanism of LGP2 by PTMs its phosphorylation was investigated by MS. Identified phosphorylation sites were further tested in functional assays by using phosphomimetic and -ablative mutants in multiple read-out systems.

2 MATERIAL AND METHODS

2.1 Material

2.1.1 Software and instruments

Table 2: Instruments.

Instruments	Provider
Analytical balance LP-3102	VWR International GmbH, Germany
Analytical fine balance LA-124i	VWR International GmbH, Germany
Biological safety cabinet Safe 2020	Thermo Fisher Scientific Inc., USA
C1000 Touch Thermal Cycler	Bio-Rad Laboratories GmbH, Germany
C1000 Touch Thermal Cycler	Bio-Rad Laboratories GmbH, Germany
Centrifuge 5424	Eppendorf AG, Germany
Centrifuge 5424 R	Eppendorf AG, Germany
Centrifuge 5810 R	Eppendorf AG, Germany
Centrifuge Sorvall RC-5C plus	Sorvall, Germany
CFX Connect™ Real-Time PCR Detection System	Bio-Rad Laboratories GmbH, Germany
CO2 Cell incubator IncuSafe	Sanyo, UK
CO2 Cell Incubator MCO-20AIC	Panasonic Healthcare Co., Ltd., Japan
ECL ChemoCam imager 3.2	INTAS Science Imaging Instruments, Germany
Electric Power Supply EPI 500/400 Amersham	Pharmacia Biotech, Germany
ELISA plate reader Multiskan Ex	Thermo Fisher Scientific Inc., USA
Freezer Liebherr Premium	Liebherr-International Deutschland GmbH, Germany
Fridge Med Line	Liebherr-International Deutschland GmbH, Germany
Gel iX imager	INTAS Science Imaging Instruments, Germany
Gel-iX-imager	Intas Science Imaging Instruments, Germany
Hamilton Gastight 50	Hamilton Messtechnik GmbH, Germany
Heidolph Duomax 1030	Heidolph Instruments GmbH & Co. KG, Germany
HI-2211 Bench Top pH & mV Meter	HANNA instruments Deutschland GmbH, Germany
Ikamag Reo Magnetic stirrer	IKA®-Werke GmbH & CO. KG, Germany
Laminar flow Safe 2020	Thermo Fisher Scientific Inc., USA
Liquid nitrogen tank	Tec-lab, Germany
Microscope Primovert	Zeiss, Germany
Microwave Oven	Clatronic, Germany
Mini Trans-Blot® Cell	Bio-Rad Laboratories GmbH, Germany
Mini-PROTEAN® Tetra Handcast Systems	Bio-Rad Laboratories GmbH, Germany

Instruments	Provider
Mini-PROTEAN® Tetra Vertical Electrophoresis Cell	Bio-Rad Laboratories GmbH, Germany
Mithras LB 940 Multimode Microplate Reader	Berthold Technologies, Germany
Mithras² LB 943 Multimode reader	Berthold Technologies, Germany
Multi-Axle Rotating mixer	NeoLab, Germany
Multi-channel pipette 10-100	Eppendorf, Germany
Multi-channel pipette 10-300	Eppendorf, Germany
NanoDrop 1000 Spectrophotometer	Thermo Fisher Scientific Inc., USA
neoLab Mini Vacuum pump and compressor	NeoLab, Germany
Nikon microscope Eclipse Ti	Nikon, Japan
PerfectBlue™ Gelsystem Mini S	VWR International, Germany
Pipetboy Acu 2 Integra	Biosciences GmbH, Germany
Pipette 10 µl, 20 µl, 200 µl, 1000µl Research plus	Eppendorf AG, Germany
PowerPacTM Basic	Bio-Rad Laboratories GmbH, Germany
PowerPacTM Hc	Bio-Rad Laboratories GmbH, Germany
ThermoForma Incubator 3862	Labotect, Germany
Thermomixer Comfort 1.5 ml	Eppendorf AG, Germany
Thermomixer F1.5	Eppendorf AG, Germany
Trans-Blot® Turbo™ System	Bio-Rad Laboratories GmbH, Germany
UV Transilluminator	VilberLourmat, Germany
Vacuubrand BVC professional	Vacuubrand GmbH & Co. KG, Germany
Vortex Genie 2	Scientific Industries Inc., USA
Waterbath GFL 1083	GFL, Germany

Table 3: Software.

Software	Provider
Bio-Rad CFX Manager	Bio-Rad Laboratories, USA
EndNote	Clarivate Analytics, USA
GraphPad Prism 8	GraphPad Software, USA
Ilastik	Sommer et al. [347], Heidelberg Collaboratory for Image Processing (HCI), University of Heidelberg, Germany
ImageJ	Wayne Rasband, NIH, USA
INTAS Chemostar	INTAS Science Imaging, Germany
LabImage 1D	Kapelan Bio-Imaging, Germany
Microsoft Office	Microsoft, USA
NIS-Elements Advanced Research	Research Nikon, Germany
SnapGene	GSL Biotech LLC, USA

2.1.2 General lab consumables

Table 4: Consumables.

Consumable	Provider
Bacteria culture plate, 10 cm	Falcon Corning GmbH, Germany
Cell culture plate, 6 well, 24 well, 96 well	Greiner Bio-One GmbH, Germany
Cell scraper	Sarstedt AG & Co., Germany
Cover slips	Karl Hecht GmbH, Germany
Cryo vials	Greiner Bio-One GmbH, Germany
Dishes 6 cm, 10 cm, 15 cm	Greiner Bio-One GmbH, Germany
Extra thick blot filter paper	Bio-Rad Laboratories GmbH, Germany
Face mask	Rösner-Mautby Meditrade Holding GmbH, Germany
Falcon, 15 ml and 50 ml	Corning GmbH, Germany
Filter 0.45 µm	GE Healthcare, USA
Glass slides SuperFrost Ultra Plus®	Carl Roth GmbH & Co. KG
Half area ELISA plate, 96 well	Greiner Bio-One GmbH, Germany
Immun-Blot® PVDF Membrane	Bio-Rad Laboratories GmbH, Germany
Neubauer counting chamber	BRAND GmbH + CO KG, Germany
Reaction tube 1.5 ml and 2 ml	Sarstedt AG & Co., Germany
Reaction tube, 1.5 ml DNA low binding	Sarstedt AG & Co., Germany
Scalpel	FEATHER®, Japan
Sealing sheets PCR plates	Bio-Rad Laboratories GmbH, Germany
Serological pipettes 2, 5, 10, 25 and 50 ml	Corning GmbH, Germany
Syringe 5, 10, 20 ml	BD, USA
Tips 10, 100 and 1000 µl, filtered	STARLAB GmbH, Germany
Tips 10, 200 and 1000 µl, refill pack	Greiner Bio-One GmbH, Germany
Whatman chromatography paper, grade 3mm	Sigma-Aldrich, USA
XCEED Nitrile Gloves, S	Ansell, Australia

2.1.3 Kits

Table 5: Kits.

Kit	Provider
CalPhos™ Mammalian transfection kit	Takara Bio, Japan
DIY Human IFN Lambda 1/2/3 (IL-29/28A/28B) ELISA	PBL Assay Science, USA
High-Capacity cDNA Reverse transcription Kit with RNase Inhibitor	Thermo Fisher Scientific Inc., USA
Monarch Plasmid Miniprep Kit	New England Biolabs GmbH, USA
Monarch Total RNA Miniprep Kit	New England Biolabs GmbH, USA
NucleoBond® PC 500	Macherey-Nagel GmBH & Co. KG, Germany
NucleoSpin® Gel and PCR Cleanup	Macherey-Nagel GmBH & Co. KG, Germany
NucleoSpin® Plasmid	Macherey-Nagel GmBH & Co. KG, Germany
NucleoSpin® RNA Plus	Macherey-Nagel GmBH & Co. KG, Germany
NucleoSpin® Tissue	Macherey-Nagel GmBH & Co. KG, Germany
Pierce™ BCA Protein Assay Kit	Thermo Fisher Scientic Inc., USA
Pierce™ Silver Stain Kit	Thermo Fisher Scientic Inc., USA

2.1.4 Reagents

Table 6: Reagents.

Reagent	Provider
4',6-Diamidino-2-Phenylindole, Dihydrochloride (DAPI)	Invitrogen, Life Technologies GmbH, USA
Acetone	Sigma-Aldrich, USA
Agarose	Sigma-Aldrich, USA
Ammonium peroxydisulfate (APS)	Carl Roth GmbH & Co. KG, Germany
Ampicillin sodium salt	MP Biomedicals, USA
Anti-HA, Agarose conjugate	Sigma-Aldrich, USA
Blasticidin S hydrochloride	MP Biomedicals, USA
Bovine serum albumin (BSA), IgG-free	Carl Roth GmbH & Co. KG, Germany
BP and LR clonase II Enzyme Mix	Life Technologies, Germany
Calf Intestinal Phosphatase (CIP)	New England Biolabs GmbH, USA
Carbenicillin disodium salt	Life Technologies, Germany
Clarity™ Western ECL Substrate	Bio-Rad Laboratories GmbH, Germany
Coelentarazine	PJK GmbH, Germany
dimethyl sulfoxide (DMSO)	VWR International, Germany
Dithiothreitol (DTT)	Life Technologies, Germany
D-Luciferin	PJK, Germany

Reagent	Provider
DMEM, high glucose	Life Technologies, Germany
DNA Gel Loading Dye (6X)	Thermo Fisher Scientific Inc, USA
DNA ladder, 100 bp, GeneRuler	Thermo Fisher Scientific Inc., USA
Dynabeads™ M-280 Streptavidin	Invitrogen, Life Technologies GmbH, USA
ECL™ Prime Western blotting detection reagent	Sigma-Aldrich, USA
EDTA	AppliChem, Germany
Ethanol	Sigma-Aldrich, USA
Fetal Calf serum (FCS)	Capricorn Scientific GmbH, Germany
Fluoromount-G®	Southern Biotech, USA
Geneticin (G418) sulfate	Santa Cruz Biotechnology, Inc, USA
Gentamicin (50 mg/mL)	Life Technologies, Germany
Glutamine, L-; (200 mM, 100x)	Life Technologies GmbH
Glycerol	Sigma-Aldrich, USA
GlycoBlue Blue Coprecipitant	Invitrogen, Life Technologies GmbH, USA
HA antibody (16B12 clone)	BioLegend, USA
Hydrocortisone-hemisuccinate	Sigma-Aldrich, USA
Insulin	Sigma-Aldrich, USA
Isopropanol	Sigma-Aldrich, USA
Kanamycin monosulfate	Sigma-Aldrich, USA
Lipofectamine 2000	Life Technologies, Germany
Lipofectamine RNAiMax	Life Technologies, Germany
Magnesium chloride hexahydrate	Merck Millipore, Germany
Methanol	Sigma-Aldrich, USA
Midori Green	Nippon Genetics Europe GmbH, Germany
Milk powder, blotting grade	Carl Roth GmbH & Co. KG, Germany
Morpholino propane sulfonic acid (MOPS)	Carl Roth GmbH & Co. KG, Germany
N-ethylmaleimide (NEM)	Sigma-Aldrich, USA
Non-essential amino acids	Life Technologies, Germany
Nonidet P-40	AppliChem, Germany
OptiMEM	Life Technologies, Germany
Paraformaldehyde	Merck Millipore, Germany
Para-nitrophenylphosphate (pNPP), disodium salt	Sigma-Aldrich, USA
Penicillin/Streptomycin	Life Technologies, Germany
Phage Lambda DNA / Sty I Marker	AppliChem, Germany
Pierce Protein A/G Magnetic Beads	Thermo Fisher Scientific Inc., USA
Poly(C) Potassium Salt	Sigma-Aldrich, USA
Poly(I:C) (HMW) Biotin	InvivoGen, France
Poly(I:C) (HMW)	InvivoGen, France
Polyethylene glycol (PEG) 8000	Sigma-Aldrich, USA
Potassium chloride (KCl)	Sigma-Aldrich, USA
Potassium dihydrogen phosphate (KH_2PO_4)	AppliChem, Germany

Reagent	Provider
Potassium hydroxide (KOH)	Sigma-Aldrich, USA
Precision Plus Protein™ Dual Color Standards	Bio-Rad Laboratories GmbH, Germany
Protease Inhibitor Cocktail, cOmplete™, EDTA-free	Roche, Germany
Puromycin dihydrochloride	Sigma-Aldrich, USA
Puromycin dihydrochloride	Sigma-Aldrich, USA
Q5® High-Fidelity DNA Polymerase	New England Biolabs GmbH, USA
qSCRIPT XLT 1-Step RT-qPCR ToughMix	Quantabio, USA
Restriction enzymes	New England Biolabs GmbH, USA
RNAse inhibitor	Thermo Fisher Scientific Inc., USA
RNAzol® RT	Sigma-Aldrich, USA
Rotiphorese® Gel 40 (29:1)	Carl Roth GmbH & Co. KG, Germany
Sodium chloride	Sigma Aldrich, USA
Sodium dodecyl sulfate (SDS)	Carl Roth GmbH & Co. KG, Germany
Sodium fluoride	Sigma-Aldrich, USA
sodium hydroxide	Sigma-Aldrich, USA
Sodium orthovanadate (Na_3VO_4)	Sigma-Aldrich, USA
SYBR® Green iTaqTM Universal Supermix	Bio-Rad Laboratories GmbH, Germany
SYBR® Green iTaqTM Universal Supermix	Bio-Rad Laboratories GmbH, Germany
T4 DNA-Ligase	Thermo Fisher Scientific Inc., USA
Tetramethylethylenediamine, TEMED	AppliChem, Darmstadt
TMB Substrate Set	BioLegend, USA
TRIS	Carl Roth GmbH & Co. KG, Germany
Triton-X-100	AppliChem, Darmstadt
Trypsin-EDTA (0.05%)	Life Technologies GmbH, Germany
Tween-20	AppliChem, Germany
Water, DNAse- and RNAse-free	MP Biomedicals, USA
William´s Medium E	Life Technologies GmbH
β-glycerophosphate (BGP), disodium salt,	Sigma-Aldrich, USA
β-mercaptoethanol	Sigma-Aldrich, USA

2.1.5 Solutions

Table 7: Solutions.

Name	Content
B+W buffer (2x)	10 mM TRIS-HCl, 1 mM EDTA, 2 M NaCl
Cryopreservation medium	FCS with 10% DMSO
DMEM supplemented	DMEM (high glucose), non-essential amino acids (1x), penicillin and streptomycin (100 IU/ml), FCS (10%, heat-inactivated at 56°C for 30 min)
EDTA (100 mM)	in RNAse free H_2O, sterile filtrated
IP buffer (RNA-IP)	20 mM MOPS, 120 mM KCl, 2 mM β-mercaptoethanol, 1x protease inhibitor, 200 IU/ml RNAse inhibitor (in RNAse free H_2O)
IP lysis buffer ("Hei")	20 mM TRIS-HCl, 150 mM NaCl, 0.5% NP-40, 1 mM EDTA, 1x protease inhibitor
IP lysis buffer ("MS")	20 mM TRIS, 100 mM NaCl, 0.1% NP-40, 50 mM NaF, 5 mM Na_3VO_4, 60 mM BGP, 15 mM pNPP, 20 mM NEM, 1x protease inhibitor
IP lysis buffer ("NG")	20 mM TRIS, 100 mM NaCl, 0.1% NP-40, 50 mM NaF, 5 mM Na_3VO_4, 20 mM NEM, 1x protease inhibitor
KCl (1M)	in RNAse free H_2O, sterile filtrated, pH 7.4
KPO_4 (0.1 M)	in H_2O, pH 7.8
Laemmli buffer (6x)	5% (v/v) glycerol, 16.25 mM TRIS (pH 6.8), 0.5% (g/v) SDS, 1.25% (v/v) β-mercaptoethanol, 10 µg/ml bromophenol blue
Luciferase assay buffer	25 mM KPO_4 (pH 7.8), 15 mM Glycyl Glycin, 15 mM $MgSO_4$, 4 mM EGTA (pH 7.6)
Luciferase lysis buffer	1% Triton X-100, 25 mM Glycyl Glycin, 15 mM $MgSO_4$, 10% Glycerol, 4 mM EGTA (pH 7.6)
Lysis buffer (RNA-IP)	20 mM MOPS, 120 mM KCl, 2 mM β-mercaptoethanol, 1x protease inhibitor, 200 IU/ml RNAse inhibitor, 0.5% NP-40 (in RNAse free H_2O)
Lysogeny broth (LB) agar	1% peptone, 0.5% yeast extract, 0.5% NaCl, 1.5 % agarose
Lysogeny broth (LB) medium	5 g/l NaCl, 10 g/l tryptone, 5 g/l yeast extract
MOPS (100 mM)	in RNAse free H_2O, sterile filtrated, pH 7.4
NaOH (1 M)	in RNAse free H_2O, sterile filtrated
NP-40 (10%)	in RNAse free H_2O
PBS (10x)	27 mM KCl, 15 mM KH_2PO_4, 1.4 M NaCl, 81 mM Na_2HPO_4, pH 7.2-7.8
PBS-Tween (PBS-T)	0.1% (v/v) Tween-20 in PBS (1x)
Resolving gel buffer for SDS-PAGE	1.5 M Tris, 0.4% SDS pH 8.8
Solution A	0.1 M NaOH, 0.05 M NaCl (in RNAse free H_2O, sterile filtrated)
Solution B	0.1 M NaCl (in RNAse free H_2O, sterile filtrated)
Stacking gel buffer for SDS-PAGE	1 M TRIS, 0.8% SDS pH 6.8

Name	Content
TBS (10x)	20 mM TRIS, 150 mM NaCl, pH 7.6
TBS-Tween (TBS-T)	0.1% (v/v) Tween-20 in TBS (1x)
TGS (10x)	25 mM TRIS, 192 mM glycine, 0.1% SDS
TRIS-HCl (200 mM)	in RNAse free H_2O, sterile filtrated, pH 7.5
Wash buffer (RNA-IP)	20 mM MOPS, 120 mM KCl, 2 mM β-mercaptoethanol, 1x protease inhibitor (in RNAse free H_2O)
WB transfer buffer (10x)	25 mM TRIS, 150 mM glycine, pH 8.3
William's E supplemented	William's E medium, 10% FCS (heat-inactivated), 2 mM L-glutamine, 50 U/ml penicillin, 50 µg/ml streptomycin, 50 µM hydrocortisone-hemisuccinate, 5 µg/ml insulin

2.1.6 Antibodies

Table 8: Primary antibodies.

Primary antibody	Origin	Clonality	Provider	Dilution
ADAR1	rabbit	mono	Cell Signaling (14175)	1:1,000
Calnexin	rabbit	poly	Enzo Life Science (ADI-SPA-865-F)	1:1,000
DHX30	rabbit	poly	Novus Biologicals (NBP1-26603)	1:1,000
DICER1	rabbit	rabbit	Cell Signaling (3363S)	1:1,000
HA	mouse	mono	Sigma-Aldrich (H3663)	1:2,000
HDAg	human	poly	Patient serum (University Hospital Heidelberg)	1:3,000
LGP2	rabbit	poly	IBL	1:100
MAVS	rabbit	poly	Enzo Life science	1:1,000
MDA5	rabbit	poly	Enzo Life Science	1:1,000
Mx1	mouse	mono	Georg Kochs (Freiburg)	1:1,000
Myc	mouse	mono	Santa Cruz (sc-40)	1:1,000
phospho-serine	mouse	mono	Millipore (05-1000)	1:1,000
phospho-threonine	mouse	mono	Cell Signaling (9386S)	1:1,000
phospho-tyrosine	rabbit	poly	Millipore (05-1050X)	1:1,000
PKR	rabbit	mono	Abcam (ab32506)	1:1,000
RIG-I	mouse	mono	Adipogen (AG-20B-0009)	1:1,000
STAU1	rabbit	mono	Abnova (H00006780-DO1)	1:1,000
α-tubulin	mouse	mono	Sigma-Aldrich (T5168)	1:8,000
β-actin	mouse	mono	Sigma-Aldrich (A5441)	1:5,000

Table 9: Secondary antibodies.

Secondary antibody	Origin	Clonality	Provider	Dilution
human Alexa Fluor 555	goat	poly	Invitrogen (A-21433)	1:1,000
mouse-HRP	goat	poly	Sigma-Aldrich (A4416-5X1ML)	1:10,000
rabbit-HRP	goat	poly	Sigma-Aldrich (A6154-5X1ML)	1:20,000

2.1.7 Primers and oligonucleotides

Table 10: Primers for guide RNA cloning.

Name	Forward (5'-3')	Reverse (3'-5')
LGP2 guide RNA-1	CACCagcttcggtcctaccaatgg	AAACccattggtaggaccgaagct
LGP2 guide RNA-2	CACCtatcatcatctggctgccca	AAACtgggcagccagatgatgata
LGP2 guide RNA-3	CACCcggctgcttatgtggccaag	AAACcttggccacataagcagccg
MAVS guide RNA-1	CACCtcagccctctgacctccagc	AAACgctggaggtcagagggctga
MAVS guide RNA-2	CACCcgctggaggtcagagggctg	AAACcagccctctgacctccagcg
MDA5 guide RNA-1	CACCggattgtgcagaaagaaaac	AAACgttttctttctgcacaatcc
MDA5 guide RNA-2	CACCaatcagagcctgttaactct	AAACagagttaacaggctctgatt
MDA5 guide RNA-3	CACCgggcatggagaataactcat	AAACatgagttattctccatgccc
NT guide RNA-1	CACCaagcgggcacacatgacaag	AAACcttgtcatgtgtgcccgctt
NT guide RNA-2	CACCggccctctagaaaagtctcg	AAACcgagacttttctagagggcc
NT guide RNA-3	CACCgcactcacatcgctacatca	AAACtgatgtagcgatgtgagtgc
RIG-I guide RNA-1	CACCctgttggagctccaggagga	AAACtcctcctggagctccaacag
RIG-I guide RNA-2	CACCtggagctccaggaggaaggc	AAACgccttcctcctggagctcca
RIG-I guide RNA-3	CACCgatatcggttgggataattc	AAACgaattatcccaaccgatatc
uppercase: overhang for BsmBI-specific restriction enzyme cloning		

Table 11: qRT-PCR primers.

qRT-PCR primer	Forward (5'-3')	Reverse (3'-5')
CXCL10	ccttatctttctgactctaagtggc	acgtggacaaaattggcttg
GAPDH	gaaggtgaaggtcggagtc	gaagatggtgatgggatttc
HDV	gcgccggcygggcaac	ttcctcttcgggtcggcatg
IFIT1	gaagcaggcaatcacagaaa	tgaaaccgaccatagtggaa
IFN-β	accaacaagtgtctcctcca	aagcctcccattcaattgcc
IFN-γ	actgacttgaatgtccaacgca	atctgactccttttcgcttcc
IFN-λ1	cgccttggaagagtcactca	gaagcctcaggtcccaattc
IL10	ggggagaacctgaagaccct	cggccttgctcttgttttca
IL22RA1	gcatggaaggttctggcaa	aggtactgtggtgtcccttcct
LGP2	ggcccagctactgattgg	ttgatcagctcccgcttc
MDA5	tcgtcaaacaggaaacaatga	gttattctccatgccccaga
Mx1	aagagccggctgtggatatg	ggcggttctgtggaggttaa
RIG-I	ccctggtttagggaggaaga	tcccaactttcaatggcttc
RSAD2	cgtgagcatcgtgagcaatg	tcttctttccttggccacgg
SARS-CoV-2	agcctcttctcgttcctcatcac	ccgccattgccagccattc
SeV*	caaaagtgagggcgaaggagaa	cgcccagatcctgagatacaga
TLR3	ttgccttgtatctacttttgggg	tcaacactgttatgtttgtgggt
ZIKV	ccgctgcccaacacaag	ccactaacgttcttttgcagacat
*from [348]		

Table 12: Sequencing primers.

Sequencing primer	Sequence (5'-3')	Direction	Usage
hU6	acgatacaaggctgttagagaga	forward	verification of guide RNA cloning
pDONR	taacgctagcatggatctc	forward	sequencing of pDONR207 gateway insert from 5' direction
pDONR	gcaatgtaacatcagagat	reverse	sequencing of pDONR207 gateway insert from 3' direction
cPPT	taatagcaacagacatac	forward	sequencing of pWPI gateway insert from 5' direction
EMCV	cggcaatatggtggaaaataac	reverse	sequencing of pWPI gateway insert from 3' direction
M13	gtaaaacgacggccagt	forward	sequencing of pENTR221 gateway insert from 5' direction
M13	aacagctatgaccatg	reverse	sequencing of pENTR221 gateway insert from 3' direction
gDNA LGP2	cctactagagcaggtgag	forward	sequencing of genomic LGP2 exon 1
gDNA LGP2	cctgaagagctaagaccc	reverse	sequencing of genomic LGP2 exon 1
LGP2 5' UTR	gcagacctacctactagagc	forward	LGP2 mRNA amplification by PCR
LGP2 3' UTR	gcactgcagcaatgaggtg	reverse	LGP2 mRNA amplification by PCR
LGP2 5' UTR short	gcagacctacctac	forward	sequencing of endogenous LGP2 mRNA
LGP2 3' UTR short	gcactgcagcaat	reverse	sequencing of endogenous LGP2 mRNA
LGP2 611	gtcaccccagaactgctg	forward	sequencing of LGP2
LGP2 763	gctgctcatacatttgcg	reverse	sequencing of LGP2
MDA5 705	cagccaaatctggagaag	forward	sequencing of MDA5
MDA5 1480	cagcttcacctggtgttg	forward	sequencing of MDA5
MDA5 2272	ccatctgattggagctg	forward	sequencing of MDA5

Table 13: Primers for cloning.

Cloning primer	Sequence (5'-3')	Direction	Usage
MDA5-GW	GGGGACAAGTTTGTACAAAAAAGCAGGCTTCatgtcgaatgggtattccacagac	forward	(1)
MDA5-stop-GW	GGGGACCACTTTGTACAAGAAAGCTGGGTCtcaatcctcatcactaaataaac	reverse	(1)
MDA5-no stop-GW	GGGGACCACTTTGTACAAGAAAGCTGGGTCatcctcatcactaaataaac	reverse	(1)
LGP2-GW	GGGGACAAGTTTGTACAAAAAAGCAGGCTTCatggagcttcggtcctacc	forward	(1)
LGP2-stop-GW	GGGGACCACTTTGTACAAGAAAGCTGGGTCctagtccagggagaggtcc	reverse	(1)
LGP2 K605E	caaggactggga**g**cctgg	forward	(2)
LGP2 K605E	ccagg**c**tcccagtccttg	reverse	(2)
LGP2 K651E	gatccaggccaaa**g**agtggtc	forward	(2)
LGP2 K651E	gaccact**c**tttggcctggatc	reverse	(2)
DDX6-GW	GGGGACAAGTTTGTACAAAAAAGCAGGCTTCatgagcacggccagaac	forward	(1)
DDX6-stop-GW	GGGGACCACTTTGTACAAGAAAGCTGGGTCctaaggtttctcatcttctacagG	reverse	(1)
LGP2 S464A	caatgaaatc**g**ccatggtccagg	forward	(2)
LGP2 S464A	cctggaccatgg**c**gatttcattg	reverse	(2)
LGP2 S464D	ccaatgaaatc**ga**catggtccaggc	forward	(2)
LGP2 S464D	gcctggaccatg**tc**gatttcattgg	reverse	(2)
LGP2 S464E	ccaatgaaatc**gag**atggtccaggc	forward	(2)
LGP2 S464E	gcctggaccat**ctc**gatttcattgg	reverse	(2)
LGP2 guide3 resistant	*tgcggcctacgtcgctaaacgc*ccacctagagactgtggatgg	forward	(2)
LGP2 guide3 resistant	*gcgtttagcgacgtaggccgca*gcccgggtcttcccgg	reverse	(2)
LGP2 S365A/D/E	ctcggggtatcatcttcacc	forward	(3)
LGP2 S365A	ggctgtt**gg****c**gctactgaac	reverse	(3)
LGP2 S365D	ggctgtt**gtc**gctactgaac	revere	(3)
LGP2 S365E	ggctgtt**ctc**gctactgaac	reverse	(3)
LGP2 S169A/D/E	ccagcacctggggtagcg	reverse	(3)
LGP2 S169E	gtctcacagcc**gag**ccaggcac	forward	(3)
LGP2 S169A	gtctcacagcc**g**ccccaggcac	forward	(3)
LGP2 S169D	gtctcacagcc**ga**cccaggcac	forward	(3)
LGP2 K30A	gcctacgtcgctaaacgccacct	forward	(4)
LGP2 K30A	cgcagcccgggtc**gc**cccggcacc	reverse	(4)

Cloning primer	Sequence (5'-3')	Direction	Usage
LGP2 Q425R	agatggaaccctgaaccttc	forward	(3)
LGP2 Q425R	tggaacttc**c**ggatcacttc	reverse	(3)
LGP2 N461S	ggctcttgacca**g**tgaaatctcc	forward	(3)
LGP2 N461S	cataacgcaccaccacattg	reverse	(3)
LGP2 R523Q	gccaagatcc**a**ggatctgc	forward	(3)
LGP2 R523Q	ctggtactcggcctggtc	reverse	(3)
LGP2 S363A S364A S365A S367A (ΔSC)	**ccaacgcc**cctcggggtatcatcttcac c	forward	(3)
LGP2 S363A S364A S365A S367A (ΔSC)	**cggcagc**gaactgcctttgcaggatc	reverse	(3)
superscript: attB1 site (forward) / attB2 site (reverse); underlined: start codon (forward) / stop codon (reverse); italic: silent mutations on guide3 target site; bolt: mutation-causing nucleotides; (1): LR cloning; (2) Fusion PCR; (3): site-directed mutagenesis by using DpnI digest, (4): site-directed mutagenesis by using DpnI digest with guide3 resistant LGP2 WT plasmid as template			

2.1.8 Plasmids

Table 14: Plasmids.

Plasmid	Prokaryotic resistance	Eukaryotic resistance
pCMV-dR8.91	ampicillin	-
pMDG.2	ampicillin	-
pENTR207 LGP2	gentamycin	-
pENTR221 LGP2[1]	kanamycin	-
pENTR207 LGP2 guide3 resistant	gentamycin	-
pENTR221 LGP2 K30A (ΔATPase)[1]	kanamycin	-
pENTR221 LGP2 K634E ((ΔRNA binding (RB)^{*single})[1]	kanamycin	-
pENTR221 LGP2 K605E K634E K651E (ΔRNA binding (RB)^{*triple})	gentamycin	-
pENTR207 LGP2 S464A	gentamycin	-
pENTR207 LGP2 S464D	gentamycin	-
pENTR207 LGP2 S365A	gentamycin	-
pENTR207 LGP2 S365D	gentamycin	-
pENTR221 LGP2 S169A	kanamycin	-
pENTR221 LGP2 S169D	kanamycin	-
pENTR207 LGP2 S365A S464D (p-mock) guide3 resistant	gentamycin	-
pENTR207 LGP2 S365D S464A (p-activated) guide3 resistant	gentamycin	-
pENTR207 DDX6	gentamycin	-
pENTR207 MDA5	gentamycin	-
pENTR207 LGP2 S363A S364A S365A S367A (Δserine cluster (SC)) guide3 resistant	gentamycin	-
pENTR207 LGP2 K30A (ΔATPase) guide3 resistant	gentamycin	-
pENTR207 LGP2 K634E (ΔRNA binding (RB)^{*single}) guide3 resistant	gentamycin	-

Plasmid	Prokaryotic resistance	Eukaryotic resistance
pENTR207 LGP2 K605E K634E K651E (ΔRNA binding^{*triple}) guide3 resistant	gentamycin	-
pENTR207 LGP2 Q425R guide3 resistant	gentamycin	-
pENTR207 LGP2 N461S guide3 resistant	gentamycin	-
pENTR207 LGP2 R523Q guide3 resistant	gentamycin	-
pENTR4 NS5A JFH1	kanamycin	-
pWPI HA-LGP2	ampicillin	puromycin
pWPI HA-LGP2	ampicillin	blasticidin
pWPI LGP2	ampicillin	puromycin
pWPI LGP2	ampicillin	blasticidin
pWPI ROSA26 MDA5	ampicillin	blasticidin
pWPI ROSA26 LGP2	ampicillin	blasticidin
pWPI HA-LGP2	ampicillin	blasticidin
pWPI HA-LGP2 K30A (ΔATPase)	ampicillin	blasticidin
pWPI HA-LGP2 K634E (ΔRNA binding (RB)^{*single})	ampicillin	blasticidin
pWPI HA-LGP2 K605E K634E K651E (ΔRNA binding^{*triple})	ampicillin	blasticidin
LentiCRISPR v2	ampicillin	puromycin
pLentiCRISPR LGP2^{KO} guide3	ampicillin	puromycin
pLentiCRISPR MDA5^{KO} guide2	ampicillin	puromycin
pLentiCRISPR RIG-I^{KO} guide2	ampicillin	puromycin
pLentiCRISPR LGP2^{KO} guide3	ampicillin	neomycin
pLentiCRISPR NT guide1	ampicillin	puromycin
pWPI HA-LGP2 guide3 resistant	ampicillin	neomycin
pWPI HA-LGP2 K30A (ΔATPase) guide3 resistant	ampicillin	neomycin
pWPI HA-LGP2 K634E (ΔRNA binding (RB)^{*single}) guide3 resistant	ampicillin	neomycin
pWPI HA-LGP2 K605E K634E K651E (ΔRNA binding^{*triple}) guide3 resistant	ampicillin	neomycin
pWPI HA-LGP2 S363A S364A S365A S367A (Δserine cluster (SC)) guide3 resistant	ampicillin	neomycin
pWPI HA-LGP2 Q425R guide3 resistant	ampicillin	neomycin
pWPI HA-LGP2 N461S guide3 resistant	ampicillin	neomycin
pWPI HA-LGP2 R523Q guide3 resistant	ampicillin	neomycin
pWPI HA-DDX6	ampicillin	puromycin
pWPI HA-LGP2 S169A	ampicillin	blasticidin
pWPI HA-LGP2 S169D	ampicillin	blasticidin
pWPI HA-LGP2 S365A	ampicillin	blasticidin
pWPI HA-LGP2 S365D	ampicillin	blasticidin
pWPI HA-LGP2 S464A	ampicillin	blasticidin
pWPI HA-LGP2 S464D	ampicillin	blasticidin
pWPI HA-LGP2 S365A S464D (p-mock) guide3 resistant	ampicillin	neomycin
pWPI HA-LGP2 S365D S464A (p-activated) guide3 resistant	ampicillin	neomycin
pWPI HA-NS5A JFH1	ampicillin	puromycin

Plasmid	Prokaryotic resistance	Eukaryotic resistance
pWPI Myc-RIG-I[2]	ampicillin	neomycin
pWPI MDA5-Flag	ampicillin	blasticidin
pWPI NTCP	ampicillin	blasticidin

[1], obtained from Dr. Antje Reuter; [2], obtained from Dr. Joschka Willemsen; [3], obtained from Dr. Florian Lempp

2.1.9 Eukaryotic cells, bacteria, viruses

Table 15: Parental eukaryotic cell lines.

Parental cell lines	Species
HEK 293T (MCB)	Homo sapiens
HepaRG	Homo sapiens
A549	Homo sapiens

Table 16: Newly established eukaryotic cell lines.

A549-derived cell lines	
empty	RIG-I^{KO} clone R2-2#10 (guide RNA-2)[1]
UT-LGP2	RIG-I^{KO} clone R2-2#1 HA-LGP2 S169A
HA-DDX6	RIG-I^{KO} clone R2-2#1 HA-LGP2 S169D
HA-LGP2	RIG-I^{KO} clone R2-2#1 HA-LGP2 S464A
HA-LGP2 Myc-RIG-I	RIG-I^{KO} clone R2-2#1 HA-LGP2 S464D
HA-LGP2 Q425R	RIG-I^{KO} clone R2-2#1 HA-LGP2 S169A
HA-LGP2 N461S	RIG-I^{KO} clone R2-2#1 HA-LGP2 S365A
HA-LGP2 R523Q	RIG-I^{KO} clone R2-2#1 HA-LGP2 S464A
RIG-I^{KO} clone R2-2#1 (guide RNA-2)[1]	MDA5^{KO} clone M2-28 (guide RNA-2 clone 28)
LGP2^{KO} clone L2-9 (guide RNA-2 clone 9)	MDA5^{KO} clone M2-28 empty
LGP2^{KO} clone L2-10 (guide RNA-2 clone 10)	MDA5^{KO} clone M2-28 HA-LGP2
LGP2^{KO} clone L3-4 (guide RNA-3 clone 4)	MDA5^{KO} clone M2-28 UT-LGP2
MDA5^{KO} clone M1-8 (guide RNA-1 clone 8)	MDA5^{KO} clone M2-28 UT-LGP2 (ROSA26)
RIG-I ^{KO} MDA5^{KO} clone 10.2-19 (R2-2#10 MDA5 guide RNA-2 clone 19)	MDA5^{KO} clone M2-28 empty
RIG-I ^{KO} MDA5^{KO} clone 1.1-20 (R2-2#1 MDA5 guide RNA-1 clone 20)	MDA5^{KO} clone M2-28 HA-LGP2
RIG-I ^{KO} MDA5^{KO} clone 1.2-12 (R2-2#1 MDA5 guide RNA-2 clone 12)	MDA5^{KO} clone M2-28 HA-LGP2 ΔATPase
RIG-I ^{KO} clone MDA5^{KO} clone 1.2-27 (R2-2#1 MDA5 guide RNA-2 clone 27)	MDA5^{KO} clone M2-28 HA-LGP2 ΔRB^{*single}
MAVS^{KO} clone 1.77[2] (guide RNA-1)	MDA5^{KO} clone M2-28 HA-LGP2 ΔRB^{*triple}
RIG-I^{KO} clone R2-2#1 empty	MDA5^{KO} clone M2-28 empty
RIG-I^{KO} clone R2-2#1 HA-LGP2	MDA5^{KO} clone M2-28 HA-LGP2
RIG-I^{KO} clone R2-2#1 UT-LGP2	MDA5^{KO} clone M2-28 HA-LGP2 S169A

A549-derived cell lines	
RIG-I^{KO} clone R2-2#1 UT-LGP2 (ROSA26)	MDA5^{KO} clone M2-28 HA-LGP2 S169D
RIG-I^{KO} clone R2-2#1 HA-LGP2 ΔATPase	MDA5^{KO} clone M2-28 HA-LGP2 S464A
RIG-I^{KO} clone R2-2#1 HA-LGP2 ΔRB^{*single}	MDA5^{KO} clone M2-28 HA-LGP2 S464D
RIG-I^{KO} clone R2-2#1 HA-LGP2 ΔRB^{*triple}	MDA5^{KO} clone M2-28 HA-LGP2 S169A
RIG-I^{KO} clone R2-2#1 UT-MDA5 (ROSA26)	MDA5^{KO} clone M2-28 HA-LGP2 S365A
RIG-I^{KO} clone R2-2#1 UT-MDA5 (ROSA26) HA-LGP2	MDA5^{KO} clone M2-28 HA-LGP2 S464A
HepaRG-derived cell lines	
HepaRG^{NTCP} (parental cell line for other cells)	LGP2^{KO} pool HA-LGP2^{GR} ΔATPase
NT control pool (guide RNA-1)	LGP2^{KO} pool HA-LGP2 ^{GR} ΔRB^{*single}
RIG-I^{KO} pool (guide RNA-2)	LGP2^{KO} pool HA-LGP2^{GR} ΔRB^{*triple}
MDA5^{KO} pool (guide RNA-2)	LGP2^{KO} pool HA-LGP2^{GR} ΔSC
LGP2^{KO} pool (guide RNA-3)	LGP2^{KO} pool HA-LGP2^{GR} Q425R
RIG-I^{KO} LGP2^{KO} pool	LGP2^{KO} pool HA-LGP2^{GR} N461S
MDA5^{KO} LGP2^{KO} pool	LGP2^{KO} pool HA-LGP2^{GR} R523Q
NT control pool empty	LGP2^{KO} pool HA-LGP2^{GR} p-mock
LGP2^{KO} pool HA-LGP2^{GR}	LGP2^{KO} pool HA-LGP2^{GR} p-activated
[1], obtained from Sandra Wüst; [2], obtained from Dr. Silke Jung; ^{GR}, LGP2 guide RNA RNA-3 resistant version; UT: untagged	

Table 17: Bacteria.

Bacterial strain	Species
DH5α	Escherichia coli

Table 18: Viruses.

Virus	Description
HDV	genotype 1
ZIKV	MR-766 strain
SARS-CoV-2	BavPat1 isolate
EMCV	Mengovirus Zinc mutant
SeV	
VSV	Firefly reporter virus
RVFV	ΔNSs-Renilla reporter virus

2.2 Methods

2.2.1 Cell culture

2.2.1.1 Cultivation of eukaryotic cells

A549 and HEK 293T cells were cultivated in Dulbecco's modified eagle medium (DMEM) containing 10% heat-inactivated fetal calf serum (FCS), 100 U/ml penicillin, 100 µg/ml streptomycin and 1x non-essential amino acids. HepaRG-derived cells were cultured in Williams E medium, no glutamine (Life Technologies) supplemented with 10% heat-inactivated FCS, 100 U/ml penicillin, 100 µg/ml streptomycin, 2 mM L-glutamine, 50 µM hydrocortisone-hemisuccinate and 5 µg/ml insulin. All cells were maintained in a humidified incubator with 5% CO_2 and 95% relative humidity at 37°C.

For passaging and seeding of cells for experiments, the medium was aspirated and cells were washed once with PBS. To detach the cells, trypsin-EDTA was added to the cell culture dish, dispersed and sucked away. After incubation at 37°C for several minutes, cells were resuspended into pre-warmed medium of the desired volume. Cells were routinely passaged twice a week. Stable cell lines were created by lentiviral transduction as described in 2.2.1.6 and cultured in selection medium in the presence of 1 mg/ml (A549 cells) or 0.6 mg/ml (HepaRG cells) G418, respectively and/or 2.5-5 µg/ml puromycin and/or 5 µg/ml blasticidin. These antibiotics used as selection markers were not added at the experiments themselves.

2.2.1.2 Cryopreservation, storage and revival

Confluent cells were detached with trypsin-EDTA as described in 2.2.1.1, directly resuspended in ice-cold cryo-medium, distributed to freezing vials (6 tubes for one full 15 cm dish with 1.5 ml total volume each) and frozen at -80°C for at least 2 days prior to long-term storage in a liquid nitrogen tank.

For the revival of frozen cells, vials were put into a water bath of 37°C until almost all cells were thawed. Cells were then rapidly added to 7 ml cold medium and centrifuged for 8 minutes at 500xg. The cell pellet was resuspended into pre-warmed medium and seeded into a 10 cm dish.

2.2.1.3 Cell counting

Cells were detached and resuspended into fresh medium as described in 2.2.1.1 by thoroughly pipetting up and down. 10 µl of cell suspension was added into a Neubauer counting chamber to determine the cell number per ml.

2.2.1.4 Lipofectamine transfection

Cells were transfected with poly(I:C) (of especially high molecular weight (HMW)) or 5'ppp-dsRNA to activate RLR signaling. Non-stimulatory poly(C) was used to keep the total RNA amount equal when using different doses of poly(I:C) or 5'ppp-dsRNA. For transfection in 24 well plates, $1x10^5$ cells were seeded per well. The next day, 100 to 1,000 ng RNA was added into OptiMEM to a total of 50 µl. 2 µl lipofectamine was incubated with 48 µl OptiMEM for 5 minutes and then added to the RNA-OptiMEM and mixed well. After 20 minutes of incubation at room temperature (RT), the mixture was added to the cells where the medium was changed to fresh medium (500 µl per well). After 4 hours of incubation, another medium change was performed.

2.2.1.5 IFN-α stimulation

IFN-2α was diluted in DMEM and stored at -80°C. For stimulation, IFN-2α was usually diluted to 200 IU/ml in the respective cell culture medium and added to the cells for 24 hours.

2.2.1.6 Lentiviral production and generation of stable cell lines

Using the CRISPR/Cas9 technology for genome editing, stable knock-in or KO cell lines were generated by lentiviral transduction. Lentiviral particles were produced in HEK 293T (MCB) cells by calcium phosphate transfection of two packaging plasmids and one plasmid of interest using CalPhos™ Mammalian transfection kit (Takara).

One day before transfection, $1.2x10^6$ 293T cells were seeded into a 6 cm dish. The next morning, the culture medium was exchanged to fresh pre-warmed medium around 30 minutes prior to transfection. 6.4 µg pCMV-dR8.91 (HIV gag-pol-expressing plasmid), 2.1 µg pMD2.G (VSV-G envelope-expressing plasmid) and 6.4 µg pWPI vector encoding the gene of interest (for stable expression of a gene) or LentiCRISPR-v2 plasmid harboring the guide RNA of interest (for stable suppression of a gene) were added into sterile water to a total volume of 438 µl. 62 µl calcium solution (2 M) and 500 µl 2-fold HEPES-buffered saline (HBS) were added to the plasmid-water mixture and strongly intermixed. The solution was added drop-wise onto the cells. The medium was changed 7 to 10 hours after transfection. The supernatant containing the lentiviruses was collected around 48 hours, 56 hours and 72 hours after transfection, filtered through a 0.45 µm pore-size filter and either aliquoted for storage at -80°C or directly used to transduce target cells.

For the generation of stable cell lines, $6x10^4$ target cells were seeded in a 6 well plate and transduced 24 hours later with 1 ml to 2 ml of lentiviral particles. To increase transduction efficiency, transduction was optionally repeated 1- to 2-times. 36 hours after the first

transduction, cells were selected by the addition of respective antibiotics into the culture medium. Non-transduced target cells served as a negative control. Cells were propagated and aliquots were frozen for long-term storage (see 2.2.1.2). Target gene expression of generated knock-in cell lines was proven by Western blot analysis. If not stated otherwise overexpression constructs were established under the EF1-α promoter. In the case of KO cell pools, knockdown efficiency was determined by Western blotting compared to corresponding WT cells. In the case of RLR^{KO} and $MAVS^{KO}$, guide RNA constructs were tested on both A549 and HepaRG cells (Figure S 35). For stable HepaRG KO cell pools, guide RNA-2 was used in the case of RIG-I and MDA5 while guide RNA-3 was used for LGP2.

To generate single A549 cell clones, selected KO cell pools were seeded into 96 well plates with a density of 0.3 cells per well. Cells were cultivated for several days and screened for clonal expansion of cells within the single wells. Dense wells were passaged to 24 well plates, then to 6 well plates and 10 cm dishes to amplify the single-cell clones. KO efficiency was either tested by Western blot (see 2.2.4.2) or gDNA sequencing (see 2.2.1.7).

2.2.1.7 gDNA isolation and sequencing

To verify the KO of single $LGP2^{KO}$ A549 clones, sequencing of the LGP2 locus spanning the target sequence of the LGP2 CRISPR/Cas9 guide RNAs (within exon 1) was performed. Therefore, up to $1x10^7$ cells of several stable LGP2 guide 2- and 3-expressing single cells clones (for generation of single KO clones, see 2.2.1.6) and WT A549 (as control) were taken up into 200 µl of buffer T1 of the NucleoSpin® Tissue kit (Macherey-Nagel). Genomic DNA (gDNA) was isolated according to the manufacturer's instructions and eluted in water. Primers designed specifically for the amplification of the first exon of the genomic LGP2 locus (gDNA LGP2 fw and rev, see Table 12) were used to amplify this region by PCR (2.2.3.1.2). PCR product was purified and sent to sequencing. The resulting chromatograms of single-cell clones were aligned to the WT LGP2 sequence. CRISP-ID was used to predict the LGP2 protein sequence of all existing alleles within each clone [349]. Clones with no residual WT sequence were considered to be full LGP2 single KO clones.

2.2.2 Virus production and infection

Viruses used in this study are indicated below. Virus infection was used to measure RLR-induced innate response and/or viral replication in the respective cell lines. Except for HDV, infection of cells was performed in normal cultivation medium one day after seeding (with a total volume of 250 µl per one well of a 24 well format). After the desired time of infection, cells and supernatants were collected for different purposes. For IFN-λ ELISA, cell culture supernatants were collected, inactivated with a final concentration of 1% Triton-X-100 and

stored at -80°C. Prior to cell lysis, cells were washed twice with PBS. For RNA isolation cells were lysed into RNA lysis buffer and stored at -80°C until isolation of RNA. For Western blot analysis, cells were lysed in 1-fold Laemmli buffer, boiled at 95°C for 5 minutes and stored at -20°C. For immunofluorescence cells were fixed in 4% PFA (or 20 minutes at RT, washed with PBS and stored at 4°C.

In the case of ZIKV, SeV and Mengo Zn virus the viral titer was announced as $TCID_{50}$/ml and in the case of RVFVΔNSs-Renilla and VSV-Firefly as PFU/ml. MOIs were calculated by using PFU/ml or $TCID_{50}$/ml, respectively. Respective MOIs are specified in the results sections (note that the MOI calculated by $TCID_{50}$ assay is therefore depicted as $TCID_{50}$/cell).

HDV

HDV stock production was performed by Dr. Zhenfeng Zhang, research group Prof. Dr. Stephan Urban. HDV was produced by co-transfection of HuH7 cells with pJC126 (encoding a 1.1 fold HDV genome, genotype 1) and pT7HB2.7 (encoding all HBV envelope proteins, genotype D). The supernatant was harvested 9 days, 11 days and 13 days post-transfection. Viruses were purified by heparin affinity chromatography and virus titer was determined by qPCR using Paul Ehrlich Institute WHO international standard for HDV as a reference.

$2.5x10^5$ HepaRG-derived cells expressing NTCP were seeded in 24 well plates. One day after seeding, cells were infected with HDV at 0.5 IU per cell (according to the Paul Ehrlich Institute standard) in the presence of 4% PEG8000 and 1.5% DMSO. Around 24 hours post-infection (pi) the cells were washed twice with PBS and replenished with fresh DMSO-containing medium (infection medium). The infection medium was changed every 2 days to 3 days over the time of infection. HDV infection experiments were performed in collaboration with Dr. Zhenfeng Zhang.

ZIKV

ZIKV MR-766 strain was kindly received by Dr. Agnieszka Plociennikowska.

SARS-CoV-2

SARS-CoV-2 stock production and infection experiments were kindly performed by Dr. Vladimir Goncalves Magalhaes. The virus was produced in Vero E6 cells by the usage of the human BavPat1 isolate.

SeV and Mengo Zn virus

SeV stock obtained from Prof. Dr. Rainer Zawatzky was used for infection experiments to stimulate RIG-I signaling. A Mengovirus mutant with a mutation in the zinc finger domain of the viral leader protein (termed Mengo Zn virus) was used to stimulate RLR signaling [313]. Mengo

Zn virus stock was provided by Dr. Pascal Mutz. The virus titer was determined on BHK cells by $TCID_{50}$ (Spearman & Kärber method) [350].

RVFV and VSV reporter viruses

RVFVΔNSs-Renilla and VSV-Firefly reporter viruses, both harboring a luciferase gene, were used to measure their replication by luciferase assays (see 2.2.4.1) and to determine RLR-induced innate immune responses.

RVFVΔNSs-Renilla was originally kindly provided by Prof. Dr. Friedemann Weber, Gießen. The virus lacks the IFN antagonist NSs, important for viral pathogenicity. The NSs locus was replaced by a Renilla luciferase gene [351]. Two different stocks of RVFVΔNSs-Renilla were used in this study. RVFVΔNSs-Renilla with unknown titer was titrated on A549 cells and viral replication was determined by luciferase assay (Figure S 34). 1:100 dilution of this stock was used for further experiments. For infection of HepaRG^{NTCP} LGP2^{KO} cells reconstituted with WT or variants of LGP2 (Figure S 22) RVFVΔNSs-Renilla stock obtained from Sandra Wüst was used. A recombinant VSV-Firefly, driving the expression of firefly luciferase, was used in this study. It was kindly provided by Sandra Wüst. VSV-Firefly was originally obtained from Dr. Gert Zimmer.

2.2.3 Molecular biological methods

2.2.3.1 DNA cloning

2.2.3.1.1 Bacterial transformation and isolation of plasmid DNA

For cloning and transformation of plasmids, the chemically competent bacterial E. coli strain DH5α was used.

DH5α were thawed on ice for around 10 minutes. Prediluted plasmid DNA for retransformation, ligation reaction (2.2.3.1.5), or LR mixture (2.2.3.1.6) for cloning were added to the bacteria, carefully mixed and incubated for 20 minutes on ice. Bacteria were then heat-shocked for 60 seconds at 42°C and immediately put on ice for at least 2 minutes before the addition of LB medium. Cells were incubated for 1 hour at 37°C on a shaking thermomixer prior to plating on LB-agar plates containing the required antibiotic (ampicillin: 0.1 mg/ml; gentamycin: 7 µg/ml; kanamycin: 0.3 mg/ml). Plates were incubated overnight at 37°C. Bacterial clones were picked the next day in the afternoon and incubated in either 4 ml or 200 ml (for mini- or maxipreparation, respectively) LB medium containing the appropriate antibiotic selection by gently shaking overnight at 37°C. Plasmids were isolated using minipreparation (Monarch Plasmid Miniprep Kit, NEB) or maxipreparation kit (NucleoBond PC 500, Macherey-Nagel) according to the manufacturer's instructions.

2.2.3.1.2 Polymerase chain reaction

Polymerase chain reaction (PCR) was used to amplify a specific DNA sample (template) by using specific DNA primers that flank the sequence of interest for downstream cloning or sequencing purposes. PCR was performed by using the Q5 high fidelity DNA polymerase purchased from NEB. Denaturation, annealing and elongation steps were performed by using primer- and target gene-specific annealing temperature and elongation time.

Standard PCR

Q5 polymerase master mix (25 µl reaction) was added into a reaction tube and PCR was performed under thermocycling conditions in a thermal cycler as described in M0491 PCR protocol using Q5® High-Fidelity DNA Polymerase from NEB. The melting temperature of the primers was calculated by Tm Calculator from NEB [352].

Overlap extension PCR

To introduce several nucleotide changes into a plasmid DNA an overlap PCR was performed. In a first step, two independent PCRs were performed, one upstream (resulting in fragment 1) and one downstream (resulting in fragment 2) of the mutational target site. PCRs were designed to have an overlap at the mutated target site by the usage of overlapping primer sequences. The overlapping reverse primer (from fragment 1) and forward primer (from fragment 2) were designed to include the desired mutation. PCR fragments 1 and 2 were purified from an agarose gel after electrophoresis by gel extraction. In a second fusion PCR both PCR fragments were used as a template with fw primer of fragment 1 and rev primer of fragment 2 resulting in amplification of the full-length mutated product. Fusion PCR product was separated on an agarose gel, purified and dissolved in water. Synonymous guide-resistant LGP2 versions were generated by this method.

Site-directed mutagenesis PCR

To introduce single nucleotide changes in the parental plasmid, site-directed mutagenesis was used. Primers were designed to amplify the whole plasmid template with one primer binding next to the target site and one primer including the desired point mutation within the target site. To remove the parental unmutated template after PCR, methylation-dependent endonuclease DpnI was used. PCR product was run on agarose gel, cut out, purified by gel extraction and eluted in water. DpnI and a final of 1-fold cut smart buffer were added and incubated at 37°C for 1 hour. The remaining linear, modified plasmid was cleaned up by column purification, eluted in water and blunt ends were phosphorylated by T4 polynucleotide kinase in 1-fold T4 ligase buffer for 20 minutes at 37°C and heat-inactivated at 70°C for 20 minutes. Thereafter, the sample was split into two halves. One half served as a negative control, the other half was

supplemented with T4 ligase. Both samples were incubated at 37°C for 1 hour prior to transformation into competent bacteria.

2.2.3.1.3 Agarose gel electrophoresis

Agarose gel electrophoresis was performed to purify and analyze DNA. 6-fold DNA loading dye was added to the DNA sample to 1-fold and loaded on 0.8% to 1.5% agarose gels (according to the size of the DNA). Agarose gels were prepared by heating the respective amount of agarose into TAE buffer. At the time of cooling Midori green (2 µl per 50 ml buffer) was supplemented and gels were firmed up in a DNA running chamber with an appropriate comb. To separate the DNA according to its size in the gel, 120 V was applied to the TAE buffer-filled chamber for around 30 minutes. DNA fragments were visualized using Gel iX imager (Intas Science Imaging Instruments). For cloning purposes, desired DNA fragments were cut out of the gel. For test digests, the resulting DNA band pattern was compared to the *in silico* prediction.

2.2.3.1.4 PCR purification and gel extraction

DNA fragments needed for further cloning were cut out of agarose gels on a UV table (UV Transilluminator, VibertLourmat). To avoid DNA damage, agarose gel was exposed to UV light as short as possible. Gel pieces containing the desired DNA fragments were purified by NucleoSpin™ gel and PCR clean-up kit (Macherey-Nagel) which was also used to directly clean up PCR reactions according to the manufacturer's instructions.

2.2.3.1.5 DNA digestion and ligation

DNA digestion was performed using restriction enzymes and their buffer systems from NEB according to the manufacturer's protocol. For test digestions, 0.2 µl enzyme and 300 ng of plasmid DNA were used. NEBcloner [353] was used to define proper buffer conditions in double digests. For cloning purposes around 2 µg plasmid DNA and 1 µl enzyme in suitable 1-fold buffer conditions were incubated for around 2hours at the enzyme-dependent incubation temperature (usually 37°C). To avoid re-ligation, digested plasmid backbones were dephosphorylated by calf intestine phosphatase (CIP, NEB) for 1 hour at 37°C. Digested DNA was purified by agarose gel electrophoresis and gel extraction (according to 2.2.3.1.3, 2.2.3.1.4). Backbone and insert DNA were ligated at a molar ratio of 1:3 overnight at 16°C by the usage of T4 ligase (NEB) according to the NEB ligation protocol M0202. To estimate the number of re-ligated empty backbones, ligation without insert was performed as a control.

2.2.3.1.6 Gateway cloning

This recombination technology invented by Invitrogen offers a restriction enzyme-free cloning method. Based on a set of recombination sequences (att sites), DNA fragments were easily shuttled into specific target plasmids.

In a first BP cloning step, a PCR product flanked by attB1 and attB2 sites was inserted by homologous recombination into a donor vector (pDONR) containing attP1 and attP2 sites. Forward and reverse primers, designed to amplify the gene of interest and used for BP reaction, need to harbor additional attB overhangs (see Table 19). The resulting entry clone (pENTR) includes the gene of interest, flanked by recombination-derived attL1 and attL2 sites and was used for LR reaction.

Table 19: Sequence of attB sites.

attB overhang	Sequence (5'-3')
fw primer	ggggacaagtttgtacaaaaaagcaggcttc
rev primer	ggggaccactttgtacaagaaagctgggtc

BP reaction was performed by addition of 150 ng pDONR207,150 ng of PCR product, 1 µl of BP clonase II enzyme mix in 1-fold TE buffer and a total volume of 8 µl. The mixture was incubated for at least 1 hour at 25°C. 1 µl proteinase K solution was then added for 10 minutes at 37°C. The whole mix was transformed into 50 µl to 100 µl of competent bacteria. Plasmids from selected clones were purified and sequenced to verify the presence of the target gene.

In a second LR cloning step, the gene of interest located on an entry vector is shuttled into one out of several destination vectors (pDEST). The multiple pDEST vectors contain different antibiotic resistances or tags. The LR reaction is again based on recombination of the attL1 and attL2 sites in the entry vector flanking the gene of interest and the attR1 and attR2 sites of the destination vector resulting in an expression vector (pWPI) suitable for expression in eukaryotic cells. The att sites of the donor and destination vector frame a ccdB gene which enables the selection of only positively recombined clones (as the ccdB gene will be exchanged by the gene of interest). Therefore, non-recombined vectors will be negatively selected enabling a high-efficiency recovery of target clones.

LR reaction was performed in a total volume of 8 µl by addition of 150 ng pENTR. 150 ng pDEST, 1 µl of LR Clonase II enzyme mix in 1-fold TE buffer. LR mix was incubated at 25°C for 1 hour, prior to the addition of 1 µl proteinase K solution to stop the reaction. LR reaction mix was then transformed into competent bacteria. Plasmids from selected clones were purified and sent for sequencing of the target gene.

For the amplification of ccdB gene containing empty plasmids the One Shot™ ccdB Survival™ 2 T1R *E. coli* strain was used (Invitrogen).

pENTR based vectors cloned in this study

Constructs were purchased from the GPCF Gateway Full ORF Clone collection (DKFZ, Germany) or self-cloned (via BP cloning, see above) from PCR products into pENTR vectors as described.

pWPI based lentiviral vectors used in this study

For stable gene expression by lentiviral transduction, genes of interest were cloned by LR reaction into gateway compatible pWPI expression vectors. Several destination vectors were used, either driven by an EF1-α or ROSA26 promoter, with or without a tag (N-terminal HA tag) and with an antibiotic resistance gene against blasticidin, puromycin, or gentamycin. Where not otherwise stated, the gene of interest is driven by the EF1-α promoter.

2.2.3.1.7 Cloning of CRISPR Cas-9 guide RNAs

CRISPR/Cas9 technology was used to generate KO cell lines by the introduction of double-strand breaks at specific locations in the genome. A guide RNA (gRNA) recruits the Cas9 nuclease to its target site containing a protospacer adjacent motif. Introduced double-strand breaks are repaired by non-homologous end joining, an error-prone repair mechanism that often leads to inserted or deleted bases causing frameshift mutations resulting in targeted KO.

To generate cell lines with specific protein KO, several specific guide RNAs of 20 bp in length were designed with the help of E-CRISP [354]. To avoid the expression of N-terminal parts of the target proteins, guide RNAs were designed to bind within the first exons, where possible, while providing low off-target prediction. Plasmid LentiCRISPRv2 encoding for Cas9 nuclease and a guide RNA scaffold under the control of U6 promoter [355] was used to introduce a target gene-specific guide RNA. Cloning was adapted from [356]. In short, a forward and reverse single-stranded oligonucleotide from Table 10 (Chapter 2.1.7) encoding the guide RNA flanked by a BsmBI-specific restriction enzyme overhang was ordered by Sigma-Aldrich. In a total of 10 µl, 1 µl of each top and bottom strand ssDNA (100 µM each) were annealed with 1 µl T4 polynucleotide kinase in 1-fold T4 ligation buffer for 30 minutes at 37°C followed by 5 minutes at 95°C, ramped down to 25°C with 5°C per minutes. The sample containing the oligo-dimers was diluted 1:200 in water and used as an insert for cloning into pLentiCRISPv2. Therefore 3 µg of LentiCRISPRv2 were digested with 10 U of BsmBI in 1-fold NEB buffer 3 at 55°C. After 1.5 hours of incubation, 10 U of CIP were added to the sample and incubated for 1 hour at 37°C. Gel electrophoresis was performed to separate the opened backbone (DNA of interest, 12,988 bp) from the filler piece (1,885 bp). Ligation of 1 µl backbone and 3 µl insert was performed in a 1:3 ratio in 1-fold ligation buffer and 10 U of T4 ligase and incubated

overnight at 16°C. The whole ligation mix was transformed into DH5α competent bacteria and plated on ampicillin-containing agar plates. Colonies were picked for plasmid minipreparation to verify guide RNA insertions by sequencing with hU6 sequencing primer.

2.2.3.1.8 Sequencing of plasmids and PCR products

LightRun Sanger sequencing of plasmids and PCR products was performed by GATC Services of Eurofins Genomics (Germany). 5 µl of plasmid DNA (with a concentration of around 100 ng/µl) or 5 µl purified PCR product were mixed with 5 µl sequencing primer of 5 µM concentration in a 1.5 ml reaction tube labeled with a barcode sticker. Sequencing results were obtained online and were analyzed by SnapGene.

2.2.3.2 RNA-based methods

For all steps working with RNA, filter tips and reaction tubes free of DNase/RNAse were used.

2.2.3.2.1 RNA isolation

Total RNA (24 well format) was extracted using the Monarch® Total RNA Miniprep Kit (NEB) or RNA extraction kit (Macherey-Nagel) following the manufacturer's instructions and stored at -80°C. NanoDrop 1000 spectrophotometer was used to determine RNA yield.

Total RNA isolation upon HDV-immunoprecipitation (IP) (see 2.2.4.3.2) was performed by using RNAzol RT (Sigma-Aldrich). Input samples (50 µl) or beads from the IP were resuspended in 500 µl RNAzol RT and 150 µl or 200 µl RNAse-free water, respectively. Samples were vortexed for 15 seconds and kept for 5 to 15 minutes at RT, followed by centrifugation at 12,000xg for 15 minutes at RT. 600 µl of supernatant were transferred into a new tube and mixed with 600 µl isopropanol and 2 µl GlycoBlue™ coprecipitant. To precipitate RNA, samples were incubated for 10 minutes at RT and afterwards centrifuged at 12,000xg for 10 minutes at RT. Pellet was washed twice with 500 µl 75% ethanol, centrifuged at 8,000xg for 2 minutes at RT. Residual ethanol was removed thoroughly and the pellet was resuspended in 40 µl RNAse-free water.

2.2.3.2.2 Reverse transcription

RNA was reverse transcribed using the High-Capacity cDNA reverse transcription kit (Thermo Fisher Scientific Inc.). For downstream measurements of relative RNA expression levels, a total master mix of 6 µl volume was used for cDNA synthesis as is shown in Table 20. After cDNA transcription, the cDNA is diluted 1:20 prior to usage for qRT-PCR. To determine absolute copy numbers in a specific amount of RNA measured by downstream qRT-PCR of cDNA, an equal amount of RNA was used for reverse transcription. Therefore, the master mix for cDNA generation was upscaled to a total of 20 µl which is depicted in Table 21 and diluted

into 30 µl of water after the cDNA run. RNA amount was always kept stable within all samples corresponding to the same experiment. If cDNA was used for measurement of HDV RNA copies by qRT-PCR, RNA samples were heated to 95°C for 5 minutes prior to shock freezing and usage for reverse transcriptase. Cycling parameters for cDNA synthesis are shown in Table 22.

Table 20: Master mix for cDNA synthesis (6 µl volume).

Volume [µl]	Component
0.6	reverse transcriptase buffer (10-fold)
0.24	dNTP mix (25-fold)
0.3	reverse transcriptase
0.3	RNAse inhibitor
0.6	random primers (10-fold)
0.96	H_2O
3	RNA

Table 21: Master mix for cDNA synthesis (20 µl volume).

Volume [µl]	Component
2	reverse transcriptase buffer (10-fold)
0.8	dNTP mix (25-fold)
1	reverse transcriptase
1	RNAse inhibitor
2	random primers (10-fold)
13.2	RNA and H_2O

Table 22: Cycling parameters for cDNA synthesis.

Temperature	Time
25°C	10 min
37°C	2 h
85°C	5 min
12°C	hold

To analyze the LGP2 mRNA sequence in HepaRG cells, cDNA synthesis was performed by using oligo(dT)-specific primers instead of random primers. 1 µg of RNA extracted from IFN-α induced (400 IU/ml for 24 h) HepaRG cells was mixed with 1 µl oligo(dT) primer (10 µM) filled with water to a final volume of 15.2 µl. Heat shock was performed for 5 minutes at 70°C and the sample was quickly put on ice for 3 minutes. In a total volume of 20 µl, dNTPs, reverse transcriptase buffer, RNAse inhibitor and reverse transcriptase were added analog to Table 21. Reverse transcription was performed at 42°C for 1.5 hours without preincubation at 25°C followed by 5 minutes at 85°C. cDNA served as a template for PCR with LGP2 mRNA-specific primers binding the 5'- and 3'-prime UTR, respectively (Table 12). PCR product was purified

from agarose gel and send to sequencing. HepaRG-derived LGP2 mRNA was confirmed to be similar to the LGP2 plasmid sequence with none of the investigated SNPs coding for Q425R, N461S and R523Q present.

2.2.3.2.3 Quantitative real-time PCR

Quantitative real-time (qRT) PCR was performed to analyze the relative or absolute expression of cellular genes and HDV RNA. Samples consisting of gene-specific primers (depicted in Table 11), iTaq universal SYBR Green Supermix and cDNA were prepared as depicted in Table 23 and run in a CFX96 thermal cycler (Bio-Rad) by using the cycling parameters from Table 24.

Table 23: Master mix for qRT-PCR.

Volume [µl]	Component
7.5	iTaq (2-fold)
1.5	primer mix (5 µM each)
3	H_2O
3	diluted cDNA

Table 24: Cycling parameters for qRT-PCR.

Step	Temperature	Time
1	95°C	3 min
2	95°C	10 sec
3	60°C	30 sec
4	measure	
5	go back to 2	45 cycles
6	65°C to 95°C	0.05 sec/ 0.5°C
7	measure every 0.5°C	

Relative mRNA amounts were determined by the ΔΔCt method described by Livak et al. [357]. Thereby, GAPDH was used as a reference. For absolute RNA quantification, plasmids containing the target genes were taken from a library of human ORFs [358] and used as standards. Standards used in qRT-PCR were prepared freshly from a concentrated stock with determined copy numbers per µl. A dilution series reaching from 10^7 to 10^0 copies per 3 µl was performed in MilliQ water. Standards were pipetted on the same plate as the samples.

For HDV RNA quantification, Universal Luna® Universal Probe qPCR Master Mix (NEB) and the TaqMan probe FAM-CGCGGTCCGACCTGGGCATCCG-BHQ were used. Copy numbers were quantified using pJC126 as standard. qRT-PCR of HDV RNA was kindly performed by Dr. Zhenfeng Zhang.

For ZIKV RNA quantification, the GAPDH- (HEX-CAAGCTTCCCGTTCTCAGCCT-TAM) and ZIKV-specific TaqMan probe (FAM-AGCCTACCTTGACAAGCAATCAGACACTCAA-TAM) were used in a one-step qRT-PCR master mix (SCRIPT XLT 1-Step RT-qPCR ToughMix, Quantabio) as described in [52]. ZIKV- and GAPDH-specific primers are listed in Table 11.

2.2.4 Biochemical and immune-based methods

2.2.4.1 Firefly and Renilla luciferase assays

Luciferase assay was performed to measure replication of VSV-Firefly and RVFVΔNSs-Renilla reporter viruses. Cells infected with RVFVΔNSs-Renilla or VSV-Firefly were washed twice with PBS and lysed in luciferase lysis buffer (100 µl for 24 well format, 25 µl for 96 well format) freshly supplemented with a final concentration of 1 mM DTT and stored at -80°C. As the substrate of Renilla luciferase, coelenterazine (stock: 1 mM in methanol) was diluted (1:625) in luciferase assay buffer. For measurement of Firefly luciferase activity, D-Luciferin was diluted (1:12.5) in luciferase assay buffer supplemented freshly with a final concentration of 1 mM DTT and 2 mM ATP (1:50 of 100 mM stock). Cell lysates were thawed directly before measurement of luciferase counts using Mithras² LB 943 Multimode reader. The protocol is depicted in Table 25 (for 24 well format). To prevent shining into neighboring wells, the reaction was stopped after measurement by the addition of 10% SDS. Samples were measured in technical duplicates (24 well format) or quadruplicates (96 well format) and uninfected samples served as a negative control.

Table 25: Set-up for measurement of luciferase activity.

Action	Procedure
inject substrate	400 µl
shake	2 sec
measure (480 nm BRET filter for Renilla)	10 sec
dispense SDS	100 µl
shake	2 sec

2.2.4.2 Western blotting

To detect specific proteins by Western blotting (WB), proteins were denatured followed by sodium dodecyl sulfate-polyacrylamide gel electrophoresis (SDS-PAGE). To run samples on SDS-PAGE, resolving gels with a concentration of 6% to 12% polyacrylamide were used. Gels were poured usually one day prior to SDS-PAGE using acrylamide and bisacrylamide stock solution (40% at a ratio of 29:1), TEMED and saturated ammonium peroxydisulfate (APS) solution to catalyze polymerization. Resolving gel was cast first with 1:5 / 1:4 / 3:10 (for

8% / 10% / 12%) acrylamide and bisacrylamide stock solution, 1:4 resolving gel buffer, 1:1000 TEMED and 1:1000 APS (filled with water) into a Bio-Rad mini gel casting system. The liquid gel solution was immediately overlaid with isopropanol to achieve a straight upper border. Isopropanol leftover on polymerized resolving gels was spilled and gel border was washed once with water. Residual water was carefully sucked off with Whatman paper. Stacking gel was prepared by mixing 1:10 acrylamide and bisacrylamide stock solution, 1:8 resolving gel buffer, 1:1000 TEMED and 3:2000 APS (filled with water) and poured on top of the resolving gel. A comb (15 well size) was added on top.

Cells lysed in a final of 1-fold Laemmli buffer and boiled at 95°C for 5 minutes were loaded on the gels. Proteins were separated by SDS-PAGE. A lane with protein marker (Bio-Rad) was included in the run to determine the protein size. Gels were run in 1-fold TGS buffer for around 20 minutes at 80 V and around 1.5 hours at 120 V until the desired resolution was achieved.

After SDS-PAGE, proteins were blotted onto a PVDF membrane by wet blot (in most of the cases) or semi-dry transfer method (Bio-Rad, Germany). The wet blot was always used to detect proteins bigger than 100 kDa or when phospho-specific antibodies were used. PVDF membranes were activated in methanol prior to use. The semi-dry transfer was performed using the Trans-Blot® Turbo™ Transfer System (Bio-Rad). The wet transfer was performed in 1-fold transfer buffer (including 20% methanol) at 4°C and 0.35 A for 1.5 to 2 hours using the Mini Trans-Blot® Cell (Bio-Rad). Afterwards, membranes were blocked with 5% milk in PBS-T or 5% BSA in TBS-T, dependent on the primary antibody used, for at least one hour at room temperature. Membranes were incubated with primary antibodies (Table 8) diluted in 2% milk in PBS-T or 2% BSA in TBS-T according to the manufacturer's instructions overnight at 4°C. Membranes were washed 3-times at least 5 minutes each with PBS-T or TBS-T at RT. Secondary anti-mouse and anti-rabbit antibodies tagged with horseradish peroxidase (Table 9) were diluted 2% milk in PBS-T or 2% BSA in TBS-T and incubated with the washed membranes for 1 hour at RT. Again, membranes were washed 3-times at least 5 minutes each with PBS-T or TBS-T at RT. Proteins were visualized by Clarity Western ECL substrate (Bio-Rad, Germany) or, if the expression of proteins was weak, ECL™ Prime Western Blotting Detection Reagent (Cytiva). Membranes were developed using ECL ChemoCam imager 3.2 (Intas Science Imaging Instruments).

For quantification of protein signals (normalized to loading control), Lab Image 1D software package (Kapelan Bio-Imaging) was used.

2.2.4.3 Immunoprecipitation

2.2.4.3.1 HA-immunoprecipitation

For immunoprecipitation (IP), cells expressing HA-tagged proteins of interest were washed twice with PBS prior to harvesting in 0.5 ml to1 ml PBS by cell scraping and were centrifuged for 8 minutes at 500xg. The cell pellet was resuspended into lysis buffer and incubated on ice for 60 minutes prior to centrifugation at 18,000xg for 30 minutes at 4°C. Supernatants were used for further analysis. For Western blot analysis, an aliquot was taken as IP input control (lysate). Anti-HA-agarose (Sigma-Aldrich, 15 µl to 20 µl per sample) was washed 3-times with lysis buffer prior to incubation with lysates for 4 hours until overnight at 4°C on a rotating wheel. To pellet the beads, samples were centrifuged at 2,300xg for 30 seconds at 4°C. Before discarding the supernatant, an aliquot was taken as post binding control for Western blot analysis. Beads were washed at 4°C 3- to 4-times with ice-cold lysis buffer for around 10 minutes each and twice with PBS. Optionally, supernatants of washing steps were kept for Western blotting. Proteins were precipitated by elution with 5% SDS in PBS. 120 µl of SDS solution was added to the beads and shaken at 1,100 rpm on a thermomixer at RT for 5 minutes. 100 µl supernatant was collected into a fresh tube. 100 µl PBS was added to the beads and again shaken 5 minutes at RT. Supernatants were collected and mixed with previous ones. 800 µl ice-cold acetone was added and samples were intensely mixed and stored overnight at -20°C. The next day samples were centrifuged at full speed for 30 minutes at 4°C. Supernatants were discarded thoroughly. Visible protein pellets were air-dried for around 5 minutes and resuspended in 1-fold Laemmli buffer and boiled for 5 minutes at 95°C.

Co-immunoprecipitation

Co-IP was performed to analyze LGP2 interaction partners. Co-IP was performed as described for HA-IP by using buffer conditions from Hei at al. [60] (called Hei buffer) and from myself (called NG buffer). Recipes are shown in Table 26 and Table 27, respectively.

Table 26: Hei buffer conditions.

Hei buffer		
20	mM	TRIS-HCl, pH 7.4
150	mM	NaCl
0.5	%	NP-40
1	mM	EDTA
1	fold	protease inhibitor

Table 27: NG buffer conditions.

NG buffer		
20	mM	TRIS
100	mM	NaCl
0.1	%	NP-40
50	mM	NaF
5	mM	Na_3VO_4
20	mM	NEM
1	fold	protease inhibitor

Immunoprecipitation for LGP2 phospho-proteome

To investigate potential phosphorylation sites of LGP2, HA-IP was performed with buffer conditions listed in Table 28 including especially phosphatase inhibitors. In quadruplicates, $4.3x10^6$ HA-LGP2-expressing A549 cells were seeded into 15 cm dishes (for viral infection) or $2.15x10^6$ HA-LGP2-expressing A549 cells were seeded into 10 cm dishes (2 per sample for transfection). Untagged LGP2 served as a negative control. Cells were infected with SeV or Mengo Zn virus or transfected with poly(I:C) as specified in the results part. IP was performed as described for HA-IP. Per sample 25 µl HA-beads were used. Cell lysates were incubated for 4 hours at 4°C prior to 4-times washing with phospho-MS buffer containing NP-40 and 4-times washing with phospho-MS buffer without NP-40. HA-beads were then shock frozen in liquid nitrogen and stored at -80°C prior to phospho-MS analysis by Dr. Pietro Scaturro in the research group of Prof. Dr. Andreas Pichlmair. IP was performed in DNAse and protease-free 1.5 ml tubes and by the usage of filter tips.

Table 28: Phospho-MS buffer conditions.

MS buffer		
20	mM	TRIS pH7.6
100	mM	NaCl
0.1	%	NP-40
10	mM	NaF
5	mM	Na_3VO_4
20	mM	NEM
60	mM	BGP
15	mM	pNPP
1	fold	protease inhibitor

Silver gel staining

After HA-IP, SDS-PAGE of IP samples was performed. To evaluate purity and yield of a specific IP condition, e.g. for LGP2 phospho-MS, Pierce silver gel kit (detection limit of around 0.25 ng protein) was used including a BSA standard for determination of protein yield.

2.2.4.3.2 RNA-immunoprecipitation

RNA-IP was performed by using magnetic beads. For the washing steps, the 1.5 ml reaction tubes containing the beads were put on a magnetic rag for 2 minutes. The liquid was sucked off by the use of a 1000 µl filter tip.

For lysis, cells were washed twice with PBS and scraped into a 1.5 ml reaction tube. Cells were centrifuged at 500xg for 8 minutes and the supernatant was discarded. Cells were resuspended in RNA-IP lysis buffer (Table 29) and incubated on ice for 20 minutes prior to centrifugation at 18,000xg for 10 minutes at 4°C. The supernatant (cell lysate) was transferred to a fresh tube and used for further analysis (see HDV-IP or poly(I:C)-IP).

HDV-immunoprecipitation

For HDV-IP, HepaRG-derived cells were seeded at a density of $3.5x10^6$ cells and infected with HDV. At 5 days pi cells were then scraped and put into 500 µl of RNA-IP lysis buffer (Table 29). Lysis was performed as described above. 25 µl cell lysate was kept as RNA input control, 10 µl for Western blotting. Pierce Protein A/G Magnetic Beads (Thermo Fisher Scientific Inc.) were labeled with HA antibody (16B12 clone, BioLegend) for 30 minutes at RT (25 µl beads and 2.5 µg antibody per sample) then washed 3-times with RNA-IP wash buffer (Table 30). HA-labeled beads were suspended into 250 µl of RNA-IP IP buffer (Table 31) and incubated with 250 µl of lysate overnight at 4°C on a rotating wheel. Beads were washed 5-times with 500 µl wash buffer and then resuspended into 250 µl. 10 µl of beads were taken out as eluate for Western blot analysis. The rest of the wash buffer was discarded. RNA from the beads (eluates) and input controls was isolated by using RNAzol RT (Thermo Fisher Scientific Inc.) and reverse transcribed prior to use for HDV RNA-specific qRT-PCR. HDV-IP was performed by Dr. Zhenfeng Zhang.

Table 29: RNA-IP lysis buffer conditions.

RNA-IP lysis buffer		
0.5	%	NP-40
200	U/ml	RNAse inhibitor
20	mM	MOPS-KOH, pH 7.4
120	mM	KCl
2	mM	β-mercaptoethanol
1	fold	protease inhibitor

Table 30: RNA-IP wash buffer conditions.

RNA-IP wash buffer		
20	mM	MOPS-KOH, pH 7.4
120	mM	KCl
2	mM	β-mercaptoethanol
1	fold	protease inhibitor

Table 31: RNA-IP IP buffer conditions.

RNA-IP IP buffer		
200	U/ml	RNAse inhibitor
20	mM	MOPS-KOH, pH 7.4
120	mM	KCl
2	mM	β-mercaptoethanol
1	fold	protease inhibitor

Poly(I:C)-immunoprecipitation

For poly(I:C)-IP, $1.8x10^6$ HepaRG-derived cells were lysed into 250 µl of RNA-IP lysis buffer. 25 µl were kept as input control for Western blotting. DYNAL™ Dynabeads™ M-280 Streptavidin (Invitrogen) were labeled with poly(I:C) (HMW) Biotin (InvivoGen) according to the manufacturer's protocol using 15 µl beads and 500 ng poly(I:C)-Biotin per sample including RNAse inhibitor and poly(C). In the case of MDA5 binding to poly(I:C), cells were pretreated with IFN-α and 25 µl of beads and 1 µg of poly(I:C) were used for the labeling. After washing, beads were resuspended in 225 µl RNA-IP IP buffer and 225 µl cell lysate added for 3 hours to 4 hours at 4°C on a rotating wheel. Beads were washed 5-times with 1 ml RNA-IP wash buffer. Beads were then directly boiled in 25-60 µl 1-fold Laemmli for 5 minutes at 95°C.

2.2.4.4 Immunofluorescence

To quantify the amount of HDV infected cells, immunofluorescence (IF) was performed analogously to [359] with some modifications. Cells were washed 3-times with PBS and fixed in 4% paraformaldehyde (PFA, in PBS) for 20 minutes at RT, then washed again 3-times and stored in PBS at 4°C prior to usage. Cells were permeabilized with 0.25% Triton-X-100 in PBS for 20 minutes at RT and washed 3-times. VUDA human anti-HDAg serum was used as primary antibody (diluted 1:3000 in 2% BSA in PBS) for 30 minutes at RT on the shaker. Cells were washed 4-times in PBS and incubated for 1 hour with goat anti-human Alexa Fluor 555 (Invitrogen, USA) as a secondary antibody (diluted 1:1000 in 2% BSA in PBS) and DAPI or Hoechst 33342 for nuclear staining. Cells were washed 4-times in PBS and shortly washed in water prior to mounting with Fluoromount G on an object slide. Images were taken with Nikon microscope Eclipse Ti. HDV infection was analyzed by ImageJ nucleus counting tool or by

Ilastik. Besides Figure 27E, HDAg IF and its data analysis were performed by Dr. Zhenfeng Zhang.

2.2.4.5 Enzyme-linked immunosorbent assay

IFN-λ1-3 in the cell culture supernatant was quantified by DIY Human IFN Lambda 1/2/3 (IL-29/28A/28B) enzyme-linked immunosorbent assay (ELISA) (PBL Assay Science) according to the instruction of the manufacturer. 96 well plates, half area, were used. Plates were coupled with 50 µl capture antibody (1 µg/ml, diluted in PBS) overnight at RT, 3-times washed with PBS-T (PBS with 0.05% Tween-20) and then blocked with 100 µl reagent diluent (final of 1% BSA in PBS) for 1 hour at RT. After 3 washing steps with PBS-T, 50 µl of cell culture supernatant (or appropriate dilutions thereof) or 50 µl of standard (2-fold series dilutions, ranging from 4,000 to 67.5 pg/ml) were added for 2 hours at RT. Reagent diluent was used to dilute samples and standards. After 3 further washing steps with PBS-T, 50 µl detection antibody (400 ng/ml, diluted in reagent diluent) was added to the plate for 2 hours. Streptavidin-HRP solution was added to the washed plate for 20 minutes at RT. After washing, 50 µl TMB substrate solution (BioLegend) was added, plate developed for 10 minutes at RT in the dark and reaction stopped with 25 µl of 2 M sulfuric acid. The optical density at 450 nm and 570 nm (latter for baseline subtraction) was immediately measured in a Multiskan Ex ELISA plate reader (Thermo Fisher Scientific Inc.). Samples and standards were measured in technical duplicates and protein concentration was calculated by Microsoft excel using standard curve measurements. Mock-treated samples and reagent diluent served as negative controls.

2.2.5 Statistics and data evaluation

Statistical analysis and generation of graphs were performed using the GraphPad Prism 8.0.1 software package. Significance was determined using unpaired Student's t-test, 2-tailed, parametric test if only two different cell lines were compared. One-way ANOVA and Dunnett's multiple comparison test were used if three or more cell lines were compared relative to one control cell line. If three or more cell lines were compared at several time points, two-way ANOVA and Dunnett's multiple comparison test was performed relative to one control cell line. To minimize the fluctuation of sample variances, $\log_{10}$ transformation was performed before statistical testing, except for Figure 8, Figure 16E, Figure 19C, Figure S 6A in the case of CXCL10 (where variances were lower for non-transformed data or zero values were present). Significance levels are indicated by asterisks: ****, $p \leq 0.0001$; ***, $p \leq 0.001$; **, $p \leq 0.01$; *, $p \leq 0.05$ (no label in case of non-significant differences). Analysis was only performed on non-normalized data ($n \geq 3$). The number of biological replicates is depicted in the respective figure legends. Error bar indicates standard deviation from two to three technical replicates, circles on top of each bar indicate the average value of individual biological replicates.

3 RESULTS

3.1 Investigation of RLR signaling and the influence of LGP2 in lung epithelial cells

Many studies describing the regulatory role of LGP2 on RLR signaling *in vitro* made use of transient plasmid transfection in HEK 293T cells enabling strong expression of RLRs and simple read-out through reporter systems [26, 27, 54, 56, 58, 61, 125, 132]. In the following chapter, IFN and ISG levels of immunocompetent lung epithelial A549 carcinoma cells were measured by qRT-PCR and IFN-λ ELISA. The cells were modified by stable overexpression and/or KO to specifically investigate the impact of each RLR on the innate immune response individually.

3.1.1 RIG-I is the major PRR sensing viral RNA in A549

To confirm that RLRs are the major intracellular PRRs in A549 cells upon RNA virus infection, specific KO A549 cells were infected with the reporter viruses SeV and Mengo Zn virus, used to activate RIG-I and MDA5, respectively (see Table 1), or kept uninfected. MAVS^{KO}, LGP2^{KO}, RIG-I^{KO}, MDA5^{KO} A549 derived from single-cell clones and a non-targeting (NT) guide RNA-expressing control A549 cell line were used. As RLRs (but not MAVS) are ISGs [360], cell lines were treated with IFN-α to verify their respective lack of protein expression by Western blotting (Figure 7A). RIG-I and MAVS protein expression could be detected in steady-state with lack of expression in respective RIG-I^{KO} and MAVS^{KO} A549. Initial MDA5 expression was weak but could be induced by IFN treatment in all cells besides MDA5^{KO} (Figure 7A). In contrast, IFN treatment was not sufficient to induce detectable protein levels of LGP2 (data not shown). This is in line with the record published in the Human Protein Atlas database where no LGP2 mRNA levels were observed in A549 cells [361]. LGP2^{KO} cell clones were therefore validated by genomic sequencing of the LGP2 locus (Figure S 2) and one clone exemplary used in Figure 7.

After 6 hours and 12 hours pi, IFIT1 mRNA was measured as a surrogate for the induction of an ISG response. In steady-state IFIT1 levels were low (Figure 7D) however increased over the time of infection in NT control, LGP2^{KO} and MDA5^{KO} cells (Figure 7B and C). SeV-induced innate immune response was stronger than that of Mengo Zn virus. Both SeV (Figure 7B) and Mengo Zn virus (Figure 7C) abrogated signaling in RIG-I^{KO} and MAVS^{KO} cells to a similar extent while MDA5^{KO} and LGP2^{KO} cells revealed quite similar induction to NT control cells (Figure 7B and C). This suggests that only RIG-I was the major PRR sensing both viruses.

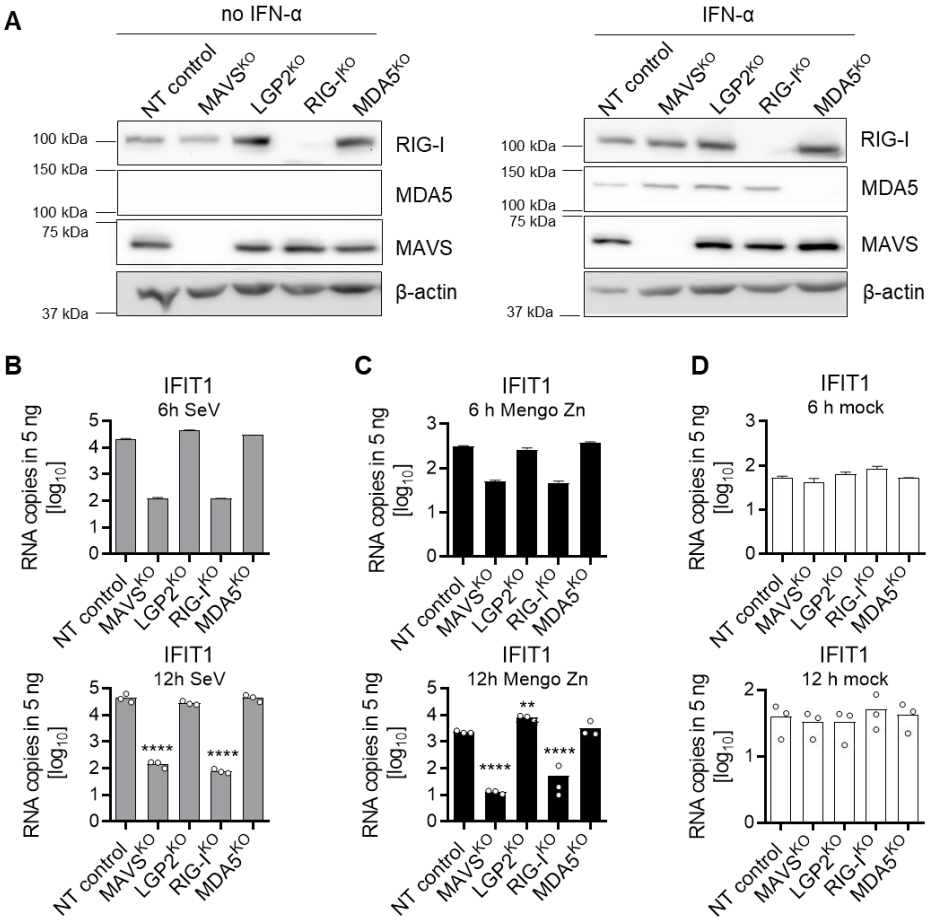

Figure 7: Induction of the IFN response upon Mengo Zn virus and SeV infection in A549 depends on MAVS and especially RIG-I.
(**A)** A549 MAVS^{KO} (clone 1.77), LGP2^{KO} (clone L2-10), RIG-I^{KO} (clone R2-2#1) and MDA5^{KO} (clone M2-28) or a non-targeting (NT) guide RNA-expressing cell pool (NT control) were unstimulated (left panel) or stimulated with 500 IU/ml of IFN-α for 24 h (right panel) before harvesting for immunoblotting with antibodies against RIG-I, MDA5, LGP2 (latter not detected, data not shown) and β-actin as a loading control. **(B-D)** Cells from (A) were infected with (B) SeV (MOI=5), (C) Mengo Zn virus (MOI=5), or kept (D) uninfected for 6h and 12h, respectively. RNA was isolated before qRT-PCR of IFIT1. **, $p \leq 0.01$; ****, $p \leq 0.0001$ (comparison between NT control and respective KO A549).

Equal to MAVS^{KO} A549, generated RIG-I-MDA5 double KO cell clones but not NT control cells abolished dsRNA sensing upon Mengo Zn virus or SeV infection and transfection of high molecular weight (HMW) poly(I:C), a synthetic stimulus with an average size of 1.5 kb to 8 kb. Feeding of poly(I:C) to the supernatant which activates TLR3 signaling [52] did neither stimulate MAVS^{KO}, RIG-I-MDA5 double KO nor NT control cells (Figure S 3). This indicates that RLR signaling is the primary dsRNA sensing pathway in A549 under those conditions.

IFN-α induced RIG-I and MDA5, but not detectable LGP2 protein levels in A549 cells although all RLRs are known to be ISGs [360]. To investigate whether the undetectable protein levels of LGP2 still influence the signaling pattern of A549 cells, LGP2^{KO} cell clones, validated by genomic sequencing (Figure S 2), were tested side-by-side with NT control A549, RIG-I^{KO} and MDA5^{KO} cells upon stimulation with synthetic dsRNA (as stimulation with SeV and Mengo Zn

virus activated especially RIG-I but not MDA5). Both 5'ppp-dsRNA and HMW poly(I:C) was used for activation of RLR signaling. LGP2^{KO} A549 maintained normal endogenous RIG-I and MDA5 levels. Even after IFN-α/β co-stimulation (which might induce a more diverse pattern of ISGs than IFN-α treatment alone [154]) none of the cell lines revealed LGP2 protein expression (Figure 8A). Upon stimulation with 5'ppp-dsRNA for 8 hours and HMW poly(I:C) for 10 hours, the IFN-λ protein levels were on average not changed in the LGP2^{KO} clones compared to non-targeting (NT) control A549 (Figure 8B). This indicates that the endogenous LGP2 protein levels did not influence the IFN response in these settings. As obtained with SeV and Mengo Zn virus infection, both synthetic stimuli activated the RIG-I but not the MDA5 response.

The aforementioned infections with SeV and Mengo Zn virus and transfections with 5'ppp-dsRNA and HMW poly(I:C) revealed a RIG-I dependent response (Figure 7B and C, Figure 8B). Steady-state MDA5 levels were low in A549 (Figure 7A, Figure 8A left-hand). Lack of RIG-I as initial IFN inducer offers an explanation why RIG-I^{KO} cells were unresponsive to especially Mengo Zn virus infection (Figure 7C) and HMW poly(I:C) (Figure 8B right-hand) – two stimuli thought to activate MDA5 signaling. To validate this hypothesis, the MDA5 pathway in RIG-I^{KO} A549 was boosted by enhancement of initial MDA5 levels and/or increased doses of stimulus. Indeed, high doses of HMW poly(I:C) were able to support the MDA5 response in RIG-I^{KO} harboring low initial MDA5 levels (Figure S 4A, Figure S 5). Moreover, MDA5 was overexpressed in two RIG-I^{KO} A549 clones to achieve protein levels comparable to IFN-α-induced MDA5 levels (Figure S 4B, see asterisk). This initial MDA5 upregulation in those two RIG-I^{KO} A549 clones revealed strong Mx1 activation upon stimulation with HMW poly(I:C) and Mengo Zn virus (but not SeV) which is similarly high compared to naïve and MDA5^{KO} A549 (Figure S 4C and D). Such induction was not achieved in RIG-I^{KO} A549 clones without MDA5 overexpression. Thus, the lack of the IFN response in RIG-I^{KO} A549 upon Mengo Zn virus infection (Figure 7C) and HMW poly(I:C) transfection (Figure 8B) was due to low levels of MDA5/LGP2 in those cells.

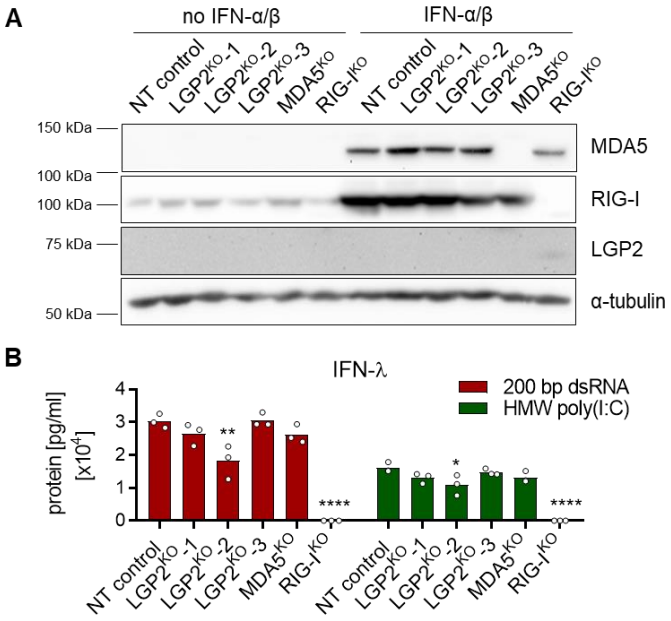

Figure 8: KO of the undetectable endogenous LGP2 protein levels in A549 cells does not alter the response towards RIG-I- or MDA5-specific stimuli.
(A) A549 cells with stable KO of LGP2 (LGP2^{KO}-1, -2, -3 corresponding to clone L2-9, L2-10, L3-4, respectively), of MDA5 (clone M2-28), of RIG-I (clone R2-2#1) and a non-targeting control cell pool (NT control) were kept unstimulated (left-hand) or were stimulated 24 h with 200 IU/ml of IFN-α and -β (right-hand). Cell lysates were used for Western blot analysis staining LGP2, MDA5, RIG-I and α-tubulin. **(B)** Cells from (A) were transfected with 1 ng of 5'ppp-dsRNA of 200 bp in length (8 h for RIG-I stimulation) or 1 µg HMW poly(I:C) (10 h for MDA5 stimulation) or analogous poly(C) transfection as a negative control. IFN-λ in the supernatant was measured using ELISA. IFN-λ production in poly(C) transfected samples was below the detection limit (data not shown). *, $p \leq 0.05$; **, $p \leq 0.01$; ****, $p \leq 0.0001$ (comparison between NT control and KO A549). n=3.

3.1.2 LGP2 overexpression inhibits RIG-I and enhances MDA5 signaling

SeV was shown to specifically induce RIG-I-mediated responses (Figure 7B). Compared to empty control cells overexpression of LGP2 (untagged or N-terminally HA-tagged) in A549 negatively influenced the IFN response upon infection with SeV (Figure S 1B). This indicates that LGP2 inhibits RIG-I induced IFN responses in A549 cells upon SeV infection, with the strongest inhibition at early time points. Moreover, HA-tagged LGP2 was functional.

As RIG-I dominated MDA5 signaling in A549 cells, the effect of LGP2 in the MDA5 response was further investigated in RIG-I^{KO} cells. To elucidate the role of LGP2 in RLR-specific responses side-by-side, MDA5^{KO} and RIG-I^{KO} A549 cells (Figure 9A) were used to overexpress LGP2 or an empty vector control (Figure 9B). For stimulation, different doses of synthetic dsRNA ligands were used as indicated. To activate RIG-I signaling in MDA5^{KO} cells, 5'ppp-dsRNA was used (Figure 9C). HMW poly(I:C), was used to stimulate MDA5 in RIG-I^{KO} cells (Figure S 9D).

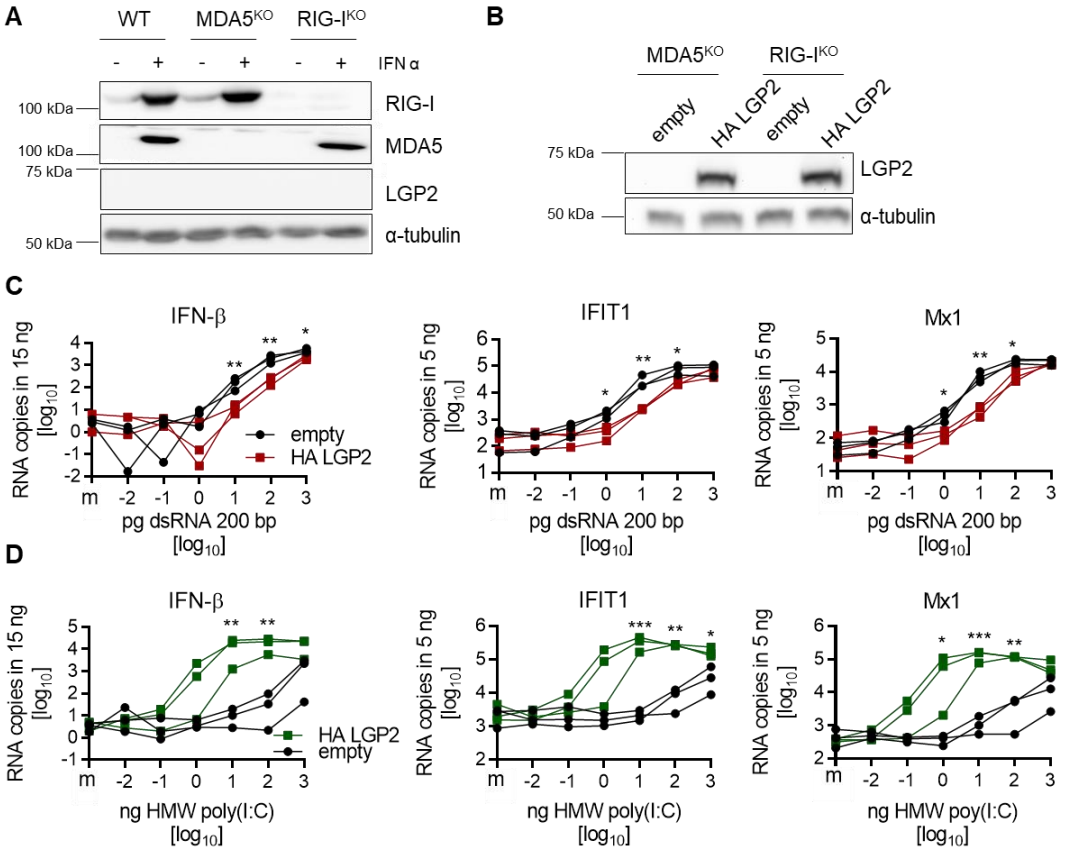

Figure 9: LGP2 suppresses RIG-I signaling and enhances MDA5 signaling upon dsRNA stimulation.

(A) Endogenous RIG-I, MDA5 and LGP2 protein expression in A549 WT, MDA5^{KO} (clone M2-28) and RIG-I^{KO} (clone R2-2#1). Cells were stimulated with 200 IU/ml of IFN-α for 24 h before harvesting for SDS-PAGE. Immunoblot was stained for LGP2, MDA5, RIG-I and α-tubulin as a loading control. **(B)** N-terminally HA-tagged LGP2 (HA-LGP2) or an empty vector control (empty) were stably introduced into A549 MDA5^{KO} and RIG-I^{KO} cells from (A) by lentiviral transduction. Immunoblot of LGP2 and α-tubulin is shown. **(C-D)** Stable cell lines generated in (B) were used to activate RIG-I and MDA5, respectively. (C) RIG-I pathway in MDA5^{KO} cells from (B) was activated by 8 h treatment with different doses of 5'ppp-dsRNA of 200 bp in length. (D) Similarly, the MDA5 pathway in RIG-I^{KO} cells from (B) was stimulated by 12 h transfection with different doses of HMW poly(I:C). Poly(C) treated cells served as a negative control (depicted as "m"). Cells were lysed for RNA isolation. IFN-β, IFIT1 and Mx1 mRNA copies were measured by qRT-PCR. Each curve represents one replicate. *, $p \leq 0.05$; **, $p \leq 0.01$; ***, $p \leq 0.001$ (comparison between HA-LGP2 and empty control at the indicated amount of stimulus). n =3.

IFN-β mRNA levels in MDA5^{KO} cells were inhibited up to 14-fold with 10 pg 5'ppp-dsRNA in the presence of LGP2 (Figure 9B, RIG-I-mediated signaling). In the case of RIG-I^{KO} A549, LGP2 increased IFN-β mRNA levels up to more than 1,000-fold with 10 ng poly(I:C) (Figure 9D, MDA5-mediated signaling). Equal to IFN-β, Mx1 and IFIT1 expression levels were similarly regulated (Figure 9C and D) with the highest differences achieved with 10 pg 5'ppp-dsRNA and 10 ng poly(I:C), respectively. For cells expressing LGP2 nearly 1,000-fold less poly(I:C) was needed to induce MDA5-mediated IFN-β, Mx1 and IFIT1 mRNA copies equal to empty control cells (Figure 9D). In the case of RIG-I, a 10-fold excess of 5'ppp-dsRNA was needed to induce similar IFN/ISG responses in cells expressing LGP2 compared to empty control cells (Figure 9C). These results indicate that LGP2 has a strong activating effect on MDA5 by

sensitizing the immune induction while it reveals a repressive and desensitizing effect on RIG-I signaling.

Overexpression of LGP2 under control of EF1-α leads to very high protein amounts. Thus, it was further investigated whether lower levels of LGP2 still contribute to the observed regulatory effects. Additionally to the EF1-α promoter, LGP2 was cloned under the control of a weaker ROSA26 promoter (Figure 10A left-hand). Both constructs were expressed in RIG-I^{KO} or MDA5^{KO} A549 cells leading to two different LGP2 expression levels (Figure 10A right-hand). Cells were challenged with MDA5- and RIG-I-specific synthetic stimuli analog to Figure 9**.**

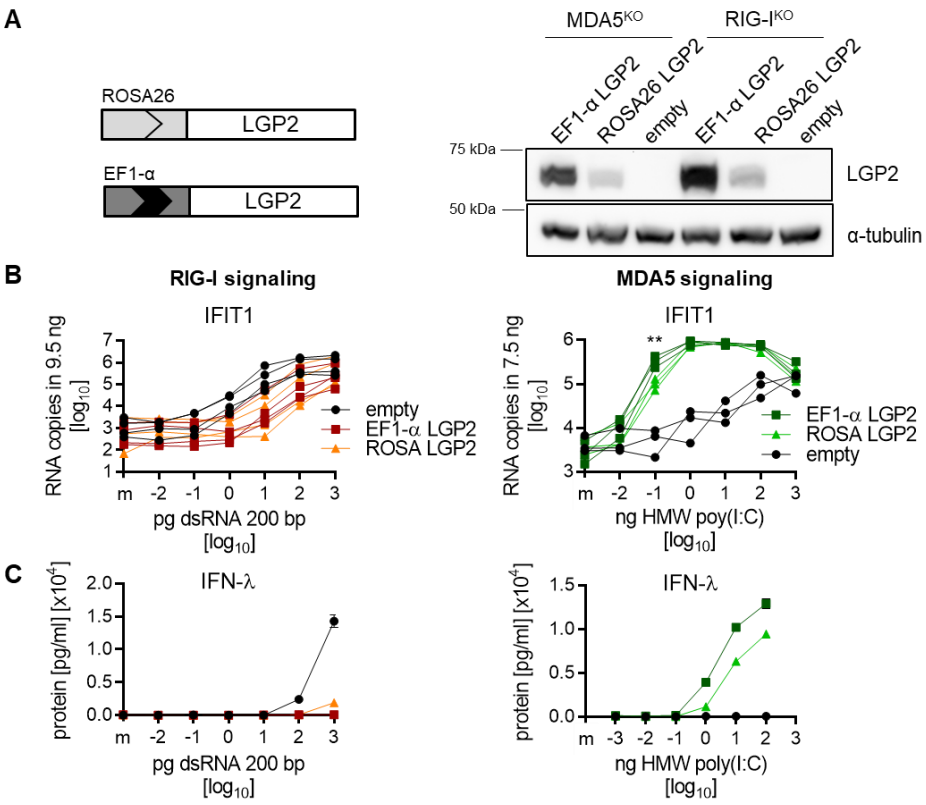

Figure 10: Exogenous, non-saturated protein levels of LGP2 are sufficient to suppress RIG-I and enhance MDA5 signaling.
(A) A549 MDA5^{KO} and RIG-I^{KO} clones (M2-28 and R2-2#1, respectively) were stably transduced with lentiviruses containing an untagged LGP2 expression construct either controlled by a weaker ROSA26 or a stronger EF1-α promoter upstream of the LGP2 gene to achieve different LGP2 expression levels (scheme depicted left-hand). Lysates of those generated cells were immunoblotted with LGP2 and α-tubulin antibodies (right-hand). **(B)** Cells from (A) were stimulated with synthetic RNA and lysed for RNA isolation. MDA5^{KO} cells were stimulated with different doses of 5'ppp-dsRNA for 8 h (left panel, RIG-I signaling) and RIG-I^{KO} cells were transfected with different doses of HMW poly(I:C) for 12 h (right panel, MDA5 signaling). Absolute IFIT1 mRNA copies were measured using qRT-PCR. Corresponding poly(C) treated cells served as negative control (depicted as "m"). Each curve represents one replicate. **p < 0.01 (comparison between ROSA26 LGP2 and EF1-α LGP2 at the indicated amount of stimulus). n=4 for RIG-I signaling, n=3 for MDA5 signaling. (**C)** Cell supernatants from a single experiment of (B) were measured for IFN-λ secretion by ELISA. RIG-I^{KO} cells expressing LGP2 (right panel) started to die with higher doses of HMW poly(I:C), thus 1000 ng HMW poly(I:C) samples were not included. "m" indicates poly(C) transfection.

The LGP2 expression driven by ROSA26, even though around 5-fold lower than that driven by EF1-α, revealed comparable regulatory activities on RIG-I and MDA5 signaling measured by mRNA induction of IFIT1 (Figure 10B). However, in the case of MDA5 signaling, lower IFN-λ protein levels were detected when LGP2 expression was weaker (Figure 10C).

These results imply that slight expression discrepancies among different LGP2 overexpression cell lines are probably negligible regarding their regulation of RIG-I and MDA5 signaling.

3.1.3 RNA binding but not ATPase hydrolysis of LGP2 is required to modulate RLR signaling in response to synthetic stimuli

ATP hydrolysis and RNA binding have been described as essential properties for LGP2's support on MDA5 signaling [56]. In contrast, both functions were proposed to be dispensable for RIG-I inhibition [122, 125]. Observations were based on read-outs in reporter systems and often include MDA5 and RIG-I overexpression. Hence, a side-by-side comparison of both pathways using physiological MDA5 and RIG-I levels was performed. To study the role of RNA binding, a single amino acid exchange (K634E) was introduced into LGP2 as two groups independently showed that this site is essential for RNA binding [26, 27]. To exclude a weak residual RNA binding potential of this mutant, two additional amino acids important for RNA binding were further mutated (K605E and K651E) resulting in a triple RNA binding mutation (K605E K634E K651E). As the Walker A motif was already extensively studied to be essential for ATP hydrolysis [22], the conserved amino acid (K30) was mutated to create an ATPase deficient version of LGP2 (K30A). For a schematic overview of the mutants see Figure 11A. WT, ATPase, single and triple RNA binding mutants of LGP2 were stably expressed in both RIG-I^{KO} and MDA5^{KO} A549 (Figure 11B). Challenging the cell lines with synthetic ligands (5'ppp-dsRNA for RIG-I signaling and HMW poly(I:C) for MDA5 signaling) revealed that ATPase hydrolysis function of LGP2 was dispensable for RIG-I and MDA5 regulation while RNA binding of LGP2 was needed (measured by IFIT1 mRNA levels, Figure 11C). In the case of MDA5, the single RNA binding mutant was still able to enhance signaling. This indicates that the weak RNA binding capability of MDA5 was stabilized even in the presence of an RNA binding deficient LGP2 (which reduced but did not abolish RNA binding, see 3.2.2). However, the low binding ability of this mutant was not enough to enable proper repression of RIG-I signaling.

In sum, the results suggest that RNA binding but not ATP hydrolysis of LGP2 is important to both inhibit RIG-I and enhance MDA5 signaling upon stimulation with synthetic dsRNA.

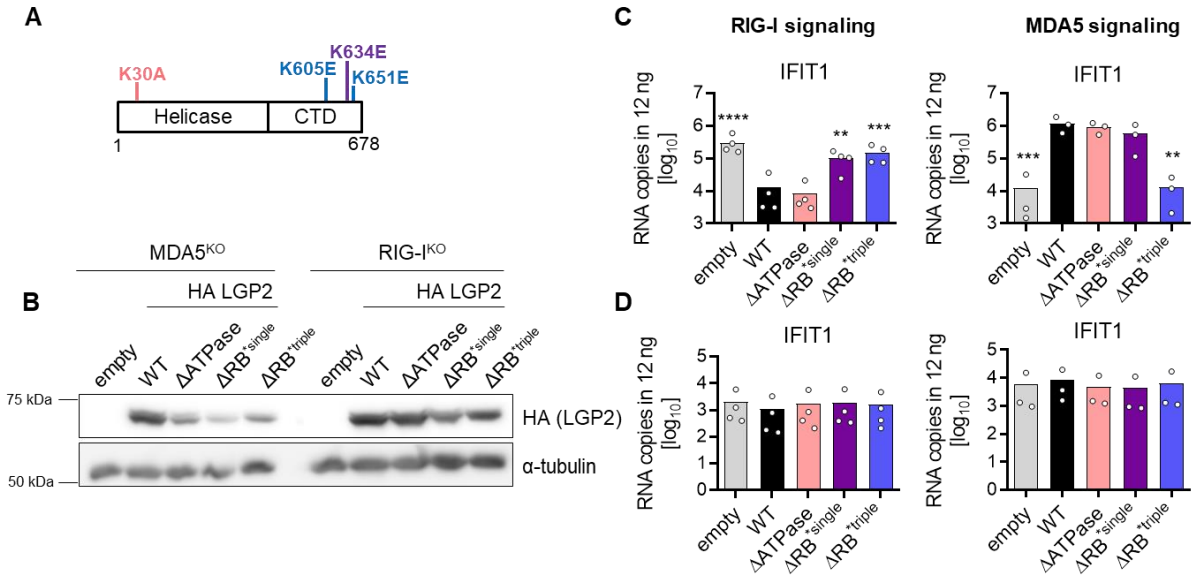

Figure 11: RNA binding but not ATPase function of LGP2 is required for the modulation of RIG-I and MDA5 signaling upon dsRNA stimulation.
(A) Strategy for generating ATPase and RNA binding defective LGP2 mutants is depicted. LGP2 ΔATPase contains the K30A mutation, mutation of LGP2 K634E is termed ΔRNA binding (RB)^{*single} and the LGP2 K605E K634E K651E triple mutation is termed ΔRB^{*triple}. **(B)** MDA5^{KO} (clone M2-28) or RIG-I^{KO} (clone R2-2#1) A549 expressing N-terminally HA-tagged LGP2 WT or respective mutants described in (A) or harboring an empty vector control (empty) were generated by lentiviral transduction. HA-immunoblot from lysates of established cell lines is shown. α-tubulin served as a loading control. **(C-D)** Cell lines from (B) were transfected with (C) 10 pg 5'ppp-dsRNA of 200 bp in length for 8 h (MDA5^{KO} cells, left-hand) or 10 ng HMW poly(I:C) for 12 h (RIG-I^{KO} cells, right-hand) to activate either RIG-I or MDA5 signaling. (D) Analogous transfection with poly(C) served as negative control (MDA5^{KO} cells, left-hand; RIG-I^{KO} cells, right-hand). IFIT1 mRNA levels were measured using qRT-PCR. RB=RNA binding. **, p ≤ 0.01; ***, p ≤ 0.001; ****, p ≤ 0.0001 (comparison between WT and mutants of LGP2 or empty control). n=4 for RIG-I signaling; n=3 for MDA5 signaling.

3.2 Impact of LGP2 on HDV replication and sensing in liver cells

LGP2 overexpression strongly activated MDA5 signaling in A549 cells (see Chapter 3.1). LGP2's contribution in viral sensing was further investigated in HepaRG cells, a hepatic cell line used as a surrogate of primary human hepatocytes [362]. In contrast to A549, these cells express detectable levels of all RLRs upon IFN-α stimulation (Figure 12A) making them an attractive tool to study the role of endogenous LGP2. Based on data from Dr. Zhenfeng Zhang, research group Prof. Dr. Stephan Urban, a collaboration was started to investigate the impact of LGP2 in the sensing of HDV, a satellite virus of HBV. Zhang et al. demonstrated that HDV is sensed by MDA5 in hepatocytes [48]. Although MDA5 has been proven to be critical for IFN activation during HDV replication, the underlying mechanism, especially the role of LGP2 in HDV RNA recognition, is unknown.

3.2.1 LGP2 is required for the MDA5-mediated IFN response upon HDV infection

Exogenous expression of NTCP, the entry receptor for HBV and HDV [363], in HepaRG cells renders these cells susceptible to HBV and HDV infection. Thus, it was introduced in all HepaRG-derived cells used in this study, designated as HepaRG^{NTCP} cells. As MDA5 was already identified as the receptor for HDV recognition [48], the role of endogenous LGP2 on the innate activation in HDV infected HepaRG^{NTCP} cells was studied in the following.

Firstly, RLR^{KO} HepaRG^{NTCP} cell pools were generated and validated by Western blot (Figure 12A). NT control, single RLR^{KO} (LGP2^{KO}, RIG-I^{KO}, MDA5^{KO}) and double RLR^{KO} cells (RIG-I^{KO}+LGP2^{KO}, MDA5^{KO}+LGP2^{KO}) were then infected with HDV to monitor their innate immune response by expression of IFN-λ1/IFN-β/RSAD2 mRNA and inhibition of HDV replication at the early and late phase of infection by HDAg IF. Strikingly, RIG-I was not needed for the induction of IFN-λ1/IFN-β/RSAD2, while either single or combined LGP2^{KO} and/or MDA5^{KO} cells abolished innate sensing to baseline levels (Figure 12B). In line with this, replication of the virus was slightly enhanced at an early and even more at a late stage of infection in either single or combined LGP2^{KO} and MDA5^{KO} cells. By contrast, RIG-I^{KO} and NT control HepaRG^{NTCP} cells showed equally lower infection rates (Figure 12C). Thus, as was already determined, RIG-I was neglectable for HDV sensing while MDA5 was the responsible sensor to activate the immune system [48]. In addition to that, LGP2 was essential for sensing HDV infection and suppression of HDV replication in HepaRG^{NTCP} cells.

First experiments with primary human hepatocytes (PHH) revealed a similar dependency of HDV-induced innate sensing on MDA5 and LGP2 (Figure S 7). As for HepaRG^{NTCP} cells, both investigated donors showed inducible and detectable protein expression of all RLRs (Figure S 7A and D). Purified lentiviruses harboring RLR-specific shRNAs or a non-targeting (shNT) control were used for reverse transduction of PHHs (donor#2) prior to HDV infection or mock treatment for 3 days. Measuring the RLR knockdown efficiency by qRT-PCR revealed at least 80% transcriptional downregulation for treatments with MDA5 shRNA-a and -b, RIG-I shRNA-a and LGP2 shRNA-b while RIG-I shRNA-b and LGP2 shRNA-c showed partially lower knockdown rates (Figure S 7C). This is in line with the observed protein levels in those cells (Figure S 7D). Measurement of IFN-β, IFN-λ1 and RSAD2 mRNA levels upon HDV infection revealed that shMDA5-a and-b and shLGP2-b treated PHHs are strongly impaired in their type I/III IFN response compared to naïve, shNT control and shRIG-I treated cells (Figure S 7F). mRNA levels of IFN-β, IFN-λ1 and RSAD2 were at least 12-times higher in naïve, shNT control and shRIG-I infected cells compared to the respective basal levels (Figure S 7E).

Moreover, the observed differences in the immune response induction were not due to discrepancies in infectivity as HDV RNA copies were high in all infected PHHs (Figure S 7G).

This data should be validated by using additional donors. Nonetheless, it leads to the assumption that the results obtained in HepaRG^{NTCP} cells can be reproduced in PHHs, indicating that in HDV infected liver cells MDA5 and LGP2 are crucial for the induction of antiviral immune responses.

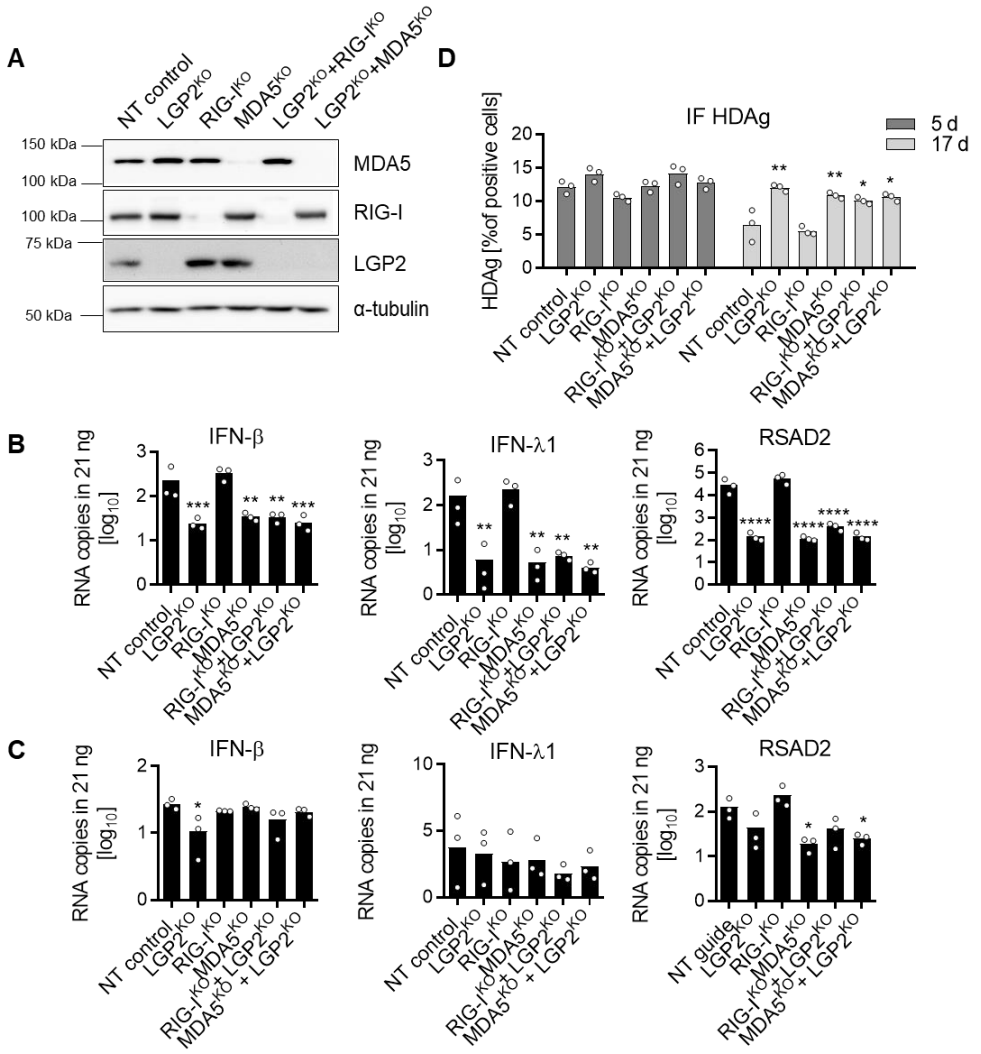

Figure 12: Both MDA5 and LGP2 are essential for IFN activation and viral suppression during HDV infection in HepaRG^{NTCP} cells.

(A) HepaRG^{NTCP} cell pools with stable KO of MDA5, RIG-I, LGP2, both LGP2 and RIG-I, both LGP2 and MDA5, or non-targeting guide (NT control) were generated. Cells were stimulated for 24 h with 200 IU/ml IFN-α before harvesting for Western blot analysis. Protein expression of MDA5, RIG-I, LGP2 and α-tubulin was determined. (**B-D)** Cell lines from (A) were infected with HDV. (B) 3 d pi IFN-β, IFN-λ1 and RSAD2 mRNA levels were measured by qRT-PCR in HDV infected samples (C) as well as in uninfected controls. n=3. (D) 5 d and 17 d pi HDV positive cells were visualized by IF of HDAg and quantified using ImageJ. Data in panel (D) generated by Dr. Zhenfeng Zhang. *, $p \leq 0.05$; **, $p \leq 0.01$; ***, $p \leq 0.001$; ****, $p \leq 0.0001$ (comparison between NT control and KO HepaRG). n=3.

3.2.2 Binding to poly(I:C) is severely reduced in K634E LGP2 and fully lost in K605E K634E K651E LGP2

As MDA5 is dependent on LGP2 for sensing HDV, the role of LGP2's ATPase hydrolysis and RNA binding function was further investigated. LGP2^{KO} HepaRG^{NTCP} cells were used to reconstitute either WT or respective mutants of LGP2 harboring silent mutations in the guide RNA binding sequence to circumvent cleavage by Cas9. Cells with endogenous LGP2, no LGP2 (Figure 13A), or the overexpressed N-terminally HA-tagged LGP2 versions (Figure 13B) were firstly used to investigate the binding capacity of LGP2 mutants to RNA. IP of cell lysates with poly(I:C)-coupled beads confirmed loss of RNA binding to almost 100% for the LGP2 triple RNA binding mutant (K605E K634E K651E), whereas a single mutation of K634E resulted in 14% RNA binding ability compared to WT LGP2 (Figure 13). ATPase deficient LGP2 was able to bind poly(I:C) with 86% binding efficiency compared to WT in this assay (Figure 13).

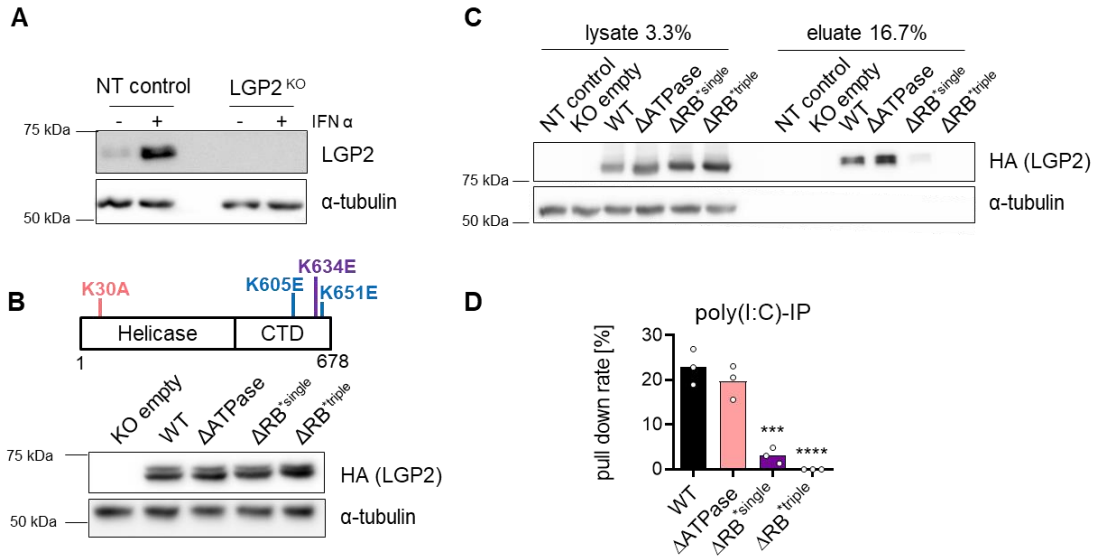

Figure 13: C-terminal lysine residues K605, K634 and K651 of LGP2 but not the ATPase hydrolysis function are important for binding to poly(I:C).
(A) HepaRG^{NTCP} cells with a non-targeting guide (NT control) RNA or an LGP2 guide-expressing CRISPR-Cas9 vector (LGP2^{KO}) were stimulated with 200 IU/ml of IFN-α for 24 h or left untreated prior to immunoblotting of LGP2 and α-tubulin. **(B)** HepaRG^{NTCP}-LGP2^{KO} cells were stably reconstituted with HA-tagged LGP2 WT, ATPase deficient (ΔATPase), or RNA binding deficient mutants with single (ΔRB^{*single}) or triple (ΔRB^{*triple}) mutations or transduced with an empty lentiviral vector control (KO empty). A schematic representation of mutation sites within LGP2 is depicted in the top panel. Expression of LGP2 in the respective cell lines was measured by immunoblot using HA antibody, see the bottom panel. α-tubulin was used as a loading control. **(C)** HepaRG^{NTCP} cells from (B) were used for poly(I:C)-IP to test the RNA binding capability of different HA-LGP2 versions. NT control-expressing cells from (A) and KO empty cells from (B) served as negative controls. Cell lysates were incubated with poly(I:C)-coupled beads for 4 h. One out of three representative poly(I:C)-IPs is depicted. HA immunoblots of cell lysates and eluates are shown. α-tubulin served as a loading control. **(D)** Quantification of the HA-LGP2 pull-down rate from (C) normalized to the respective lysate. No quantification was performed for NT control and KO empty, as there was no detectable HA band in the lysate and eluate. RB=RNA binding. ***, $p \leq 0.001$ ****, $p \leq 0.0001$ (WT was compared to mutants of LGP2). n=3.

These results indicate that the LGP2 triple mutant is fully RNA binding deficient while a single mutation of K634E maintains some weak residual binding, matching the results in A549 cells (Figure 11C, right panel). In contrast, ATPase hydrolysis did not influence LGP2's binding behavior to poly(I:C). This is consistent with previous publications that claim RNA binding of Walker A mutants [22, 56].

3.2.3 LGP2 ATPase hydrolysis and RNA binding are important to mount an HDV-induced IFN response

To investigate the effect of the LGP2 mutants from the previous chapter (3.2.2) on the HDV-induced innate response, cells either expressing endogenous LGP2, $LGP2^{KO}$ transduced with an empty lentiviral vector control (KO empty, Figure 13A) or reconstituted with the respective LGP2 versions (Figure 13B) were infected with HDV and further cultivated for up to 17 days. The IFN response was measured by the production of IFN-β, IFN-λ1 and RSAD2 mRNA expression levels (Figure 14A). Throughout the investigated time frame, the triple RNA binding mutant of LGP2 did not show any IFN response. This reveals the importance of LGP2 and its RNA binding function to support MDA5. Only minor innate signaling defects were seen for the single RNA binding mutant because this mutant is still able to bind weakly to RNA (Figure 13D). In the case of WT LGP2, overexpressed levels displayed an advantage in the early time of infection, as sensing was faster and/or more sensitive compared to NT control cells harboring only endogenous LGP2 (see 2 days pi, Figure 14A). With the progress of the infection, endogenous LGP2 levels led to a saturated IFN response (through its own upregulation as ISG, see Figure S 11A). Overexpressed LGP2 levels did not further trigger signaling 3 days pi (when the IFN response was highest). ATPase hydrolysis function is important for the upregulation of the innate antiviral response upon stimulation with HDV, even though to a minor extent than the LGP2 RNA binding function (Figure 14A). This is in contrast to the results obtained with A549 cells, where ATPase function was neglectable for the MDA5 enhancement upon HMW poly(I:C) transfection (Figure 11C, right panel).

A negative correlation between the speed and strength of the IFN induction and HDV replication was expected. Indeed, in line with the induction of IFN signaling (Figure 14A), HDV replication (measured by HDV RNA copies) was least suppressed in KO empty cells without LGP2 reconstitution and cells expressing the triple RNA binding mutant (Figure 14B). Control cells with endogenous LGP2 levels showed the same HDV replication kinetics as single RNA binding and ATPase hydrolysis mutants, whereas overexpression of WT LGP2 strongly decreased intracellular HDV RNA. Besides the measurement of HDV RNA, infection rates were validated by IF of HDAg. As for intracellular HDV RNA levels, the HDAg IF results

negatively correlate with those of the IFN responses: highest infection rates for KO empty and triple RNA binding mutant and lowest infection rate for exogenous LGP2 expression cell line (Figure 14C). Western blotting against small and large HDAg (S-HDAg, L-HDAg) at 17 days pi revealed the lowest HDAg levels in NT control cells and cells with exogenous LGP2 (WT). Moreover, the strongest protein expression of S-HDAg, which is needed for HDV replication [223], was found in KO empty and triple RNA binding mutant-expressing HepaRG^{NTCP} (Figure S 10).

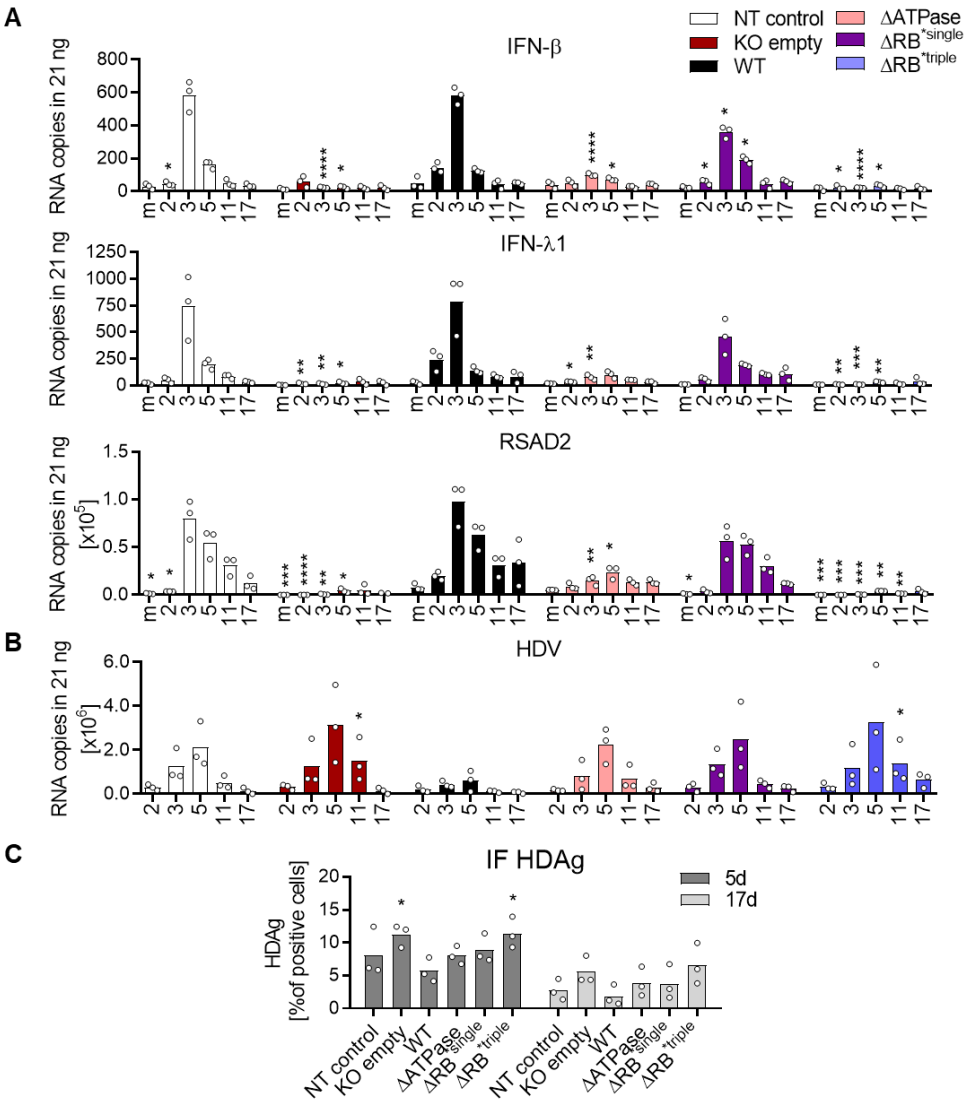

Figure 14: Both ATPase and RNA binding functions of LGP2 are critical for IFN activation and viral suppression during HDV infection in HepaRG^{NTCP} cells.
(A-B) Cell lines shown in Figure 13B and the NT control HepaRG^{NTCP} cell line from Figure 13A were infected with HDV or mock treated. (A) The mRNA levels of IFN-λ1, IFN-β and RSAD2 and of (B) HDV RNA at 2 d, 3 d, 5 d, 11 d and 17 d pi were quantified by qRT-PCR. "m" in post HDV infected cells depicts 2 d mock infected cells. Cell seeding and infection were performed by Dr. Zhenfeng Zhang. **(C)** The percentage of HDV positive cells at 5 d and 17 d pi was analyzed by IF of HDAg and quantified using ImageJ. Data in panels (B) and (C) generated by Dr. Zhenfeng Zhang. *, $p \leq 0.05$; **, $p \leq 0.01$; ***, $p \leq 0.001$; ****, $p \leq 0.0001$ (mutants of LGP2 or control cell lines were compared to WT LGP2 at the depicted time points). n=3.

These results indicate the importance of especially the RNA binding and to some extent the ATPase function of LGP2 in crucially supporting MDA5-dependent IFN responses and suppression of HDV replication in HepaRG^{NTCP} cells. The importance of RNA binding of LGP2 for MDA5 synergy was already proven in A549 cells (Figure 11C, right panel).

3.2.4 LGP2 binds HDV RNA

HDV infection of LGP2 single RNA binding mutant-expressing cells showed only minor innate signaling defects (Figure 14A) thus leading to the speculation that this mutant is still at least partially able to bind HDV RNA, similar to the results seen with poly(I:C) (Figure 13C and D). To investigate the potential of WT LGP2, LGP2 single and triple RNA binding mutant and ATPase mutant to directly bind to HDV RNA, an HA pull-down assays of all LGP2 variants (N-terminally HA-tagged) was performed and the amount of bound HDV RNA was measured by qRT-PCR (Figure 15). HDV RNA binding was completely abolished in the triple RNA binding mutant (1% of WT), however, the single RNA binding mutant could still bind HDV RNA to a minor extent (18% of WT) as expected from the previous results by using poly(I:C). The HDV RNA binding efficiency of the ATPase mutant was 76% of WT LGP2.

Altogether, this data strongly coincides with the binding strengths of the respective LGP2 variants to HMW poly(I:C) (Figure 13).

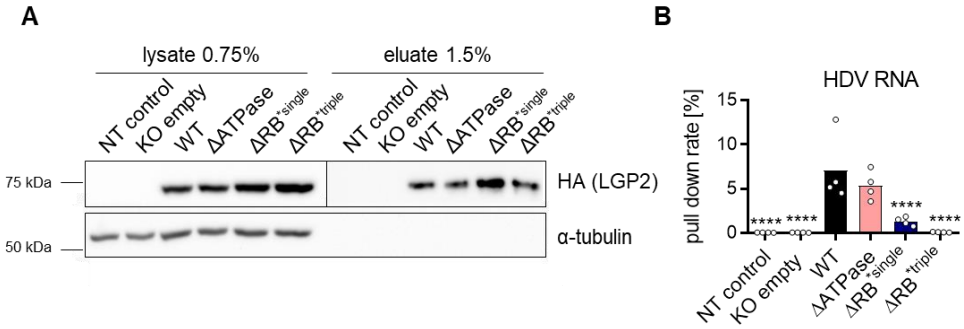

Figure 15: LGP2 binding to HDV RNA is dependent on K605, K634 and K651 in the C-terminal domain and independent of its ATPase function.
(A) HepaRG^{NTCP} cells used in Figure 13 were infected with HDV. At 5 d after HDV infection, cells were lysed and immunoprecipitated by using HA-coupled magnetic beads. HA-LGP2 expression in lysates and eluates was measured by Western blotting. α-tubulin served as a loading control. Lysates and eluates with different exposure times. One representative Western blot is shown. **(B)** Lysate and eluate of the HA-immunoprecipitations from (A) were used for RNA isolation and qRT-PCR to determine the amount of HDV RNA bound to LGP2. HDV RNA copies of the eluate were normalized to the copy numbers in the respective lysate designating the pull-down rate. HDV-IP was performed by Dr. Zhenfeng Zhang. RB=RNA binding. ****, $p \leq 0.0001$ (WT compared to LGP2 mutants or control cell lines). n=4.

3.3 Effect of LGP2 and its polymorphisms in several viral infections

So far, only polymorphisms of MDA5 and RIG-I were functionally investigated and correlated to differential diseases outcomes (see 1.1.3.5). As the outcome of naturally occurring LGP2 polymorphisms on RLR signaling is unknown, three human non-synonymous LGP2 variants were further investigated in the context of different viral infections. These abundant variants either harbor an amino acid exchange in the helicase domain (Q425R, N461S) or within the pincer region [20] (R523Q) of LGP2 and were taken from the study of Vasseur et al. [114].

3.3.1 Naturally occurring Q425R LGP2 enhances the IFN response upon HDV infection in HepaRG cells

Data obtained in Chapter 3.2 highlights the importance of both functional RNA binding and ATPase hydrolysis functions of LGP2 for proper innate signaling towards HDV infection. To date, the effect of naturally occurring LGP2 polymorphisms in combating viral infections remains elusive. Three naturally and frequently occurring LGP2 variants and their role in HDV infection were investigated. (Figure 16A, left-hand). They are present with different allele frequencies in the human populations ranging from 2% to 85% (Figure 16A, right-hand).

Analog to Figure 14, stable overexpression cell lines of WT or LGP2 variants were generated into LGP2^{KO} HepaRG^{NTCP} harboring an N-terminal HA-tag and a Cas9 cleavage resistant LGP2 sequence (Figure 16B). LGP2^{KO} HepaRG^{NTCP} harboring an empty vector control (KO empty) served as a further negative control. Cells were infected with HDV, further cultivated for 17 days and measured for their innate immune gene expression and HDV replication.

IFN-β, IFN-λ1 and RSAD2 mRNA expression levels in LGP2 variants did not reveal any difference compared to WT LGP2 upon infection (Figure 16C, Figure S 12). As an exception, only Q425R LGP2 revealed a significantly higher, accelerated RSAD2 expression 2 days pi (Figure S 12B, upper panel). Comparing steady-state expression of antiviral genes, Q425R LGP2 (but not the other LGP2 variants) showed enhanced baseline IFN-λ1 and RSAD2 mRNA expression levels when compared to WT LGP2 (Figure 16C, Figure S 12B). This increase was not due to different expression levels of the LGP2 variants that were well comparable (Figure 16B).

The stronger initial IFN response in the Q425R LGP2 cells and their accelerated response at 2 days pi might explain the mild but significant decrease of HDV positive cells at 5 days and

17 days pi in Q425R LGP2 cells compared to WT LGP2 cells (Figure 16E). This is in line with slightly reduced intracellular HDV RNA levels in those cells (Figure 16D). In contrast, LGP2 N461S and R523Q resemble WT LGP2 in mock and HDV infected states (Figure 16C-E, Figure S 12). It should only be noted that the IFN-λ1 mRNA levels of R523Q LGP2-expressing cells were enhanced at 3 days pi (Figure 16C, upper panel).

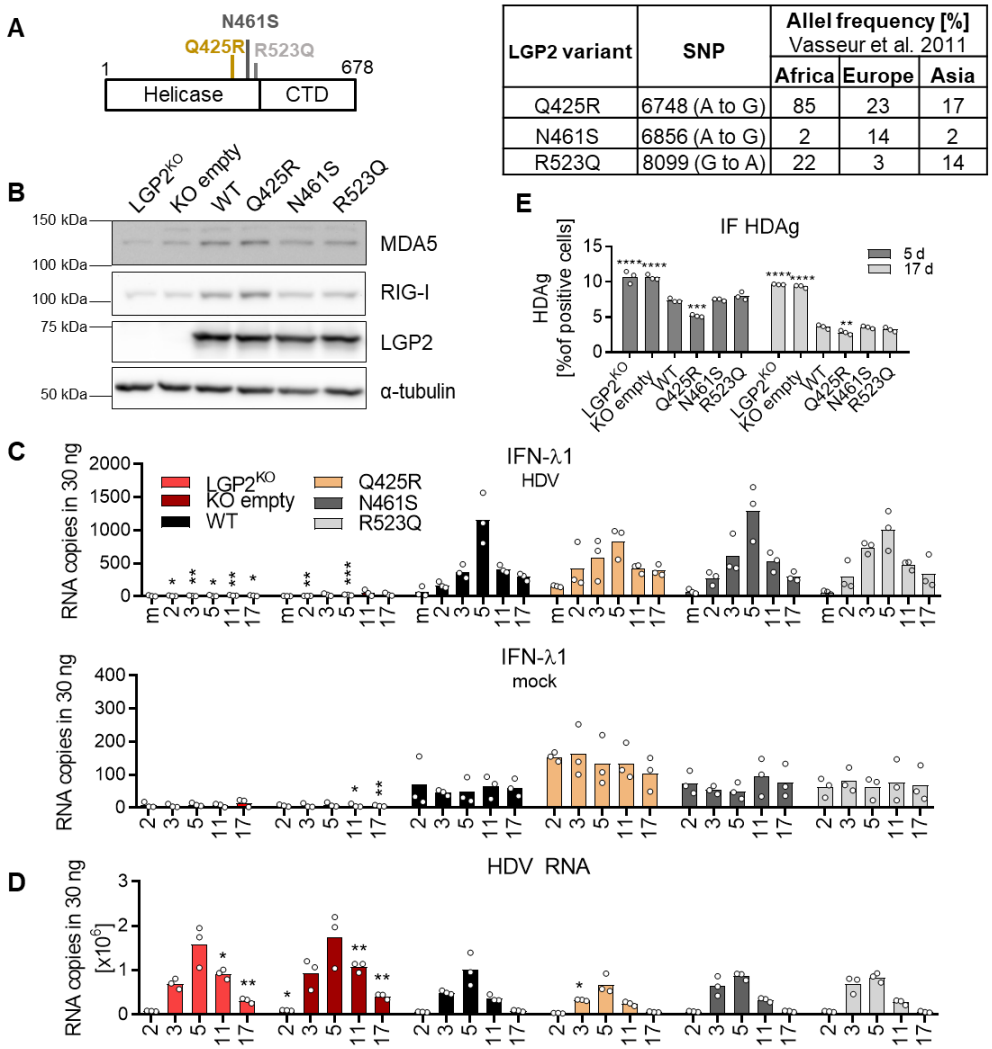

LGP2 variant	SNP	Allel frequency [%] Vasseur et al. 2011		
		Africa	Europe	Asia
Q425R	6748 (A to G)	85	23	17
N461S	6856 (A to G)	2	14	2
R523Q	8099 (G to A)	22	3	14

Figure 16: Q425R LGP2 variant enhances steady-state and accelerates HDV-induced IFN response and increases HDV repression.

(A) Schematic representation of three abundant non-synonymous single nucleotide polymorphisms (SNPs) within LGP2 (left-hand). The table shows the percentage of the LGP2 SNP frequency in different human populations and their position according to Vasseur et al. 2011 (right-hand). **(B)** HepaRG^{NTCP} cells stably expressing N-terminally HA-tagged WT or SNP LGP2 versions from (A) in an LGP2^{KO} background were generated and immunoblotted. LGP2^{KO} HepaRG^{NTCP} and LGP2^{KO} cells harboring an empty vector (KO empty) served as negative controls. The cell lysate was stained for MDA5, RIG-I, LGP2 and α-tubulin as a loading control. **(C)** Cells generated in (B) were infected with HDV and harvested at 2 d, 3 d, 5 d, 11 d and 17 d pi. Gene expression of IFN-λ1 in mock and HDV infected cells and **(D)** HDV RNA in HDV infected cells was measured by qRT-PCR. n=3. "m" in post HDV infected cells depicts 2 d mock infected cells. **(E)** At 5 d and 17 d pi, the percentage of HDV positive cells was analyzed by IF of HDAg and quantified using ImageJ. Infection experiments and further analysis were performed by Dr. Zhenfeng Zhang. *, p ≤ 0.05; **, p ≤ 0.01; ***, p ≤ 0.001; ****, p ≤ 0.0001 (comparison between WT and mutants of LGP2 at the depicted time points). n=3.

In sum, this data indicates that Q425R LGP2 accelerates the IFN response at early times in HepaRG^{NTCP} cells leading to slight but significantly stronger repression of HDV than WT LGP2. There was no difference for N461S and R523Q in the IFN response and viral repression compared to WT LGP2.

3.3.2 Q425R LGP2 enhances RLR-mediated signaling compared to WT LGP2 upon Mengo Zn virus and SeV infection in HepaRG cells

Q425R LGP2 revealed an accelerated IFN response upon HDV infection while the other two investigated LGP2 SNPs (N461S or R523Q) behaved almost the same as WT LGP2 (see Chapter 3.3.1). As next, it should be addressed whether the enhanced functionality seen with Q425R LGP2 upon HDV infection is rather generic or virus-specific. Therefore, LGP2^{KO} HepaRG^{NTCP} reconstituted with either WT or variants of LGP2 (from Figure 16) were tested in other viral infections, with non-targeting (NT) or LGP2^{KO} HepaRG^{NTCP} cells as controls. Thus these, HepaRG^{NTCP} cells were challenged with Mengo Zn virus and SeV to investigate the induction of IFN response. Both viruses were already used to induce MDA5- (Mengo Zn virus) and RIG-I-specific (SeV) responses (Table 1) also in HuH7.5^{NTCP}, another hepatic cell line [48].

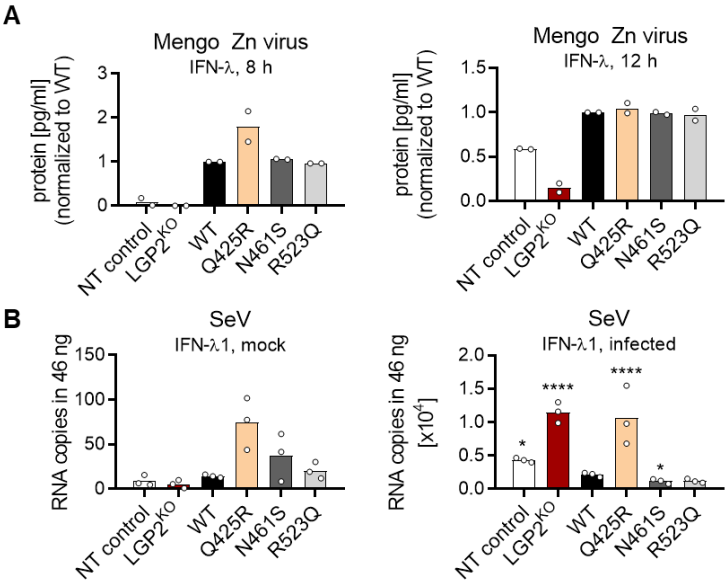

Figure 17: Q425R LGP2 enhances the IFN response after Mengo Zn virus and SeV infection in HepaRG^{NTCP}cells compared to WT.
(A) HepaRG^{NTCP} LGP2^{KO} cells stably expressing N-terminally HA-tagged WT or LGP2 variants described in Figure 16 and a non-targeting guide-expressing HepaRG^{NTCP} control cells (NT control) were infected with Mengo Zn virus (MOI=5) for 8 h and 12 h or kept uninfected prior to IFN-λ protein measurement by ELISA. Mock cells without IFN-λ secretion (data not shown). n=2. **(B)** HepaRG^{NTCP} cells from (A) were used for SeV infection (MOI=1). Cells were kept uninfected or infected for 24 h prior to RNA isolation and qRT-PCR to evaluate IFN-λ1 mRNA copy numbers. *, p ≤ 0.01; ****, p ≤ 0.0001 (WT compared to mutants of LGP2 or control cell lines). n=3.

In the case of Mengo Zn virus, cells were infected for 8 hours and 12 hours and IFN-λ secretion was measured by ELISA. LGP2 overexpression enhanced the IFN-λ production upon infection with Mengo Zn virus, while its knockdown repressed it (Figure 17A). This underlines the results from Figure S 16A where Mengo Zn virus was dominantly sensed by MDA5 in HepaRG cells, together with the help of LGP2. Of note, the presence of Q425R LGP2 accelerated IFN-λ protein production. 8 hours pi IFN-λ secretion was around 1.8-fold higher in Q425R compared to WT LGP2, however, no further upregulation was seen after 12 hours (Figure 17A). N461S and R523Q LGP2 behaved as WT at both time points. This data underlines the assumption that (i) the MDA5-enhancing effect of Q425R LGP2 is a rather general property of this mutant and that (ii) it rather influences the early outcome of MDA5 response.

Next, the IFN response of the HepaRG^{NTCP} cells expressing the LGP2 variants was studied upon SeV infection. SeV was not only shown to be exclusively sensed by RIG-I in A549 (Figure 7B**,** Figure S 4D) but also HepaRG (Figure S 19D) cells in this study. Cells were infected with SeV or were mock treated for 24 hours. IFN-λ1 mRNA was measured by qRT-PCR to analyze the outcome of the immune response. Q425R LGP2 induced stronger basal IFN-λ1 RNA expression (Figure 17B, left panel) as already seen beforehand (Figure 16C, Figure S 12B). Upon infection significantly stronger innate response was revealed with LGP2^{KO}, indicating that RIG-I activity is repressed by endogenous LGP2 in HepaRG^{NTCP} cells (Figure 17B, right panel). Enhancing the LGP2 levels through overexpression significantly decreased RIG-I-dependent induction of IFN-λ1 mRNA compared to NT control cells. WT, N461S and R523Q LGP2 indicated similar RIG-I repressive functions upon SeV infection (Figure 17B). Strikingly, Q425R LGP2 lost its inhibitory effect on RIG-I signaling as IFN-λ1 levels were comparable to LGP2^{KO} cells. Thus, this data indicates that Q425R LGP2 also enhances IFN production upon SeV infection probably by loss of its negative effect on RIG-I.

3.3.3 Q425R LGP2 enhances MDA5-dependent IFN response upon SARS-CoV-2 infection in A549 cells

The effect of LGP2 polymorphisms was further investigated in an infection with a relevant human pathogen. SARS-CoV-2, currently causing a worldwide pandemic, was further used to understand the importance of the natural LGP2 variants in the MDA5 response. SARS-CoV-2 causes respiratory disease, so the infection was tested in A549 lung epithelial cells. Based on recent publications, MDA5 plays a major role in the sensing of SARS-CoV-2 (see 1.2.2 and Table 1).

Stable A549 cell lines expressing either an empty vector control (empty) or reconstituted with N-terminally HA-tagged WT or variants of LGP2 were generated. The cell lines reveal comparable protein amounts of LGP2 (Figure 18A). SARS-CoV-2 depends on the host receptor angiotensin-converting enzyme 2 (ACE2) and transmembrane protease serine subtype 2 (TMPRSS2) for early viral entry [364] which are poorly expressed in A549 cells [365, 366]. Thus, 24 hours prior to infection cells were transiently transduced with lentiviruses encoding for ACE2 and TMPRSS2. SARS-CoV-2 (MOI=0.001 and MOI=0.1) infected or mock treated cells were harvested 24 hours pi. Immune response and viral replication were analyzed by qRT-PCR of IFN-β, IFN-λ1, RSAD2 and SARS-CoV-2 nucleocapsid.

In line with the results of Q425R LGP2-expressing HepaRG^{NTCP}cells, IFN-λ1 and RSAD2 mRNA steady-state levels were slightly enhanced in Q425R LGP2-expressing A549 compared to WT LGP2-expressing cells (Figure 18B). In infected empty cells, the induction of RLR-mediated immune response was almost absent in line with other reports [367, 368]. However, LGP2 expression enabled a more robust innate immune induction, especially at higher MOI (Figure 18B, Figure S 13A). N461S and R523Q LGP2 showed quite comparable IFN/ISG mRNA activation with WT LGP2-expressing A549. At MOI=0.1, WT LGP2-expressing cells showed on average an around 13-fold to 35-fold higher IFN/ISG response compared to empty cells. This underlines the importance of LGP2's support in SARS-CoV-2-induced innate immune induction in A549 cells expressing only low initial MDA5 (Figure 18B, Figure S 13A). Q425R LGP2 further enhanced the upregulation of IFN-λ1, RSAD2 and IFN-β compared to WT LGP2 around 5-fold at MOI=0.1 (Figure 18B, Figure S 13A).

The strength of the IFN response in the respective cell lines did not robustly correlate with the antiviral activity. SARS-CoV-2 replication is not strikingly different in the different cell lines neither 24 hours pi (Figure 18BC) nor 6 hours pi (Figure S 13B). At MOI=0.1 (which was more IFN stimulatory at 24 hours pi), the percentage of infected cells seemed slightly reduced with Q425R LGP2 and slightly enhanced with the other LGP2 variants 6 hours pi in a first pilot experiment (Figure S 13C).

In sum, the data demonstrates Q425R LGP2 to be a stronger enhancer of the MDA5-mediated innate immune response upon SARS-CoV-2 infection in A549 cells than WT LGP2.

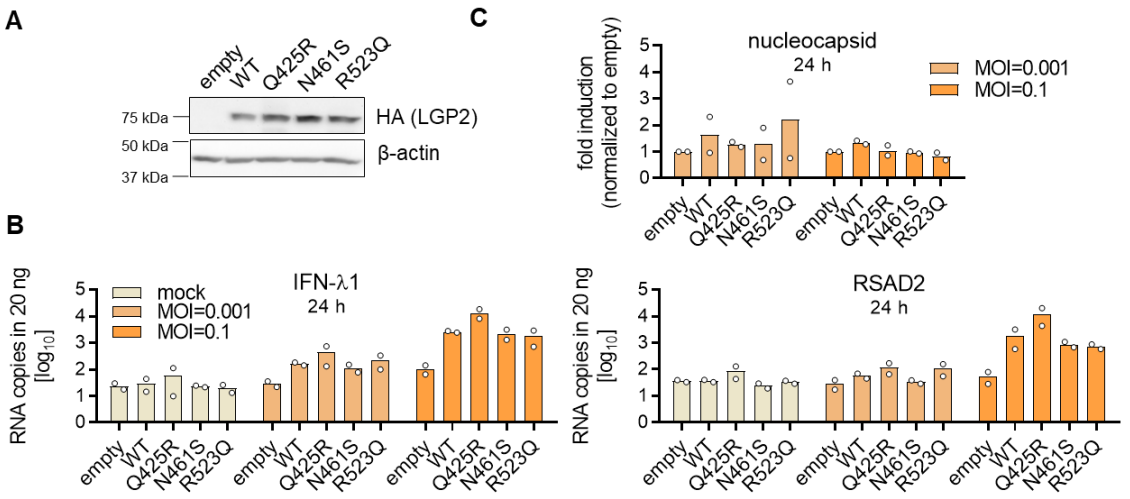

Figure 18: Q425R LGP2 enhances the IFN response upon SARS-CoV-2 infection in A549 cells. **(A)** Naïve A549 cells were stably transduced with lentiviruses encoding for an empty vector control (empty), N-terminally HA-tagged LGP2 WT or Q425R, N461S, or R523Q variants. Cell lysates were analyzed by Western blot analysis for LGP2 expression levels using HA antibody. β-actin served as a loading control. **(B-C)** Cells from (A) were transiently transduced with ACE2 and TMPRSS2 encoding lentiviruses. 24 h later, cells were kept uninfected (mock) or infected with SARS-CoV-2 (MOI=0.001 and MOI=0.1) for further 24 h, prior to harvesting for RNA isolation and qRT-PCR. mRNA levels of (B) IFN-λ1 and RSAD2 were measured as well as (C) SARS-CoV-2 nucleocapsid expression (normalized to GAPDH and infected empty cells). n=2. Lentivirus transduction, infection and harvesting were done by Dr. Vladimir Goncalves Magalhaes, research group Marco Binder. One out of two qRT-PCRs from (B) and (C) was measured by Dr. Zhenfeng Zhang.

3.3.4 Q425R LGP2 partially loses the repressive effect on RIG-I signaling upon SeV and ZIKV infection in A549 cells

In the previous chapters (3.3.1 to 3.3.3), Q425R LGP2 was shown to enhance MDA5-mediated immune responses upon HDV, Mengo Zn virus and SARS-CoV-2 infection, respectively. Moreover, the negative effect of WT LGP2 on RIG-I signaling was lost with Q425R LGP2 in HepaRG^{NTCP} cells when infected with SeV (Figure 17B). To further confirm this RIG-I-specific phenotype in A549 cells, cell lines generated in 3.3.3 were infected with SeV and measured for their immune response and viral replication. As in Figure 18, steady-state mRNA levels of especially IFN-λ1 were slightly enhanced in Q425R LGP2-expressing A549 compared to empty control, WT or N461S or R523Q LGP2 (Figure 19A, left panel).

Eight hours pi, empty control cells showed a significantly stronger innate response than WT LGP2-expressing A549 cells measured by IFN-λ1 and RSAD2 mRNA levels (Figure 19A, right panel) and IFN-λ protein levels (Figure 19C). This once more affirms the observed negative role of LGP2 on RIG-I signaling in SeV infected A549 (Figure S 1B). The N461S LGP2 variant revealed some tendency of slightly stronger repression both on IFN-λ1 and RSAD2 mRNA

levels and IFN-λ protein secretion compared to WT LGP2 while R523Q LGP2 behaved analog to WT LGP2 8 hours pi (Figure 19A and C). In contrast, Q425R LGP2 partially lost the repressive effect on RIG-I-signaling. Eight hours pi the IFN-λ1 mRNA and protein secretion of Q425R LGP2-expressing A549 were around 2-fold higher while RSAD2 mRNA expression was around 4-fold higher compared to WT LGP2 (Figure 19A and C).

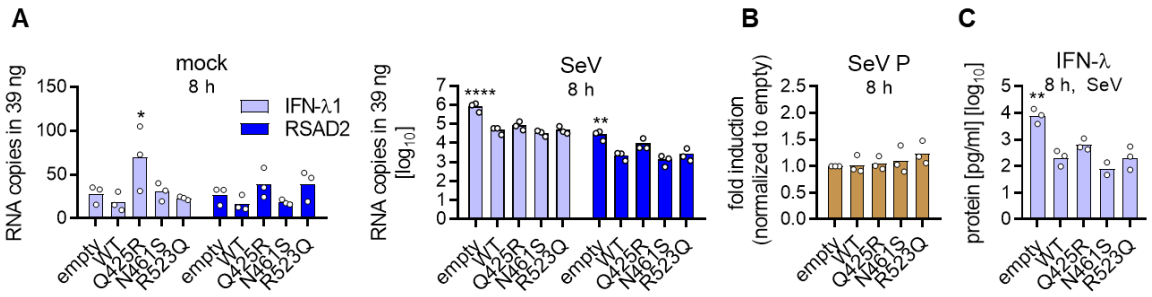

Figure 19: Q425R LGP2 reduces the IFN response upon SeV infection to a lesser extent than WT in A549 cells.

(A-C) Cells from Figure 18A were mock treated (left panel) or infected with SeV (MOI=1) (right panel) for 8 h prior to harvesting for RNA isolation and qRT-PCR. mRNA levels of (A) IFN-λ1, RSAD2 and (B) SeV phosphoprotein (P) of SeV infected cells were measured as well as (C) IFN-λ protein secretion by ELISA. No IFN-λ secretion was detected in mock cells (data not shown). SeV P expression was normalized to GAPDH and infected empty cells. *, $p \leq 0.05$; **, $p \leq 0.01$; ****, $p \leq 0.0001$ (comparison between WT and mutants of LGP2 or control cell line). n=3.

Even though the strength of the immune induction varied in the respective cell lines at 8 hours post-SeV infection, this did not influence SeV replication which was comparable in all cell lines used (Figure 19B). First data with longer infection of SeV indicates that the observed effects seen with the different LGP2 variants described at 8 hours are still maintained at 24 hours (Figure S 14). This is in line with the results obtained with HepaRG^{NTCP} cells reconstituted with WT or variants of LGP2 24 hours post-SeV infection (Figure 17B).

In literature, paramyxovirus V protein interaction with LGP2 prevents its MDA5-mediated enhancement of innate signaling [61]. Moreover, a minimal V protein binding region (MVBR, amino acids 351 to 479 in LGP2) conserved within MDA5 and LGP2 helicase domain (encompassing motif IV, V and VI) was shown to be the binding site for V proteins [62]. Combined substitutions of amino acids R455L, G457E and L458Y within LGP2 strongly impaired its interaction with parainfluenza virus 5 and measles virus V proteins. This LGP2 mutant could still support the residual MDA5 signaling in the presence of those antagonists [61].

To exclude that the lower inhibitory effect on RIG-I signaling with Q425R LGP2 (which is part of the LGP2 MVBR) is due to a specific phenotype caused by paramyxoviruses, another (in A549 cells) RIG-I-dependent virus from the unrelated virus family of Flaviviridae, ZIKV, was used (see Table 1). Analog to Figure 18 and Figure 19, A549 cells either expressing WT or LGP2 variants or an empty control vector were infected with ZIKV MR-766 (African isolate) for

24 hours and 48 hours prior to harvesting for qRT-PCR of immune gene induction by using IFN-λ1 and RSAD2 as surrogates.

Twenty-four hours pi WT and variants of LGP2 inhibited IFN-λ1 and RSAD2 expression compare to empty control cells. This inhibition was less pronounced or absent at 48 hours pi (Figure 20B, Figure S 15A and B right panels) indicating a transient negative effect on RIG-I signaling or an additional involvement of MDA5 at later stages. N461S and R523Q LGP2 behaved similarly to WT LGP2 at both time points pi, except for some higher IFN-λ1 levels 48 hours pi in R523Q LGP2 (Figure S 15A and B, right panels). Especially on RSAD2 mRNA levels, Q425R LGP2 differed from WT LGP2 and the other variants. Lower RSAD2 mRNA reduction was seen at 24 hours pi with Q425R compared to WT LGP2 (which was around 2-fold increased). Upon 48 hours pi, the RSAD2 mRNA copies with Q425R LGP2 even dominated those of empty cells (Figure 20B and Figure S 15C, right panels) indicating an overall positive regulatory effect under those conditions. In contrast, analogous activating effects with Q425R LGP2 were not observed within the IFN induction measured by IFN-λ1 mRNA as these copies were more equal to WT LGP2 (Figure S 15A and B, right panels). Moreover, as was the case for SeV replication, no difference in the ZIKV MR-766 replication between the different cell lines could be observed neither 24 hours nor 48 hours pi.

In sum, this hints at a (partially) lower negative effect of Q425R LGP2 on the ISG response (measured by RSAD2 mRNA levels) induced by ZIKV compared to WT LGP2. This is analog to the results with SeV. The induced IFN response, in contrast, seems rather unaffected by the different LGP2 versions upon ZIKV infection.

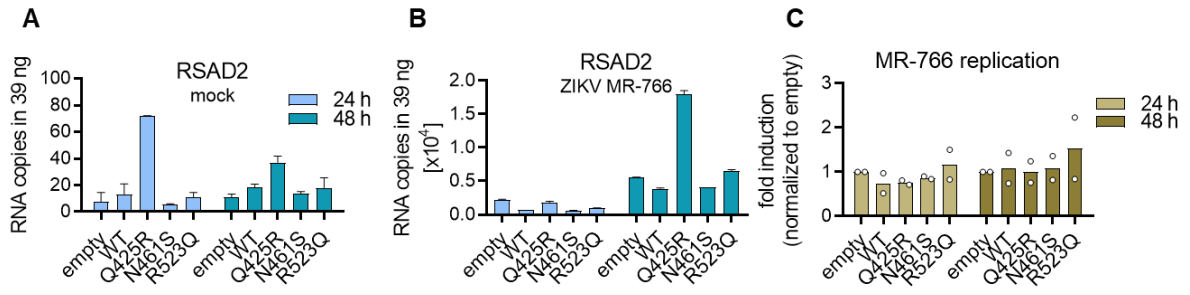

Figure 20: Q425R LGP2 reduces the RSAD2 response upon ZIKV infection to a lesser extent than WT in A549 cells.

(A-C) Cells from Figure 18A were infected with ZIKV strain MR-766 (MOI=0.5) or were mock treated for 24 h and 48 h prior to harvesting for RNA isolation and qRT-PCR. RSAD2 mRNA levels of (A) mock and (B) ZIKV MR-766 infected cells were measured. 1 out of 2 representative biological replicates is shown. (C) ZIKV infected RNA samples were measured for ZIKV replication. ZIKV RNA levels were normalized to GAPDH and infected empty control cells. n=2.

3.4 Mode of action of LGP2 variants in MDA5 enhancement

3.4.1 LGP2 and its polymorphisms reveal equal poly(I:C) binding in HepaRG cells

As next, the mode of action (MOA) of the gain-of-function Q425R LGP2 variant on MDA5 signaling was investigated. Different scenarios could explain its enhanced MDA5 support seen in the previous chapters. Compared to WT LGP2, the Q425R variant might reveal (i) enhanced RNA binding capacity, (ii) better recruitment of MDA5 to RNA and/or (iii) a broader spectrum of RNA ligands.

To investigate the RNA binding behavior of the different naturally occurring LGP2 variants, poly(I:C)-IPs of HepaRG^{NTCP} cells stably expressing WT or Q425R, N461S, or R523Q LGP2 (all N-terminally HA-tagged) were performed. Analog to Figure 13, pull-down experiments were conducted using streptavidin-coated magnetic beads labeled with biotin-tagged HMW poly(I:C). Levels of poly(I:C)-bound LGP2, MDA5 and RIG-I were analyzed by Western blot and quantified from three independent experiments (Figure 21A and B). All LGP2 variants revealed similar poly(I:C) affinity, arguing for unchanged RNA binding efficiency of the three variants compared to WT LGP2. The efficiency of RIG-I-poly(I:C) interaction was also not affected by the LGP2 variants (Figure 21A and B). However, MDA5 precipitated by HMW poly(I:C) was only detectable in the cell line expressing Q425R LGP2, but not in cells with WT, N461S, or R523Q LGP2 (Figure 21A). However, MDA5 levels were also higher in the lysate of Q425R LGP2-expressing cells compared to those expressing WT, N461S, or R523Q LGP2. Together with the very low binding levels, no solid conclusion on the MDA5 recruitment by the different LGP2 versions can be drawn from this experiment.

The generally low RNA binding affinity of MDA5 was already observed in a previous poly(I:C) pull-down experiment where IFN-pretreated HepaRG^{NTCP} cells were used to enrich initial MDA5 levels. However, no poly(I:C)-bound MDA5 was detectable under those conditions, while LGP2 and RIG-I were pulled down (Figure S 17A). This is in line with the literature, where MDA5 is described as the weakest RNA binder within the RLR family [57]. Low steady-state levels of MDA5 and its weak RNA binding capability, impede the pull-down of MDA5 on RNA.

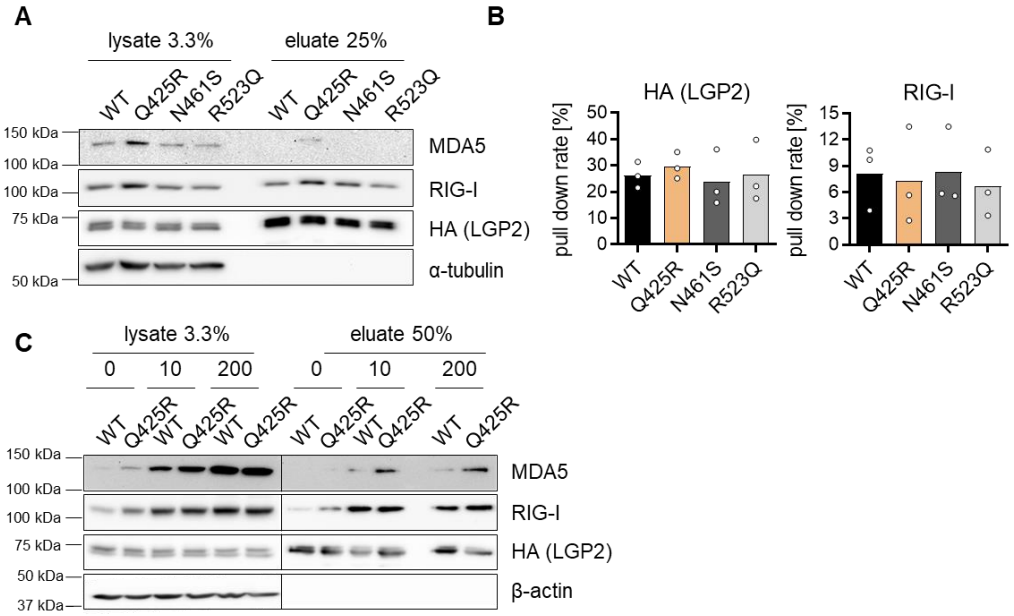

Figure 21: Q425R, N461S and R523Q LGP2 bind HMW poly(I:C) similar to WT LGP2.
(A) HepaRG^{NTCP} cells from Figure 16 were used for poly(I:C)-IP to test the RNA binding capability of the different HA-LGP2 variants, RIG-I and MDA5. Cell lysates were incubated with poly(I:C)-coupled beads for 4 h. One out of three representative HA, RIG-I and MDA5 immunoblots of cell lysates and eluates is shown. **(B)** Quantification of the HA and RIG-I immunoblots is shown. HA and RIG-I levels in the eluates were normalized to those in respective lysates designating the pulldown rate. No quantification was performed for MDA5, as there was no MDA5 signal in the eluates besides Q425R LGP2. n=3. **(C)** HepaRG^{NTCP} cells from (B) expressing HA-LGP2 WT or Q425R were stimulated with 0, 10, or 200 IU/ml of IFN-α for 24 h prior to harvesting for poly(I:C)-IP. IFN stimulation was performed by Dr. Zhenfeng Zhang. Western blot analysis of lysates and eluates was performed using antibodies against MDA5, RIG-I and HA. β-actin served as a loading control. Treatment with 0, 10, or 200 IU/ml of IFN-α is indicated by 0, 10 and 200 on top of the blot, respectively. n=1.

Thus, after upscaling of the poly(I:C)-IP conditions and IFN-α pretreatment of cells, an enrichment of poly(I:C)-bound MDA5 was possible in HepaRG^{NTCP} cells expressing WT and Q425R LGP2 (Figure 21C). In this initial experiment, levels of RNA-bound MDA5 were much weaker in HepaRG^{NTCP} cells expressing WT LGP2 than in cells expressing Q425R LGP2 – even though initial MDA5 expression was comparable upon IFN-α pretreatment in both cell lines. This suggests that, in comparison to WT LGP2, Q425R LGP2 might enhance the MDA5 recruitment to RNA and/or might stabilize the MDA5-RNA interaction while it did not interfere with RIG-I-RNA binding.

Overall, compared to WT LGP2, all variants bind equally well to poly(I:C). Thus, the enhanced activity in Q425R LGP2-expressing cells cannot be explained by differences in RNA-binding and might rather be a result of better MDA5-RNA-recruitment.

3.4.2 LGP2, especially Q425R LGP2, enhances MDA5-RNA interaction in HepaRG cells

It is known that LGP2 increases the initial MDA5 binding on RNA and stabilizes its filament formation, thus enhancing MDA5 activation [58]. How LGP2 mechanistically contributes to the recognition of HDV RNA by MDA5 and how Q425R LGP2 generally boosts the IFN activation was further addressed in this part of the study.

Thus, co-precipitation experiments in HepaRG^{NTCP} cells were conducted to investigate the MDA5-poly(I:C) binding behavior in the presence or absence of WT LGP2 or LGP2 mutants which revealed altered immune phenotypes upon HDV infection. A poly(I:C) pulldown enabling the investigation of the MDA5-specific recruitment to RNA was already established in 3.3.1 (Figure 21C). Under those conditions (using 200 IU/ml IFN-α pretreatment), WT, Q425R and ATPase deficient LGP2 bound equally well to poly(I:C) whereas triple RNA binding mutant LGP2 was unable to do so (Figure 22). Moreover, in all cell lines RIG-I bound poly(I:C) equally, independently of the expressed LGP2 variants. These results match those of previous pulldown experiments in 3.2.2 and 3.4.1 (Figure 13C and D, Figure 21A and B). MDA5 only bound RNA in the presence of LGP2 with functional RNA-binding domain (Figure 22A). Both ATPase deficient LGP2 and WT LGP2 were able to recruit/stabilize MDA5 to poly(I:C) in a comparable manner (around 2% of total MDA5). In contrast, no MDA5 was found to bind poly(I:C) in the presence of fully binding deficient LGP2 (RNA triple binding mutant). This highlights the importance of LGP2 and its RNA binding ability to enhance MDA5-RNA binding and as a consequence thereof MDA5 signaling. Q425R LGP2 was able to significantly enhance MDA5 binding to poly(I:C) around 3-fold compared to WT LGP2 (Figure 22A and B). The enhanced MDA5-RNA interaction in the presence of Q425R LGP2 can explain the stronger immune phenotype observed with this LGP2 variant. The accelerated IFN responsiveness of HepaRG^{NTCP} cells expressing Q425R LGP2 upon HDV infection might thus be a result of faster HDV sensing through MDA5 supported by Q425R LGP2. Similarly, Q425R LGP2 might enhance/accelerate the MDA5 sensing of Mengo Zn virus and SARS-CoV-2 RNA.

In sum, this data indicates that Q425R LGP2 sensitizes the RNA recognition by MDA5, thus leading to faster response in the infected cells.

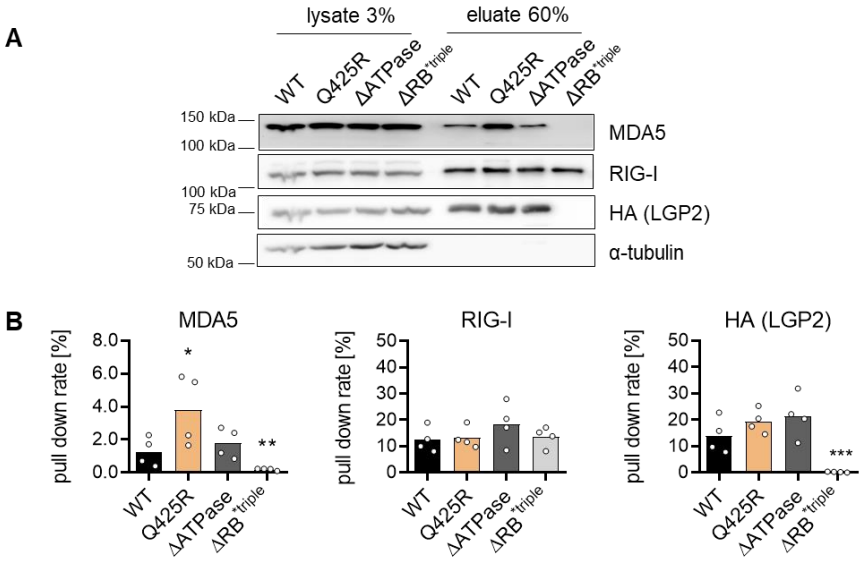

Figure 22: MDA5 binding to RNA is only detectable in the presence of RNA binding capable LGP2 and is enhanced with Q425R LGP2.
(A) HepaRG^{NTCP} cells stably expressing N-terminally HA-tagged WT, Q425R, ATPase deficient (ΔATPase) or RNA binding deficient LGP2 with a triple mutation (ΔRB^{*triple}) (from Figure 13 and Figure 16, respectively) were used for poly(I:C)-IP to test the HMW poly(I:C) binding capability of those LGP2 versions, RIG-I and MDA5 upon stimulation with 200 IU/ml IFN-α for 24 h. IFN stimulation was performed by Dr. Zhenfeng Zhang. Cell lysates of prestimulated cells were incubated with poly(I:C)-coupled beads for 3 h. One out of four representative HA, RIG-I and MDA5 immunoblots of cell lysates and eluates is shown. **(B)** Quantification of the HA, RIG-I and MDA5 pull-down rate was normalized to the respective sample lysate of HA, RIG-I and MDA5 immunoblots. *, $p \leq 0.05$; **, $p \leq 0.01$; ***, $p \leq 0.001$ (comparison between WT and versions of LGP2). n=4.

The fraction of poly(I:C)-bound RIG-I is enhanced by IFN-α pre-treatment in respective cell lines from around 8% in untreated (Figure 21B) to 15% in IFN-α pre-treated cells (Figure 22B). In contrast, poly(I:C) binding of LGP2 was not enhanced by IFN-α pre-treatment (WT LGP2 poly(I:C)-bound fraction was around 14% of total LGP2 with (Figure 22B) and 26% without IFN-α treatment (Figure 21B). The poly(I:C) pulldown experiments overall confirm the published data of the strength of RNA binding capability of LGP2, RIG-I and MDA5, with LGP2 binding the strongest and MDA5 the weakest to poly(I:C).

3.4.3 Basal IFN/ISG induction is mediated by MDA5/LGP2 axis in HepaRG cells

HepaRG^{NTCP} cells expressing WT LGP2 showed higher basal RSAD2 mRNA expression compared to cells expressing an RNA binding deficient LGP2 (Figure S 9) and were highest in the presence of Q425R LGP2 (Figure S 12B lower panel). Moreover, the mRNA levels of basal RSAD2 positively correlated with the LGP2 and MDA5 expression levels (Figure S 9, Figure 12). LGP2 has a stronger RNA binding capability than MDA5 (Figure 22) and sensitizes the MDA5 response (Figure 9D). This leads to the assumption that the basal IFN signaling in HepaRG^{NTCP} cells might be triggered by MDA5 in the presence of RNA binding-capable LGP2,

potentially recognizing endogenous substrates. To test this hypothesis, MDA5 and ADAR1 were transiently knocked down in HepaRG^{NTCP} cells expressing WT, Q425R or triple RNA binding deficient LGP2 using lentiviruses encoding shRNAs targeting MDA5 or ADAR1 or harboring a non-targeting control shRNA (shNT). shRNA sequences can be found in Table S 1.

Knockdown efficiency of MDA5 (left panel) and ADAR1 (right panel) were validated by Western blotting 4 days post lentiviral transduction (Figure 23A). Compared to the respective transduction with shNT, shMDA5-treated WT and Q425R LGP2-expressing cells revealed more than 95% MDA5 reduction. ADAR1 knockdown was stronger for shADAR1-c-treated cells with around 80% reduction of p110 isoform compared to the shNT control treatment (Figure 23A). The lentiviral treatment itself increased the IFN response in shNT-transduced WT and Q425R LGP2-expressing cells compared to untransduced (naive) cells, visible by higher protein levels of the ISGs MDA5 and Mx1 (Figure 23A). Analogously, baseline IFN-λ1 and RSAD2 mRNA copies were elevated in shNT-transduced WT and Q425R LGP2 (Figure 23B). In contrast, HepaRG^{NTCP} expressing triple RNA binding deficient LGP2 (ΔRB^{*triple}) did not show elevated ISG response in any of the treatments (Figure 23A and B).

Comparing steady-state mRNA levels of IFN-λ1 and RSAD2 in untreated cells, they were highest in Q425R LGP2, followed by WT LGP2-expressing HepaRG and were lowest in RNA triple binding mutant LGP2-expressing cells (Figure 23B), analogous to previous results. Knockdown of ADAR1 increased IFN-λ1 and RSAD2 levels in WT and Q425R LGP2-expressing cells compared to respective shNT-transduced cells but not in cells expressing triple RNA binding mutant LGP2 (Figure 23B). Overall, the IFN-λ1 and RSAD2 mRNA levels were slightly higher (~1.4-fold) in cells with Q425R LGP2 than those with WT LGP2 upon ADAR1 knockdown. Knockdown of MDA5 abolished the IFN/ISG response in WT and Q425R LGP2-expressing cells (Figure 23A and B). This indicates that MDA5 was the responsible activator of the basal IFN/ISG response in the presence of LGP2. MDA5 sensing of unedited, endogenous RNA in ADAR1 knockdown cells was fully dependent on the RNA binding function of LGP2.

The phenotype observed in Figure 23 was reproduced twice by Dr. Zhenfeng Zhang with purified lentiviruses to circumvent the induction of IFN/ISG response upon treatment with shNT control lentiviruses.

In sum, basal IFN/ISG mRNA expression in HepaRG^{NTCP} cells is mediated by MDA5 that requires RNA binding functional LGP2.

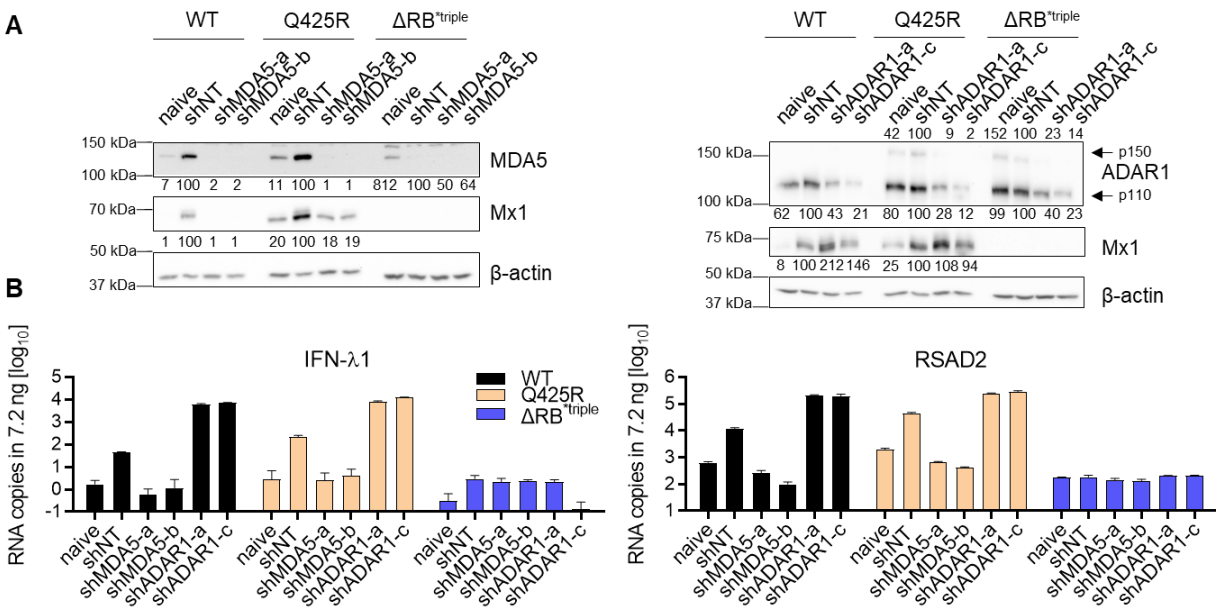

Figure 23: Q425R LGP2 sensitizes basal immune gene induction through MDA5 signaling.
HepaRG^{NTCP} cells stably expressing N-terminally HA-tagged LGP2 WT, Q425R, or an RNA binding deficient mutant with triple mutation (ΔRB^{*triple}) (from Figure 13 and Figure 16, respectively) were used for transient transduction with lentiviruses encoding shRNAs targeting MDA5, ADAR1, or a non-targeting control (NT). Cells were transduced in suspension during cell seeding and the medium was changed 24 h later. At 3 d post lentivirus transduction, the medium was changed into 300 µl per well in a 24 well plate. At 4 d, the medium was harvested for IFN-λ1/2/3 ELISA and cells were lysed for Western blotting and RNA extraction. **(A)** Knockdown efficiency of ADAR1 and MDA5 was determined by Western blotting using β-actin as a loading control. IFN response activation was measured by using an Mx1 antibody. Numbers below the Western blot bands (of MDA5, Mx1, ADAR1 p110) and above the Western blot band (of ADAR p150 isoform) indicate the percentage of knockdown efficiency relative to corresponding shNT control cells and normalized to β-actin. **(B)** IFN-λ1 and RSAD2 mRNA levels were measured by qRT-PCR. RB=RNA binding. shRNA containing lentiviruses were produced by Dr. Zhenfeng Zhang. n=1.

3.5 Analysis of LGP2 phosphorylation

To analyze possible PTMs within LGP2 which might be relevant for the regulation of its ambivalent roles in RLR signaling, an MS approach was performed focusing on phosphorylation sites within LGP2. So far, RIG-I and MDA5 are known to be phosphorylated on their CARDs and CTDs [93, 369] to block antiviral signaling, however, the role of LGP2 phosphorylation is unclear.

3.5.1 Phospho-MS identifies three phosphorylation sites within LGP2

To investigate whether LGP2 might be phosphorylated in steady-state, pull-down experiments were performed in buffer conditions including several phosphatase inhibitors (2.2.4.3.1, Table 28). A549 cells were generated either expressing HA-tagged LGP2 or the HA-tagged control protein DDX6 to equal levels (Figure S 23A). Additionally, untagged (UT) LGP2-expressing cells were used as a further control. After HA-IP, eluates were analyzed by Western blotting using phospho-specific antibodies. As expected, only HA-DDX6 and HA-LGP2 but no UT-LGP2 could be detected in the respective eluates upon staining with an HA-specific antibody (Figure S 23B). Only in the HA-LGP2 eluates anti-phospho- (p) threonine (T), p-tyrosine (Y) and p-serine (S) staining revealed a faint band at the correct size of HA-LGP2 (see asterisk Figure S 23B), supporting the hypothesis that LGP2 is phosphorylated at steady-state.

The HA-IP conditions in the presence of phosphatase and protease inhibitors were used for a first MS test run to identify the sites of LGP2 phosphorylation. A549 cells either overexpressing HA-tagged or UT-LGP2 were infected with SeV or left untreated and harvested after 3 hours. In parallel to samples for the MS HA-IP, test samples for validation of immune induction and HA-IP efficiency were prepared. To analyze the HA-IP efficiency and purity under the actual conditions, samples generated for test IP were analyzed by Western blot and Silver gel (Figure 24A and B). HA-LGP2 was pulled down in both mock and SeV infection conditions whereas UT-LGP2 was absent in the eluate (Figure 24A). Moreover, SeV induced Mx1 mRNA as measured by qRT-PCR indicating successful infection and activation of RLR signaling (Figure 24C). IP of MS samples was performed analogously and all samples were performed in quadruplicates. After the last PBS washing step beads were shock frozen in liquid nitrogen before further MS analysis by Dr. Pietro Scaturro in the research group of Prof. Dr. Andreas Pichlmair (Munich). MS analysis revealed specific phosphorylation (p) of LGP2 at S464 (pS464) which was detectable in all quadruplicates of steady-state HA-LGP2 samples (Figure 24D and E). No phosphorylation was seen for any of the SeV infected HA-LGP2 samples nor for the UT-LGP2 negative control (Figure 24D and E).

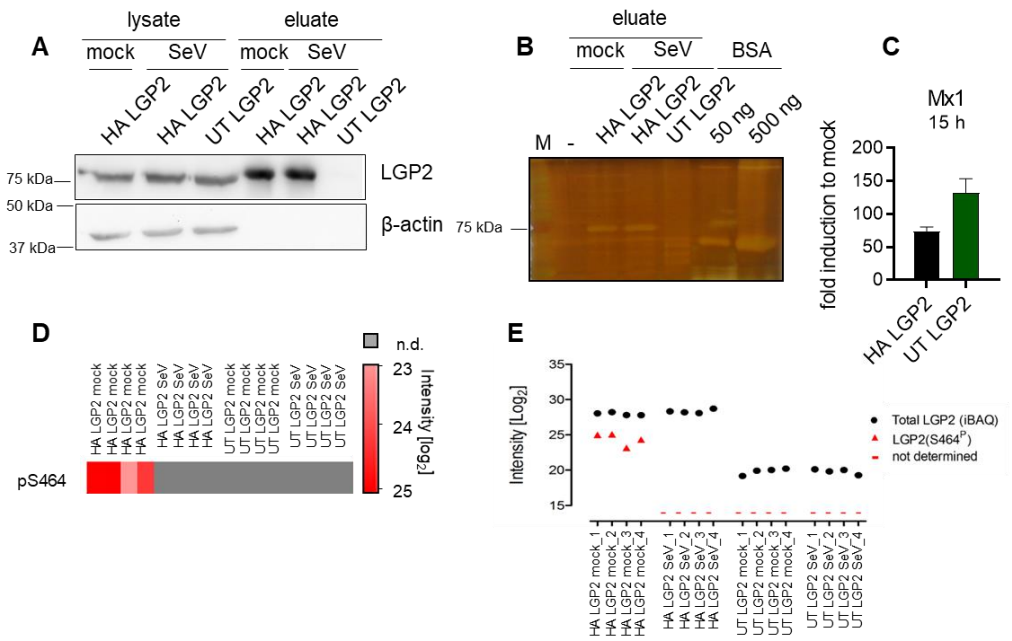

Figure 24: MS run I identifies LGP2 S464 as a phosphorylation site in steady-state which is absent upon SeV infection.
A549 cells stably expressing HA-tagged and untagged (UT) LGP2 were infected with SeV (MOI=5) or kept uninfected (in quadruplicates). 3 h pi, cell lysates were used for HA-immunoprecipitation (IP). HA-beads were shock frozen in liquid nitrogen after the last washing step. In parallel, cells for control IP were similarly handled. **(A)** LGP2 protein staining of lysates and eluates from control IP as well as **(B)** silver gels were performed. Bovine serum albumin (BSA) served as a reference for protein yield. **(C)** To verify the activation of cells upon infection, additional HA-LGP2 and UT-LGP2 A549 (in 24 well plates) were infected with SeV for 15 h or kept uninfected before harvesting for Mx1 qRT-PCR. Error bars indicate SD from three technical replicates. **(D)** Heat map of the LGP2 S464 phosphorylation site detected in MS from HA-IPs. Measurements were performed from four independent IPs per cell line and condition; log2 intensities are indicated by color (n.d.= not determined). **(E)** Unnormalized raw intensities of total LGP2 protein levels (based on 70 unique peptides identified; 78.3% sequence coverage) and LGP2 S464-containing phospho-peptide across replicates is shown. MS run and data evaluation kindly performed by Dr. Pietro Scaturro. (E) and (F) created by Dr. Pietro Scaturro.

Thus, this data reveals LGP2's phosphorylation in resting cells at S464 which was shown to be absent upon SeV virus infection.

As SeV specifically activates the RIG-I pathway, a follow-up MS was performed including two further stimulations: Mengo Zn virus and synthetic poly(I:C). This broader set-up was designed to gain a more detailed insight (i) into how the phosphorylation is regulated after stimulation with different RNAs/viral infections and (ii) if the phosphorylation is counteracted by viral antagonists. In addition, a late time point (12 hours) was included to decipher the time-resolved regulation of the phosphorylation as it probably depicts a highly dynamic process (Figure S 25A). Samples (in quadruplicates) were prepared analog to Figure 24 and validated for their activation upon the respective stimulations prior to HA-IP. Both HA-LGP2 and UT-LGP2-expressing cells revealed comparable IFN-λ1 mRNA levels in steady-state (Figure S 25B left panel). In comparison to respective mock infected/mock transfected control cells, IFN-λ1 mRNA of stimulated cells was enhanced especially at 12 hours post-stimulation (Figure S 25B,

right panel). poly(I:C) transfection was the strongest and Mengo Zn virus infection was the lowest innate signaling inductor (Figure S 25B, right panel). HA-IP of those samples was performed. Again, MS analysis of LGP2 phosphorylation was conducted in the research group of Prof. Dr. Andreas Pichlmair. In that new set of samples, the previously identified pS464 could not be detected. However, a further phosphorylation site of LGP2 at position S365 was identified (Figure S 25C). Due to technical inconsistencies, this second MS run was analogously repeated in a third MS run (Figure 25). Samples of the third MS were equally activated to those of the second MS (Figure 25B). The analysis confirmed the pS365 LGP2 identified in the MS II (Figure 25C). Again, no p464 LGP2 was found in MS III, however, additional phosphorylation at S169 was revealed and the S365 phosphorylation of run II was reproduced (Figure 25C). pS169 did not show a specific regulation pattern, while pS365 was only found in late viral infection (12 hours) and in poly(I:C) treatment (3 hours and 12 hours).

In sum, the analysis of three independent MS runs identified pS169, pS365 and pS464 LGP2. pS464 LGP2 was found to be a regulated phosphosite (phosphorylation in resting state and no phosphorylation in early SeV infection). pS464 was not identified in the second and third MS run and might therefore not be very abundant. pS169 LGP2 was only detected in the third MS run and was found to be non-specifically regulated upon RLR activation. pS365 LGP2 was identified as a specifically regulated phosphosite (phosphorylation by late virus infection and poly(I:C) stimulation) identified in both MS run II and III. A schematic summary of the identified phosphorylation sites within LGP2 is shown in Figure S 28A, upper panel.

Moreover, the data from the phospho-MS was reused for the analysis of LGP2 interaction partners. As the MS was specially set to identify LGP2 phosphosites, the proteome data lacks a suitable negative control. Nonetheless, by comparing different stimuli (HMW poly(I:C), Mengo Zn virus and SeV) early after stimulation (3 hours, where upregulation of ISGs should not have started yet) and by excluding ISGs, some potential hits were found (Figure S 24, Figure S 26, Figure S 27).

The next aim was to characterize the influence of the identified phosphosites in functional assays. To achieve this goal, A549 and HepaRG^{NTCP} cells overexpressing the respective LGP2 phosphomutants were generated. Of each identified phosphosite, alanine (A) substitutions were generated resulting in phospho-dead versions of the respective serine sites (S169A, S365A, S464A). To investigate the effect of stable phosphorylation, the serine sites were changed into the negatively charged amino acid aspartic acid (D) resulting in phosphomimetic versions (S169D, S365D, S464D).

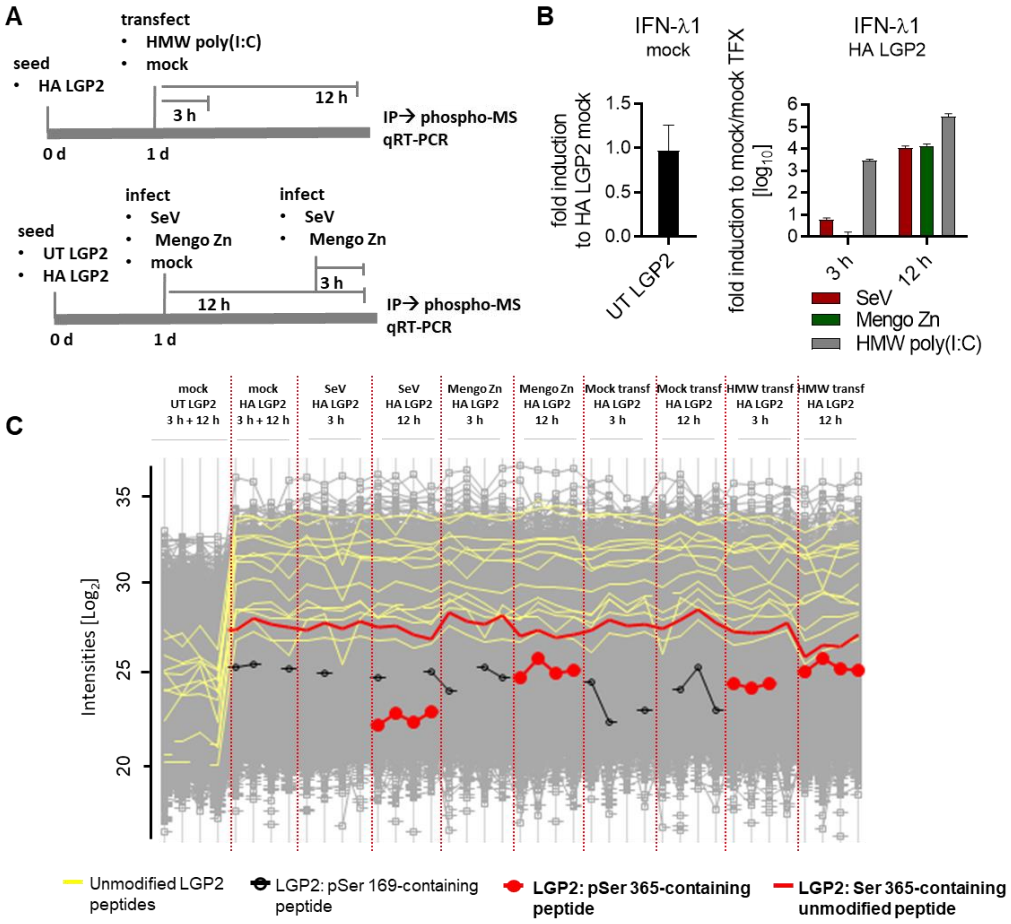

Figure 25: MS run III reproduces LGP2 phosphorylation at position S365 and identifies S169 as a new phosphorylation site.
(A) Experimental set-up is shown. A549 cells stably expressing HA-tagged LGP2 were transfected with 3 µg HMW poly(I:C) (per 10 cm dish) or mock transfected for 3 h or 12 h respectively. In parallel to synthetic stimulation, cells were infected with Mengo Zn virus (MOI=5) and SeV (MOI=5) for 3 h and 12 h, respectively, or kept uninfected. Untagged (UT) LGP2-expressing mock cells served as a further control. Cells were harvested for immunoprecipitation (IP) prior to MS analysis and a small aliquot was kept for RNA isolation and qRT-PCR. IP was performed in Munich by Dr. Pietro Scaturro. **(B)** RNA from (A) was used for cDNA synthesis and qRT-PCR of IFN-λ1. IFN-λ1 mRNA levels were normalized to GAPDH and respective mock/mock transfection (TFX). Error bars indicate SD from three technical replicates. **(C)** MS results depicted as unnormalized raw intensities of total LGP2, LGP2 S365 phospho-peptide, LGP2 S365 unmodified peptide and LGP2 S169 phospho-peptide. Measurements were performed in quadruplicates from four independent IPs. IPs, MS run and its data analysis were performed by Dr. Pietro Scaturro. Figure (C) was obtained from Dr. Pietro Scaturro.

Preliminary experiments with phosphoablative S169A, S464A and S365A LGP2 single mutants suggested that the inability to phosphorylate S169, S365 or S464 within LGP2 did not influence the MDA5 enhancement or RIG-I repression in A549 cells (Figure S 28). As an exception, the phospho-dead S169A LGP2 in RIG-I signaling revealed an enhanced repressor function. This was investigated in more detail (see 3.5.2).

The S365 phosphorylation site was the most reproducibly detected in the MS and was regulated upon different set-ups. However, phosphoablative S365A LGP2 behaved similarly to WT LGP2 upon stimulation of MDA5 and RIG-I signaling in A549 cells (Figure S 28C). Even

a mutant harboring additional, combined phosphoablative substitutions of the surrounding serines (S363, S364, S367), called Δserine cluster (SC) LGP2, revealed no striking difference to WT LGP2 in MDA5 enhancement or viral suppression upon long-term HDV infection (followed up to 17 days, Figure S 30) or upon RVFVΔNSs-Renilla and Mengo Zn virus infection (Figure S 21) in HepaRG^{NTCP} cells.

3.5.2 Phosphoablative S169A LGP2 reveals stronger RIG-I repression in A549 cells

Upon stimulation with 5'ppp-dsRNA, 80% stronger RIG-I inhibition was observed with S169A LGP2 compared to WT LGP2 expressing MDA5^{KO} A549 in a pilot experiment (Figure S 28C left panel); measured by IFIT1 mRNA levels as a surrogate for innate immune induction. Hereafter, this effect was further investigated.

Phosphoablative and phosphomimetic substitutions of S169 and S464 were simultaneously examined for their potential effects on both RIG-I (Figure 26A) and MDA5 (Figure S 29) regulation. For that, those LGP2 phosphomutants were expressed in either MDA5^{KO} or RIG-I^{KO} A549 background analog to Figure 9 and Figure 11 (in 3.1.2 and 3.1.3). MDA5^{KO} A549 were stimulated with 10 pg 5'ppp-dsRNA (for RIG-I activation) and RIG-I^{KO} cells with 10 ng HMW poly(I:C) (for MDA5 activation). At those dsRNA doses, LGP2 showed strong regulatory effects (on RNA levels) on RIG-I and MDA5 signaling (Figure 9C and D, Figure S 5, Figure 10B in 3.1.2). To enlarge the possible measurement window of S169A LGP2-mediated repression of RIG-I signaling, a stronger dose of 5'ppp-dsRNA (1000 pg) was additionally included. This high amount of stimulus should overall increase the immune activation, including cells expressing LGP2, see 3.1.2 (Figure 9, Figure 10). As a negative control, cells were transfected with non-immune stimulative poly(C).

All overexpressing cell lines showed consistent LGP2 protein levels (Figure 26B, Figure S 29B). After stimulation of MDA5^{KO} A549, IFN-β mRNA levels were measured as a surrogate of the IFN response activation. The repressive effect of WT LGP2 was overall stronger at low dose dsRNA stimulation (70-fold) than at high dose (16-fold) compared to empty control A549 cells (Figure 26C left panel). This is analog to previous data. Compared to WT LGP2, RIG-I suppression was somewhat higher with S169D or S464A LGP2 at low levels of stimulus, while the differences were even less obvious at high levels of dsRNA stimulation for S464A (Figure 26C). When analyzing RIG-I signaling, S169A LGP2 revealed more than 90% lower IFN-β mRNA levels after both low and high doses of 5'ppp-dsRNA stimulation (Figure 26C, left panel) when compared to WT LGP2. This affirms the data from the pilot experiment (Figure S 28C left panel).

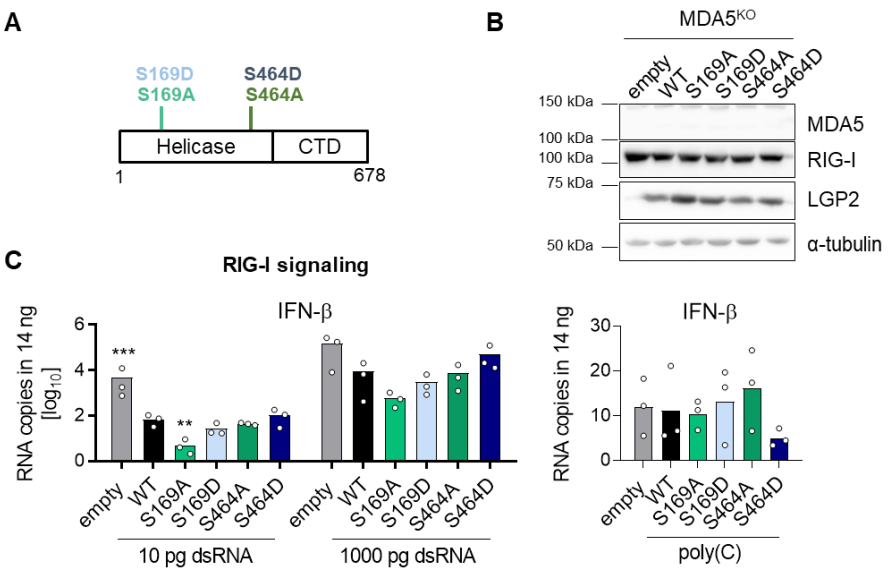

Figure 26: S169A LGP2 reveals enhanced RIG-I signaling repression.
(A) Schematic representation of phosphoablative (alanine; A) and -mimetic (aspartic acid; D) S169 and S464 sites within LGP2. **(B)** A549 cells stably expressing N-terminally HA-tagged LGP2 WT, S169A, S169D, S464A, S464D or an empty vector control (empty) were generated in an MDA5^{KO} background by using a single KO clone (clone M2-28). RLR expression was measured by immunoblot using RIG-I, MDA5- and LGP2-specific antibodies. α-tubulin served as a loading control. Cells were treated with 200 IU/ml of IFN-α for 24 h prior to harvesting for Western blotting. **(C)** MDA5^{KO} A549 generated in (B) were transfected with 10 pg and 1000 pg 5'ppp-dsRNA of 200 bp in length to stimulate RIG-I signaling (left panel, n=3). Poly(C) transfected cells served as negative control (right panel, n=3). Cells were harvested 8 h post-transfection. Circles on top of each bar indicate the average value of individual biological replicates. **, p ≤ 0.01; ***, p ≤ 0.001 (WT compared to mutants of LGP2 or control cell lines at the depicted amount of stimulus).

In contrast to RIG-I signaling, MDA5 signaling was equally well enhanced by S169A LGP2 when compared to WT LGP2 (Figure S 29C). Equal to WT, phosphomimetic and -ablative S169 and S464 LGP2 versions strongly facilitated IFN-β response to HMW poly(I:C) while empty control cells were almost uninduced. 1,000-fold higher IFN-β mRNA copies were observed with WT LGP2 compared to empty control cells – analog to results from Figure 9D (left panel).

In sum, this data indicates a strengthened RIG-I repressive effect of S169A LGP2 whereas its effect on MDA5 enhancement was unchanged compared to WT LGP2.

3.5.3 S365A S464D LGP2 reveals reduced MDA5 support upon HDV infection in HepaRG cells

The role of S365 and S464 phosphorylation remains elusive, as no striking influence of those sites was observed in functional assays. One explanation for the missing phenotype could be that these sites have mutual effects. To investigate this, S365 and S464 mutation sites were combined. Both phosphosites were found to be regulated upon stimulation – with S464 being

phosphorylated in resting state (and undetectable upon SeV infection) and S365 phosphorylated at the late stage of viral infection and upon poly(I:C) stimulation. This indicates that the phosphorylation status of LGP2 in the (late) infected state probably consists of a combination of S365 phosphorylation and S464 dephosphorylation. In steady-state LGP2 probably reveals S365 dephosphorylation and S464 phosphorylation. To mimic both the infected/stimulated and uninfected/steady-state of LGP2, the phosphorylation patterns of S365 and S464 were combined. S365A S464D LGP2 should reflect the steady-state and S365D S464A LGP2 should mimic the activated state phosphorylation pattern (Figure 27A). These two LGP2 mutants were designated p-mock (S365A S464D) and p-activated (S365D S464A).

$LGP2^{KO}$ $HepaRG^{NTCP}$ cells were reconstituted with p-mock, p-activated or WT LGP2, or an empty vector control (KO empty). Non-targeting (NT) guide-expressing $HepaRG^{NTCP}$ served as a further control cell line (NT control). p-mock, p-activated and WT LGP2 showed equal expression levels of LGP2, with some lower expression for p-activated LGP2 (Figure 27B). The generated cell lines were tested for their immune response activation upon HDV infection. 2 days, 3 days, 5 days and 17 days post HDV or mock infection, the IFN response was measured by IFN-λ1, RSAD2, IFI44 mRNA levels. HDV replication was measured by HDV RNA levels and its infection rate was determined by IF.

First, to demonstrate the stable KO of LGP2 in KO empty cells during the course of HDV infection, LGP2 mRNA levels were compared to NT control cells (harboring endogenous LGP2). No upregulation of endogenous LGP2 mRNA levels in KO empty cells was observed. However, in NT control cells LGP2 mRNA started to accumulate 3 days pi (Figure S 31A). This correlates with upregulated LGP2 protein levels 5 days (but not 2 days) pi in NT control but not KO empty $HepaRG^{NTCP}$ cells (Figure S 11B).

When infected with HDV, exogenously driven WT LGP2 enhanced early immune responses compared to NT control cells at 2 days pi while KO empty blunted the overall immune response (Figure 27C), analog to the results observed in Figure 12B and Figure 14A (3.2.1 and 3.2.3). Cells expressing p-activated LGP2 revealed a fast immune gene upregulation at 2 days pi, similar to cells expressing WT LGP2 (Figure 27C). In contrast, p-mock LGP2 showed a delayed immune response when compared to WT LGP2 and was equal to that of NT control cells (Figure 27C, see the arrows at 2 days) suggesting less efficient MDA5 activation of p-mock LGP2. In contrast to KO empty cells, p-mock LGP2 cells are not completely signaling-deficient (Figure 27C), indicating that the S365 and S464 phosphorylation sites are not the only regulatory sites within LGP2.

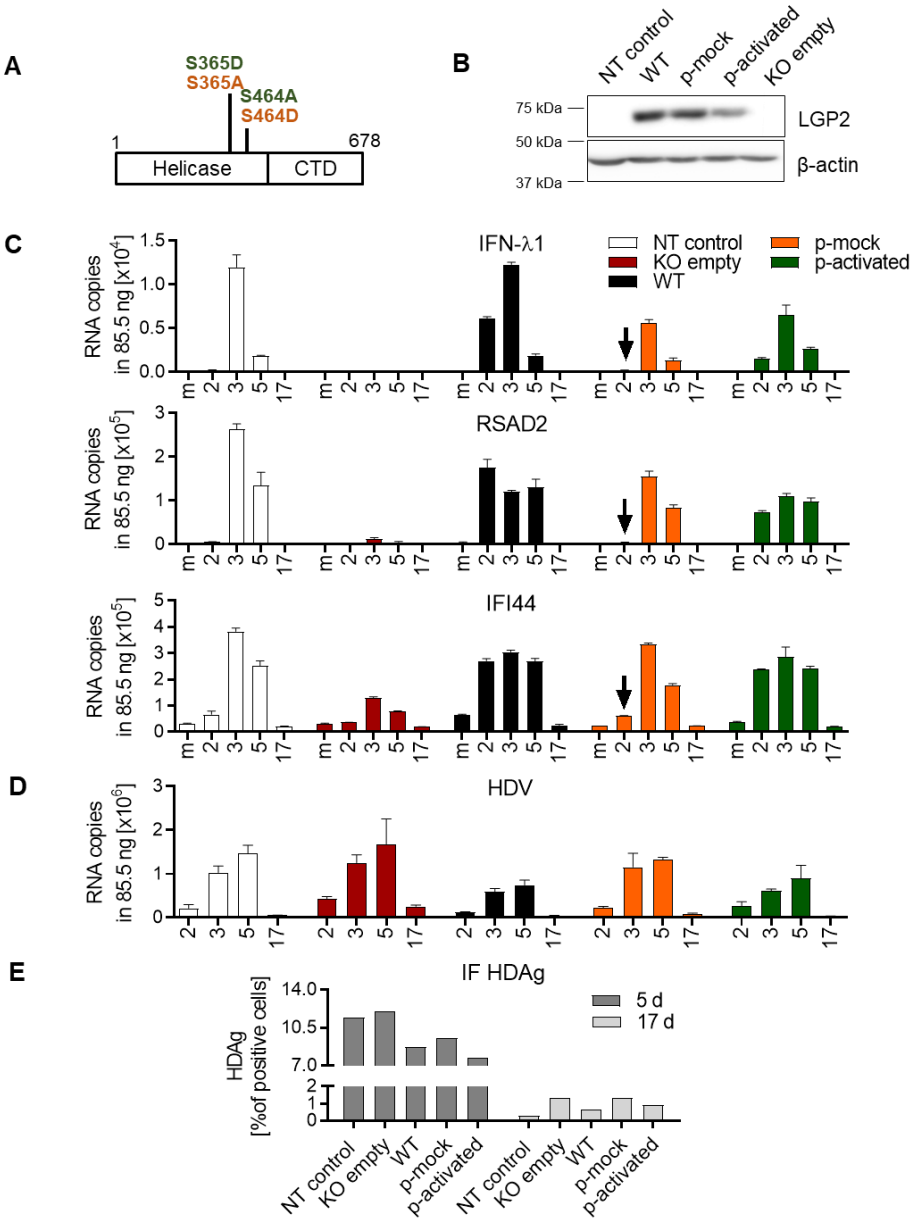

Figure 27: LGP2 combined phosphomutants mimicking mock and infected state reveal a slower innate response for p-mock LGP2 after HDV infection.

(A) Schematic representation of phosphomutations of LGP2 mimicking the phosphorylation pattern of LGP2 in the steady-state (S365A S464D, orange) and activated state (S365D S464A, green). **(B)** HepaRG^{NTCP} cells harboring an LGP2 guide-expressing CRISPR-Cas9 vector were reconstituted with either Cas9 cleavage resistant N-terminally HA-tagged LGP2 WT or LGP2 phosphomutants mimicking the phospho-status of mock (S365A S464D, p-mock) or activated (S365D S464A, p-activated) LGP2. As controls, empty lentiviral vector transduced HepaRG^{NTCP} LGP2^{KO} (KO empty) and non-targeting guide RNA-expressing HepaRG^{NTCP} (NT control) were used. LGP2 expression was measured by immunoblot using LGP2 antibody. α-tubulin served as a loading control. **(C-D)** Cells generated in (B) were infected with HDV. (C) mRNA expression levels of IFN-λ1, RSAD2, IFI44 and (D) HDV RNA in HDV infected cells were measured by qRT-PCR. n=1. “m” in post HDV infected cells depicts 2 d mock infected cells. **(E)** At 5 d and 17 d pi the percentage of HDV positive cells was analyzed by IF of HDAg and quantified using Ilastik. n=1. Data in panel (D) generated by Dr. Zhenfeng Zhang. The slower RSAD2 response with LGP2 p-mock upon 2 d post HDV infection (marked with arrow) was already seen in a previous experiment.

The differences in the immune response kinetics between the cell lines reflect the corresponding HDV replication patterns. WT and p-activated LGP2 showed the lowest HDV RNA levels and a lower percentage of infected cells at 17 days pi than KO empty and p-mock (Figure 27D and E). At 17 days pi p-mock LGP2-expressing cells and cells lacking LGP2 had equally high infectivity rates. Moreover, starting from 3 days pi, higher intracellular HDV RNA levels were observed in p-mock compared to WT and p-infected LGP2 HepaRG^{NTCP} cells.

ADAR1 and MDA5 silencing experiments in Figure 23 (3.4.2) revealed that the basal IFN/ISG expression was mediated by LGP2 enhancement of MDA5 signaling. In line with this, IFN/ISG baseline levels of the cells from Figure 27 revealed the strongest IFN-λ1, RSAD2 and IFI44 expression in WT LGP2-expressing HepaRG^{NTCP} followed by NT control and p-activated LGP2-expressing HepaRG^{NTCP} (Figure S 31B). p-mock LGP2-expressing cells showed a lack of basal immune genes expression similar to KO empty cells indicating a blocked steady-state innate signaling of p-mock LGP2 (and thus a deficiency in proper MDA5 support).

In sum, this data indicates that p-mock LGP2 is a less MDA5-activating LGP2 version thus leading to delayed MDA5-mediated immune responses and stronger HDV replication.

4 DISCUSSION

4.1 MDA5 and LGP2 synergy

The present study made use of two different IFN-competent cell culture models to deeper characterize the role of LGP2 in MDA5-mediated signaling. Several *in vivo* and *in vitro* studies already consistently demonstrated a positive effect of LGP2 on MDA5 signaling [58, 60, 119, 125]. This is in line with this work. Ectopic LGP2 expression in the A549 system (where no endogenous LGP2 protein levels could be reliably detected) highly enhanced MDA5 signaling. Analog findings were revealed in HepaRG^{NTCP} cells (and a pilot experiment with PHHs) where MDA5-dependent signaling was reduced or rather abolished when depleting endogenous, IFN-inducible LGP2 in several viral infections (HDV, Mengo Zn virus, RVFV, Figure 12B, Figure S 7F, Figure S 19A-C). This not only highlights an enhancement of the MDA5 response by LGP2 but rather suggests some real dependency. In the A549 system stimulus titrations with the synthetic dsRNA analog HMW poly(I:C) in the absence of RIG-I indicated that especially when both the RNA and MDA5 are at quite low levels, MDA5 alone hardly induced any downstream signaling (Figure 9D, Figure S 4, Figure S 5, Figure 10B and C right panel). Boosting the LGP2 expression sensitized and accelerated the MDA5-mediated IFN response in both A549 and HepaRG^{NTCP} cells (Figure 9D, Figure 14A, Figure 27C). However, this dependency declined when increasing the amounts of initial MDA5 and/or of the substrate in A549 cells. This finding underlines the special importance of LGP2 when (i) initial MDA5 levels are low and (ii) low amounts of the substrate are present. Thus, LGP2 was found to act as a catalyst of MDA5-dependent responses with special importance at rather early stages of innate signaling. This is in line with published data, that also suggested the importance of LGP2 in sensitizing the immune response at especially low substrate levels [125]. This view moreover fits the current mechanistic understanding of LGP2-mediated enhancement of MDA5 signaling. An *in vitro* model of the MDA5-LGP2 synergism [58, 59] demonstrated that MDA5 filament formation is catalyzed and stabilized by LGP2's binding to RNA. Hence LGP2 behaves as a nucleator of MDA5 driving its activation.

4.1.1 Importance of LGP2 RNA binding

Results in this study clearly showed that the MDA5-induced IFN signaling was dependent on LGP2's RNA binding ability in both the A549 and the HepaRG system. Dose-response curves in A549 indicted a very strong sensitization of MDA5-RNA recognition only in the presence of RNA binding capable LGP2 (Figure 11C right panel), in line with data from literature [53, 125]. Similarly, only RNA binding capable LGP2 was able to support MDA5 signaling upon HDV infection in HepaRG^{NTCP} cells (Figure 14A). LGP2 was proposed to be the strongest RNA

binder within the RLR family and MDA5 the weakest [22, 57], thus supporting MDA5 in initial RNA sensing and signaling. Pulldown experiments of RLRs on HMW poly(I:C) performed in this study validated the strongest RNA binding affinity of LGP2 and weakest affinity of MDA5 (Figure 21B, Figure 22B).

Based on crystal structures of the RNA-bound LGP2 CTD, positions K605, K634 and K651 were shown to be directly involved in the association with RNA [26, 27]. In this study, this led to the design of two RNA binding mutants of LGP2, namely ΔRB^{*single} (K634E) and ΔRB^{*triple} (K605E K634E K651E). K634E LGP2 was shown to abolish the RNA binding capacity in some studies [26, 27]. Li et al. and Childs et al. claimed that K634E LGP2 fully lost RNA binding [26, 125]. However, Li et al. tested the binding on only a 10 bp long dsRNA [26]. In contrast, poly(I:C) and HDV binding studies from this work revealed still weak binding affinity of ΔRB^{*single}, while only ΔRB^{*triple} revealed a complete RNA binding deficiency (Figure 13C and D, Figure 15). This is in line with the phenotypic outcome of the two mutants in MDA5 signaling as LGP2 ΔRB^{*single} still enabled some MDA5 support (Figure 11C right panel, Figure 14C). RLRs have different substrate specificity and therefore their RNA binding affinity is probably influenced by the substrate used. The overall RNA binding strength of LGP2 and its mutants might therefore depend on the dsRNA used. This could explain the observed discrepancies in the RNA binding efficiency of ΔRB^{*single}. Thus, testing of RNA binding efficiency should be performed on substrates also used in functional assays to avoid wrong assumptions.

Further factors might shape RLR RNA binding affinity and/or sensitivity, e.g. the available amount of substrate or co-factors, RLR expression strength or the presence of regulatory PTMs. Observations in this study revealed, that LGP2 RNA binding seemed to be reduced around 50% with pretreatment of IFN-α (Figure 21B versus Figure 22B). Whether this reflects a weakness of the assay (e.g. measurement fluctuations, differences due to protein overexpression) or rather points towards some negative regulation of LGP2 in the IFN context (e.g. some IFN-induced upregulation of negative co-factors or PTMs or some lost positive regulations) needs future research. A weaker RNA-LGP2 binding at later stages would support the assumption of a stronger initial influence on MDA5 enhancement.

Enhancing the substrate width of MDA5?

In literature, it was suggested that LGP2 enables MDA5 to sense non-MDA5-specific structures. In the presence of LGP2, cells revealed an enhanced IFN response activation with a rather RIG-I-specific, short synthetic RNA structure, so-called low molecular weight poly(I:C) – probably due to the ability of MDA5 to detect this RNA under those settings [132]. It was already described that LGP2 assists the formation of shorter signaling competent MDA5 filaments [58]. In the case of the rather exotic and short circular HDV genome, only the presence of LGP2 enabled HDV sensing by MDA5 in this study. Thus, HDV seemed not to be

an MDA5 suitable substrate. To date, high-order structures are thought to be a natural agonist of MDA5 [43]. However, there is still a lack of knowledge of the specific general MDA5 PAMP structure/motif [360]. LGP2 might broaden MDA5's range of viral PAMP recognition, including HDV and other shorter substrates. Further research investigating the MDA5-RNA binding spectrum in the presence and absence of LGP2 can help to fully understand the scope of LGP2-mediated enhancement of MDA5.

4.1.2 Importance of LGP2 ATPase function

The usage of different agonists in this study (several viruses, synthetic dsRNA) revealed different importance of the LGP2 ATP hydrolysis for MDA5-mediated enhancement. This is in line with some data from the literature. Even though the necessity of ATP hydrolysis function of LGP2 in the enhancement of MDA5 is widely accepted [56, 120], there exist set-ups in which ATP hydrolysis function was shown to be unimportant [125]. HDV infection in HepaRG^{NTCP} cells revealed the importance of ATP hydrolysis function in the enhancement of MDA5 signaling (see ΔATPase, Figure 14A). However, when using synthetic poly(I:C) stimulation in A549 cells, an LGP2 mutant lacking the ATP hydrolysis function was still able to support MDA5 signaling (Figure 11C, right-hand). This is in line with another study [125]. Thus, the importance of the ATPase hydrolysis function might be dependent on the substrate (and its structure) used and might be neglectable when using synthetic dsRNA.

Data obtained by others further affirms this hypothesis. It was postulated that LGP2 has dsRNA-independent basal ATPase hydrolysis that enhances its substrate recognition [56]. Bulged substrates with imperfect dsRNA structure and completely complementary dsRNA were recognized by LGP2 to a similar extent only in the presence of ATP. In the absence of ATP, especially bulged RNA was less well bound [56].

Even though HDV RNA contains some bulges, similar HDV RNA binding behavior was observed for K30A LGP2 and WT LGP2 in the present study (Figure 15). Yet, K30A LGP2-expressing cells showed reduced IFN signaling indirectly suggesting that signaling-competent MDA5-HDV RNA binding is affected in the presence of K30A LGP2. Due to technical difficulties, this hypothesis could so far not be experimentally confirmed. In a recent model, the ATP hydrolysis function of LGP2 helps signaling-competent MDA5 filaments to dissociate from RNA enabling their translocation to and activation of MAVS [59]. In this scenario, the LGP2 ATP hydrolysis function would not be responsible for the MDA5 binding to RNA but rather for its dissociation that is needed for downstream signaling. However, this postulated mechanism would not explain why K30A LGP2 is still able to enhance MDA5 signaling upon stimulation with HMW poly(I:C) similar to WT LGP2 which was observed in this study (Figure 11C right panel).

Thus, as suggested above, the dominating LGP2 ATPase function might rather be to enable MDA5-mediated enhancement in the presence of imperfect/weak RNA substrates. Like known for other SF2 helicases, LGP2 might open specific RNA structures with help of its ATP hydrolysis function making them accessible for MDA5 [20, 370, 371]. dsRNA unwinding was shown for RIG-I which also required ATP hydrolysis [372]. Such potential RNA "opening" might be relevant for the detection of viruses that contain a tightly packaged RNA genome and might be less important when the genomic viral RNA is loosely structured or when synthetic RNA is used. This could explain the discrepancies observed with the LGP2 ATPase mutant in the different set-ups used (e.g. poly(I:C) versus HDV).

Moreover, ATP hydrolysis of LGP2 could not only be required for the unwinding of viral RNA but also for protein displacement [373]. This could improve the PAMP accessibility and could allow direct counteraction of viral replication. In the case of RIG-I, ATP hydrolysis-dependent RNA translocation was demonstrated [56, 374] which is important for its filament formation and activation of downstream signaling [375]. Moreover, it could displace viral proteins from RNA or prevent their binding [374, 376]. Indeed, both MDA5 and RIG-I were responsible for freeing viral proteins from bound RNA [377] resulting in a direct antiviral effect. In the present study, an initial trial could neither observe an IFN-independent, direct antiviral effect for LGP2 nor MDA5 (Figure S 34). So far another study could also not identify dsRNA translocation of LGP2 [56]. This fits structural studies with the CTD of LGP2 bound to RNA where only monomer and dimer formation was observed [126]. This might question a potential ATPase-driven translocation function of LGP2. Still, LGP2 might compete with other RNA binding proteins for RNA binding.

In sum, the overall role of ATP hydrolysis of LGP2 in MDA5-mediated signaling might be context-dependent. More work is needed to test the ability of LGP2 to open RNA structures and/or to dissociate RNA binding proteins that could influence MDA5-RNA sensing.

4.1.3 Importance of LGP2 and MDA5 expression levels

Independent of the strength of LGP2 expression, it always positively affected MDA5 signaling in this study. This is in contrast with overexpression studies in HEK 293T cells by others, where exaggerated overexpression of LGP2 repressed rather than activated MDA5 signaling [56, 58]. The authors suggested a switch from positive to negative regulation of LGP2 with increased LGP2 expression over the time of infection (as an inherent feedback loop). However, as plasmid transfection in 293T cells enables the overexpression of proteins to a very high extent, these results are probably rather artificial and not reproducible in stable cell lines. Comparing endogenously upregulated and overexpressed LGP2 levels in HepaRG^{NTCP} cells upon HDV infection in this study, the overexpression already showed artificially high protein levels (Figure

S 11). Nonetheless, the overall strength of the IFN response with overexpressed LGP2 was either slightly enhanced (at early time points) or unchanged (at later stages, when endogenous LGP2 was upregulated) compared to endogenous LGP2 in HDV infected HepaRG^{NTCP} cells (Figure 14A, Figure 27C). This suggests that (i) the response was already saturated with induced endogenous LGP2 levels and that (ii) overexpressed levels of LGP2 did not change the phenotype in an unphysiological way. Overexpression of LGP2 in A549 cells did not show any negative effect on MDA5 signaling, too (Figure 10B and C). Thus, a negative correlation might only exist in rather unphysiological set-ups. To draw a clear-cut conclusion, yet, a side-by-side comparison would be needed to validate the expression strengths of LGP2 in the different settings and their outcome on the MDA5 response.

Basal signaling

Data from literature revealed that the pure overexpression of MDA5 already activated IFN signaling in reporter assays in the absence of any additional stimulation [56]. Boosting the weak initial MDA5 levels by strong exogenous expression using EF1-α promoter, similar observations could be observed in A549 cells (data not shown). This preactivation was not visible neither when using a weaker ROSA26 promoter for MDA5 induction nor when overexpressing EF1-α-driven LGP2 alone. However, when combining the ROSA26-driven MDA5 and EF1-α-driven LGP2 expression in A549 cells, these cells revealed induced steady-state expression of Mx1 and IFIT1 (Figure S 5).

Beyond that, the observed basal IFN/ISG signature (measured by especially IFN-λ1 and RSAD2 mRNA levels) in HepaRG^{NTCP} cells was also shown to be dependent on the MDA5 axis in the presence of LGP2. The basal and virus-induced signaling hint at a similar mechanism of LGP2-mediated MDA5 enhancement in sensing both foreign and endogenous RNAs. Whether the MDA5/LGP2-mediated basal signaling observed in cell culture is physiologically relevant *in vivo*, e.g. in rendering cells more protective against viral infections, needs further investigation. As RLR expression is tightly regulated at the steady-state, the basal induction is probably highly fine-balanced *in vivo*.

So far, the role of LGP2 in basal IFN/ISG signaling is under-investigated. In ADAR1 editing-deficient mice, it was determined that the unedited, endogenous RNA is sensed by MDA5 leading to an exaggerated IFN response and lethality *in vivo* [183]. In the present study, LGP2-RNA binding was shown to be important for the MDA5-mediated sensing of endogenous RNA in an ADAR1 knockdown setting (Figure 23B). This was unknown so far. By use of a mouse model that reflects the most common human ADAR1 mutation (P193A, a cause of human Aicardi-Goutières syndrome) a similar role of LGP2 in endogenous RNA sensing could be shown recently. LGP2 was essential for MDA5-dependent disease progression in those mice [378]. Additional involvement of PKR was demonstrated, linking PKR to MDA5/LGP2 signaling

[378]. A connection of PKR and LGP2 has previously been described however its outcome was unknown (see 1.1.3.6.2). Moreover, this study connects LGP2 with immune pathology for the first time and underlines the importance to include LGP2 in further studies correlated to RLR-driven disease.

A mathematical model describing the IFN outcome in the context of different MDA5 and LGP2 expression strengths and substrate availability would help to better understand the impact of those factors under both steady-state and infected conditions. More efforts need to be made to understand which endogenous RNAs can be sensed by MDA5 and LGP2.

4.2 RIG-I inhibition

As mentioned in 1.1.3.6.1 the exact outcome and underlying mechanism of LGP2's regulation of RIG-I-induced signaling is still controversial. Even though many publications claim a repressive function of LGP2 on RIG-I, there also exists some work suggesting opposing effects. Discrepancies in the observations may also arise from the systems used. In this section, the potential repressive function of LGP2 on RIG-I signaling is addressed. Potential explanations for RIG-I inhibition and factors potentially involved in the regulation will be discussed.

Several aspects of LGP2-mediated RIG-I regulation were illuminated in this study. SeV infection of respective single RLR^{KO} $HepaRG^{NTCP}$ cells showed RIG-I-dependent signaling and induced a stronger IFN response in the absence of LGP2 (Figure 17B, Figure S 19D). In $MDA5^{KO}$ A549 cells, the IFN response was repressed by overexpression of LGP2 (Figure 9C, Figure 10B and C left panels, Figure 11C left panel). Thus, in both cellular systems used in this work, LGP2 negatively regulated RIG-I being in line with many other publications [26, 54, 119, 125]. An obvious difference to the activation of MDA5 is that the overall effect of LGP2 in RIG-I signaling was milder (Figure 9C and D). This suggests that its negative influence on RIG-I-dependent responses might be less severe than the positive influence on MDA5-dependent ones. Thus, LGP2-mediated enhancement of MDA5 is probably LGP2's primary role in RLR regulation.

Digging deeper into the parameters involved in LGP2-mediated RIG-I inhibition this study reveals some parallelism to the parameters involved in MDA5 enhancement. Titration of a RIG-I-specific stimulus (5'ppp-dsRNA) in $MDA5^{KO}$ A549 cells revealed that LGP2 overexpression inhibits RIG-I-induced innate signaling by desensitizing its capability of RNA recognition (Figure 9C, Figure 10B and C, Figure 11C right panel). The magnitude of inhibition was dependent on the amount of stimulus used and was less pronounced with high levels of dsRNA

where it almost reached a plateau. A similar dependency of the stimulus dose was shown for the LGP2-mediated MDA5 enhancement.

Moreover, differences in RIG-I inhibition were observed related to the kinetics, with stronger repression at earlier time points. Experiments with SeV revealed reduced LGP2-mediated RIG-I inhibition at later time points (Figure S 1). Similarly, the strength of LGP2-mediated MDA5 enhancement was also dependent on the timing.

4.2.1 Importance of LGP2 RNA binding

By use of LGP2 RNA binding mutants, this study supports the idea that the negative effect on RIG-I signaling was (at least partially) dependent on LGP2's RNA binding function. Weakened RIG-I inhibition by using RNA binding deficient LGP2 was shown with synthetic RNA (Figure 11C, left-hand) and was further confirmed by experiments with SeV infection (data not shown, poster presentation at the 28th Annual Meeting of the Society for Virology, 2018, Würzburg). Thus, as in the case of MDA5 enhancement, LGP2 RNA binding capability influenced its negative effect on RIG-I signaling assuming that LGP2 blocks RIG-I-RNA interaction. It may explain why the repression is rather found at early time points (when there is still low viral RNA) or with non-saturated dsRNA levels. As LGP2 was supposed to enable RNA binding at the ends, equal to RIG-I, rather than from the stem of the RNA (as does MDA5) [26, 53], it might sequester the viral RNA from binding to RIG-I while still able to enhance MDA5 filament formation. LGP2 RNA binding and subsequent RIG-I inhibition was one working model for the MOA of RIG-I inhibition postulated by literature, too [27, 57, 118, 379]. It is underlined by the fact that LGP2 is the strongest RNA binder upon all RLRs [22, 57] (Figure 21A and B, Figure S 16) and binds substrates of RIG-I [26, 55], thus competing with RIG-I for RNA binding. Assuming RNA-mediated RIG-I inhibition, the magnitude could vary with the substrate used. When using poly(I:C) instead of a short 5'ppp-dsRNA, the strength of RIG-I inhibition by LGP2 differed slightly (data not shown). Moreover, RIG-I binding to poly(I:C) was equal in the presence or absence of functional LGP2 (Figure S 17, Figure 22). Further studies with different substrates could follow to clarify whether the strength of inhibition is substrate-dependent.

Besides competition on RNA, additional mechanisms could be involved in the regulation of LGP2-mediated RIG-I inhibition. The competition of LGP2 and RIG-I on RNA as MOA of the inhibitory regulation was questioned by several papers. They observed RIG-I inhibition with LGP2 mutants that lost or reduced RNA binding in reporter assays [22, 26, 125]. The inhibition experiments were performed with K634E and/or K651E LGP2 single mutants on 27 bp long dsRNA [26] or in the absence of stimulation [125]. Bamming and Horvath analyzed LGP2 variants with mutations in conserved helicase motifs which all lost ATP hydrolysis and partially reduced RNA binding. Still, some RNA-binding deficient mutants retained inhibition of RIG-I

when stimulated with SeV [22]. This prompted the authors to speculate that RNA binding cannot be important for RIG-I inhibition. The phenotypic analysis with those mutants was performed in 2fTGH and HeLa cells, two signaling competent cell lines. Whether those cells have endogenous LGP2 levels that might interfere with the effect of the mutants was not tested. Overall, the distinct results regarding the importance of LGP2 RNA binding in RIG-I inhibition observed in the present study and by others might originate from technical differences. Nonetheless, more efforts are needed to verify the significance of LGP2 RNA binding on its negative regulation.

Other data from the literature underlines the hypothesis that the MOA of LGP2 inhibition of RIG-I appears at least upstream of RIG-I CARD activation. LGP2 was not able to inhibit constitutive signaling induced by pure overexpression of the CARDs of RIG-I [57] assuming that competition appeared either on RNA binding or by direct RIG-I interaction. Some work suggested a direct interaction between LGP2 and RIG-I [121], however, several other data, including this work, could not identify a direct LGP2-RIG-I interaction [27, 118, 130, 132] (Figure S 33D).

4.2.2 Importance of further factors

LGP2 protein interactions were further supposed to be essential for RIG-I inhibition. Binding of LGP2 to components of the RLR signaling pathway was thought to block activation. Data obtained by others suggested the LGP2 inhibition to occur downstream of MAVS. MAVS and TRAF interactions were postulated as MOA for LGP2's negative role in antiviral signaling [122, 124], however, this assumption would argue against a positive regulation of MDA5. A more recent study revealed LGP2 binding to TRIM25 which blocked TRIM25 ubiquitin ligase activity and thus RIG-I activation (as RIG-I ubiquitination is needed for activation) [54]. Even though TRIM25 was also shown to regulate MDA5 [380], one of its best-described roles is RIG-I activation by ubiquitination [28, 381]. TRIM25 dependency might thus be more pronounced in the case of RIG-I and could explain why LGP2 only inhibits RIG-I. However, there seems to be a redundancy in E3 ubiquitin ligases modifying RIG-I [382, 383] which weakens the assumption that LGP2 regulates RIG-I only via TRIM25 blockage.

Importance of LGP2 ATPase function

ATP hydrolysis function of LGP2 was consistently shown to be neglectable for its suppressive effect [22, 54]. This reveals some differences to the regulation of MDA5 enhancement. In line with this, K30A LGP2 showed inhibition on RIG-I signaling comparable to WT LGP2 in A549 (Figure 11C, left-hand).

In sum, the LGP2-mediated RIG-I repression might have several facets making it difficult to draw a clear-cut conclusion about the MOA. Data available in the literature and the present study suggest several aspects being important. Especially RNA binding of LGP2, the timing, dosage and the kind of stimulus influence RIG-I inhibition in this study. However, more systematic and comparative studies are needed to understand the exact mechanism and to solve the circulating discrepancies and open questions in the field.

4.3 Differences in RIG-I- and MDA5-specific receptor usage

In the following, the importance of RIG-I and MDA5 in the IFN activation within the two different cellular systems used in this study (A549 and HepaRG^{NTCP} cells) are discussed.

In A549 cells RIG-I signaling was critical for fast innate response in various set-ups: RVFVΔNSs-Renilla (Figure S 19C), SeV and Mengo Zn virus (Figure 7B and C), dsRNA transfection (Figure 8B). In contrast, when using HepaRG^{NTCP} cells, several viral infections were dominantly sensed by the MDA5/LGP2 axis, e.g. HDV (Figure 12B), Mengo Zn virus and RVFVΔNSs-Renilla (Figure S 19A and B). Some of these results were counterintuitive, as several publications claimed an MDA5-mediated response upon Mengo Zn virus infection and a RIG-I-mediated response upon RVFVΔNSs-Renilla infection (Table 1). Different RLR expression levels in A549 and HepaRG^{NTCP} offer an explanation for this discrepancy. Steady-state RIG-I expression seemed to dominate over MDA5/LGP2 in A549 (Figure 8A, Figure S 20). This biased initial receptor availability can explain an especially RIG-I-dependent RNA sensing in A549 cells. The increase of initial MDA5 levels enabled A549 cells to respond exclusively with MDA5 upon Mengo Zn virus infection (Figure S 4D). In the case of HepaRG cells, a rather balanced RLR expression was found in the steady-state (Figure S 20) which correlated with their ability to respond exclusively with MDA5/LGP2 upon viral infections. LGP2 was important for MDA5-dependent responses in HepaRG^{NTCP} cells (Figure S 19A and B, Figure 12B) Thus, differences seen in RLR sensing and signaling are not only due to differential RLR substrate recognition (1.1.3.2) but also limited by the (initial and induced) RLR abundancy in specific cell-types. It seems plausible that the influence of RLR sensing changes in different cell types, amongst others, due to the individual availability of the respective RLRs and that of their co-factors. This should be taken into consideration when using respective cell systems for basic research.

Observations of MDA5^{KO} and RIG-I^{KO} mice upon West Nile virus (WNV) infection showed different temporal defects in the IFN response which implied an early RIG-I versus delayed and prolonged MDA5 signaling [384]. This indicates that RLR sensing might moreover be

temporally regulated. Different kinetics of RIG-I and MDA5 are postulated as a result of different PAMP recognition, with MDA5 probably sensing viral replication intermediates that are produced later upon infection. Moreover, prolonged IFN signaling induced by IRF7, a prominent positive feedback regulator of RLR signaling [161, 162], was suggested to be rather connected to MDA5 than RIG-I signaling [384-386]. The potential kinetics of fast RIG-I and prolonged MDA5/LGP2 signaling should be tested with more viral infections and in more cellular systems and should be connected to their protein availability. Probably not all viral structures can be sensed by all RLRs, as in the case of HDV. Whether the lack of RIG-I activation upon infection in HepaRG^{NTCP} cells is due to some unknown counteraction by HDV or if the extraordinary structure is just no suitable substrate that activates RIG-I is not yet clarified.

4.4 Q425R LGP2 as gain-of-function polymorphism

Many studies on RIG-I and especially MDA5 polymorphisms exist, analyzing their role in innate immunity, their impact on autoimmune disease and their potential MOA. This study investigated three non-synonymous SNPs within LGP2 (Q425R, rs2074158; N461S, rs34016093; R523Q, rs2074160) on their ability to regulate RLR signaling.

The investigation of the aforementioned LGP2 variants revealed a special behavior for Q425R LGP2 in RLR signaling – both in A549 and HepaRG^{NTCP} cells. In contrast, this study could not observe any strikingly altered phenotype for N461S or R523Q LGP2 compared to WT LGP2.

4.4.1 Q425R LGP2 and MDA5 signaling

MDA5-mediated signaling was accelerated and sensitized in the presence of Q425R LGP2 upon HDV (Figure 16C, Figure S 18B), Mengo Zn virus and SARS-CoV-2 infection (Figure 18B, Figure 17, Figure 19A and C-E, Figure 20A, B and D). Compared to WT LGP2, Q425R LGP2 additionally enhanced MDA5-mediated steady-state levels of IFN-λ1 and RSAD2 mRNA (Figure 16C lower panel, Figure 17B left panel, Figure 23B). Q425R and WT LGP2 equally bound RNA – at least on HMW poly(I:C) (Figure 21A and B, Figure 22) and HDV RNA (data not shown, n=1). Nonetheless, Q425R LGP2 enhanced the recruitment of MDA5 to RNA (Figure 22).

This leads to the following mechanistic model of MDA5 enhancement: Q425R LGP2 binding to RNA strengthens the recruitment of MDA5 to RNA and/or stabilizes MDA5-RNA binding compared to WT LGP2, resulting in more frequent signaling competent MDA5 filaments that

can induce stronger signaling (Figure 28). This could even sensitize the MDA5 activation on endogenous RNA in steady-state.

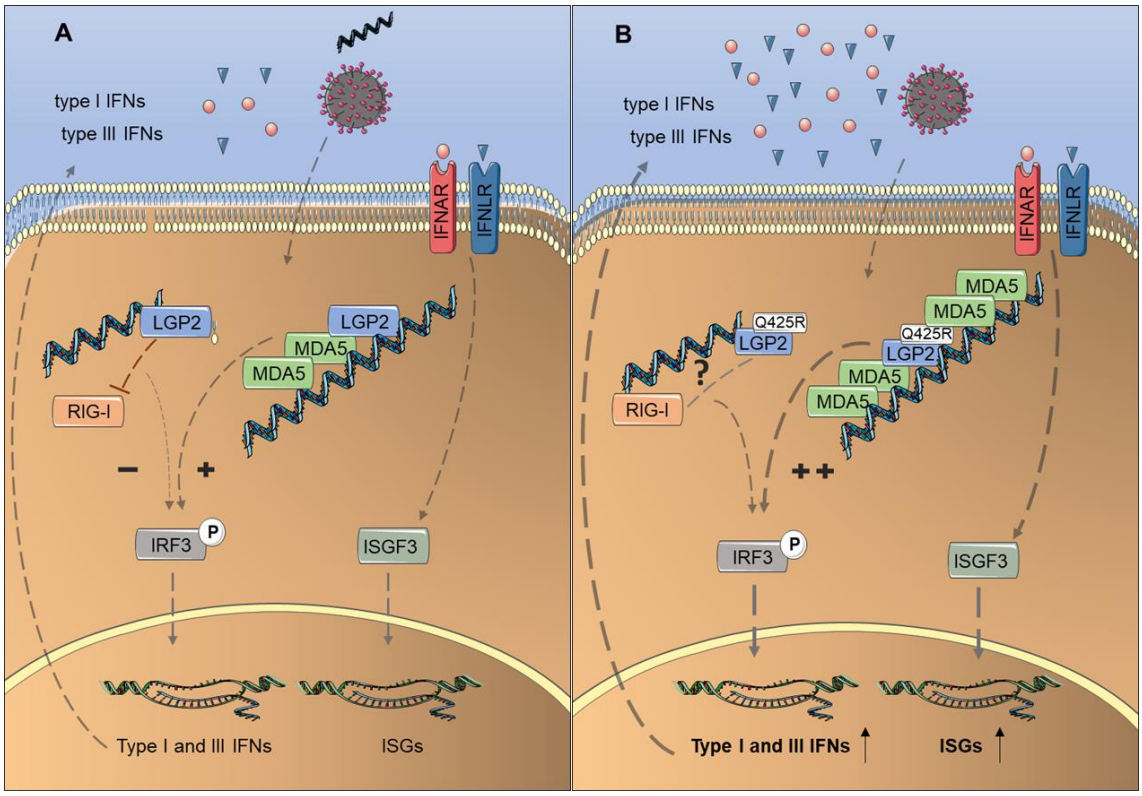

Figure 28: Simplistic model describing the role of WT and Q425R LGP2 in RLR signaling. Comparison between WT LGP2 and Q425R LGP2 in the regulation of RLR signaling. **(A)** WT LGP2 binds viral or synthetic dsRNA upon infection or transfection of the cell. This leads to the recruitment of signaling competent MDA5 enabling downstream activation and induction of type I and III IFNs upon infection (HDV, SARS-CoV-2, Mengo Zn) or HMW poly(I:C) transfection. In the case of RIG-I, WT LGP2 RNA binding reduces RIG-I-mediated signaling leading to lower production of type I and III IFNs upon 5'ppp-dsRNA transfection. Produced IFNs are secreted and activate JAK-STAT signaling and downstream expression of IFN stimulated genes (ISGs). **(B)** Q425R LGP2 binds dsRNA similar to WT LGP2. This however leads to stronger recruitment of MDA5 in the presence of Q425R LGP2 and enhanced MDA5-mediated signaling upon infection (HDV and SARS-CoV-2), resulting in higher secretion of type I and III IFNs. Therefore, stronger JAK-STAT signaling enhances the expression of ISGs compared to WT LGP2. In the case of RIG-I-induced signaling upon infection (SeV and ZIKV), the mechanism of action of Q425R LGP2 remains elusive. Lower repression of IFN/ISG induction was obtained with Q425R compared to WT LGP2 upon SeV and partially ZIKV infection. The figure was created using modified Smart Servier Medical Art images, licensed under a Creative Commons Attribution 3.0 Unported License.

Thus, the model not only offers an explanation for the enhanced innate signaling with Q425R LGP2 upon stimulation but also for the higher basal gene expression in the presence of Q425R LGP2. Pulldown experiments and subsequent RNA seq analysis of WT and Q425R LGP2 should follow to address the RNA substrate width of MDA5 in the presence of WT and Q425R LGP2. Q425R LGP2 bound synthetic poly(I:C) equal to WT LGP2 (Figure 21A and B). However, it seems conceivable that Q425R LGP2 enables the MDA5 recognition of more diverse RNA structures, including endogenous ones. Whether such potentially enhanced self-recognition also occurs with lower expression levels of Q425R LGP2, should be further

addressed (e.g. by using endogenous genome editing). So far, the results were only obtained with overexpression of LGP2 variants. Yet, the overall expression between WT and Q425R LGP2 was similar and high LGP2 expression did not alter the LGP2 function in this study. Thus, it is likely that the observed differences with WT and Q425R LGP2 upon infection and in steady-state are retained by using endogenous expression levels. Whether the gain-of-function Q425R LGP2 variant can be correlated with (i) better outcome upon viral infections or (ii) increased risk to develop autoimmune diseases needs to be addressed in the future. Especially Africans harbor a Q425R LGP2 genetic background. Whether they are at some higher risk to develop autoimmune diseases is an open question.

Using bioinformatic approaches, Vasseur et al. speculated Q425R LGP2 to be a gain-of-function LGP2 version which is underpinned by the results obtained in this work. The authors moreover hypothesized that the enhanced antiviral potential indeed might be at the cost of higher risk for autoimmunity [114]. They assume that viral pressure kept the Q425R LGP2 version in the evolution of Africans whereas it seemed to be disadvantageous in the evolution of Asians and Europeans which gained back the original Q425 [114]. The existence of higher viral pressure within Africa seems plausible especially since that continent displays a hotspot for zoonotic viral diseases [387]. Whether a correlation between Q425R LGP2 carriers and enhanced frequency of autoimmunity exists should be addressed. However, it is also conceivable that humans with Q425R LGP2 background might have other adaptations counteracting overshooting responses that had not been considered in this study.

4.4.2 Q425R LGP2 and its role in RIG-I signaling

An additional unexpected observation with Q425R LGP2 was its (partially) lower negative effect on RIG-I signaling upon SeV and ZIKV infection (Figure 17B, Figure 19A and C-E, Figure 20A, B and D). The underlying mechanism of reduced/lost RIG-I inhibition can so far not be explained (Figure 28B). RIG-I binding to poly(I:C) was unchanged in the presence of WT or Q425R LGP2 (Figure 22) assuming no competition of LGP2 and RIG-I on this substrate.

In the case of paramyxoviruses, which include SeV, it was hypothesized that the V protein can bind LGP2 in a complex with RIG-I, thus enhancing the repressive function of LGP2 [388]. In that study they used V protein of parainfluenza virus type 5 (PIV5) which interacted with LGP2 amino acids 327 to 465, a region thus encompassing Q425. This region is quite similar to the postulated MVBR postulated by another group; yet, these authors conclude unaltered LGP2 inhibition of RIG-I in the presence of V proteins [61]. However, they postulate that a V protein binding resistant LGP2 (in contrast to WT) was able to activate MDA5 in the presence of V protein [61]. Whether Q425R LGP2 impairs V protein binding thus potentially either directly limiting RIG-I inhibition or enabling some MDA5 activation has not been investigated so far.

Pulldown experiments of WT and Q425R LGP2 with V proteins would be the first starting point to address this question.

As ZIKV infection revealed partially reduced inhibition of immune signaling with Q425R LGP2, too, probably a paramyxovirus unrelated mechanism of action exists. Other potential interaction partners might be differently associated with Q425R LGP2, e.g. lost or lower TRIM25 binding. Quicke et al. claimed the helicase domain of LGP2 is important for RIG-I inhibition via TRIM25 interaction [54]. Whether Q425R LGP2 reduces the binding of RIG-I interactors, potentially important for negative regulation, is unknown. The interactome of Q425R and WT LGP2 by MS could give useful insights into the mechanism of differential RIG-I inhibition.

As the experiments with Q425R LGP2 on RIG-I signaling were performed in cells harboring both MDA5 and RIG-I, further experimental repetitions should follow in MDA5^{KO} cells to avoid any potential impact that is mediated by MDA5. Moreover, synthetic stimuli would help to circumvent any virus-specific effects. Thus, using A549 MDA5^{KO} and synthetic stimulus titrations in the future, a more detailed and clear-cut picture of Q425R LGP2 in RIG-I signaling could be drawn.

4.5 Influence of Q425R LGP2 in virus control

As discussed in 4.4, compared to WT LGP2, Q425R LGP2 enhanced the RIG-I- and MDA5-mediated IFN responses. Thus, potential biological consequences of this phenotype on viral control will be addressed in this chapter.

Even though Q425R LGP2 enhanced the immune response in several infection settings, no potential connection between the strength of immune activation and SeV or ZIKV replication repression could be drawn in this study (Figure 19B, Figure 20C). Moreover, only inconclusive results were observed with SARS-CoV-2 (Figure 18C). Several aspects might be responsible for this observation. In the case of SARS-CoV-2, it cannot be excluded that RIG-I plays a role in viral repression, independent of its function in the IFN response induction (as was already postulated [271]). SeV, ZIKV and SARS-CoV-2 probably sufficiently counteract the immune response leading to low viral vulnerability by the IFN system in infected cells (for their virus-specific counteractions see the respective part in 1.2). Viral immune evasion strategies, including fast replication kinetics and/or expression of viral antagonists, could explain why differences in the IFN activation of the different cell lines were not reflected in altered viral replication. Moreover, the observed changes in immune induction might rather be important in more complex systems, where fast responses in primary infected cells can be linked to improved activation and subsequent stronger responses in specialized immune cells. In the

mono cell culture used in this study, replication differences might therefore be especially visible in IFN sensitive infection settings or when very high differences in IFN responses are achieved. Indeed, when investigating the replication of two IFN sensitive reporter viruses (VSV-Firefly and RVFVΔNSs-Renilla) lacking IFN antagonists in a pilot experiment, LGP2 influenced viral repression (Figure S 22). Viral replication was affected by LGP2 with both low and high MOIs used, especially when using Q425R LGP2.

In the case of HDV, moderate changes in virus replication could be observed between WT and Q425R expressing cells which correlated to the strength of the respective immune response (Figure 16D and E). HDV was shown to be sensitive to pretreatment with IFN-α however was less IFN sensitive when stimulation occurred pi [389]. Q425R LGP2 revealed higher resistance towards initial HDV infection (Figure 16E, see 5 days pi). Thus, increased basal and accelerated virus-induced IFN responses, probably render Q425R LGP2 cells more immune against HDV infection. The mechanism of viral repression by Q425R LGP2 still needs to be analyzed in more depth. It seems plausible that the slightly enhanced basal IFN/ISG levels with Q425R LGP2 reveal some antiviral effects as seen in some lower initial infectivity. The Q425R LGP2-triggered latent signaling might induce a faint positive feedback loop. Potentially small amounts of secreted IFNs could then prime cells in an autocrine and paracrine manner. Transwell systems and/or a secretome analysis could help to analyze whether Q425R LGP2 expressing cells can prime neighboring cells. Moreover, the stronger MDA5 sensitization by Q425R LGP2 can also explain the lower HDV replication at later infection stages (Figure 16E, see 17 days pi). The observed Q425R LGP2 effects reflect the bioinformatically predicted fitness status by Vasseur et al., claiming the Q425R LGP2 substitution benign [114].

HDV cell division-mediated spread is IFN sensitive (Zhang et al., submitted). Thus, cell division-mediated spread experiments in HepaRG^{NTCP} cells expressing different LGP2 versions revealed strong differences in HDV replication (Dr. Zhenfeng Zhang, personal communication). In those settings, both WT and Q425R LGP2 blocked HDV replication to a maximum extent which was not the case for IFN signaling deficient ATPase and RNA binding LGP2 mutants. As no changes were seen for WT and Q425R LGP2, this hints at already saturated responses in those settings probably due to high LGP2 expression levels. Subtle differences would probably be more visible with low expression levels of the LGP2 variants. Yet, overall, this highlights the importance of LGP2 in antiviral signaling upon HDV infection, especially in conditions where the virus spreads via cell division.

Overall, Q425R LGP2 might have provided a selective advantage in fighting viral infections by accelerating the initial IFN response. However, the cellular systems used in this study can only help to understand the role of LGP2 (and its natural Q425R variant) in initially infected cells and their neighbors. As such, these systems fail to recapitulate the overall outcome of an

infection *in vivo*. Whether differences observed with Q425R LGP2 in the IFN response in cell culture might have real implications in the disease outcome of individuals or even populations needs to be tested in the future. As Q425R LGP2 is dominantly present in Africans it is tempting to speculate that Africans might have a better prognosis upon viral infections.

With regards to HDV, the Q425R LGP2 triggered IFN response might affect the long-term progression of disease thus influencing chronicity. Of course, many factors might be also involved in the development of pathogenicity in HDV infected patients. Nonetheless, two recent studies indeed showed that Africans had more often a less severe form of HDV-associated viral hepatitis and less often developed cirrhosis [390, 391] which was independent of the HDV genotype [390]. The identified frequency of cirrhosis (18%) [390], a hint for a severe disease outcome, corresponds to Q425 LGP2 frequency in Africans (15%) [114]. This might just be a co-incidence, however, could also be a real correlation between Q425R LGP2 and less severe outcome of hepatitis D. Spaan et al. claimed an association between HDV genotype 5 infection and lower frequency of cirrhosis or hepatic decompensation [391]. Interestingly, all HDV genotype 5 infected patients were Africans while genotype 1 infected patients were mostly from Europe. This raises the question of whether the HDV genotype or not rather the patient's genetic background is responsible for the reported association with the disease severity. To address this, further studies are needed.

Similar to HDV, correlation studies between the LGP2 polymorphisms and disease outcome in patients infected with SARS-CoV-2 should also be performed. Genetic predispositions for severe COVID19 are quite unclear [392]. A recent study claimed deficiencies within the type I IFN signaling to be a genetic risk factor for life-threatening COVID19 disease [268]. Unbalanced, low antiviral IFN signaling with still normal proinflammatory responses could be the outcome in severe COVID19 patients [367, 393]. On the contrary, children were found to be barely affected by severe COVID19. Their stronger innate immune response offers one explanation for that [394]. In line with this assumption, higher steady-state expression of innate signaling genes, including RLRs, was detected in airway epithelial cells of children when compared to adults assuming that viral sensing can happen faster in children [395]. This hints at the special importance of the IFN system in disease control upon SARS-CoV-2 infection. As SARS-CoV-2 is a very fast virus and establishes its replication within hours (around 8 to 12 h for one replication cycle in Vero cells [366, 396]), even small differences in the IFN kinetic or signaling strength might determine the overall disease outcome in a broad scale. Whether Q425R LGP2 can fine balance the IFN response, enabling the host to be a little ahead of the virus and enabling virus control, needs further research. Moreover, whether the high genetic prevalence of Q425R LGP2 in the African population enables better SARS-CoV-2 counteraction and thus impacts COVID19 severity in those infected individuals is unknown.

COVID19 might have affected the African continent indeed to a lesser extent compared to other parts of the world [397], however, with diverse possible reasons.

To further understand the physiological role of Q425R LGP2 in fighting human pathogens like SARS-CoV-2 and HDV, its influence should be validated by using patient's material. Potential correlations between the virus-induced disease outcome and the presence of Q425R LGP2 should be determined, especially for infections with HDV and SARS-CoV-2, two viruses that account for major worldwide disease burden. Trying to understand the genetics driving disease progression might help to predict the disease severity in individuals and thus to implement personalized medical care.

4.6 LGP2 phosphorylation

Multiple MDA5 and RIG-I PTMs, including phosphorylation, have been identified while there is a lack of knowledge about the PTMs within LGP2 (see Chapter 1.1.3.4). One-third of all proteins are supposed to be phosphorylated [398], thus phosphorylation depicts a very abundant PTM. Indeed, MS analysis of LGP2 phosphorylation in this study could also identify three serines to be phosphorylated: S169, S365 and S464. The higher frequency of serine phosphorylation in comparison to threonine and tyrosine phosphorylation [399] might explain why especially this amino acid was found to be phosphorylated.

Sequence comparison of the identified phospho-sites showed that S169 is conserved among all human paralogues (namely MDA5 and RIG-I) as well as LGP2 orthologs of mouse, rat and chicken. It is part of the conserved RLR helicase motif III consisting of threonine (T), alanine (A), serine (S) (amino acids 167 to 169 in LGP2) [22]. This explains its conservation in orthologous and paralogous proteins. It implies that S169 phosphorylation could be important for the regulation of motif III functionality. In contrast to S169, S365 and S464 LGP2 are not conserved in MDA5 and RIG-I paralogues and cannot be observed in the chicken ortholog. While S464 is present in mouse and rat LGP2, S365 cannot be identified in those orthologous genes. However, due to its reproducible detection in MS and specific occurrence upon stimulation, S365 phosphorylation was assumed to be important for LGP2 regulation. Phenotypic assays from this work however indicate that single phosphomimetic and phosphoablative mutants of S365 and S464 regulate RLR signaling similar to WT LGP2. In contrast, phosphoablative S169A LGP2 revealed a stronger repressive effect on RIG-I signaling compared to WT LGP2 (Figure S 28C left panel, Figure 26C upper panel).

The lack of a phenotype for S365A/D and S464A/D LGP2 mutants in those functional assays can have many reasons. It could simply be explained by the lack of any biological relevance for S365 and S464 LGP2 phosphorylation. However, a combined phosphomutant

counteracted that hypothesis (see 4.6.1). Thus, other explanations for their missing phenotypes are possible. (i) While not affecting the investigated RLR signaling, they could influence other, even yet undiscovered LGP2 features [400]. (ii) Moreover, several phosphorylation sites within a protein might have redundant functions. (iii) Simulation of potential phospho-sites by negatively charged aspartate or glutamate might be not optimal. These amino acids should mimic the negative charge of a phosphosite, however, do not reflect the true steric and charged feature of a phosphoryl-modification [401]. (iv) Moreover, amino acid substitutions cannot reflect the reversible phosphorylation regulation. These various technical problems could explain the lack of phospho-specific phenotypes in functional assays.

4.6.1 Importance of combined S365 and S464 LGP2 phosphosites

As phosphorylation sites might not only work separately but also in combination, potential effects might only occur when combined [400]. Therefore, the combination of S365 and S464 sites was also performed in this study. S365 and S464 phosphorylation patterns were found to be regulated differently over time: phosphorylation of S365 at late stage versus phosphorylation of S464 in steady-state. Combined phosphomutants either mimicking the phosphorylation pattern of S365 and S464 in the steady-state (p-mock) or the infected state (p-stimulated) were analyzed. p-mock LGP2 revealed a delayed activation of MDA5-induced IFN response upon HDV infection while p-stimulated rather reflected WT LGP2 conditions. This indicates that a simultaneous regulation on both sites of LGP2 seems to be involved in the MDA5 support. As both phosphorylation sites lay within the helicase domain and do not belong to any conserved motif, they might be involved in protein-protein interactions. Further MS analysis and co-IP studies are needed to investigate whether p-mock LGP2 reveals altered protein interaction. S464 is framed by two conserved RNA binding motifs, motif V and VI and thus its phosphorylation could also weaken RNA binding (Prof. Dr. Dahai Luo, personal communication). Therefore, the RNA binding capability of p-mock should also be tested. Both dampened MDA5 recruitment to RNA and delayed/reduced RNA binding ability of p-mock LGP2 could explain lower basal and HDV-induced MDA5-mediated signaling. Further experiments are needed to test these possibilities and to understand the underlying mechanism of delayed MDA5 support. The effect seen with p-mock should be verified in the future by further repetitions and usage of other MDA5 activating viruses and cellular systems. It might also be of interest to check the effect of p-mock LGP2 in RIG-I signaling.

Thus far, it is tempting to speculate that simultaneous (de-)phosphorylation at S365 and S464 (reflected by p-mock) is locking LGP2 signaling capacity in the steady-state, indicated by blocked steady-state expression of innate immune genes in the case of p-mock. Additional

PTMs are likely important to regulate LGP2 upon stimulation as p-mock did not completely abolish MDA5 enhancement upon HDV infection. However, the delayed MDA5 responsiveness observed in p-mock LGP2-expressing cells reveals retardation in the activation kinetics. Further experiments and in-depth characterization of p-mock LGP2 need to clarify the role of this steady-state phosphorylation pattern of LGP2 in more detail.

4.6.2 Importance of S169 LGP2 phosphosites

The identified S169 phosphorylation within motif III of LGP2 raises several questions. Motif III was suggested to be important for RNA unwinding of proteins of the DEAD-box RNA helicase family [402]. Motif III deficient LGP2 was shown to lose ATP hydrolysis activity and to reduce RNA binding [22]. Nonetheless, it still inhibited RIG-I signaling in reporter assays [22]. If the single mutation in S169A alone is already enough to eliminate ATP hydrolysis function and to reduce RNA binding needs further investigation. However, as S169A did not reveal any effect on MDA5 signaling, which needs RNA binding capable LGP2, it could be assumed that RNA binding is at least not fully abolished in S169A. The phosphorylation pattern of S169 was very dynamic (found both with and without stimulation), indicating that its function is independent of the infection status. How LGP2 S169A specifically affects RIG-I signaling is still elusive. Specific protein interactions involved in RIG-I signaling might account for this discrepancy, e.g. LGP2 blockage of TRIM25 [54], as was already discussed for Q425R LGP2, too (see 4.4.2). In their work, Quicke et al. tested LGP2 motif III mutant which was still able to bind TRIM25 [54]. They showed that TRIM25 protein levels were decreased when interacting with LGP2 leading to the author's suggestion that direct LGP2 binding might interfere with TRIM25 stabilization [54]. If S169A even enhances TRIM25 interaction leading to its degradation and subsequent inhibition of RIG-I will need further investigation. Even though other E3 ligases were claimed to be important for RIG-I activation, stronger TRIM25 interaction could offer one explanation for its enhanced RIG-I inhibition.

4.6.3 MS limitations and future directions

The applied MS for the detection of phosphorylation had some limitations. The generated peptide pattern might lead to some peptides that are hard to analyze. Thus it cannot be ruled out that some phosphorylation sites were not identified [401]. Moreover, no statement can be made regarding the abundance of the respective phosphorylated sites in comparison to their unphosphorylated counterparts. The reliability to reproduce the phospho-sites within several experimental replicates might give only a hint for their abundance. S464 phosphorylation could be exclusively identified in the first MS run, hypothesizing that only a marginal percentage of phosphorylated to unphosphorylated S464 exists. Additionally, sensitive MS-approaches

might identify alterations/phosphorylations at low stoichiometries [400]. Some of these low abundant sites might even be functionally irrelevant [401].

In sum, the initial investigation of LGP2 phosphorylation opens new questions. Future studies should focus on the ability of S169A and p-mock LGP2 to bind RNA and hydrolyze ATPase, two major functions of LGP2. Moreover, insights into the interaction landscape of those phospho-mutants and their MOA might help to better understand the regulation of LGP2's ambivalent functions in RLR signaling.

5 REFERENCES

1. Aristizábal, B. and Á. González. *Innate immune system (Chapter 2). In Autoimmunity: From Bench to Bedside [Internet]*. 2013; Available from: https://www.ncbi.nlm.nih.gov/books/NBK459455/.
2. Alberts, B., et al. *Innate Immunity. In Molecular Biology of the Cell. 4th edition.* 2002; Available from: https://www.ncbi.nlm.nih.gov/books/NBK26846/.
3. Paludan, S.R., et al., *Constitutive immune mechanisms: mediators of host defence and immune regulation.* Nat Rev Immunol, 2021. **21**(3): p. 137-150.
4. Leiva-Juarez, M.M., J.K. Kolls, and S.E. Evans, *Lung epithelial cells: therapeutically inducible effectors of antimicrobial defense.* Mucosal Immunol, 2018. **11**(1): p. 21-34.
5. Robinson, M.W., C. Harmon, and C. O'Farrelly, *Liver immunology and its role in inflammation and homeostasis.* Cell Mol Immunol, 2016. **13**(3): p. 267-76.
6. van Zelm M.C., R.M.B., Staal F.J.T. , *Hematopoiesis and Lymphocyte Development: An Introduction*, in *Principles of Immunopharmacology*. 2019, Springer, Cham.
7. Fitzgerald-Bocarsly, P. and D. Feng, *The role of type I interferon production by dendritic cells in host defense.* Biochimie, 2007. **89**(6-7): p. 843-55.
8. Wu, L. and Y.J. Liu, *Development of dendritic-cell lineages.* Immunity, 2007. **26**(6): p. 741-50.
9. Steinman, R.M., *Linking innate to adaptive immunity through dendritic cells.* Novartis Found Symp, 2006. **279**: p. 101-9; discussion 109-13, 216-9.
10. Paust, S., B. Senman, and U.H. von Andrian, *Adaptive immune responses mediated by natural killer cells.* Immunol Rev, 2010. **235**(1): p. 286-96.
11. El-Zayat, S.R., H. Sibaii, and F.A. Mannaa, *Toll-like receptors activation, signaling, and targeting: an overview.* Bulletin of the National Research Centre, 2019. **43**(1): p. 187.
12. Dambuza, I.M. and G.D. Brown, *C-type lectins in immunity: recent developments.* Curr Opin Immunol, 2015. **32**: p. 21-7.
13. Li, K. and D.M. Underhill, *C-Type Lectin Receptors in Phagocytosis.* Curr Top Microbiol Immunol, 2020. **429**: p. 1-18.
14. Abe, T., Y. Marutani, and I. Shoji, *Cytosolic DNA-sensing immune response and viral infection.* Microbiol Immunol, 2019. **63**(2): p. 51-64.
15. Hornung, V., et al., *AIM2 recognizes cytosolic dsDNA and forms a caspase-1-activating inflammasome with ASC.* Nature, 2009. **458**(7237): p. 514-8.
16. Motwani, M., S. Pesiridis, and K.A. Fitzgerald, *DNA sensing by the cGAS-STING pathway in health and disease.* Nat Rev Genet, 2019. **20**(11): p. 657-674.
17. Kersse, K., et al., *NOD-like receptors and the innate immune system: coping with danger, damage and death.* Cytokine Growth Factor Rev, 2011. **22**(5-6): p. 257-76.
18. Rehwinkel, J. and M.U. Gack, *RIG-I-like receptors: their regulation and roles in RNA sensing.* Nat Rev Immunol, 2020. **20**(9): p. 537-551.
19. Lassig, C. and K.P. Hopfner, *Discrimination of cytosolic self and non-self RNA by RIG-I-like receptors.* J Biol Chem, 2017. **292**(22): p. 9000-9009.
20. Luo, D., et al., *Structural insights into RNA recognition by RIG-I.* Cell, 2011. **147**(2): p. 409-22.
21. Walker, J.E., et al., *Distantly related sequences in the alpha- and beta-subunits of ATP synthase, myosin, kinases and other ATP-requiring enzymes and a common nucleotide binding fold.* EMBO J, 1982. **1**(8): p. 945-51.
22. Bamming, D. and C.M. Horvath, *Regulation of signal transduction by enzymatically inactive antiviral RNA helicase proteins MDA5, RIG-I, and LGP2.* J Biol Chem, 2009. **284**(15): p. 9700-12.
23. Caruthers, J.M. and D.B. McKay, *Helicase structure and mechanism.* Curr Opin Struct Biol, 2002. **12**(1): p. 123-33.
24. Cordin, O. and J.D. Beggs, *RNA helicases in splicing.* RNA Biol, 2013. **10**(1): p. 83-95.
25. Dillingham, M.S., P. Soultanas, and D.B. Wigley, *Site-directed mutagenesis of motif III in PcrA helicase reveals a role in coupling ATP hydrolysis to strand separation.* Nucleic Acids Res, 1999. **27**(16): p. 3310-7.

26. Li, X., et al., *The RIG-I-like receptor LGP2 recognizes the termini of double-stranded RNA.* J Biol Chem, 2009. **284**(20): p. 13881-91.
27. Pippig, D.A., et al., *The regulatory domain of the RIG-I family ATPase LGP2 senses double-stranded RNA.* Nucleic Acids Res, 2009. **37**(6): p. 2014-25.
28. Onomoto, K., K. Onoguchi, and M. Yoneyama, *Regulation of RIG-I-like receptor-mediated signaling: interaction between host and viral factors.* Cell Mol Immunol, 2021. **18**(3): p. 539-555.
29. Kowalinski, E., et al., *Structural basis for the activation of innate immune pattern-recognition receptor RIG-I by viral RNA.* Cell, 2011. **147**(2): p. 423-35.
30. Louber, J., et al., *Kinetic discrimination of self/non-self RNA by the ATPase activity of RIG-I and MDA5.* BMC Biol, 2015. **13**: p. 54.
31. Wu, B., et al., *Structural basis for dsRNA recognition, filament formation, and antiviral signal activation by MDA5.* Cell, 2013. **152**(1-2): p. 276-89.
32. Lu, C., et al., *The structural basis of 5' triphosphate double-stranded RNA recognition by RIG-I C-terminal domain.* Structure, 2010. **18**(8): p. 1032-43.
33. Hornung, V., et al., *5'-Triphosphate RNA is the ligand for RIG-I.* Science, 2006. **314**(5801): p. 994-7.
34. Kato, H., et al., *Length-dependent recognition of double-stranded ribonucleic acids by retinoic acid-inducible gene-I and melanoma differentiation-associated gene 5.* J Exp Med, 2008. **205**(7): p. 1601-10.
35. Goubau, D., et al., *Antiviral immunity via RIG-I-mediated recognition of RNA bearing 5'-diphosphates.* Nature, 2014. **514**(7522): p. 372-375.
36. Schlee, M., et al., *Recognition of 5' triphosphate by RIG-I helicase requires short blunt double-stranded RNA as contained in panhandle of negative-strand virus.* Immunity, 2009. **31**(1): p. 25-34.
37. Loo, Y.M., et al., *Distinct RIG-I and MDA5 signaling by RNA viruses in innate immunity.* J Virol, 2008. **82**(1): p. 335-45.
38. Furr, S.R., et al., *RIG-I mediates nonsegmented negative-sense RNA virus-induced inflammatory immune responses of primary human astrocytes.* Glia, 2010. **58**(13): p. 1620-9.
39. Kato, H., et al., *Differential roles of MDA5 and RIG-I helicases in the recognition of RNA viruses.* Nature, 2006. **441**(7089): p. 101-5.
40. Habjan, M., et al., *Processing of genome 5' termini as a strategy of negative-strand RNA viruses to avoid RIG-I-dependent interferon induction.* PLoS One, 2008. **3**(4): p. e2032.
41. Chazal, M., et al., *RIG-I Recognizes the 5' Region of Dengue and Zika Virus Genomes.* Cell Rep, 2018. **24**(2): p. 320-328.
42. Triantafilou, K., et al., *Visualisation of direct interaction of MDA5 and the dsRNA replicative intermediate form of positive strand RNA viruses.* Journal of Cell Science, 2012. **125**(20): p. 4761-4769.
43. Pichlmair, A., et al., *Activation of MDA5 requires higher-order RNA structures generated during virus infection.* J Virol, 2009. **83**(20): p. 10761-9.
44. Feng, Q., et al., *MDA5 detects the double-stranded RNA replicative form in picornavirus-infected cells.* Cell Rep, 2012. **2**(5): p. 1187-96.
45. Wang, J.P., et al., *MDA5 and MAVS mediate type I interferon responses to coxsackie B virus.* J Virol, 2010. **84**(1): p. 254-60.
46. Gitlin, L., et al., *Essential role of mda-5 in type I IFN responses to polyriboinosinic:polyribocytidylic acid and encephalomyocarditis picornavirus.* Proc Natl Acad Sci U S A, 2006. **103**(22): p. 8459-64.
47. Du, X., et al., *Hepatitis C virus replicative double-stranded RNA is a potent interferon inducer that triggers interferon production through MDA5.* J Gen Virol, 2016.
48. Zhang, Z., et al., *Hepatitis D virus replication is sensed by MDA5 and induces IFN-beta/lambda responses in hepatocytes.* J Hepatol, 2018. **69**(1): p. 25-35.
49. Yin, X., et al., *MDA5 Governs the Innate Immune Response to SARS-CoV-2 in Lung Epithelial Cells.* Cell Rep, 2021. **34**(2): p. 108628.

50. Kato, H., et al., *Cell type-specific involvement of RIG-I in antiviral response.* Immunity, 2005. **23**(1): p. 19-28.
51. Schilling, M., et al., *RIG-I Plays a Dominant Role in the Induction of Transcriptional Changes in Zika Virus-Infected Cells, which Protect from Virus-Induced Cell Death.* Cells, 2020. **9**(6).
52. Plociennikowska, A., et al., *TLR3 activation by Zika virus stimulates inflammatory cytokine production which dampens the antiviral response induced by RIG-I-like receptors.* J Virol, 2021.
53. Uchikawa, E., et al., *Structural Analysis of dsRNA Binding to Anti-viral Pattern Recognition Receptors LGP2 and MDA5.* Mol Cell, 2016. **62**(4): p. 586-602.
54. Quicke, K.M., et al., *RNA Helicase LGP2 Negatively Regulates RIG-I Signaling by Preventing TRIM25-Mediated Caspase Activation and Recruitment Domain Ubiquitination.* J Interferon Cytokine Res, 2019. **39**(11): p. 669-683.
55. Takahasi, K., et al., *Solution structures of cytosolic RNA sensor MDA5 and LGP2 C-terminal domains: identification of the RNA recognition loop in RIG-I-like receptors.* J Biol Chem, 2009. **284**(26): p. 17465-74.
56. Bruns, A.M., et al., *ATP hydrolysis enhances RNA recognition and antiviral signal transduction by the innate immune sensor, laboratory of genetics and physiology 2 (LGP2).* J Biol Chem, 2013. **288**(2): p. 938-46.
57. Yoneyama, M., et al., *Shared and unique functions of the DExD/H-box helicases RIG-I, MDA5, and LGP2 in antiviral innate immunity.* J Immunol, 2005. **175**(5): p. 2851-8.
58. Bruns, A.M., et al., *The innate immune sensor LGP2 activates antiviral signaling by regulating MDA5-RNA interaction and filament assembly.* Mol Cell, 2014. **55**(5): p. 771-81.
59. Duic, I., et al., *Viral RNA recognition by LGP2 and MDA5, and activation of signaling through step-by-step conformational changes.* Nucleic Acids Res, 2020. **48**(20): p. 11664-11674.
60. Hei, L. and J. Zhong, *Laboratory of genetics and physiology 2 (LGP2) plays an essential role in hepatitis C virus infection-induced interferon responses.* Hepatology, 2017. **65**(5): p. 1478-1491.
61. Rodriguez, K.R. and C.M. Horvath, *Paramyxovirus V protein interaction with the antiviral sensor LGP2 disrupts MDA5 signaling enhancement but is not relevant to LGP2-mediated RLR signaling inhibition.* J Virol, 2014. **88**(14): p. 8180-8.
62. Parisien, J.P., et al., *A shared interface mediates paramyxovirus interference with antiviral RNA helicases MDA5 and LGP2.* J Virol, 2009. **83**(14): p. 7252-60.
63. Andrejeva, J., et al., *The V proteins of paramyxoviruses bind the IFN-inducible RNA helicase, mda-5, and inhibit its activation of the IFN-beta promoter.* Proc Natl Acad Sci U S A, 2004. **101**(49): p. 17264-9.
64. Childs, K., et al., *mda-5, but not RIG-I, is a common target for paramyxovirus V proteins.* Virology, 2007. **359**(1): p. 190-200.
65. Barral, P.M., et al., *RIG-I is cleaved during picornavirus infection.* Virology, 2009. **391**(2): p. 171-6.
66. Randall, R.E. and S. Goodbourn, *Interferons and viruses: an interplay between induction, signalling, antiviral responses and virus countermeasures.* J Gen Virol, 2008. **89**(Pt 1): p. 1-47.
67. Fortier, M.E., et al., *The viral mimic, polyinosinic:polycytidylic acid, induces fever in rats via an interleukin-1-dependent mechanism.* Am J Physiol Regul Integr Comp Physiol, 2004. **287**(4): p. R759-66.
68. Binder, M., et al., *Molecular mechanism of signal perception and integration by the innate immune sensor retinoic acid-inducible gene-I (RIG-I).* J Biol Chem, 2011. **286**(31): p. 27278-87.
69. Patel, J.R., et al., *ATPase-driven oligomerization of RIG-I on RNA allows optimal activation of type-I interferon.* EMBO Rep, 2013. **14**(9): p. 780-7.
70. Peisley, A., et al., *RIG-I forms signaling-competent filaments in an ATP-dependent, ubiquitin-independent manner.* Mol Cell, 2013. **51**(5): p. 573-83.

71. Hou, F., et al., *MAVS forms functional prion-like aggregates to activate and propagate antiviral innate immune response.* Cell, 2011. **146**(3): p. 448-61.
72. Wu, B. and S. Hur, *How RIG-I like receptors activate MAVS.* Curr Opin Virol, 2015. **12**: p. 91-8.
73. Zerbe, C.M., D.J. Mouser, and J.L. Cole, *Oligomerization of RIG-I and MDA5 2CARD domains.* Protein Sci, 2020. **29**(2): p. 521-526.
74. Liu, S., et al., *MAVS recruits multiple ubiquitin E3 ligases to activate antiviral signaling cascades.* Elife, 2013. **2**: p. e00785.
75. Paz, S., et al., *A functional C-terminal TRAF3-binding site in MAVS participates in positive and negative regulation of the IFN antiviral response.* Cell Res, 2011. **21**(6): p. 895-910.
76. Paz, S., et al., *Induction of IRF-3 and IRF-7 phosphorylation following activation of the RIG-I pathway.* Cell Mol Biol (Noisy-le-grand), 2006. **52**(1): p. 17-28.
77. Kumar, H., et al., *Essential role of IPS-1 in innate immune responses against RNA viruses.* J Exp Med, 2006. **203**(7): p. 1795-803.
78. Meylan, E., et al., *Cardif is an adaptor protein in the RIG-I antiviral pathway and is targeted by hepatitis C virus.* Nature, 2005. **437**(7062): p. 1167-72.
79. Loo, Y.M. and M. Gale, Jr., *Immune signaling by RIG-I-like receptors.* Immunity, 2011. **34**(5): p. 680-92.
80. Michalska, A., et al., *A Positive Feedback Amplifier Circuit That Regulates Interferon (IFN)-Stimulated Gene Expression and Controls Type I and Type II IFN Responses.* Front Immunol, 2018. **9**: p. 1135.
81. Thomas, E. and T. Saito, *Special Issue "IFN-Independent ISG Expression and its Role in Antiviral Cell-Intrinsic Innate Immunity".* Viruses, 2019. **11**(11).
82. Ashley, C.L., et al., *Interferon-Independent Innate Responses to Cytomegalovirus.* Front Immunol, 2019. **10**: p. 2751.
83. Ashley, C.L., et al., *Interferon-Independent Upregulation of Interferon-Stimulated Genes during Human Cytomegalovirus Infection is Dependent on IRF3 Expression.* Viruses, 2019. **11**(3).
84. Grandvaux, N., et al., *Transcriptional profiling of interferon regulatory factor 3 target genes: direct involvement in the regulation of interferon-stimulated genes.* J Virol, 2002. **76**(11): p. 5532-9.
85. Liu, T., et al., *NF-kappaB signaling in inflammation.* Signal Transduct Target Ther, 2017. **2**.
86. Iwanaszko, M. and M. Kimmel, *NF-kappaB and IRF pathways: cross-regulation on target genes promoter level.* BMC Genomics, 2015. **16**: p. 307.
87. Ren, Z., et al., *Regulation of MAVS Expression and Signaling Function in the Antiviral Innate Immune Response.* Front Immunol, 2020. **11**: p. 1030.
88. Gack, M.U., et al., *Phosphorylation-mediated negative regulation of RIG-I antiviral activity.* J Virol, 2010. **84**(7): p. 3220-9.
89. Maharaj, N.P., et al., *Conventional protein kinase C-alpha (PKC-alpha) and PKC-beta negatively regulate RIG-I antiviral signal transduction.* J Virol, 2012. **86**(3): p. 1358-71.
90. Nistal-Villan, E., et al., *Negative role of RIG-I serine 8 phosphorylation in the regulation of interferon-beta production.* J Biol Chem, 2010. **285**(26): p. 20252-61.
91. Wies, E., et al., *Dephosphorylation of the RNA sensors RIG-I and MDA5 by the phosphatase PP1 is essential for innate immune signaling.* Immunity, 2013. **38**(3): p. 437-49.
92. Sun, Z., et al., *Phosphorylation of RIG-I by casein kinase II inhibits its antiviral response.* J Virol, 2011. **85**(2): p. 1036-47.
93. Takashima, K., et al., *RIOK3-mediated phosphorylation of MDA5 interferes with its assembly and attenuates the innate immune response.* Cell Rep, 2015. **11**(2): p. 192-200.
94. Choi, S.J., et al., *HDAC6 regulates cellular viral RNA sensing by deacetylation of RIG-I.* EMBO J, 2016. **35**(4): p. 429-42.

95. Oshiumi, H., et al., *Riplet/RNF135, a RING finger protein, ubiquitinates RIG-I to promote interferon-beta induction during the early phase of viral infection.* J Biol Chem, 2009. **284**(2): p. 807-17.
96. Gao, D., et al., *REUL is a novel E3 ubiquitin ligase and stimulator of retinoic-acid-inducible gene-I.* PLoS One, 2009. **4**(6): p. e5760.
97. Gack, M.U., et al., *TRIM25 RING-finger E3 ubiquitin ligase is essential for RIG-I-mediated antiviral activity.* Nature, 2007. **446**(7138): p. 916-920.
98. Brisse, M. and H. Ly, *Comparative Structure and Function Analysis of the RIG-I-Like Receptors: RIG-I and MDA5.* Front Immunol, 2019. **10**: p. 1586.
99. Hu, M.M., et al., *Innate immunity to RNA virus is regulated by temporal and reversible sumoylation of RIG-I and MDA5.* J Exp Med, 2017. **214**(4): p. 973-989.
100. Kim, M.J., et al., *Negative feedback regulation of RIG-I-mediated antiviral signaling by interferon-induced ISG15 conjugation.* J Virol, 2008. **82**(3): p. 1474-83.
101. Du, Y., et al., *LRRC25 inhibits type I IFN signaling by targeting ISG15-associated RIG-I for autophagic degradation.* EMBO J, 2018. **37**(3): p. 351-366.
102. Nguyen, N.T., et al., *Ubiquitin-like modifier FAT10 attenuates RIG-I mediated antiviral signaling by segregating activated RIG-I from its signaling platform.* Sci Rep, 2016. **6**: p. 23377.
103. Lee, N.R., et al., *Activation of RIG-I-Mediated Antiviral Signaling Triggers Autophagy Through the MAVS-TRAF6-Beclin-1 Signaling Axis.* Front Immunol, 2018. **9**: p. 2096.
104. Shigemoto, T., et al., *Identification of loss of function mutations in human genes encoding RIG-I and MDA5: implications for resistance to type I diabetes.* J Biol Chem, 2009. **284**(20): p. 13348-54.
105. Nejentsev, S., et al., *Rare variants of IFIH1, a gene implicated in antiviral responses, protect against type 1 diabetes.* Science, 2009. **324**(5925): p. 387-9.
106. Lamborn, I.T., et al., *Recurrent rhinovirus infections in a child with inherited MDA5 deficiency.* J Exp Med, 2017. **214**(7): p. 1949-1972.
107. Jang, M.A., et al., *Mutations in DDX58, which encodes RIG-I, cause atypical Singleton-Merten syndrome.* Am J Hum Genet, 2015. **96**(2): p. 266-74.
108. Miyasaka, M. and K. Takatsu, *Chronic Inflammation: Mechanisms and Regulation*. 2016, Springer.
109. Gorman, J.A., et al., *The A946T variant of the RNA sensor IFIH1 mediates an interferon program that limits viral infection but increases the risk for autoimmunity.* Nat Immunol, 2017. **18**(7): p. 744-752.
110. Liu, S., et al., *IFIH1 polymorphisms are significantly associated with type 1 diabetes and IFIH1 gene expression in peripheral blood mononuclear cells.* Hum Mol Genet, 2009. **18**(2): p. 358-65.
111. Cen, H., et al., *Association of IFIH1 rs1990760 polymorphism with susceptibility to autoimmune diseases: a meta-analysis.* Autoimmunity, 2013. **46**(7): p. 455-62.
112. Hoffmann, F.S., et al., *Polymorphisms in melanoma differentiation-associated gene 5 link protein function to clearance of hepatitis C virus.* Hepatology, 2015. **61**(2): p. 460-70.
113. Fumagalli, M., et al., *Population genetics of IFIH1: ancient population structure, local selection, and implications for susceptibility to type 1 diabetes.* Mol Biol Evol, 2010. **27**(11): p. 2555-66.
114. Vasseur, E., et al., *The selective footprints of viral pressures at the human RIG-I-like receptor family.* Hum Mol Genet, 2011. **20**(22): p. 4462-74.
115. National Center for Biotechnology Information. *Reference SNP (rs) Report: rs34016093*. 2021 August 13, 2021; Available from: https://www.ncbi.nlm.nih.gov/snp/rs34016093.
116. National Center for Biotechnology Information. *Reference SNP (rs) Report: rs2074158*. 2021 August 13, 2021; Available from: https://www.ncbi.nlm.nih.gov/snp/rs2074158.
117. National Center for Biotechnology Information. *Reference SNP (rs) Report: rs2074160*. 2021 August 13, 2021; Available from: https://www.ncbi.nlm.nih.gov/snp/rs2074160.

118. Rothenfusser, S., et al., *The RNA helicase Lgp2 inhibits TLR-independent sensing of viral replication by retinoic acid-inducible gene-I.* J Immunol, 2005. **175**(8): p. 5260-8.
119. Venkataraman, T., et al., *Loss of DExD/H box RNA helicase LGP2 manifests disparate antiviral responses.* J Immunol, 2007. **178**(10): p. 6444-55.
120. Satoh, T., et al., *LGP2 is a positive regulator of RIG-I- and MDA5-mediated antiviral responses.* Proc Natl Acad Sci U S A, 2010. **107**(4): p. 1512-7.
121. Saito, T., et al., *Regulation of innate antiviral defenses through a shared repressor domain in RIG-I and LGP2.* Proc Natl Acad Sci U S A, 2007. **104**(2): p. 582-7.
122. Komuro, A. and C.M. Horvath, *RNA- and virus-independent inhibition of antiviral signaling by RNA helicase LGP2.* J Virol, 2006. **80**(24): p. 12332-42.
123. Parisien, J.P., et al., *RNA sensor LGP2 inhibits TRAF ubiquitin ligase to negatively regulate innate immune signaling.* EMBO Rep, 2018.
124. Parisien, J.P., et al., *RNA sensor LGP2 inhibits TRAF ubiquitin ligase to negatively regulate innate immune signaling.* EMBO Rep, 2018. **19**(6).
125. Childs, K.S., R.E. Randall, and S. Goodbourn, *LGP2 plays a critical role in sensitizing mda-5 to activation by double-stranded RNA.* PLoS One, 2013. **8**(5): p. e64202.
126. Murali, A., et al., *Structure and function of LGP2, a DEX(D/H) helicase that regulates the innate immunity response.* J Biol Chem, 2008. **283**(23): p. 15825-33.
127. Bruns, A.M. and C.M. Horvath, *LGP2 synergy with MDA5 in RLR-mediated RNA recognition and antiviral signaling.* Cytokine, 2015. **74**(2): p. 198-206.
128. Rodriguez, K.R., A.M. Bruns, and C.M. Horvath, *MDA5 and LGP2: accomplices and antagonists of antiviral signal transduction.* J Virol, 2014. **88**(15): p. 8194-200.
129. Bruns, A.M. and C.M. Horvath, *Antiviral RNA recognition and assembly by RLR family innate immune sensors.* Cytokine Growth Factor Rev, 2014. **25**(5): p. 507-12.
130. Li, S., et al., *Mapping a dynamic innate immunity protein interaction network regulating type I interferon production.* Immunity, 2011. **35**(3): p. 426-40.
131. van der Veen, A.G., et al., *The RIG-I-like receptor LGP2 inhibits Dicer-dependent processing of long double-stranded RNA and blocks RNA interference in mammalian cells.* EMBO J, 2018. **37**(4).
132. Sanchez David, R.Y., et al., *LGP2 binds to PACT to regulate RIG-I- and MDA5-mediated antiviral responses.* Sci Signal, 2019. **12**(601).
133. Komuro, A., et al., *The TAR-RNA binding protein is required for immunoresponses triggered by Cardiovirus infection.* Biochem Biophys Res Commun, 2016. **480**(2): p. 187-193.
134. Miyamoto, M. and A. Komuro, *PACT is required for MDA5-mediated immunoresponses triggered by Cardiovirus infection via interaction with LGP2.* Biochem Biophys Res Commun, 2017.
135. Takahashi, T., et al., *LGP2 virus sensor regulates gene expression network mediated by TRBP-bound microRNAs.* Nucleic Acids Res, 2018. **46**(17): p. 9134-9147.
136. Takahashi, T., et al., *LGP2 virus sensor enhances apoptosis by upregulating apoptosis regulatory genes through TRBP-bound miRNAs during viral infection.* Nucleic Acids Res, 2020. **48**(3): p. 1494-1507.
137. Patel, R.C. and G.C. Sen, *PACT, a protein activator of the interferon-induced protein kinase, PKR.* EMBO J, 1998. **17**(15): p. 4379-90.
138. Daher, A., et al., *Two dimerization domains in the trans-activation response RNA-binding protein (TRBP) individually reverse the protein kinase R inhibition of HIV-1 long terminal repeat expression.* J Biol Chem, 2001. **276**(36): p. 33899-905.
139. Liu, Y., et al., *PUM1 is a biphasic negative regulator of innate immunity genes by suppressing LGP2.* Proc Natl Acad Sci U S A, 2017. **114**(33): p. E6902-E6911.
140. Suthar, M.S., et al., *The RIG-I-like receptor LGP2 controls CD8(+) T cell survival and fitness.* Immunity, 2012. **37**(2): p. 235-48.
141. Zheng, W., et al., *RIG-I-Like Receptor LGP2 Is Required for Tumor Control by Radiotherapy.* Cancer Res, 2020. **80**(24): p. 5633-5641.
142. Nagano, Y. and Y. Kojima, *[Immunizing property of vaccinia virus inactivated by ultraviolets rays].* C R Seances Soc Biol Fil, 1954. **148**(19-20): p. 1700-2.

143. Isaacs, A. and J. Lindenmann, *Virus interference. I. The interferon.* Proc R Soc Lond B Biol Sci, 1957. **147**(927): p. 258-67.
144. Tan, Y.H., *Chromosome 21 and the cell growth inhibitory effect of human interferon preparations.* Nature, 1976. **260**(5547): p. 141-3.
145. Meager, A., et al., *Involvement of a gene on chromosome 9 in human fibroblast interferon production.* Nature, 1979. **280**(5722): p. 493-5.
146. Tan, Y.H., J. Tischfield, and F.H. Ruddle, *The linkage of genes for the human interferon-induced antiviral protein and indophenol oxidase-B traits to chromosome G-21.* J Exp Med, 1973. **137**(2): p. 317-30.
147. Mesev, E.V., R.A. LeDesma, and A. Ploss, *Decoding type I and III interferon signalling during viral infection.* Nat Microbiol, 2019. **4**(6): p. 914-924.
148. LaFleur, D.W., et al., *Interferon-kappa, a novel type I interferon expressed in human keratinocytes.* J Biol Chem, 2001. **276**(43): p. 39765-71.
149. Egli, A., et al., *The impact of the interferon-lambda family on the innate and adaptive immune response to viral infections.* Emerg Microbes Infect, 2014. **3**(7): p. e51.
150. Kobayashi, M., et al., *Identification and purification of natural killer cell stimulatory factor (NKSF), a cytokine with multiple biologic effects on human lymphocytes.* J Exp Med, 1989. **170**(3): p. 827-45.
151. Schoenborn, J.R. and C.B. Wilson, *Regulation of interferon-gamma during innate and adaptive immune responses.* Adv Immunol, 2007. **96**: p. 41-101.
152. Leonard, W.J. and J.J. O'Shea, *Jaks and STATs: biological implications.* Annu Rev Immunol, 1998. **16**: p. 293-322.
153. Sadler, A.J. and B.R. Williams, *Interferon-inducible antiviral effectors.* Nat Rev Immunol, 2008. **8**(7): p. 559-68.
154. Lavoie, T.B., et al., *Binding and activity of all human alpha interferon subtypes.* Cytokine, 2011. **56**(2): p. 282-9.
155. Schreiber, G. and J. Piehler, *The molecular basis for functional plasticity in type I interferon signaling.* Trends Immunol, 2015. **36**(3): p. 139-49.
156. Lazear, H.M., J.W. Schoggins, and M.S. Diamond, *Shared and Distinct Functions of Type I and Type III Interferons.* Immunity, 2019. **50**(4): p. 907-923.
157. Pervolaraki, K., et al., *Differential induction of interferon stimulated genes between type I and type III interferons is independent of interferon receptor abundance.* PLoS Pathog, 2018. **14**(11): p. e1007420.
158. Horvath, C.M. and J.E. Darnell, *The state of the STATs: recent developments in the study of signal transduction to the nucleus.* Curr Opin Cell Biol, 1997. **9**(2): p. 233-9.
159. Platanitis, E., et al., *A molecular switch from STAT2-IRF9 to ISGF3 underlies interferon-induced gene transcription.* Nat Commun, 2019. **10**(1): p. 2921.
160. Wang, W., et al., *Unphosphorylated ISGF3 drives constitutive expression of interferon-stimulated genes to protect against viral infections.* Sci Signal, 2017. **10**(476).
161. Sato, M., et al., *Positive feedback regulation of type I IFN genes by the IFN-inducible transcription factor IRF-7.* FEBS Lett, 1998. **441**(1): p. 106-10.
162. Marie, I., J.E. Durbin, and D.E. Levy, *Differential viral induction of distinct interferon-alpha genes by positive feedback through interferon regulatory factor-7.* EMBO J, 1998. **17**(22): p. 6660-9.
163. Ning, S., J.S. Pagano, and G.N. Barber, *IRF7: activation, regulation, modification and function.* Genes Immun, 2011. **12**(6): p. 399-414.
164. Shuai, K., J. Liao, and M.M. Song, *Enhancement of antiproliferative activity of gamma interferon by the specific inhibition of tyrosine dephosphorylation of Stat1.* Mol Cell Biol, 1996. **16**(9): p. 4932-41.
165. Wang, D., et al., *Naturally occurring dominant negative variants of Stat5.* Mol Cell Biol, 1996. **16**(11): p. 6141-8.
166. Azam, M., et al., *Functionally distinct isoforms of STAT5 are generated by protein processing.* Immunity, 1997. **6**(6): p. 691-701.
167. Caldenhoven, E., et al., *STAT3beta, a splice variant of transcription factor STAT3, is a dominant negative regulator of transcription.* J Biol Chem, 1996. **271**(22): p. 13221-7.

168. Masuhara, M., et al., *Cloning and characterization of novel CIS family genes.* Biochem Biophys Res Commun, 1997. **239**(2): p. 439-46.
169. Suzuki, R., et al., *CIS3 and JAB have different regulatory roles in interleukin-6 mediated differentiation and STAT3 activation in M1 leukemia cells.* Oncogene, 1998. **17**(17): p. 2271-8.
170. Starr, R., et al., *A family of cytokine-inducible inhibitors of signalling.* Nature, 1997. **387**(6636): p. 917-21.
171. Endo, T.A., et al., *A new protein containing an SH2 domain that inhibits JAK kinases.* Nature, 1997. **387**(6636): p. 921-4.
172. Naka, T., et al., *Structure and function of a new STAT-induced STAT inhibitor.* Nature, 1997. **387**(6636): p. 924-9.
173. Liu, B., et al., *Inhibition of Stat1-mediated gene activation by PIAS1.* Proc Natl Acad Sci U S A, 1998. **95**(18): p. 10626-31.
174. Liu, B., et al., *A transcriptional corepressor of Stat1 with an essential LXXLL signature motif.* Proc Natl Acad Sci U S A, 2001. **98**(6): p. 3203-7.
175. Chung, C.D., et al., *Specific inhibition of Stat3 signal transduction by PIAS3.* Science, 1997. **278**(5344): p. 1803-5.
176. Schoggins, J.W., *Interferon-Stimulated Genes: What Do They All Do?* Annu Rev Virol, 2019. **6**(1): p. 567-584.
177. Schneider, W.M., M.D. Chevillotte, and C.M. Rice, *Interferon-stimulated genes: a complex web of host defenses.* Annu Rev Immunol, 2014. **32**: p. 513-45.
178. Pindel, A. and A. Sadler, *The role of protein kinase R in the interferon response.* J Interferon Cytokine Res, 2011. **31**(1): p. 59-70.
179. Garcia, M.A., E.F. Meurs, and M. Esteban, *The dsRNA protein kinase PKR: virus and cell control.* Biochimie, 2007. **89**(6-7): p. 799-811.
180. Lamers, M.M., B.G. van den Hoogen, and B.L. Haagmans, *ADAR1: "Editor-in-Chief" of Cytoplasmic Innate Immunity.* Front Immunol, 2019. **10**: p. 1763.
181. Choi, U.Y., et al., *Oligoadenylate synthase-like (OASL) proteins: dual functions and associations with diseases.* Exp Mol Med, 2015. **47**: p. e144.
182. Malathi, K., et al., *Small self-RNA generated by RNase L amplifies antiviral innate immunity.* Nature, 2007. **448**(7155): p. 816-9.
183. Liddicoat, B.J., et al., *RNA editing by ADAR1 prevents MDA5 sensing of endogenous dsRNA as nonself.* Science, 2015. **349**(6252): p. 1115-20.
184. Samuel, C.E., *Adenosine deaminases acting on RNA (ADARs) are both antiviral and proviral.* Virology, 2011. **411**(2): p. 180-93.
185. Sun, T., et al., *Decoupling expression and editing preferences of ADAR1 p150 and p110 isoforms.* Proc Natl Acad Sci U S A, 2021. **118**(12).
186. Verhelst, J., P. Hulpiau, and X. Saelens, *Mx proteins: antiviral gatekeepers that restrain the uninvited.* Microbiol Mol Biol Rev, 2013. **77**(4): p. 551-66.
187. Haller, O., et al., *Mx GTPases: dynamin-like antiviral machines of innate immunity.* Trends Microbiol, 2015. **23**(3): p. 154-63.
188. Helbig, K.J. and M.R. Beard, *The role of viperin in the innate antiviral response.* J Mol Biol, 2014. **426**(6): p. 1210-9.
189. Ghosh, S. and E.N.G. Marsh, *Viperin: An ancient radical SAM enzyme finds its place in modern cellular metabolism and innate immunity.* J Biol Chem, 2020. **295**(33): p. 11513-11528.
190. Gizzi, A.S., et al., *A naturally occurring antiviral ribonucleotide encoded by the human genome.* Nature, 2018. **558**(7711): p. 610-614.
191. Rivera-Serrano, E.E., et al., *Viperin Reveals Its True Function.* Annu Rev Virol, 2020. **7**(1): p. 421-446.
192. Pidugu, V.K., et al., *Emerging Functions of Human IFIT Proteins in Cancer.* Front Mol Biosci, 2019. **6**: p. 148.
193. Allan, R.K. and T. Ratajczak, *Versatile TPR domains accommodate different modes of target protein recognition and function.* Cell Stress Chaperones, 2011. **16**(4): p. 353-67.

194. Vladimer, G.I., M.W. Gorna, and G. Superti-Furga, *IFITs: Emerging Roles as Key Anti-Viral Proteins.* Front Immunol, 2014. **5**: p. 94.
195. Mears, H.V. and T.R. Sweeney, *Better together: the role of IFIT protein-protein interactions in the antiviral response.* J Gen Virol, 2018. **99**(11): p. 1463-1477.
196. Pichlmair, A., et al., *IFIT1 is an antiviral protein that recognizes 5'-triphosphate RNA.* Nat Immunol, 2011. **12**(7): p. 624-30.
197. Rizzetto, M., et al., *Immunofluorescence detection of new antigen-antibody system (delta/anti-delta) associated to hepatitis B virus in liver and in serum of HBsAg carriers.* Gut, 1977. **18**(12): p. 997-1003.
198. Kos, A., et al., *The hepatitis delta (delta) virus possesses a circular RNA.* Nature, 1986. **323**(6088): p. 558-60.
199. Taylor, J.M., *Hepatitis Delta Virus*, in *Encyclopedia of Virology (Third Edition)*, B.W.J. Mahy and M.H.V. Van Regenmortel, Editors. 2008, Academic Press: Oxford. p. 375-377.
200. Netter, H.J., et al., *Hepatitis Delta Virus (HDV) and Delta-Like Agents: Insights Into Their Origin.* Front Microbiol, 2021. **12**: p. 652962.
201. International Committee on Taxonomy of Viruses. *ICTV Taxonomy history: Deltavirus*. 2020 August 5, 2021; Available from: https://talk.ictvonline.org/taxonomy/p/taxonomy-history?taxnode_id=202005347.
202. Wille, M., et al., *A Divergent Hepatitis D-Like Agent in Birds.* Viruses, 2018. **10**(12).
203. Hetzel, U., et al., *Identification of a Novel Deltavirus in Boa Constrictors.* mBio, 2019. **10**(2).
204. Chang, W.S., et al., *Novel hepatitis D-like agents in vertebrates and invertebrates.* Virus Evol, 2019. **5**(2): p. vez021.
205. Rasche, A., et al., *Evolutionary biology of human hepatitis viruses.* J Hepatol, 2019. **70**(3): p. 501-520.
206. Le Gal, F., et al., *Genetic diversity and worldwide distribution of the deltavirus genus: A study of 2,152 clinical strains.* Hepatology, 2017. **66**(6): p. 1826-1841.
207. Wang, K.S., et al., *Structure, sequence and expression of the hepatitis delta (delta) viral genome.* Nature, 1986. **323**(6088): p. 508-14.
208. Abou-Jaoude, G., et al., *Myristoylation signal transfer from the large to the middle or the small HBV envelope protein leads to a loss of HDV particles infectivity.* Virology, 2007. **365**(1): p. 204-9.
209. Sharmeen, L., et al., *Antigenomic RNA of human hepatitis delta virus can undergo self-cleavage.* J Virol, 1988. **62**(8): p. 2674-9.
210. Wu, H.N., et al., *Human hepatitis delta virus RNA subfragments contain an autocleavage activity.* Proc Natl Acad Sci U S A, 1989. **86**(6): p. 1831-5.
211. Sharmeen, L., M.Y. Kuo, and J. Taylor, *Self-ligating RNA sequences on the antigenome of human hepatitis delta virus.* J Virol, 1989. **63**(3): p. 1428-30.
212. Ferre-D'Amare, A.R., K. Zhou, and J.A. Doudna, *Crystal structure of a hepatitis delta virus ribozyme.* Nature, 1998. **395**(6702): p. 567-74.
213. Webb, C.H. and A. Luptak, *HDV-like self-cleaving ribozymes.* RNA Biol, 2011. **8**(5): p. 719-27.
214. Casey, J.L., *Control of ADAR1 editing of hepatitis delta virus RNAs.* Curr Top Microbiol Immunol, 2012. **353**: p. 123-43.
215. Zhang, Z. and S. Urban, *Interplay between Hepatitis D Virus and the Interferon Response.* Viruses, 2020. **12**(11).
216. Taylor, J.M., *Infection by Hepatitis Delta Virus.* Viruses, 2020. **12**(6).
217. Yan, H., et al., *Sodium taurocholate cotransporting polypeptide is a functional receptor for human hepatitis B and D virus.* Elife, 2012. **1**: p. e00049.
218. Zhang, Z. and S. Urban, *New insights into HDV persistence: The role of interferon response and implications for upcoming novel therapies.* J Hepatol, 2020.
219. Alves, C., N. Freitas, and C. Cunha, *Characterization of the nuclear localization signal of the hepatitis delta virus antigen.* Virology, 2008. **370**(1): p. 12-21.
220. Chou, H.C., et al., *Hepatitis delta antigen mediates the nuclear import of hepatitis delta virus RNA.* J Virol, 1998. **72**(5): p. 3684-90.

221. Fu, T.B. and J. Taylor, *The RNAs of hepatitis delta virus are copied by RNA polymerase II in nuclear homogenates.* J Virol, 1993. **67**(12): p. 6965-72.
222. Chang, J., et al., *Transcription of hepatitis delta virus RNA by RNA polymerase II.* J Virol, 2008. **82**(3): p. 1118-27.
223. Kuo, M.Y., M. Chao, and J. Taylor, *Initiation of replication of the human hepatitis delta virus genome from cloned DNA: role of delta antigen.* J Virol, 1989. **63**(5): p. 1945-50.
224. Casey, J.L. and J.L. Gerin, *Hepatitis D virus RNA editing: specific modification of adenosine in the antigenomic RNA.* J Virol, 1995. **69**(12): p. 7593-600.
225. Wong, S.K. and D.W. Lazinski, *Replicating hepatitis delta virus RNA is edited in the nucleus by the small form of ADAR1.* Proc Natl Acad Sci U S A, 2002. **99**(23): p. 15118-23.
226. Chao, M., S.Y. Hsieh, and J. Taylor, *Role of two forms of hepatitis delta virus antigen: evidence for a mechanism of self-limiting genome replication.* J Virol, 1990. **64**(10): p. 5066-9.
227. Chang, F.L., et al., *The large form of hepatitis delta antigen is crucial for assembly of hepatitis delta virus.* Proc Natl Acad Sci U S A, 1991. **88**(19): p. 8490-4.
228. Modahl, L.E. and M.M. Lai, *The large delta antigen of hepatitis delta virus potently inhibits genomic but not antigenomic RNA synthesis: a mechanism enabling initiation of viral replication.* J Virol, 2000. **74**(16): p. 7375-80.
229. Glenn, J.S., et al., *Identification of a prenylation site in delta virus large antigen.* Science, 1992. **256**(5061): p. 1331-3.
230. Tavanez, J.P., et al., *Hepatitis delta virus ribonucleoproteins shuttle between the nucleus and the cytoplasm.* RNA, 2002. **8**(5): p. 637-46.
231. Lee, C.H., et al., *A novel chromosome region maintenance 1-independent nuclear export signal of the large form of hepatitis delta antigen that is required for the viral assembly.* J Biol Chem, 2001. **276**(11): p. 8142-8.
232. Wang, Y.H., et al., *Novel nuclear export signal-interacting protein, NESI, critical for the assembly of hepatitis delta virus.* J Virol, 2005. **79**(13): p. 8113-20.
233. Macnaughton, T.B. and M.M. Lai, *Genomic but not antigenomic hepatitis delta virus RNA is preferentially exported from the nucleus immediately after synthesis and processing.* J Virol, 2002. **76**(8): p. 3928-35.
234. Giersch, K., et al., *Persistent hepatitis D virus mono-infection in humanized mice is efficiently converted by hepatitis B virus to a productive co-infection.* J Hepatol, 2014. **60**(3): p. 538-44.
235. Zhang, Z., Y. Ni, and S. Urban, *SAT-202-Endogenous and exogenous IFN responses suppress HDV persistence during proliferation of hepatocytes in vitro.* Journal of Hepatology, 2019. **70**(1, Supplement): p. e718-e719.
236. Mutz, P., et al., *HBV Bypasses the Innate Immune Response and Does Not Protect HCV From Antiviral Activity of Interferon.* Gastroenterology, 2018. **154**(6): p. 1791-1804 e22.
237. Suarez-Amaran, L., et al., *A new HDV mouse model identifies mitochondrial antiviral signaling protein (MAVS) as a key player in IFN-beta induction.* J Hepatol, 2017. **67**(4): p. 669-679.
238. George, C.X., M.V. Wagner, and C.E. Samuel, *Expression of interferon-inducible RNA adenosine deaminase ADAR1 during pathogen infection and mouse embryo development involves tissue-selective promoter utilization and alternative splicing.* J Biol Chem, 2005. **280**(15): p. 15020-8.
239. Jayan, G.C. and J.L. Casey, *Inhibition of hepatitis delta virus RNA editing by short inhibitory RNA-mediated knockdown of ADAR1 but not ADAR2 expression.* J Virol, 2002. **76**(23): p. 12399-404.
240. Pugnale, P., et al., *Hepatitis delta virus inhibits alpha interferon signaling.* Hepatology, 2009. **49**(2): p. 398-406.
241. Hartwig, D., et al., *Interferon-alpha stimulation of liver cells enhances hepatitis delta virus RNA editing in early infection.* J Hepatol, 2004. **41**(4): p. 667-72.
242. World Health Organization. *Fact sheets: Hepatitis B*. 2021 August 19, 2021; Available from: https://www.who.int/news-room/fact-sheets/detail/hepatitis-b.

243. Palom, A., et al., *Long-term clinical outcomes in patients with chronic hepatitis delta: the role of persistent viraemia.* Aliment Pharmacol Ther, 2020. **51**(1): p. 158-166.
244. Miao, Z., et al., *Estimating the Global Prevalence, Disease Progression, and Clinical Outcome of Hepatitis Delta Virus Infection.* J Infect Dis, 2020. **221**(10): p. 1677-1687.
245. Yurdaydin, C., et al., *Natural history and treatment of chronic delta hepatitis.* J Viral Hepat, 2010. **17**(11): p. 749-56.
246. Da, B.L., T. Heller, and C. Koh, *Hepatitis D infection: from initial discovery to current investigational therapies.* Gastroenterol Rep (Oxf), 2019. **7**(4): p. 231-245.
247. World Health Organization. *Fact sheet: Hepatitis D*. 2021 August 10, 2021; Available from: https://www.who.int/news-room/fact-sheets/detail/hepatitis-d.
248. Turon-Lagot, V., et al., *Targeting the Host for New Therapeutic Perspectives in Hepatitis D.* J Clin Med, 2020. **9**(1).
249. Chen, H.Y., et al., *Prevalence and burden of hepatitis D virus infection in the global population: a systematic review and meta-analysis.* Gut, 2019. **68**(3): p. 512-521.
250. Abbas, Z., et al., *Treatment of chronic hepatitis D patients with pegylated interferon: a real-world experience.* Antivir Ther, 2014. **19**(5): p. 463-8.
251. Terrault, N.A., et al., *Update on prevention, diagnosis, and treatment of chronic hepatitis B: AASLD 2018 hepatitis B guidance.* Hepatology, 2018. **67**(4): p. 1560-1599.
252. Heidrich, B., et al., *Late HDV RNA relapse after peginterferon alpha-based therapy of chronic hepatitis delta.* Hepatology, 2014. **60**(1): p. 87-97.
253. Muir, A.J., et al., *A randomized phase 2b study of peginterferon lambda-1a for the treatment of chronic HCV infection.* J Hepatol, 2014. **61**(6): p. 1238-46.
254. Bogomolov, P., et al., *Treatment of chronic hepatitis D with the entry inhibitor myrcludex B: First results of a phase Ib/IIa study.* J Hepatol, 2016. **65**(3): p. 490-8.
255. European Medicines Agency. *EU/3/15/1500*. 2021 August 26, 2021; Available from: https://www.ema.europa.eu/en/medicines/human/orphan-designations/eu3151500.
256. Koh, C., et al., *Oral prenylation inhibition with lonafarnib in chronic hepatitis D infection: a proof-of-concept randomised, double-blind, placebo-controlled phase 2A trial.* Lancet Infect Dis, 2015. **15**(10): p. 1167-1174.
257. Lai, M.M. and D. Cavanagh, *The molecular biology of coronaviruses.* Adv Virus Res, 1997. **48**: p. 1-100.
258. Graham, R.L. and R.S. Baric, *Recombination, reservoirs, and the modular spike: mechanisms of coronavirus cross-species transmission.* J Virol, 2010. **84**(7): p. 3134-46.
259. Chen, B., et al., *Overview of lethal human coronaviruses.* Signal Transduct Target Ther, 2020. **5**(1): p. 89.
260. Cui, J., F. Li, and Z.L. Shi, *Origin and evolution of pathogenic coronaviruses.* Nat Rev Microbiol, 2019. **17**(3): p. 181-192.
261. Poletti, P., et al., *Probability of symptoms and critical disease after SARS-CoV-2 infection*. 2020, arXiv.
262. Oran, D.P. and E.J. Topol, *Prevalence of Asymptomatic SARS-CoV-2 Infection : A Narrative Review.* Ann Intern Med, 2020. **173**(5): p. 362-367.
263. Lui, D.T.W., et al., *Long COVID in Patients with Mild to Moderate Disease: Do Thyroid Function and Autoimmunity Play a Role?* Endocr Pract, 2021.
264. Barek, M.A., M.A. Aziz, and M.S. Islam, *Impact of age, sex, comorbidities and clinical symptoms on the severity of COVID-19 cases: A meta-analysis with 55 studies and 10014 cases.* Heliyon, 2020. **6**(12): p. e05684.
265. Felgenhauer, U., et al., *Inhibition of SARS-CoV-2 by type I and type III interferons.* J Biol Chem, 2020. **295**(41): p. 13958-13964.
266. Lokugamage, K.G., et al., *Type I Interferon Susceptibility Distinguishes SARS-CoV-2 from SARS-CoV.* J Virol, 2020. **94**(23).
267. Mantlo, E., et al., *Antiviral activities of type I interferons to SARS-CoV-2 infection.* Antiviral Res, 2020. **179**: p. 104811.
268. Zhang, Q., et al., *Inborn errors of type I IFN immunity in patients with life-threatening COVID-19.* Science, 2020. **370**(6515).

269. Bastard, P., et al., *Autoantibodies against type I IFNs in patients with life-threatening COVID-19.* Science, 2020. **370**(6515).
270. Kindler, E., V. Thiel, and F. Weber, *Interaction of SARS and MERS Coronaviruses with the Antiviral Interferon Response.* Adv Virus Res, 2016. **96**: p. 219-243.
271. Yang, D., et al., *Differential roles of RIG-I-like receptors in SARS-CoV-2 infection.* bioRxiv, 2021.
272. Thorne, L.G., et al., *SARS-CoV-2 sensing by RIG-I and MDA5 links epithelial infection to macrophage inflammation.* bioRxiv, 2020: p. 2020.12.23.424169.
273. Yamada, T., et al., *RIG-I triggers a signaling-abortive anti-SARS-CoV-2 defense in human lung cells.* Nat Immunol, 2021. **22**(7): p. 820-828.
274. Wu, J., et al., *SARS-CoV-2 ORF9b inhibits RIG-I-MAVS antiviral signaling by interrupting K63-linked ubiquitination of NEMO.* Cell Rep, 2021. **34**(7): p. 108761.
275. Moustaqil, M., et al., *SARS-CoV-2 proteases PLpro and 3CLpro cleave IRF3 and critical modulators of inflammatory pathways (NLRP12 and TAB1): implications for disease presentation across species.* Emerg Microbes Infect, 2021. **10**(1): p. 178-195.
276. Chen, K., et al., *SARS-CoV-2 Nucleocapsid Protein Interacts with RIG-I and Represses RIG-Mediated IFN-beta Production.* Viruses, 2020. **13**(1).
277. Kumar, A., et al., *SARS-CoV-2 Nonstructural Protein 1 Inhibits the Interferon Response by Causing Depletion of Key Host Signaling Factors.* J Virol, 2021. **95**(13): p. e0026621.
278. Sui, L., et al., *SARS-CoV-2 Membrane Protein Inhibits Type I Interferon Production Through Ubiquitin-Mediated Degradation of TBK1.* Front Immunol, 2021. **12**: p. 662989.
279. Yuen, C.K., et al., *SARS-CoV-2 nsp13, nsp14, nsp15 and orf6 function as potent interferon antagonists.* Emerg Microbes Infect, 2020. **9**(1): p. 1418-1428.
280. Ahmed-Hassan, H., et al., *Innate Immune Responses to Highly Pathogenic Coronaviruses and Other Significant Respiratory Viral Infections.* Front Immunol, 2020. **11**: p. 1979.
281. Teijaro, J.R. and D.L. Farber, *COVID-19 vaccines: modes of immune activation and future challenges.* Nat Rev Immunol, 2021.
282. Agumadu, V.C. and K. Ramphul, *Zika Virus: A Review of Literature.* Cureus, 2018. **10**(7): p. e3025.
283. Althaus, C.L. and N. Low, *How Relevant Is Sexual Transmission of Zika Virus?* PLoS Med, 2016. **13**(10): p. e1002157.
284. Besnard, M., et al., *Evidence of perinatal transmission of Zika virus, French Polynesia, December 2013 and February 2014.* Euro Surveill, 2014. **19**(13).
285. Barjas-Castro, M.L., et al., *Probable transfusion-transmitted Zika virus in Brazil.* Transfusion, 2016. **56**(7): p. 1684-8.
286. Dick, G.W., *Epidemiological notes on some viruses isolated in Uganda; Yellow fever, Rift Valley fever, Bwamba fever, West Nile, Mengo, Semliki forest, Bunyamwera, Ntaya, Uganda S and Zika viruses.* Trans R Soc Trop Med Hyg, 1953. **47**(1): p. 13-48.
287. Dick, G.W., S.F. Kitchen, and A.J. Haddow, *Zika virus. I. Isolations and serological specificity.* Trans R Soc Trop Med Hyg, 1952. **46**(5): p. 509-20.
288. Dowall, S.D., et al., *Lineage-dependent differences in the disease progression of Zika virus infection in type-I interferon receptor knockout (A129) mice.* PLoS Negl Trop Dis, 2017. **11**(7): p. e0005704.
289. Duffy, M.R., et al., *Zika virus outbreak on Yap Island, Federated States of Micronesia.* N Engl J Med, 2009. **360**(24): p. 2536-43.
290. Cao-Lormeau, V.M., et al., *Zika virus, French polynesia, South pacific, 2013.* Emerg Infect Dis, 2014. **20**(6): p. 1085-6.
291. Musso, D., E.J. Nilles, and V.M. Cao-Lormeau, *Rapid spread of emerging Zika virus in the Pacific area.* Clin Microbiol Infect, 2014. **20**(10): p. O595-6.
292. Zorrilla, C.D., et al., *Zika Virus Infection in Pregnancy: Maternal, Fetal, and Neonatal Considerations.* J Infect Dis, 2017. **216**(suppl_10): p. S891-S896.
293. Simonin, Y., et al., *Differential virulence between Asian and African lineages of Zika virus.* PLoS Negl Trop Dis, 2017. **11**(9): p. e0005821.

294. Wu, Y., et al., *Zika virus evades interferon-mediated antiviral response through the co-operation of multiple nonstructural proteins in vitro.* Cell Discov, 2017. **3**: p. 17006.
295. Estevez-Herrera, J., et al., *Zika Virus Pathogenesis: A Battle for Immune Evasion.* Vaccines (Basel), 2021. **9**(3).
296. Serman, T.M. and M.U. Gack, *Evasion of Innate and Intrinsic Antiviral Pathways by the Zika Virus.* Viruses, 2019. **11**(10).
297. Lee, J.Y., T.T.N. Nguyen, and J. Myoung, *Zika Virus-Encoded NS2A and NS4A Strongly Downregulate NF-kappaB Promoter Activity.* J Microbiol Biotechnol, 2020. **30**(11): p. 1651-1658.
298. Ngueyen, T.T.N., et al., *Zika Virus Proteins NS2A and NS4A Are Major Antagonists that Reduce IFN-beta Promoter Activity Induced by the MDA5/RIG-I Signaling Pathway.* J Microbiol Biotechnol, 2019. **29**(10): p. 1665-1674.
299. Kumar, A., et al., *Zika virus inhibits type-I interferon production and downstream signaling.* EMBO Rep, 2016. **17**(12): p. 1766-1775.
300. Grant, A., et al., *Zika Virus Targets Human STAT2 to Inhibit Type I Interferon Signaling.* Cell Host Microbe, 2016. **19**(6): p. 882-90.
301. Bowen, J.R., et al., *Zika Virus Antagonizes Type I Interferon Responses during Infection of Human Dendritic Cells.* PLoS Pathog, 2017. **13**(2): p. e1006164.
302. Lazear, H.M., et al., *A Mouse Model of Zika Virus Pathogenesis.* Cell Host Microbe, 2016. **19**(5): p. 720-30.
303. Bayer, A., et al., *Type III Interferons Produced by Human Placental Trophoblasts Confer Protection against Zika Virus Infection.* Cell Host Microbe, 2016. **19**(5): p. 705-12.
304. Corry, J., et al., *Organotypic models of type III interferon-mediated protection from Zika virus infections at the maternal-fetal interface.* Proc Natl Acad Sci U S A, 2017. **114**(35): p. 9433-9438.
305. Caine, E.A., et al., *Interferon lambda protects the female reproductive tract against Zika virus infection.* Nat Commun, 2019. **10**(1): p. 280.
306. Reddacliff, L.A., et al., *Encephalomyocarditis virus infections in an Australian zoo.* J Zoo Wildl Med, 1997. **28**(2): p. 153-7.
307. Wells, S.K., et al., *Encephalomyocarditis Virus: Epizootic in a Zoological Collection.* Journal of Zoo and Wildlife Medicine, 1989. **20**(3): p. 291-296.
308. Canelli, E., et al., *Encephalomyocarditis virus infection in an Italian zoo.* Virol J, 2010. **7**: p. 64.
309. Carocci, M. and L. Bakkali-Kassimi, *The encephalomyocarditis virus.* Virulence, 2012. **3**(4): p. 351-67.
310. Oberste, M.S., et al., *Human febrile illness caused by encephalomyocarditis virus infection, Peru.* Emerg Infect Dis, 2009. **15**(4): p. 640-6.
311. Deddouche, S., et al., *Identification of an LGP2-associated MDA5 agonist in picornavirus-infected cells.* Elife, 2014. **3**: p. e01535.
312. Papon, L., et al., *The viral RNA recognition sensor RIG-I is degraded during encephalomyocarditis virus (EMCV) infection.* Virology, 2009. **393**(2): p. 311-8.
313. Hato, S.V., et al., *The mengovirus leader protein blocks interferon-alpha/beta gene transcription and inhibits activation of interferon regulatory factor 3.* Cell Microbiol, 2007. **9**(12): p. 2921-30.
314. Drexler, J.F., et al., *Bats host major mammalian paramyxoviruses.* Nat Commun, 2012. **3**: p. 796.
315. Plattet, P., et al., *Measles Virus Fusion Protein: Structure, Function and Inhibition.* Viruses, 2016. **8**(4): p. 112.
316. Thibault, P.A., et al., *Zoonotic Potential of Emerging Paramyxoviruses: Knowns and Unknowns.* Adv Virus Res, 2017. **98**: p. 1-55.
317. Eaton, B.T., et al., *Hendra and Nipah viruses: different and dangerous.* Nat Rev Microbiol, 2006. **4**(1): p. 23-35.
318. Halpin, K., et al., *Pteropid bats are confirmed as the reservoir hosts of henipaviruses: a comprehensive experimental study of virus transmission.* Am J Trop Med Hyg, 2011. **85**(5): p. 946-51.

319. UniProt. *Taxonomy - Respirovirus*. 2021 July 14, 2021].
320. Park, A., et al., *Sendai virus, an RNA virus with no risk of genomic integration, delivers CRISPR/Cas9 for efficient gene editing.* Mol Ther Methods Clin Dev, 2016. **3**: p. 16057.
321. Slobod, K.S., et al., *Safety and immunogenicity of intranasal murine parainfluenza virus type 1 (Sendai virus) in healthy human adults.* Vaccine, 2004. **22**(23-24): p. 3182-6.
322. Gotoh, B., et al., *Paramyxovirus accessory proteins as interferon antagonists.* Microbiol Immunol, 2001. **45**(12): p. 787-800.
323. Strahle, L., et al., *Activation of the beta interferon promoter by unnatural Sendai virus infection requires RIG-I and is inhibited by viral C proteins.* J Virol, 2007. **81**(22): p. 12227-37.
324. Young, D.F., et al., *Paramyxoviridae use distinct virus-specific mechanisms to circumvent the interferon response.* Virology, 2000. **269**(2): p. 383-90.
325. Lu, L.L., et al., *Select paramyxoviral V proteins inhibit IRF3 activation by acting as alternative substrates for inhibitor of kappaB kinase epsilon (IKKe)/TBK1.* J Biol Chem, 2008. **283**(21): p. 14269-76.
326. Didcock, L., et al., *The V protein of simian virus 5 inhibits interferon signalling by targeting STAT1 for proteasome-mediated degradation.* J Virol, 1999. **73**(12): p. 9928-33.
327. Parisien, J.P., et al., *The V protein of human parainfluenza virus 2 antagonizes type I interferon responses by destabilizing signal transducer and activator of transcription 2.* Virology, 2001. **283**(2): p. 230-9.
328. Goodbourn, S. and R.E. Randall, *The regulation of type I interferon production by paramyxoviruses.* J Interferon Cytokine Res, 2009. **29**(9): p. 539-47.
329. Lazzarini, R.A., J.D. Keene, and M. Schubert, *The origins of defective interfering particles of the negative-strand RNA viruses.* Cell, 1981. **26**(2 Pt 2): p. 145-54.
330. Baum, A., R. Sachidanandam, and A. Garcia-Sastre, *Preference of RIG-I for short viral RNA molecules in infected cells revealed by next-generation sequencing.* Proc Natl Acad Sci U S A, 2010. **107**(37): p. 16303-8.
331. Mura, M., et al., *Nonencapsidated 5' Copy-Back Defective Interfering Genomes Produced by Recombinant Measles Viruses Are Recognized by RIG-I and LGP2 but Not MDA5.* J Virol, 2017. **91**(20).
332. Yount, J.S., et al., *MDA5 participates in the detection of paramyxovirus infection and is essential for the early activation of dendritic cells in response to Sendai Virus defective interfering particles.* J Immunol, 2008. **180**(7): p. 4910-8.
333. Boshra, H., et al., *Rift valley fever: recent insights into pathogenesis and prevention.* J Virol, 2011. **85**(13): p. 6098-105.
334. Mansfield, K.L., et al., *Rift Valley fever virus: A review of diagnosis and vaccination, and implications for emergence in Europe.* Vaccine, 2015. **33**(42): p. 5520-5531.
335. Ikegami, T. and S. Makino, *The pathogenesis of Rift Valley fever.* Viruses, 2011. **3**(5): p. 493-519.
336. Wright, D., et al., *Rift Valley fever: biology and epidemiology.* J Gen Virol, 2019. **100**(8): p. 1187-1199.
337. Vialat, P., et al., *The S segment of rift valley fever phlebovirus (Bunyaviridae) carries determinants for attenuation and virulence in mice.* J Virol, 2000. **74**(3): p. 1538-43.
338. Bouloy, M., et al., *Genetic evidence for an interferon-antagonistic function of rift valley fever virus nonstructural protein NSs.* J Virol, 2001. **75**(3): p. 1371-7.
339. Habjan, M., et al., *NSs protein of rift valley fever virus induces the specific degradation of the double-stranded RNA-dependent protein kinase.* J Virol, 2009. **83**(9): p. 4365-75.
340. Ikegami, T., et al., *Rift Valley fever virus NSs protein promotes post-transcriptional downregulation of protein kinase PKR and inhibits eIF2alpha phosphorylation.* PLoS Pathog, 2009. **5**(2): p. e1000287.
341. Peck, D.E., et al., *Management Strategies for Reducing the Risk of Equines Contracting Vesicular Stomatitis Virus (VSV) in the Western United States.* J Equine Vet Sci, 2020. **90**: p. 103026.

342. Ludwig, A. and H. Hengel, *Vesicular Stomatitis Virus Infection*, in *Encyclopedia of Molecular Mechanisms of Disease*, F. Lang, Editor. 2009, Springer Berlin Heidelberg: Berlin, Heidelberg. p. 2204-2205.
343. Felt, S.A. and V.Z. Grdzelishvili, *Recent advances in vesicular stomatitis virus-based oncolytic virotherapy: a 5-year update.* J Gen Virol, 2017. **98**(12): p. 2895-2911.
344. Hastie, E., et al., *Understanding and altering cell tropism of vesicular stomatitis virus.* Virus Res, 2013. **176**(1-2): p. 16-32.
345. Cronin, J., X.Y. Zhang, and J. Reiser, *Altering the tropism of lentiviral vectors through pseudotyping.* Curr Gene Ther, 2005. **5**(4): p. 387-98.
346. Yoneyama, M., et al., *The RNA helicase RIG-I has an essential function in double-stranded RNA-induced innate antiviral responses.* Nat Immunol, 2004. **5**(7): p. 730-7.
347. Sommer, C., et al. *Ilastik: Interactive learning and segmentation toolkit*. in *2011 IEEE International Symposium on Biomedical Imaging: From Nano to Macro*. 2011.
348. Yang, W., et al., *G3BP1 inhibits RNA virus replication by positively regulating RIG-I-mediated cellular antiviral response.* Cell Death Dis, 2019. **10**(12): p. 946.
349. Dehairs, J., et al., *CRISP-ID: decoding CRISPR mediated indels by Sanger sequencing.* Sci Rep, 2016. **6**: p. 28973.
350. Binder, M. *TCID50_calculator_v2*. 2017 July 14, 2021; Available from: https://www.klinikum.uni-heidelberg.de/zentrum-fuer-infektiologie/molecular-virology/welcome/downloads.
351. Kuri, T., et al., *Species-independent bioassay for sensitive quantification of antiviral type I interferons.* Virol J, 2010. **7**: p. 50.
352. New England Biolabs. *Tm Calculator*. 2021 July 14, 2021; version 1.13.0; Available from: https://tmcalculator.neb.com/#!/main.
353. New England Biolabs. *NEBcloner*. 2021 July 14, 2021; version 1.6.0; Available from: http://nebcloner.neb.com/#!/redigest.
354. Heigwer, F., G. Kerr, and M. Boutros, *E-CRISP: fast CRISPR target site identification.* Nat Methods, 2014. **11**(2): p. 122-3.
355. Sanjana, N.E., O. Shalem, and F. Zhang, *Improved vectors and genome-wide libraries for CRISPR screening.* Nat Methods, 2014. **11**(8): p. 783-784.
356. Mali, P., K.M. Esvelt, and G.M. Church, *Cas9 as a versatile tool for engineering biology.* Nat Methods, 2013. **10**(10): p. 957-63.
357. Livak, K.J. and T.D. Schmittgen, *Analysis of relative gene expression data using real-time quantitative PCR and the 2(-Delta Delta C(T)) Method.* Methods, 2001. **25**(4): p. 402-8.
358. Yang, X., et al., *A public genome-scale lentiviral expression library of human ORFs.* Nat Methods, 2011. **8**(8): p. 659-61.
359. Lamas Longarela, O., et al., *Proteoglycans act as cellular hepatitis delta virus attachment receptors.* PLoS One, 2013. **8**(3): p. e58340.
360. Dias Junior, A.G., N.G. Sampaio, and J. Rehwinkel, *A Balancing Act: MDA5 in Antiviral Immunity and Autoinflammation.* Trends Microbiol, 2019. **27**(1): p. 75-85.
361. The Human Protein Atlas. *DHX58*. 2021 July 14, 2021; Available from: https://www.proteinatlas.org/ENSG00000108771-DHX58/cell.
362. Tascher, G., et al., *In-Depth Proteome Analysis Highlights HepaRG Cells as a Versatile Cell System Surrogate for Primary Human Hepatocytes.* Cells, 2019. **8**(2).
363. Yan, H., et al., *Sodium taurocholate cotransporting polypeptide is a functional receptor for human hepatitis B and D virus.* Elife, 2012. **3**.
364. Hoffmann, M., et al., *SARS-CoV-2 Cell Entry Depends on ACE2 and TMPRSS2 and Is Blocked by a Clinically Proven Protease Inhibitor.* Cell, 2020. **181**(2): p. 271-280 e8.
365. Murgolo, N., et al., *SARS-CoV-2 tropism, entry, replication, and propagation: Considerations for drug discovery and development.* PLoS Pathog, 2021. **17**(2): p. e1009225.
366. Koch, J., et al., *TMPRSS2 expression dictates the entry route used by SARS-CoV-2 to infect host cells.* EMBO J, 2021. **40**(16): p. e107821.
367. Neufeldt, C.J., et al., *SARS-CoV-2 infection induces a pro-inflammatory cytokine response through cGAS-STING and NF-κB.* bioRxiv, 2020: p. 2020.07.21.212639.

368. Blanco-Melo, D., et al., *Imbalanced Host Response to SARS-CoV-2 Drives Development of COVID-19.* Cell, 2020. **181**(5): p. 1036-1045 e9.
369. Wallach, D. and A. Kovalenko, *Phosphorylation and dephosphorylation of the RIG-I-like receptors: a safety latch on a fateful pathway.* Immunity, 2013. **38**(3): p. 402-3.
370. Fairman-Williams, M.E., U.P. Guenther, and E. Jankowsky, *SF1 and SF2 helicases: family matters.* Curr Opin Struct Biol, 2010. **20**(3): p. 313-24.
371. Pyle, A.M., *Translocation and unwinding mechanisms of RNA and DNA helicases.* Annu Rev Biophys, 2008. **37**: p. 317-36.
372. Takahasi, K., et al., *Nonself RNA-sensing mechanism of RIG-I helicase and activation of antiviral immune responses.* Mol Cell, 2008. **29**(4): p. 428-40.
373. Schmidt, A., S. Rothenfusser, and K.P. Hopfner, *Sensing of viral nucleic acids by RIG-I: from translocation to translation.* Eur J Cell Biol, 2012. **91**(1): p. 78-85.
374. Myong, S., et al., *Cytosolic viral sensor RIG-I is a 5'-triphosphate-dependent translocase on double-stranded RNA.* Science, 2009. **323**(5917): p. 1070-4.
375. Cadena, C. and S. Hur, *Filament-like Assemblies of Intracellular Nucleic Acid Sensors: Commonalities and Differences.* Mol Cell, 2019. **76**(2): p. 243-254.
376. Jankowsky, E., et al., *Active disruption of an RNA-protein interaction by a DExH/D RNA helicase.* Science, 2001. **291**(5501): p. 121-5.
377. Yao, H., et al., *ATP-dependent effector-like functions of RIG-I-like receptors.* Mol Cell, 2015. **58**(3): p. 541-548.
378. Maurano, M., et al., *Protein kinase R and the integrated stress response drive immunopathology caused by mutations in the RNA deaminase ADAR1.* Immunity, 2021.
379. Inn, K.S., et al., *Linear ubiquitin assembly complex negatively regulates RIG-I- and TRIM25-mediated type I interferon induction.* Mol Cell, 2011. **41**(3): p. 354-65.
380. Lee, N.R., et al., *Regulation of MDA5-MAVS Antiviral Signaling Axis by TRIM25 through TRAF6-Mediated NF-kappaB Activation.* Mol Cells, 2015. **38**(9): p. 759-64.
381. Martin-Vicente, M., et al., *TRIM25 in the Regulation of the Antiviral Innate Immunity.* Front Immunol, 2017. **8**: p. 1187.
382. Hayman, T.J., et al., *RIPLET, and not TRIM25, is required for endogenous RIG-I-dependent antiviral responses.* Immunol Cell Biol, 2019. **97**(9): p. 840-852.
383. Choudhury, N.R., G. Heikel, and G. Michlewski, *TRIM25 and its emerging RNA-binding roles in antiviral defense.* Wiley Interdiscip Rev RNA, 2020. **11**(4): p. e1588.
384. Errett, J.S., et al., *The essential, nonredundant roles of RIG-I and MDA5 in detecting and controlling West Nile virus infection.* J Virol, 2013. **87**(21): p. 11416-25.
385. Roulois, D., et al., *DNA-Demethylating Agents Target Colorectal Cancer Cells by Inducing Viral Mimicry by Endogenous Transcripts.* Cell, 2015. **162**(5): p. 961-73.
386. Wan, Q., et al., *MDA5 Induces a Stronger Interferon Response than RIG-I to GCRV Infection through a Mechanism Involving the Phosphorylation and Dimerization of IRF3 and IRF7 in CIK Cells.* Front Immunol, 2017. **8**: p. 189.
387. Chauhan, R.P., et al., *Systematic Review of Important Viral Diseases in Africa in Light of the 'One Health' Concept.* Pathogens, 2020. **9**(4).
388. Childs, K., R. Randall, and S. Goodbourn, *Paramyxovirus V proteins interact with the RNA Helicase LGP2 to inhibit RIG-I-dependent interferon induction.* J Virol, 2012. **86**(7): p. 3411-21.
389. Winer, B.Y., et al., *Analysis of Host Responses to Hepatitis B and Delta Viral Infections in a Micro-scalable Hepatic Co-culture System.* Hepatology, 2020. **71**(1): p. 14-30.
390. Roulot, D., et al., *Origin, HDV genotype and persistent viremia determine outcome and treatment response in patients with chronic hepatitis delta.* J Hepatol, 2020. **73**(5): p. 1046-1062.
391. Spaan, M., et al., *Hepatitis delta genotype 5 is associated with favourable disease outcome and better response to treatment compared to genotype 1.* J Hepatol, 2020. **72**(6): p. 1097-1104.
392. Anastassopoulou, C., et al., *Human genetic factors associated with susceptibility to SARS-CoV-2 infection and COVID-19 disease severity.* Hum Genomics, 2020. **14**(1): p. 40.

393. Acharya, D., G. Liu, and M.U. Gack, *Dysregulation of type I interferon responses in COVID-19.* Nat Rev Immunol, 2020. **20**(7): p. 397-398.
394. Dhochak, N., et al., *Pathophysiology of COVID-19: Why Children Fare Better than Adults?* Indian J Pediatr, 2020. **87**(7): p. 537-546.
395. Loske, J., et al., *Pre-activated antiviral innate immunity in the upper airways controls early SARS-CoV-2 infection in children.* Nat Biotechnol, 2021.
396. Eymieux, S., et al., *Ultrastructural modifications induced by SARS-CoV-2 in Vero cells: a kinetic analysis of viral factory formation, viral particle morphogenesis and virion release.* Cell Mol Life Sci, 2021. **78**(7): p. 3565-3576.
397. Kalungi, A., et al., *Less Severe Cases of COVID-19 in Sub-Saharan Africa: Could Co-infection or a Recent History of Plasmodium falciparum Infection Be Protective?* Front Immunol, 2021. **12**: p. 565625.
398. Cohen, P., *The origins of protein phosphorylation.* Nat Cell Biol, 2002. **4**(5): p. E127-30.
399. Ardito, F., et al., *The crucial role of protein phosphorylation in cell signaling and its use as targeted therapy (Review).* Int J Mol Med, 2017. **40**(2): p. 271-280.
400. Lienhard, G.E., *Non-functional phosphorylations?* Trends Biochem Sci, 2008. **33**(8): p. 351-2.
401. Dephoure, N., et al., *Mapping and analysis of phosphorylation sites: a quick guide for cell biologists.* Mol Biol Cell, 2013. **24**(5): p. 535-42.
402. Pause, A. and N. Sonenberg, *Mutational analysis of a DEAD box RNA helicase: the mammalian translation initiation factor eIF-4A.* EMBO J, 1992. **11**(7): p. 2643-54.

6 PRESENTATIONS

6.1 Poster presentations

1) SFB/Transregio 179: Determinants and dynamics of elimination versus persistence of hepatitis virus infection; Ettal (2017): Mode of action of RIG-I like receptor LGP2 in the innate immune system after viral infections. Nadine Gillich, Silke Bender, Antje Reuter, Pietro Scaturro, Andreas Pichlmair, Marco Binder and Ralf Bartenschlager.

2) 28th Annual Meeting of the Society for Virology; Würzburg (2018): Mode of action of the RIG-I like receptor LGP2 in the interferon response triggered by viral infections. Nadine Gillich, Silke Bender, Antje Reuter, Marco Binder and Ralf Bartenschlager.

3) 6th Annual Meeting of the International Cytokine & Interferon Society; Boston (2018): Mode of action of the RIG-I like receptor LGP2 in the interferon response triggered by viral infections. Nadine Gillich, Silke Jung, Antje Reuter, Pietro Scaturro, Andreas Pichlmair, Marco Binder, Ralf Bartenschlager.

4) 30th Annual Meeting of the Society for Virology; online (2021): LGP2 is essential for IFN response activation and viral repression during hepatitis D virus infection and the natural Q425R LGP2 variant depicts stronger antiviral activity. Nadine Gillich, Zhenfeng Zhang, Marco Binder, Stephan Urban and Ralf Bartenschlager.

6.2 Oral presentations

1) SFB/Transregio 179: Determinants and dynamics of elimination versus persistence of hepatitis virus infection, Student Retreat; Bad Herrenalb (2017): Elucidating the role of LGP2 in the RLR pathway and its regulation. Nadine Gillich, Silke Bender, Antje Reuter, Andreas Pichlmair, Marco Binder and Ralf Bartenschlager.

2) SFB/Transregio 179: Determinants and dynamics of elimination versus persistence of hepatitis virus infection, Student Retreat; Herrsching (2018): Mode of action of the RIG-I like receptor LGP2 in the interferon response triggered by viral infections. Nadine Gillich, Silke Bender, Antje Reuter, Pietro Scaturro, Andreas Pichlmair, Marco Binder and Ralf Bartenschlager.

3) SFB/Transregio 179: Determinants and dynamics of elimination versus persistence of hepatitis virus infection, Student Retreat; St. Peter (2019): Mode of action of the RIG-I like receptor LGP2 in the interferon response triggered by viral infections. Nadine Gillich, Silke Jung, Antje Reuter, Marco Binder and Ralf Bartenschlager.

4) 7th Annual Meeting of the International Cytokine & Interferon Society; Vienna (2019): Deciphering the mode of action of the RIG-I like receptor LGP2 in the interferon response triggered by viral infections. Nadine Gillich, Pietro Scaturro, Andreas Pichlmair, Marco Binder, Ralf Bartenschlager.

7 APPENDIX

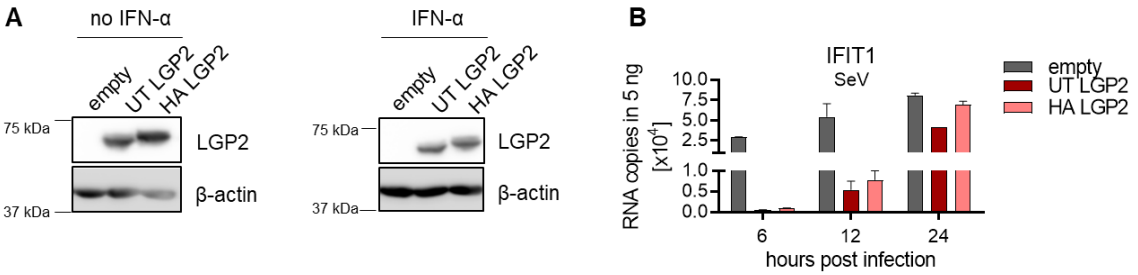

Figure S 1: Lower LGP2-mediated inhibition of RIG-I at later time points post-SeV infection in A549.

(A) N-terminally HA-tagged or untagged (UT) LGP2- or empty vector-expressing A549 cells were generated through lentiviral transduction. Western blot analysis was performed on untreated (left panel) or IFN-α treated (24 h, 500 IU/ml, right panel) cells staining for LGP2 and β-actin. **(B)** Cells from (A) were infected with Sendai virus (SeV) (MOI=5) for 6 h, 12 h or 24 h. After RNA isolation, absolute IFIT1 mRNA copies were measured by qRT-PCR. Mock cells did not reveal IFIT1 induction (data not shown). n=1 for 6 h and 24 h, n=3 for 12 h. These experiments were performed in parallel to Figure 7**.**

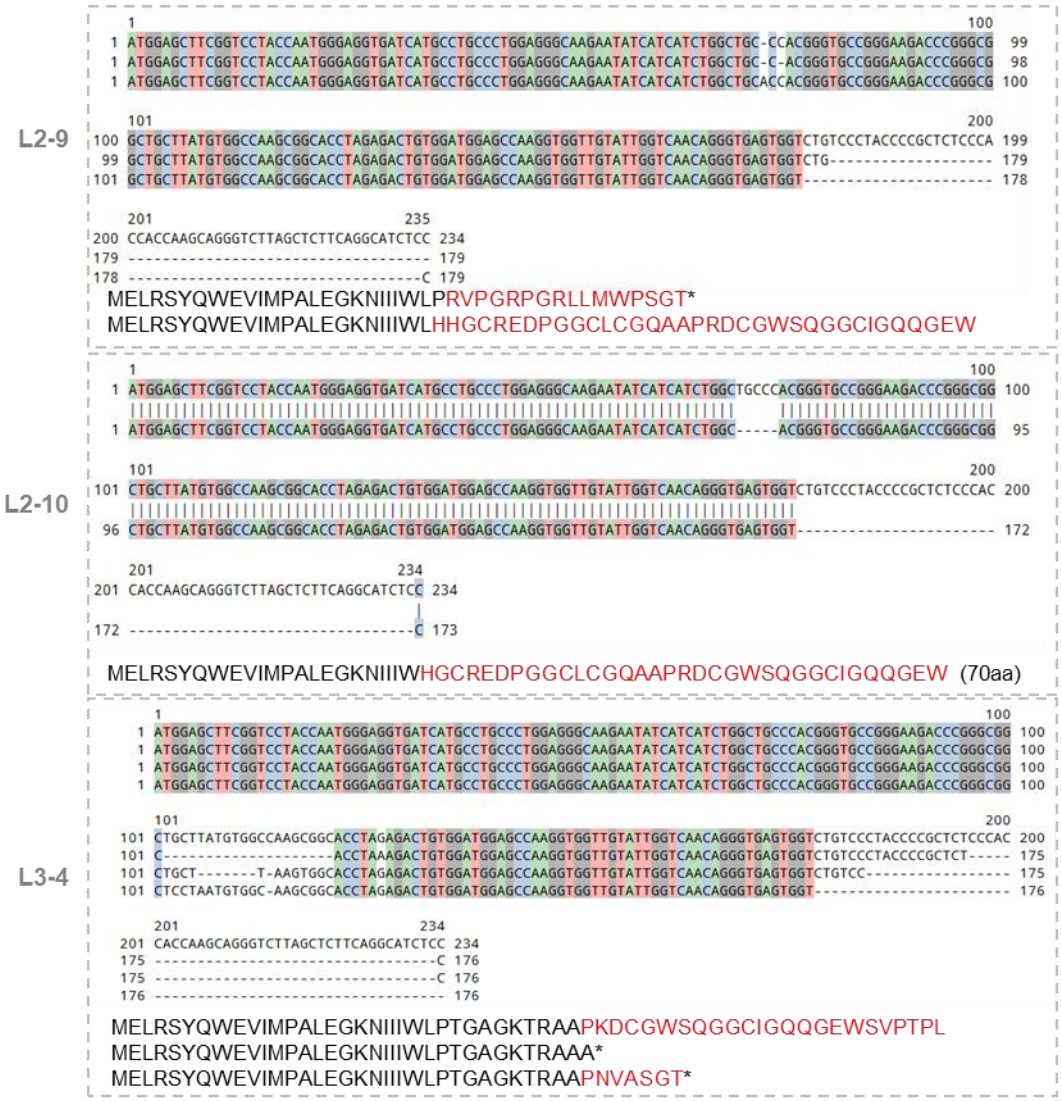

Figure S 2: Altered sequences of single LGP2^{KO} A549 clones.
Three validated A549 LGP2^{KO} clones were generated by single-cell expansion of transduced A549 with lentiviruses harboring one out of two different guide RNAs for LGP2 (named L2 for guide2 or L3 for guide3). As LGP2 was undetectable in Western blotting, clones were validated by Sanger sequencing of PCR products spanning the genomic LGP2 region targeted by the respective guide RNAs and Cas9. The resulting chromatograms were aligned to the WT LGP2 sequence. CRISP-ID [349] was used to predict the LGP2 protein sequence of all alleles in each clone. Amino acids depicted in red represent mismatches compared to WT; stars represent translational stop. Note that in none of the three LGP2^{KO} clones (L2#9, L2#10, L3#4) a WT allele was left.

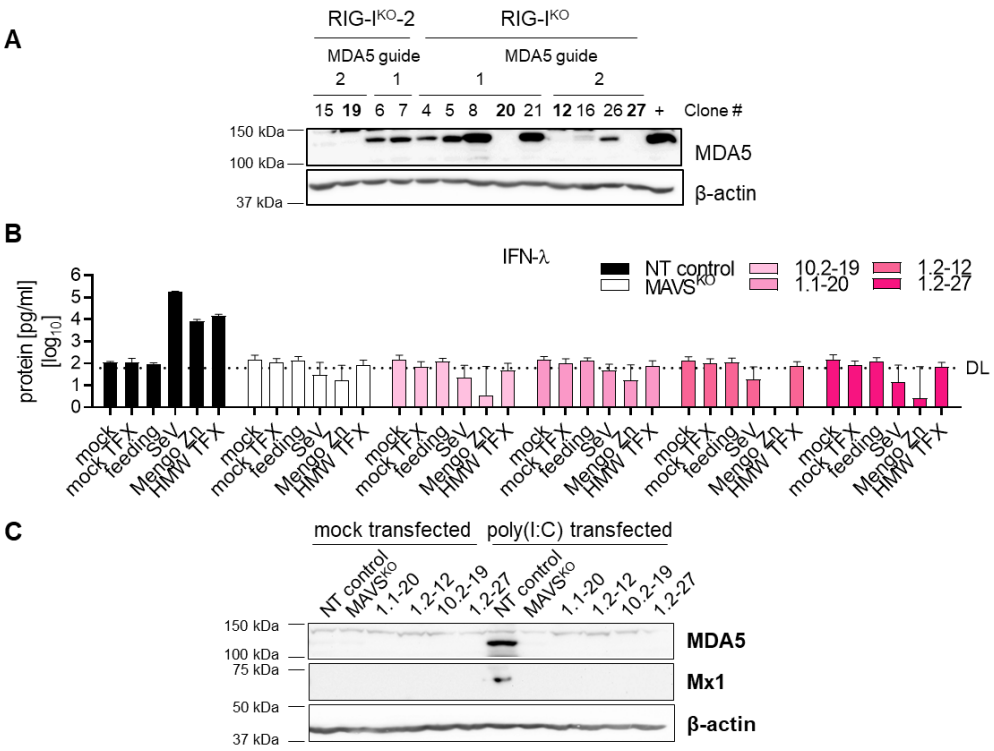

Figure S 3: Generation and functional analysis of RIG-I-MDA5 double KO A549 clones reveal behavior similar to MAVS^{KO}.

(A) Generation of RIG-I-MDA5 double KO A549. Two A549 RIG-I^{KO} clones (R2-2#1 and R2-2#10, designated RIG-I^{KO} and RIG-I^{KO}-2, respectively) were transduced with CRISPR Cas9 containing lentiviruses harboring one out of two different guide RNAs against MDA5. Single-cell clones were generated and tested for KO of MDA5. Cells were treated with 500 IU/ml of IFN-α for 24 h to induce MDA5. MDA5 and β-actin protein levels were determined by Western blot. Clone number indicates screened RIG-I-MDA5 double KO clones. Clones showing MDA5^{KO} are highlighted with bolt numbers. **(B)** A549 non-targeting guide-expressing cells (NT control), MAVS^{KO} clone (1.77) and verified RIG-I-MDA5 double KO clones from (A) (10.2-19, 1.1-20, 1.2-12, 1.2-27) were transfected with 100 ng HMW poly(I:C) or mock transfected for 36 h before harvesting for ELISA of IFN-λ. TFX: transfection. HMW: high molecular weight poly(I:C). n=1. **(C)** Mock transfected and HMW poly(I:C) transfected cells from (B) were additionally harvested for Western blotting 36 h post-stimulation to stain for MDA5, Mx1 and β-actin expression. Nomination of clones is based on the following: The first number indicates RIG-I KO clone (1 for R2-2#1 and 10 for 2-2#10), the second number indicates MDA5 guide RNA 1 or 2, last number indicates clone number of RIG-I-MDA5 double KO clone.

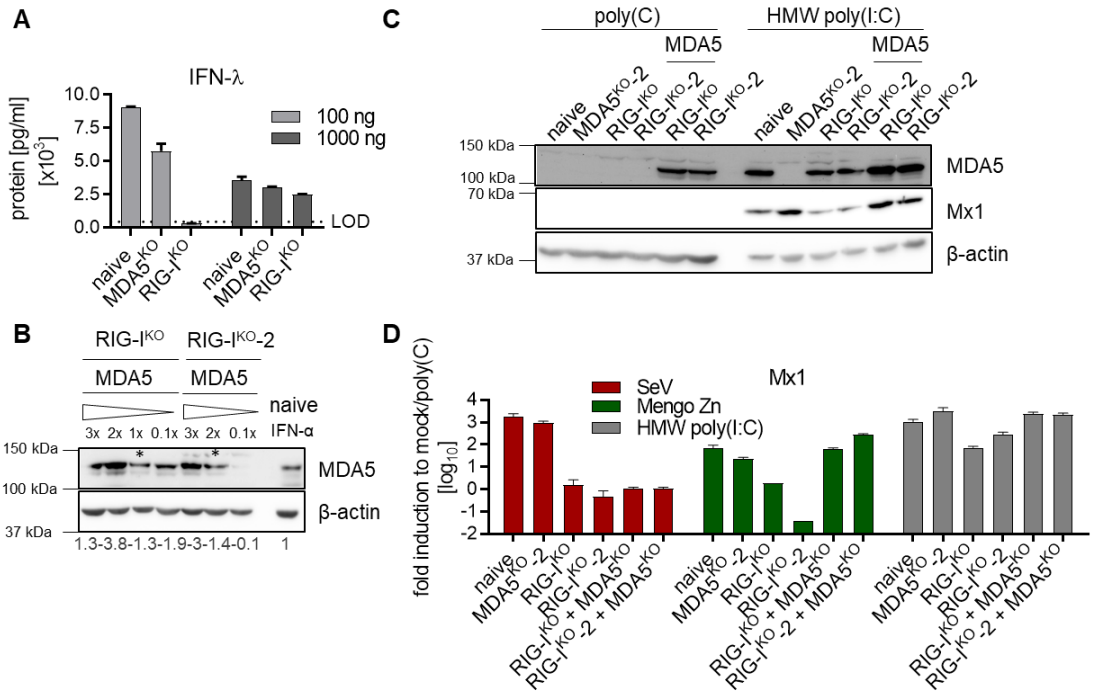

Figure S 4: Similar to LGP2, increased MDA5 or poly(I:C) amounts strengthen MDA5-dependent signaling in RIG-I^{KO} A549.

(A) MDA5^{KO} (clone M2-28) and RIG-I^{KO} (clone R2-2#1) A549 and naive A549 from Figure 9A were transfected with 100 ng and 1000 ng HMW poly(I:C) for 12 h before the performance of IFN-λ ELISA. n=1. No IFN-λ production in poly(C) transfected samples (data not shown). LOD: limit of detection. **(B)** Two RIG-I^{KO} clones (R2-2#1 and R2-2#10 designated as RIG-I^{KO} and RIG-I^{KO}-2) were stably transduced with different doses of lentiviruses (0.1-fold to 3-fold) containing MDA5 under ROSA26 promoter. Generated cell lines were stained for MDA5 and β-actin expression on Western blot. IFN-α treated A549 cells served as an MDA5 expression control. β-actin served as a loading control. Numbers below the blot indicate MDA5 levels normalized to β-actin and IFN-α treated naive cells. RIG-I^{KO} MDA5 1-fold and RIG-I^{KO}-2 MDA5 2-fold transduced cells reflect endogenously, IFN-α-induced MDA5 expression levels the most (marked with a star) and were used in (C-D). **(C)** Naive A549, MDA5^{KO}-2 (clone M1-8) and cells from (B) were transfected with 100 ng HMW poly(I:C) or poly(C) for 12 h before harvesting for Western blotting and staining of MDA5 and Mx1 protein levels. β-actin served as a loading control. n=1. **(D)** Cells from (C) were infected with SeV (MOI=5), Mengo Zn virus (MOI=5) or transfected with 100 ng HMW poly(I:C) for 12 h. Mock or poly(C) transfected cells served as unstimulated controls. Cells were lysed and RNA was isolated. Mx1 mRNA induction levels to respective unstimulated cells were measured by qRT-PCR and were normalized to GAPDH. n=1.

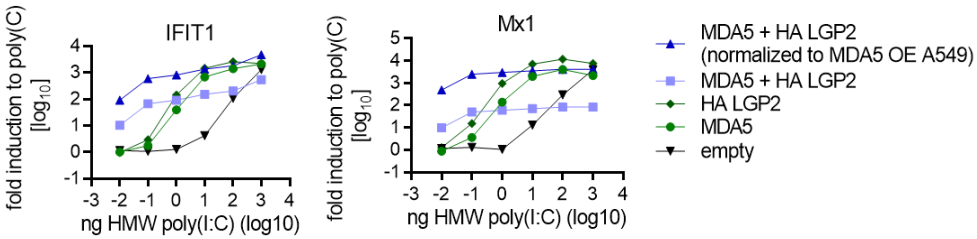

Figure S 5: Stronger initial MDA5 increases its sensitivity towards poly(I:C) in A549 cells.
RIG-I^{KO} (clone R2-2#1, MDA5 signaling) A549 stably expressing HA-tagged LGP2 and/or MDA5 under ROSA26 promoter were stimulated with different doses of HMW poly(I:C) for 12 h – analog to Figure 9. poly(C) transfection served as unstimulated control. Empty vector-expressing A549 RIG-I^{KO} served as control. qRT-PCR measurements of IFIT1 and Mx1 mRNA fold induction to respective poly(C) transfected cells and relative to GAPDH are shown. As exogenous co-expression of MDA5 and HA-LGP2 preactivated the cells, they were additionally normalized to mock transfected MDA5 overexpressing (OE) cells. n=1 (technical duplicates).

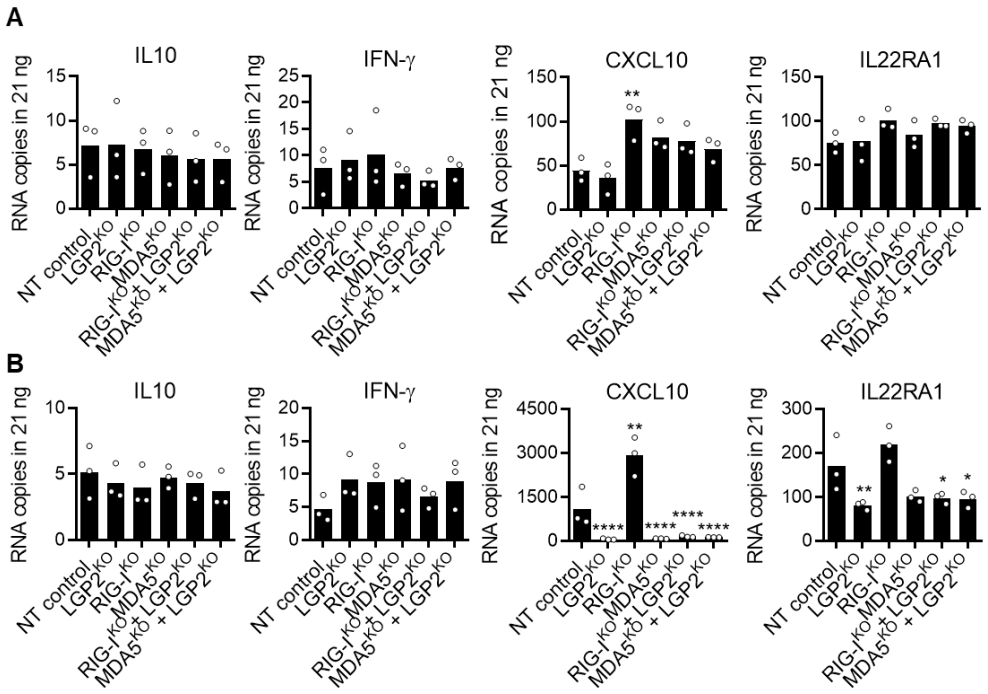

Figure S 6: IL10 and IFN-γ are not induced while IL22RA1 and CXCL10 are upregulated with MDA5/LGP2-dependence in HDV infected HepaRG^{NTCP} cells (suppl. to Figure 12).
(A-B) HepaRG^{NTCP} with stable KO of MDA5, RIG-I, LGP2, both LGP2 and RIG-I, both LGP2 and MDA5, or cells stably transduced with a non-targeting guide RNA containing lentiviral vector (NT control) were measured 3 d post (A) mock treatment and (B) HDV infection (samples similar to Figure 12). *, p ≤ 0.05; **, p ≤ 0.01; ****, p ≤ 0.0001 (comparison between NT control and KO HepaRG). n=3.

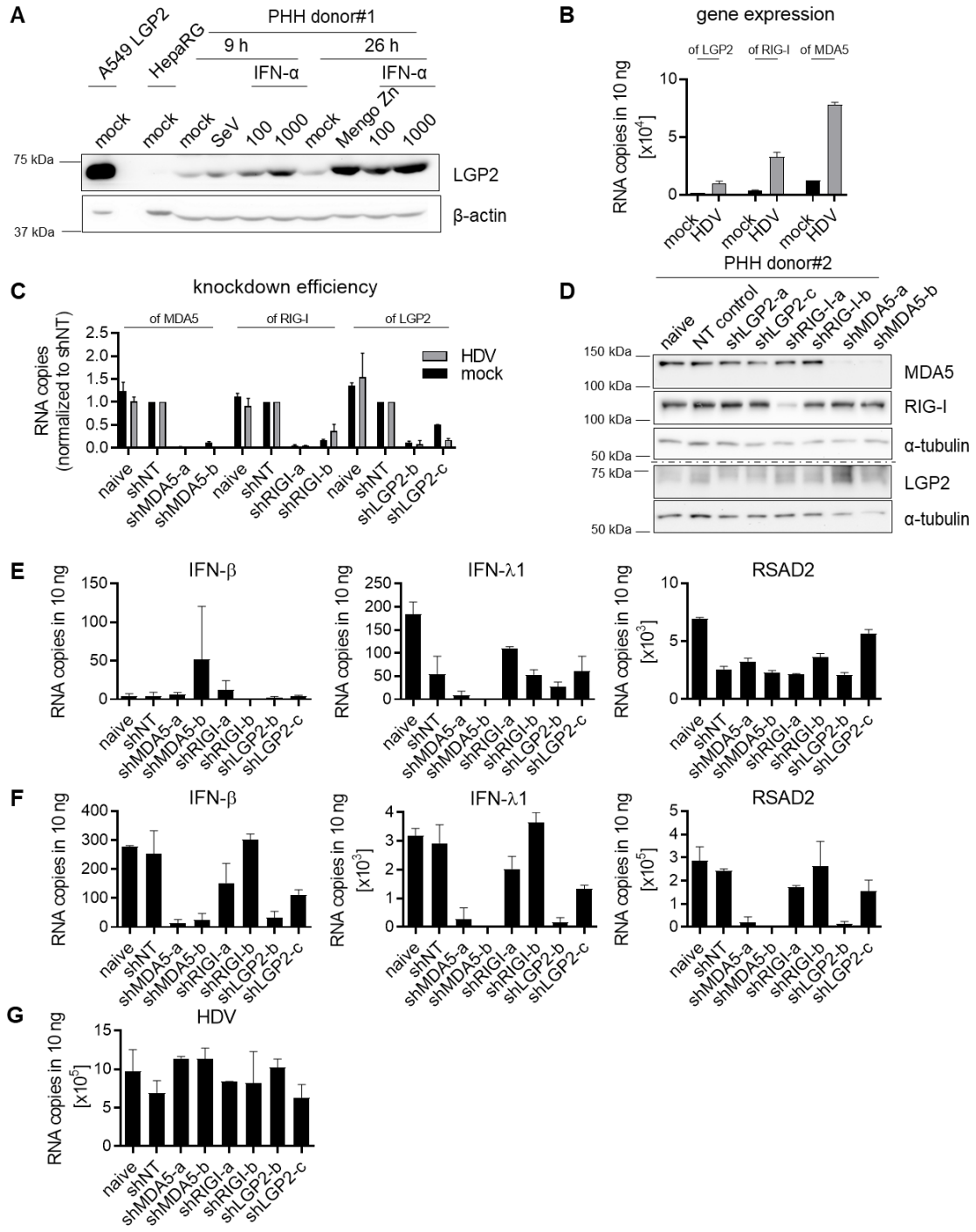

Figure S 7: MDA5 and LGP2 are the dominant RLRs sensing HDV in PHHs.
(A) PHHs (donor#1) (isolated by Dr. Pascal Mutz) were stimulated for either 9 h with 100 IU/ml or 1000 IU/ml IFN-α or SeV (MOI=5), or 26 h with 100 IU/ml or 1000 IU/ml IFN-α or Mengo Zn virus (MOI=5). Cells were lysed for Western blot analysis of LGP2 and β-actin. Mock treated PHHs (donor#1), HepaRG and A549 cells expressing exogenous LGP2 served as expression controls. **(B-G)** Cryopreserved PHHs (from BioIVT, donor#2) were thawed and reverse transduced with purified lentiviruses (MOI=40, titrated on HeLa cells) harboring a non-targeting shRNA control (shNT), an MDA5-specific shRNA (shMDA5-a and -b), a RIG-I-specific shRNA (shRIG-I-a and -b), an LGP2-specific shRNA (shLGP2-b and -c) or kept untransduced. 24 h later, cells were infected with HDV or kept uninfected before being harvested for RNA isolation 5 d pi. (B) Untransduced PHHs (donor#2) and (C) untransduced as well as lentivirus transduced PHHs (donor#2) upon HDV and mock treatment were measured for their RIG-I, MDA5 and LGP2 mRNA levels using qRT-PCR. RLR specification above each fraction of bars indicates RLR-specific primers used in qRT-PCR. (D) Western blot analysis of MDA5,

Figure S 7: legend continued.
RIG-I, LGP2 and α-tubulin of untransduced and lentivirus transduced PHHs (donor#2) upon 200 IU/ml of IFN-α treatment for 24 h. IFN-β, IFN-λ1 and RSAD2 mRNA levels in (E) mock and (F) HDV infected PHHs (donor#2) were measured by qRT-PCR, as (G) HDV copies in HDV infected cells. Error bar from two technical replicates. Data in panels (B), (C), (E) to (G) generated by Dr. Zhenfeng Zhang, research group Prof. Dr. Stephan Urban.

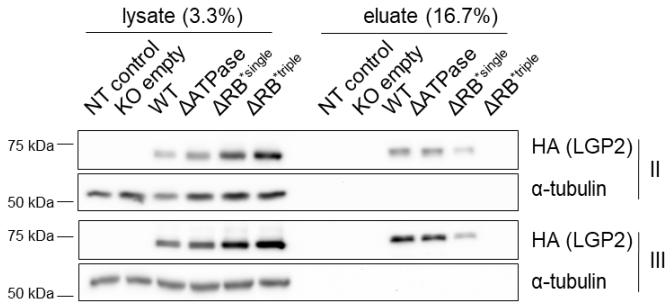

Figure S 8: Two replicates of HA immunoblots from the poly(I:C) IP of Figure 13C.
Two out of three representative HA immunoblots of cell lysates and eluates used for quantification in Figure 13D are shown. α-tubulin served as a loading control.

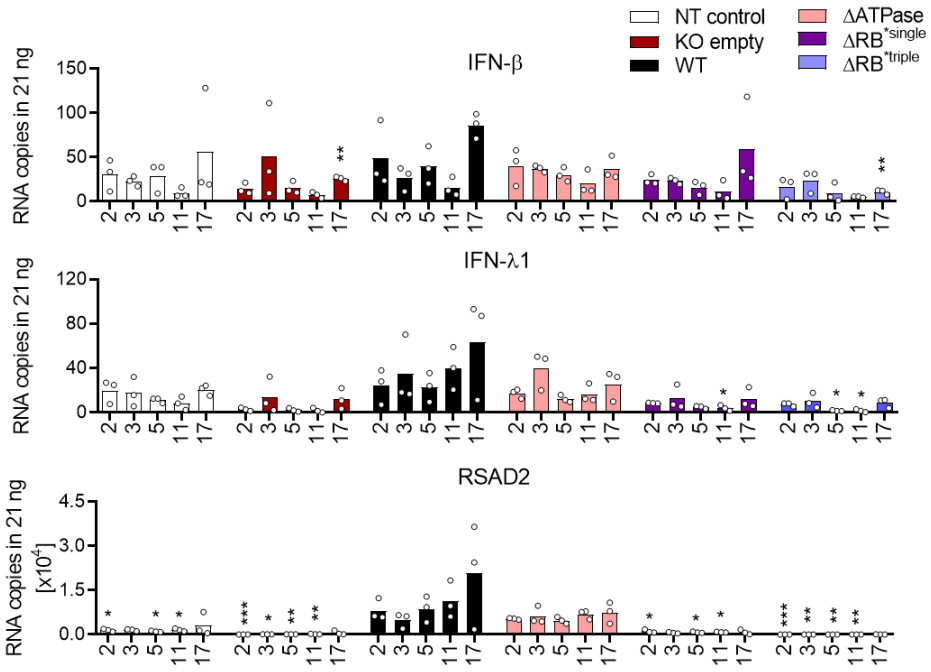

Figure S 9: Basal mRNA levels of IFN-β, IFN-λ1 and RSAD2 in HepaRG^{NTCP} cells (suppl. to Figure 14).
Cell lines shown in Figure 13B and the NT control HepaRG^{NTCP} cell line from Figure 13A were infected with HDV or mock treated for 2 d, 3 d, 5 d, 11 d and 17 d. The mRNA levels of IFN-λ1, IFN-β and RSAD2 post mock treatment were quantified by qRT-PCR (as part of Figure 14). RB=RNA binding. *, p ≤ 0.05; **, p ≤ 0.01; ***, p ≤ 0.001 (WT was compared to mutants of LGP2 or control cell lines at the depicted time points). n=3.

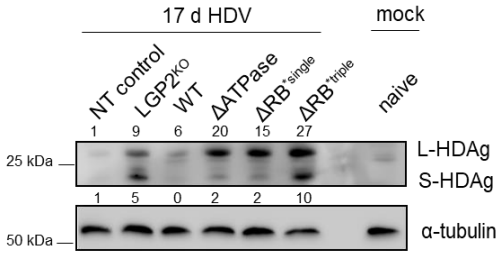

Figure S 10: Both ATPase and RNA binding functions of LGP2 are needed for HDV suppression in HepaRG^{NTCP} cells.

HepaRG^{NTCP} cells used in Figure 14 were immunoblotted 17 d post HDV infection with HDAg antibody and α-tubulin as a loading control. Numbers below and above the HDAg blot indicate L-HDAg and S-HDAg expression levels relative to NT control. n=1.

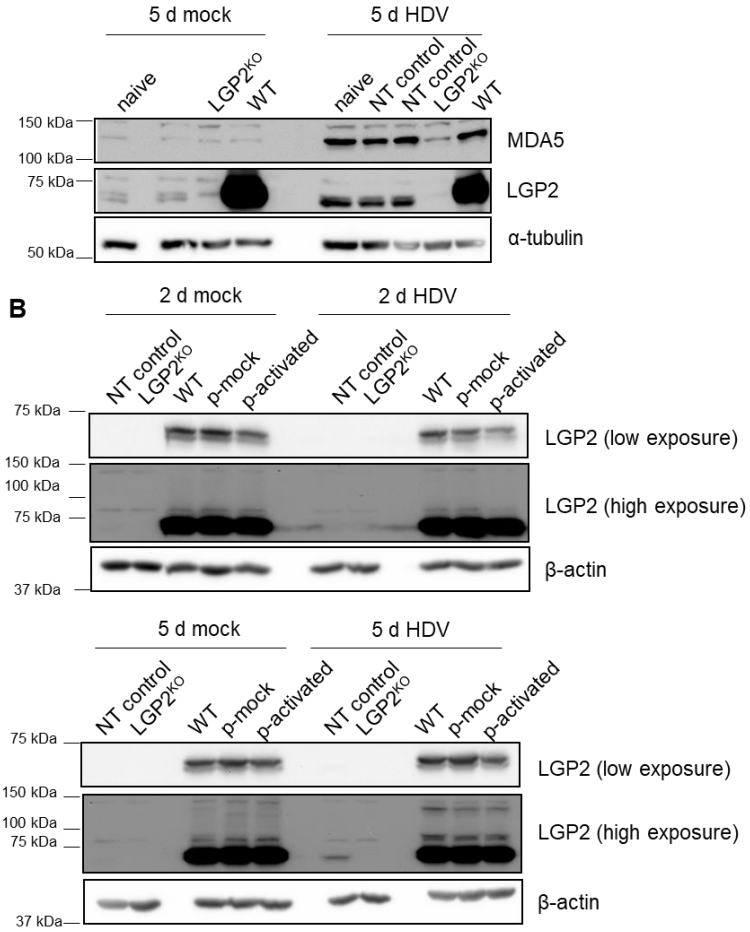

Figure S 11: Endogenous LGP2 and MDA5 protein levels are upregulated upon HDV infection in HepaRG^{NTCP} cells.

(A) Naïve HepaRG^{NTCP}, non-targeting guide (NT control) RNA-expressing cells, cells with a stable KO of LGP2 or reconstituted with N-terminally HA-tagged WT LGP2 were analyzed 5 d post mock treatment and HDV infection for their MDA5 and LGP2 protein expression by Western blotting. α-tubulin served as a loading control. n=1. **(B)** Equal to (A), however with additional reconstitution of N-terminally HA-tagged LGP2 phosphomutants mimicking its phosphorylated mock (LGP2 S365A+S464D=p-mock) and activated state (LGP2 S365D+S464A=p-activated), cells were infected with HDV for 2 d and 5 d or kept uninfected prior to Western blot analysis by using LGP2 and β-actin antibodies. n=1.

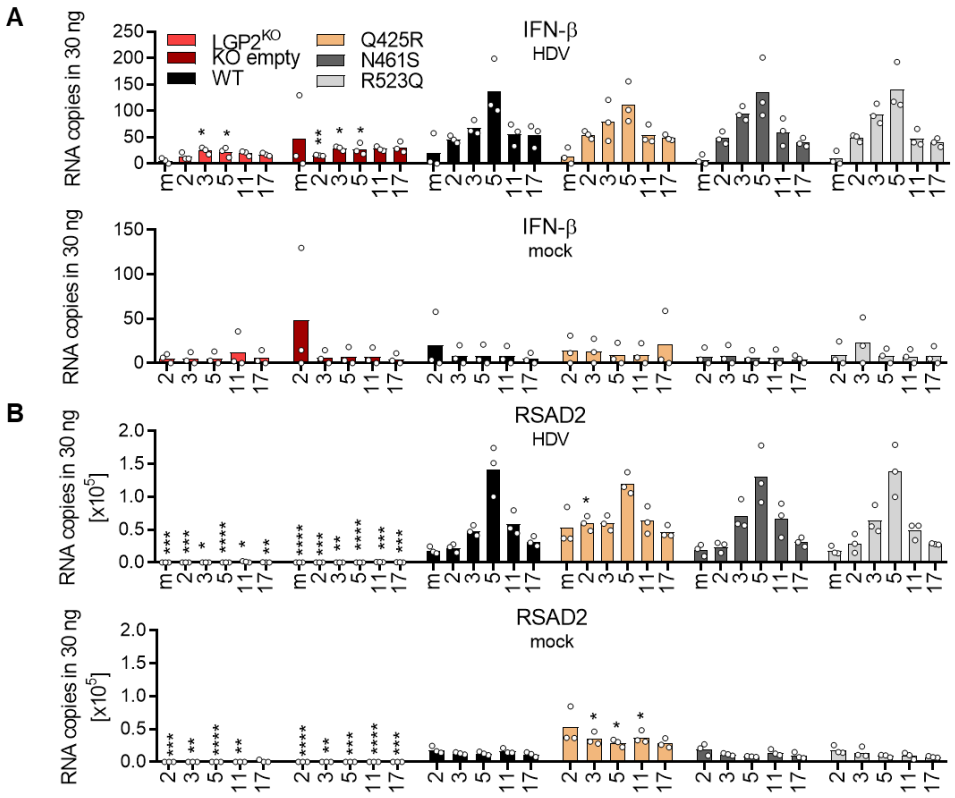

Figure S 12: IFN-β and RSAD2 mRNA levels in mock or HDV infected HepaRG^{NTCP} cells expressing LGP2 variants (suppl. to Figure 16).

Basal and HDV-induced mRNA levels of **(A)** IFN-β and **(B)** RSAD2 of HepaRG^{NTCP} cells from Figure 16 were measured 2 d, 3 d, 5 d, 11 d and 17 d pi. Cells consist of a stable knockout (KO) of LGP2 and were reconstituted with an HA-tagged WT LGP2, a natural variant of LGP2 (Q425R, N461S, R523Q). Non-reconstituted LGP2^{KO} HepaRG^{NTCP} (LGP2^{KO}) and LGP2^{KO} cells harboring an empty vector (KO empty) served as negative controls. “m” in post HDV infected cells depicts 2 d mock infected cells. Data was performed by Dr. Zhenfeng Zhang. *, p ≤ 0.05; **, p ≤ 0.01; ***, p ≤ 0.001; ****, p ≤ 0.0001 (WT compared to mutants of LGP2 or control cell lines at the depicted time points). n=3.

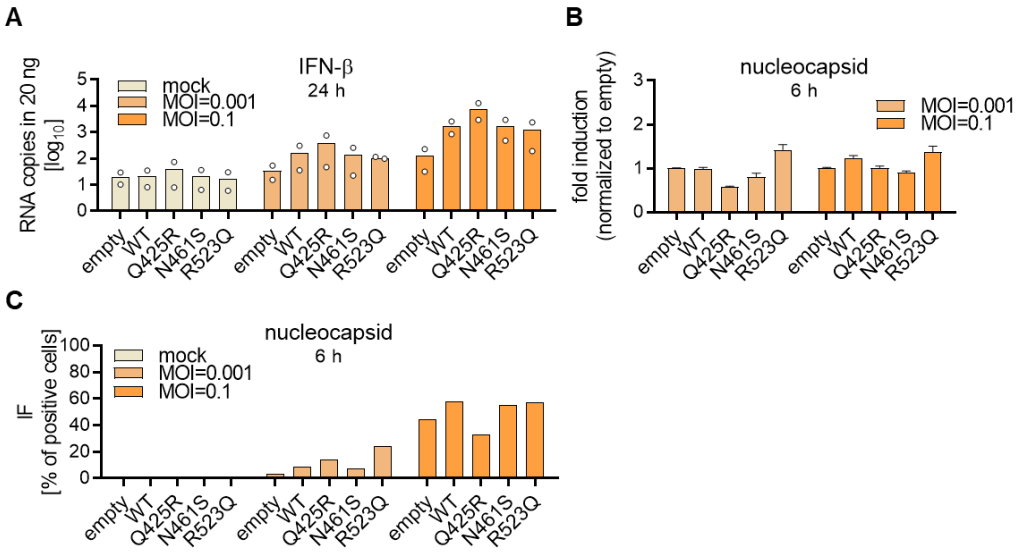

Figure S 13: IF and mRNA levels of SARS-CoV-2 nucleocapsid and IFN-β mRNA levels in mock or infected A549 cells expressing LGP2 variants (suppl. to Figure 18).

(A-C) Naïve A549 cells were stably transduced with lentiviruses encoding for an empty vector control (empty), N-terminally HA-tagged LGP2 WT or Q425R, N461S, or R523Q variants. These cells were transiently transduced with ACE2 and TMPRSS2 encoding lentiviruses. 24 h later, cells were kept uninfected (mock) or infected with SARS-CoV-2 (MOI=0.001 and MOI=0.1) for further 6 h or 24 h, prior to harvesting for RNA isolation and qRT-PCR or IF. (A) IFN-β mRNA levels of SARS-CoV-2 infected cells 24 h pi from Figure 18. n=2. (B) SARS-CoV-2 nucleocapsid mRNA of 6 infected cells from Figure 18A relative to GAPDH and normalized to empty infected cells. n=1. (C) SARS-CoV-2 nucleocapsid IF of 6 infected cells from Figure 18A. n=1. Lentivirus transduction, infection and harvesting were done by Dr. Vladimir Goncalves Magalhaes, research group Dr. Marco Binder. One out of two qRT-PCRs in (A) and IF in (C) were performed by Dr. Zhenfeng Zhang.

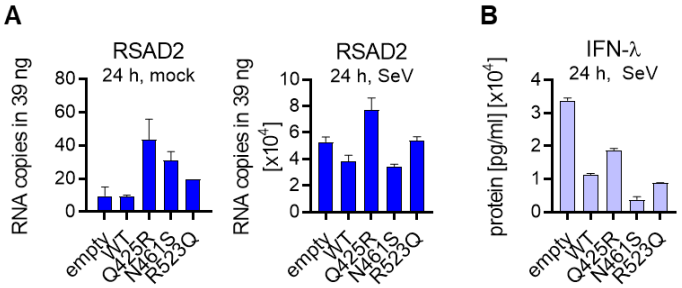

Figure S 14: RSAD2 mRNA and IFN-λ protein levels 24 h post-SeV infection in mock or infected A549 cells expressing LGP2 variants (supp. to Figure 19).

(A-B) 24 h time point of SeV infection of the experiment from Figure 19. Cells from Figure 18A were mock treated or infected with SeV (MOI=1) for 24 h prior to RNA isolation and qRT-PCR of (A) RSAD2 mRNA levels and (B) IFN-λ ELISA of cell supernatant. No IFN-λ secretion was detected in mock cells (data not shown). n=1.

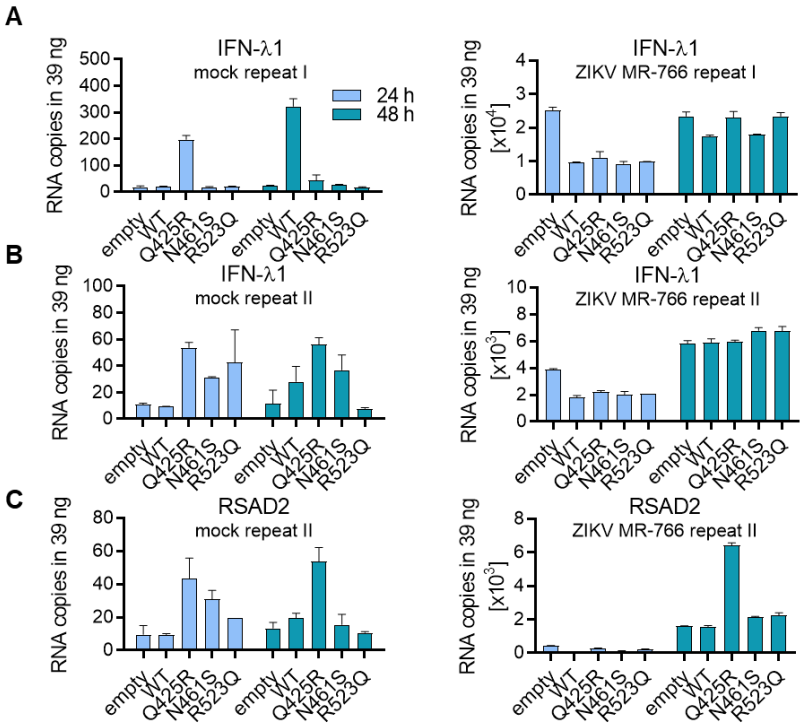

Figure S 15: IFN-λ1 and RSAD2 mRNA levels in mock or ZIKV MR-766 infected A549 cells expressing LGP2 variants (suppl. to Figure 20).

(A) Basal and ZIKV MR-766-induced RNA levels of IFN-λ1 of A549 cells from Figure 20A+B were measured. **(B-C)** Second repetition of the experiment from Figure 20. Cells from Figure 18A were infected with ZIKV strain MR-766 (MOI=0.5) or mock treated for 24 h and 48 h prior to harvesting for RNA isolation and qRT-PCR. (B) IFN-λ1 and (C) RSAD2 mRNA levels of mock (left-hand) and ZIKV MR-766 infected cells (right-hand) were measured.

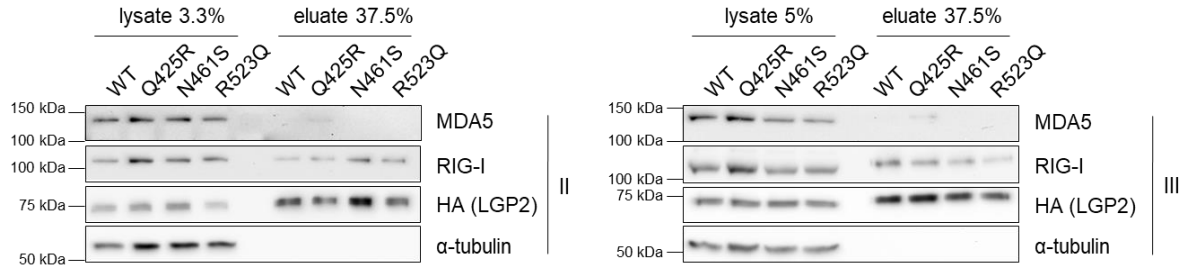

Figure S 16: Two replicates of HA, RIG-I and MDA5 immunoblots (suppl. to Figure 21A).

Two out of three HA, RIG-I and MDA5 immunoblots of cell lysates and eluates used for quantification in Figure 21B are shown.

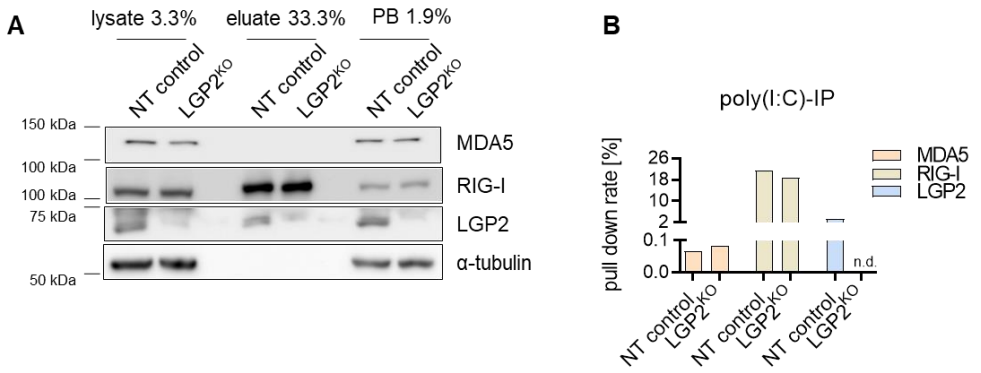

Figure S 17: MDA5 binding to poly(I:C) is weak.
(A-B) HepaRG^{NTCP} LGP2^{KO}- and NT guide RNA-expressing cells were stimulated overnight with 200 IU/ml of IFN-α before harvesting for poly(I:C)-IP. (A) The cell lysate was incubated for 3 h with poly(I:C) coupled beads, washed and eluted with Laemmli buffer before immunoblotting with MDA5-, RIG-I-, LGP2- and α-tubulin-specific antibodies. n=1. PB= post binding. (B) Quantification of the MDA5, RIG-I and LGP2 immunoblots is shown. Protein levels in the eluates were normalized to those in respective lysates designating the pulldown rate. No quantification was performed for LGP2 in LGP2^{KO} cells. n.d.=not determined.

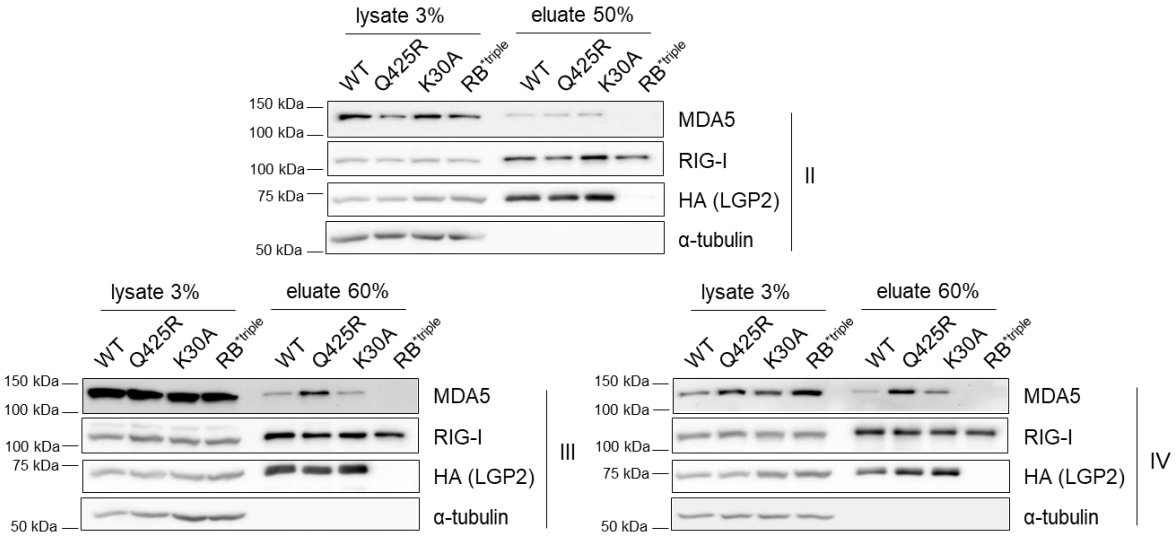

Figure S 18: Three replicates of HA, RIG-I and MDA5 immunoblots (suppl. to Figure 22A).
Three out of four HA, RIG-I and MDA5 immunoblots of cell lysates and eluates used for quantification in Figure 22B are shown.

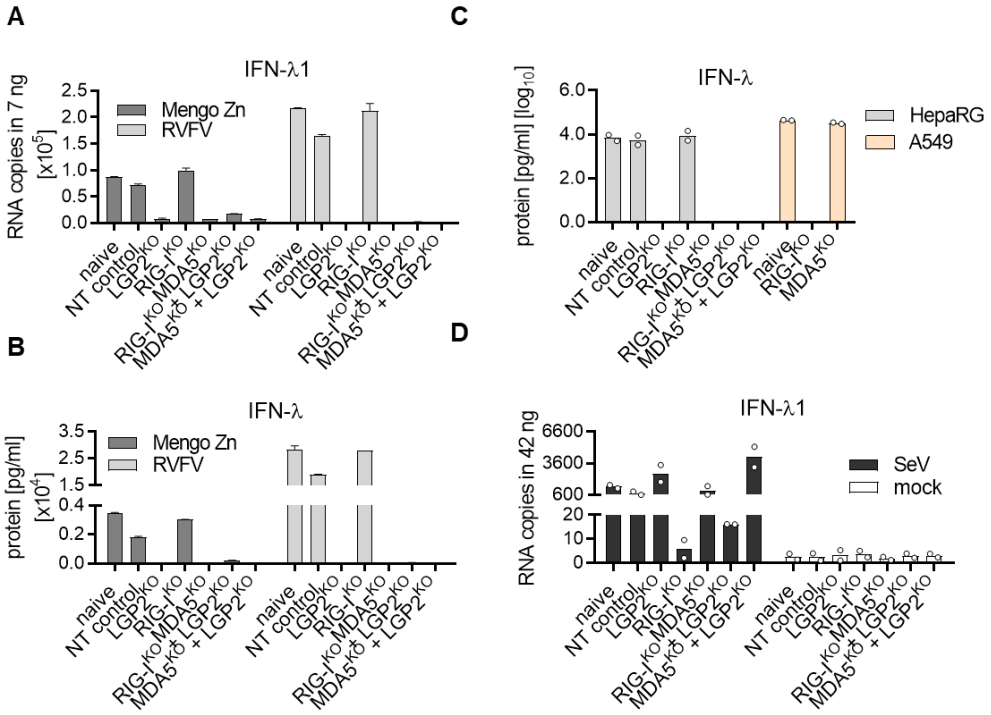

Figure S 19: Mengo Zn virus and RVFVΔNSs-Renilla are sensed by LGP2 and MDA5 while SeV is sensed by RIG-I in HepaRG^{NTCP}.

(A) Naïve HepaRG^{NTCP} cells and cells from Figure 12 were infected with Mengo Zn virus (MOI=5) and RVFVΔNSs-Renilla (1:100) for 12 h or were mock treated. RNA was isolated for subsequent qRT-PCR measurement of IFN-λ1 RNA. RNA levels of mock cells were below 5 copies/7 ng and are not shown. n=1. **(B)** ELISA of cell supernatants from (A) was performed to measure IFN-λ protein levels. Mock cells without any detectable IFN-λ levels (data not shown). n=1. Error bar indicates SD from two technical replicates. **(C)** RVFVΔNSs-Renilla infection from (A) was repeated side-by-side with naïve, RIG-I^{KO} or MDA5^{KO} A549 and IFN-λ ELISA was performed. No IFN-λ protein levels are detectable in mock cells (data not shown). n=2. (**D)** Cells used in (A) were infected with SeV (MOI=1) or mock treated for 24 h to measure IFN-λ1 mRNA levels. n=2.

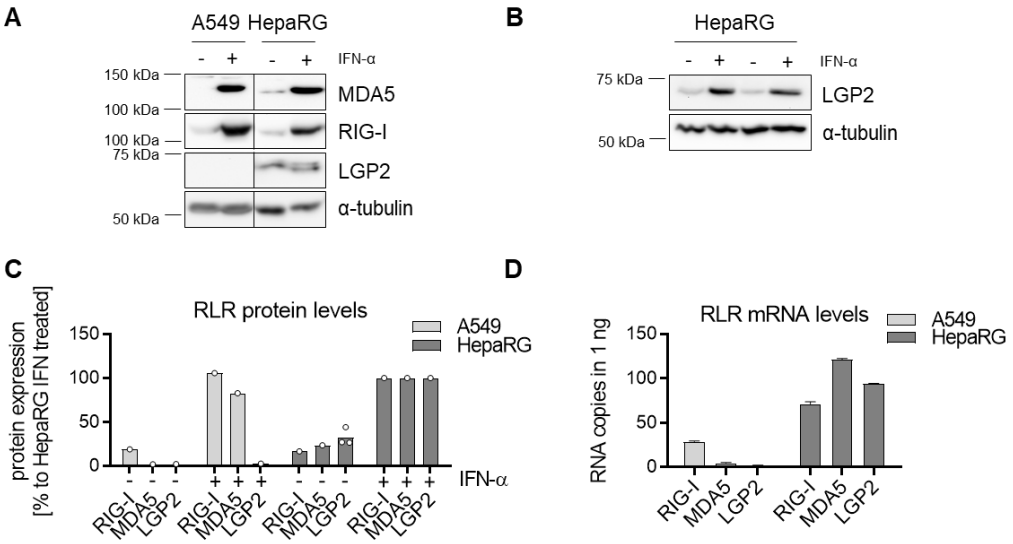

Figure S 20: RLR expression ratio is different in A549 and HepaRG.
(A) Naïve A549 and HepaRG were kept untreated or treated with 200 IU/ml of IFN-α for 24 h before harvesting for SDS-PAGE. A side-by-side comparison of RLR protein levels between A549 and HepaRG cells by Western blot analysis using MDA5-, RIG-I- and LGP2-specific antibodies is shown. α-tubulin served as a loading control. **(B)** Repetition of LGP2 protein staining in HepaRG cells on Western blot analog to (A). α-tubulin served as a loading control. **(C)** Quantification of RLR protein levels from (A) and (B) normalized to α-tubulin. RIG-I, MDA5 and LGP2 levels of IFN-α treated HepaRG cells were set to 100%. **(D)** HepaRG^{NTCP} and A549 NT guide RNA-expressing cells were compared for their mRNA RLR abundance in steady-state. RNA from previous experiments (12 h mock treatment) was used for qRT-PCR of RIG-I, MDA5 and LGP2. n=1.

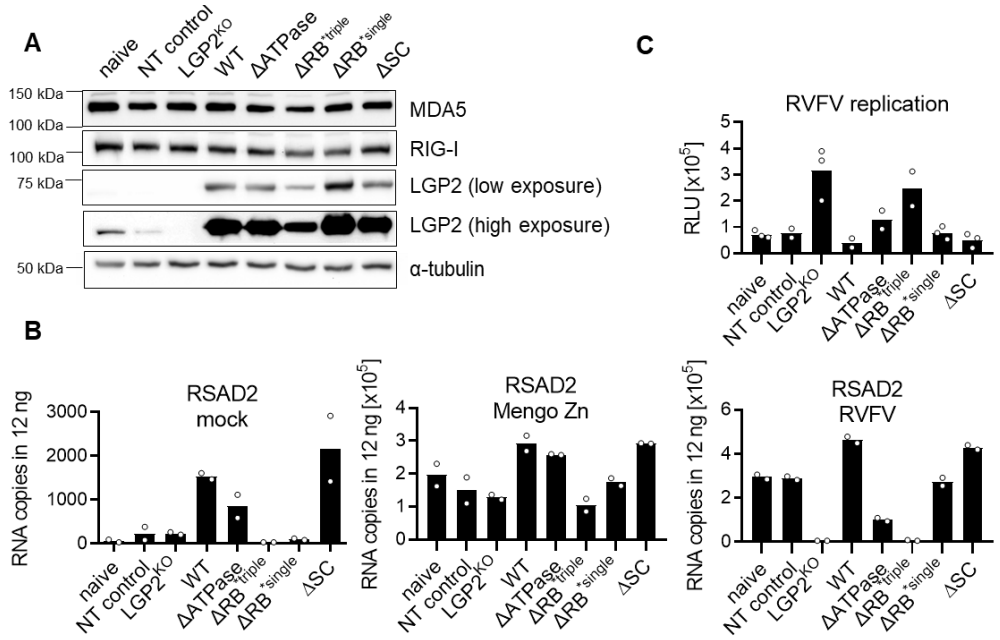

Figure S 21: LGP2 RNA binding is essential for its MDA5 support upon Mengo Zn virus and RVFVΔNSs-Renilla infection in HepaRG^{NTCP}.
(A) An LGP2 serine cluster (SC) at amino acid positions 363, 364, 365 and 367 was mutated to alanine and this LGP2 version was introduced into LGP2^{KO} HepaRG^{NTCP} (called ΔSC LGP2). Naïve HepaRG^{NTCP} cells, ΔSC LGP2 HepaRG^{NTCP} and HepaRG^{NTCP} from Figure 14 were stimulated 24 h with 200 IU/ml of IFN-α prior to Western blotting of MDA5, RIG-I, LGP2 and α-tubulin. **(B)** Cells from (A) were kept uninfected or infected with Mengo Zn virus (MOI=5) or RVFVΔNSs-Renilla (1:100) for 12 h. RNA was isolated and RSAD2 expression levels were determined by qRT-PCR. n=2. **(C)** Cells from (A) were infected with RVFVΔNSs-Renilla (1:100) for 24 h. Renilla luciferase counts were measured as a surrogate for virus replication. n=2-3. RLU: relative luminescence unit. RB=RNA binding.

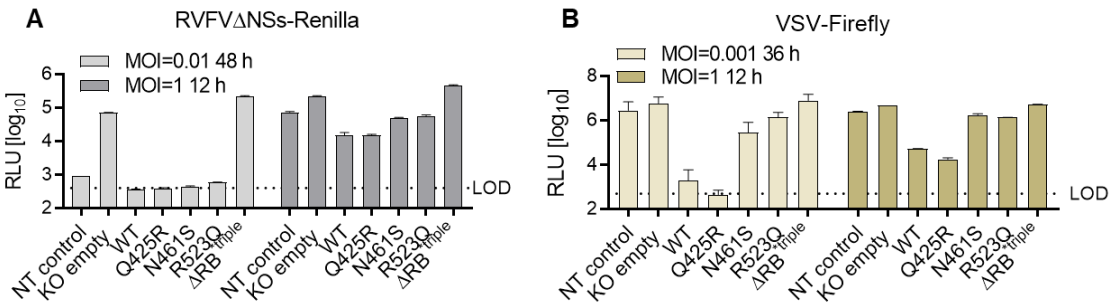

Figure S 22: Q425R LGP2 reveals stronger replication repressive effect towards VSV-Firefly infection than WT in HepaRG^{NTCP}.
HepaRG^{NTCP} cells from Figure 15 (NT control, LGP2^{KO} harboring an empty vector (KO empty), ΔRB^{*triple} LGP2) and Figure 16 (WT, Q425R, N461S, R523Q LGP2) were infected with **(A)** RVFVΔNSs-Renilla or **(B)** VSV-Firefly at the indicated MOIs and time points. Renilla and Firefly luciferase counts were measured as a surrogate for virus replication (n=1). RLU: relative luminescence unit. LOD: limit of detection.

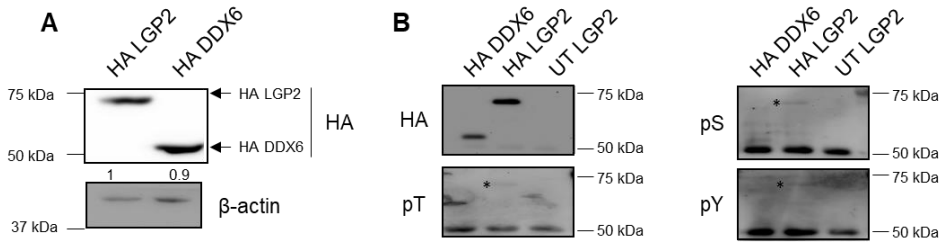

Figure S 23: Immunoblot staining with phospho-specific antibodies hints at LGP2 as a phosphoprotein.

(A) A549 cells stably expressing N-terminally HA-tagged RNA helicase DDX6 were generated by lentiviral transduction. The cell lysate was analyzed by Western blot for its HA-DDX6 expression strength compared to HA-LGP2 A549 cells using HA antibody. Numbers below the blot indicate DDX6 expression strength relative to LGP2 and normalized to β-actin. **(B)** HA-immunoprecipitation of HA-LGP2 and HA-DDX6 A549 cells from (A) and of untagged LGP2 (UT-LGP2)-expressing A549 was performed. Eluates were used for Western blot analysis. Anti-HA, anti-phospho-threonine (pT), anti-phopsho-serine (pS) and anti-phospho-tyrosine (pY) antibodies were used. Star highlights protein band in HA-LGP2 eluates.

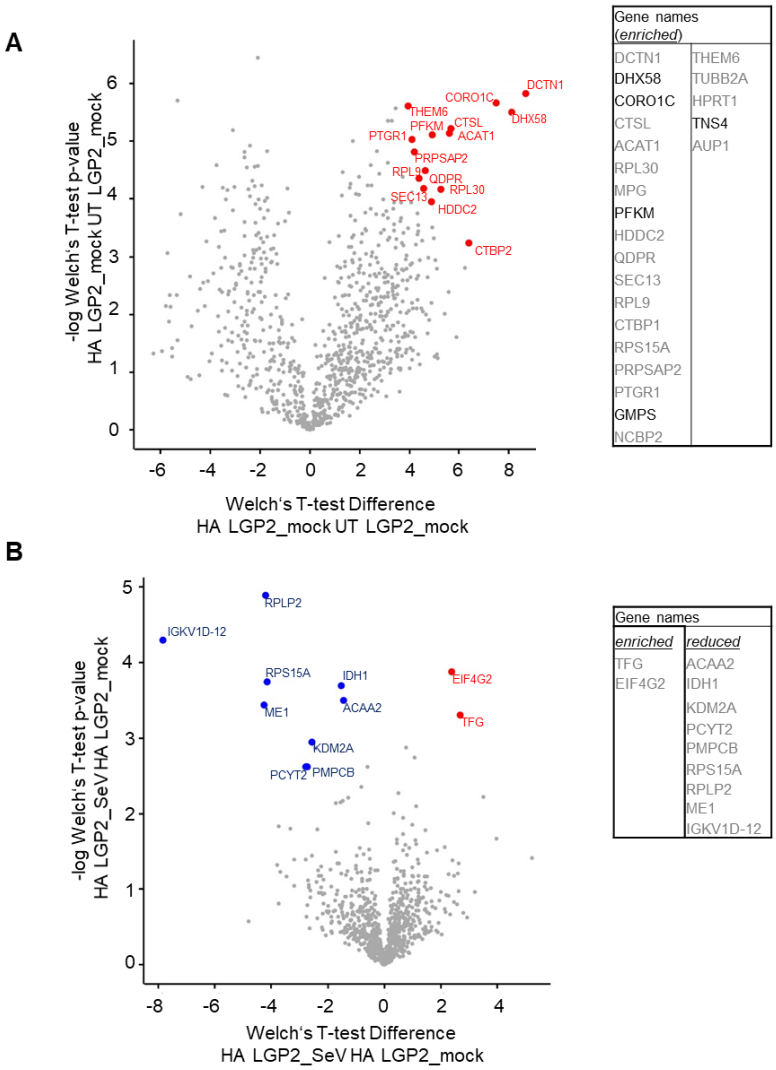

Figure S 24: phospho-MS run I identifies potential LGP2 interactors in steady-state and upon SeV infection (suppl. to Figure 24).

Vulcano plots (left-hand) and hit list (right-hand) of significantly enriched proteins of **(A)** A549 cells expressing HA-LGP2 mock versus A549 cells expressing UT LGP2 mock and **(B)** HA-LGP2 A549 cells SeV infected for 3 h versus A549 HA-LGP2 mock cells (from MS run I, Figure 24). In the Vulcano plots, protein hits were plotted in pairwise comparisons. The x-axis shows the relative fold-enrichment of hits over the control bait whereas the y-axis shows their relative -log2 p values. p <0.05 (using Welch‘s T-test). Statistically significant proteins were highlighted in red (enriched over control) or blue (reduced over control) and labeled with the corresponding gene name. Hit list in (A) shows only most enriched (Welch‘s T-test Difference >3.5) and most significant hits (-Log Welch's T-test p-value >3.5), hits in (B) show all significant ones. Hits labeled in grey in the hit list were not found in the repeated analysis of MS run III. Hits are sorted by their enrichment. Results need to be interpreted with caution as there was no HA-tagged unrelated control. Data analysis performed by and Volcano plots originated from Dr. Pietro Scaturro.

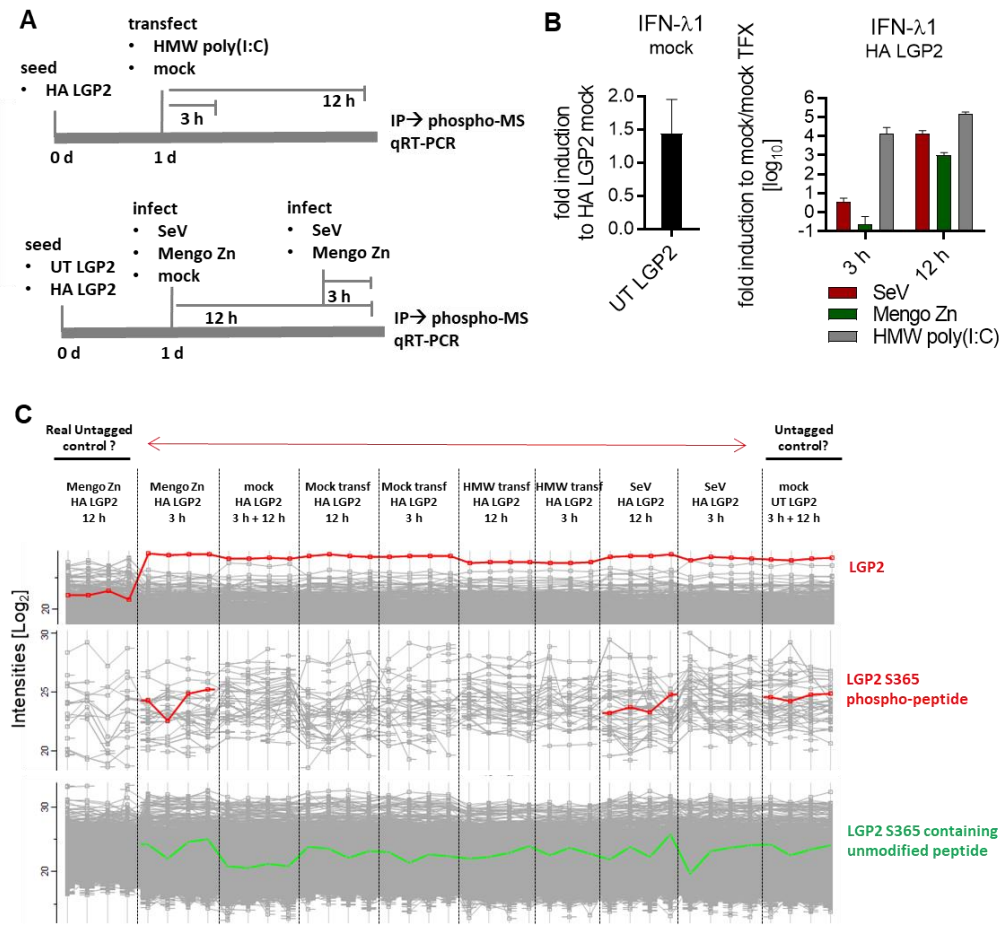

Figure S 25: LGP2 MS run II identifies an additional phosphorylation site of LGP2 at position S365.

(A) Experimental set-up is shown. A549 cells stably expressing HA-tagged LGP2 were transfected with 3 µg HMW poly(I:C) (per 10 cm dish) or mock transfected for 3 h or 12 h respectively. In parallel to synthetic stimulation, cells were infected with Mengo Zn (MOI=5) and SeV (MOI=5) for 3 h and 12 h or kept uninfected. Untagged (UT) LGP2-expressing mock cells served as a further control. Cells were harvested for IP prior to MS and a small aliquot was kept for RNA isolation and qRT-PCR. **(B)** RNA from (A) was used for cDNA synthesis and qRT-PCR of IFN-λ1. **(C)** MS results depicted as unnormalized raw intensities of total LGP2, LGP2 S365 phospho-peptide and LGP2 S365 unmodified peptide. Measurements were performed in quadruplicates from four independent IPs. MS run and its data analysis were performed by Dr. Pietro Scaturro. Figure (C) was created by Dr. Pietro Scaturro.

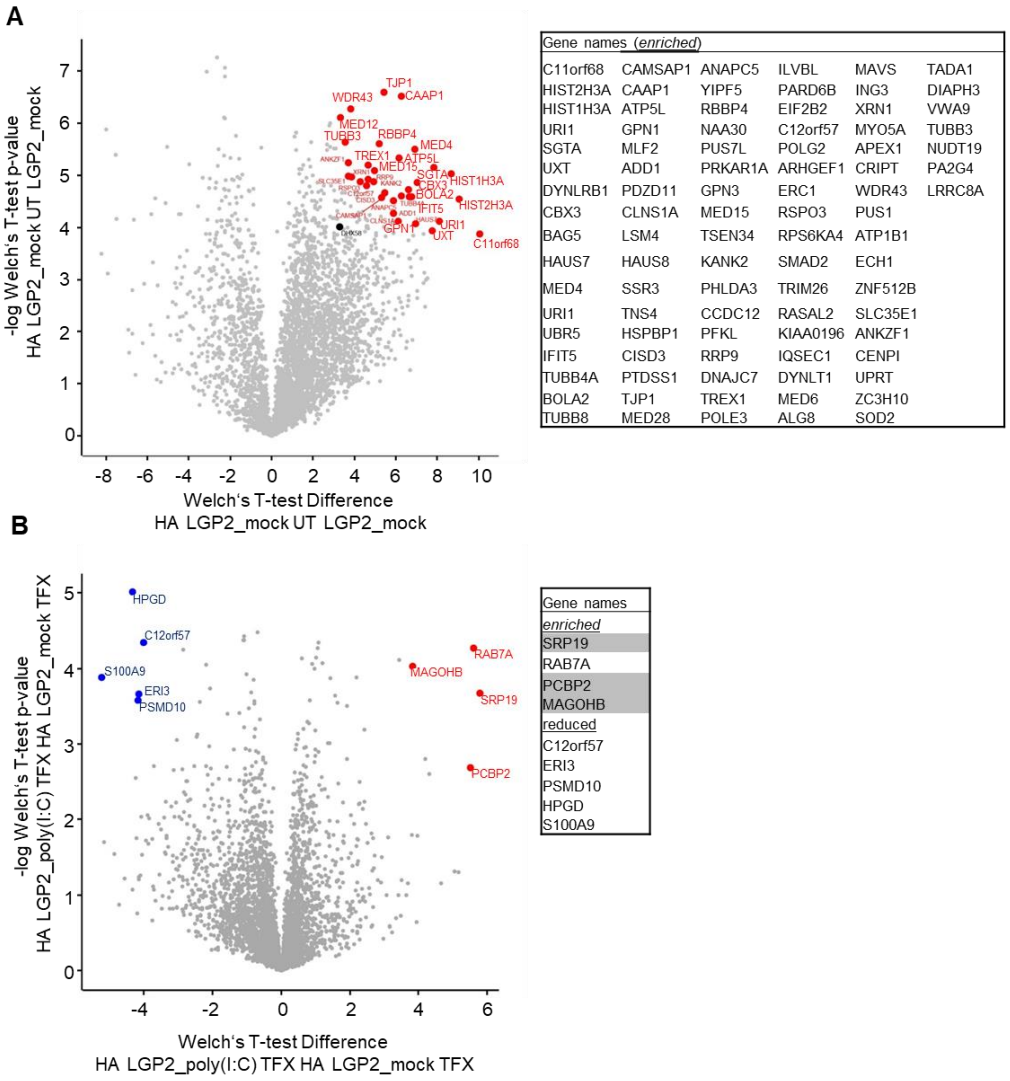

Figure S 26: phospho-MS run III identifies potential LGP2 interactors in steady-state and upon poly(I:C) transfection (suppl. to Figure 25).

Vulcano plots (left-hand) and hit list (right-hand) of significantly enriched proteins of **(A)** A549 cells expressing HA-LGP2 mock versus A549 cells expressing UT LGP2 mock and **(B)** A549 HA-LGP2 cells transfected for 3 h with HMW poly(I:C) versus A549 HA-LGP2 mock-transfected cells (from MS run III, Figure 25). In the Vulcano plots, MS protein hits were plotted in pairwise comparisons. The x-axis shows the relative fold-enrichment of hits over the control bait whereas the y-axis shows their relative -log2 p values. $p<0.05$ (using Welch's T-test). Statistically significant proteins were highlighted in red (enriched over control) or blue (reduced over control) and labeled with the corresponding gene name. Hit list in (A) shows only most enriched (Welch's T-test Difference >3.5) and most significant hits (-Log Welch's T-test p-value >3.5), hits in (B) show all significant ones. Hits are sorted by their enrichment; gene names marked in grey indicate significance at 12 h, too. Results need to be interpreted with caution as there was no HA-tagged unrelated control. Analysis was focused on early time points (3 h after stimulation) to avoid enrichment due to IFN/ISG upregulation due to stimulation. TFX: transfection. Data analysis performed by and Volcano plots originated from Dr. Pietro Scaturro.

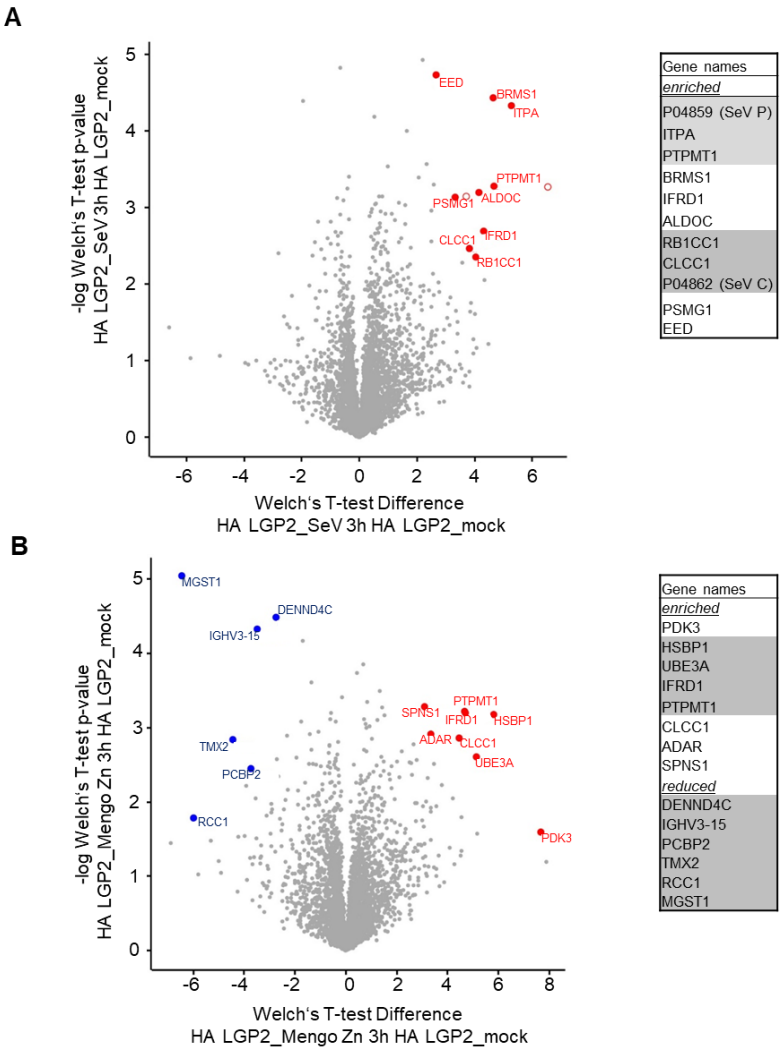

Figure S 27: phospho-MS run III identifies potential LGP2 interactors upon virus infection (suppl. to Figure 25).

Vulcano plots (left-hand) and hit list (right-hand) of all significantly enriched proteins of **(A)** A549 cells expressing HA-LGP2 SeV infected for 3 h versus A549 cells expressing HA-LGP2 mock and **(B)** A549 cells expressing HA-LGP2 Mengo Zn infected for 3 h versus A549 cells expressing HA-LGP2 mock (from MS run III, Figure 25). In the Vulcano plots, MS protein hits were plotted in pairwise comparisons. The x-axis shows the relative fold-enrichment of hits over the control bait whereas the y-axis shows their relative -log2 p values. p value<0.05 (using Welch's T-test). All statistically significant proteins were highlighted in red (enriched over control) or blue (reduced over control) and labeled with the corresponding gene name. Hits are sorted by their enrichment; gene names marked in grey indicate significance at 12 h, too. Results need to be interpreted with caution as there was no HA-tagged unrelated control. Analysis was focused on early time points (3 h after stimulation) to avoid enrichment due to IFN/ISG upregulation due to stimulation. TFX: transfection. Data analysis performed by and Volcano plots originated from Dr. Pietro Scaturro.

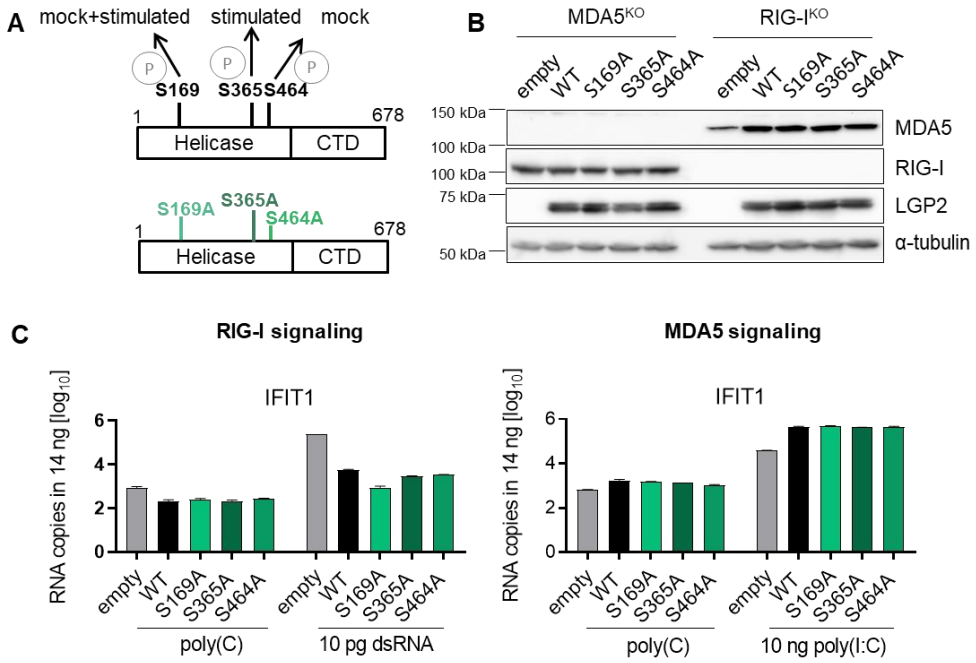

Figure S 28: S169A LGP2 reduces RIG-I signaling stronger than WT in A549.
(A) Schematic summary of identified LGP2 phosphorylation sites and their occurrence (upper panel). Representation of phosphoablative (alanine; A) LGP2 mutants (lower panel). **(B)** A549 cells stably expressing N-terminally HA-tagged LGP2 WT, S169A, S365A or S464A LGP2 or cells expressing an empty vector control (empty) were generated in MDA5^{KO} and RIG-I^{KO} background by using M2-28 and R2-2-#1 single knock-out clones, respectively. Expression of RIG-I, MDA5, LGP2 (WT and phosphoablative versions) were measured by Western blot using RLR-specific antibodies. α-tubulin was used as a loading control. Before harvesting cells were treated with 200 IU/ml of IFN-α for 24 h. **(C)** MDA5^{KO} A549 generated in (B) were transfected with 10 pg 5'ppp-dsRNA of 200 bp in length to stimulate RIG-I signaling (left-hand). RIG-I^{KO} A549 from (B) were transfected with 10 ng HMW poly(I:C) to stimulate MDA5 signaling (right-hand). Poly(C) transfected cells served as a negative control. Cells were harvested 8 h (MDA5^{KO}, for RIG-I signaling) and 12 h (RIG-I^{KO}, for MDA5 signaling) post-transfection. n=1.

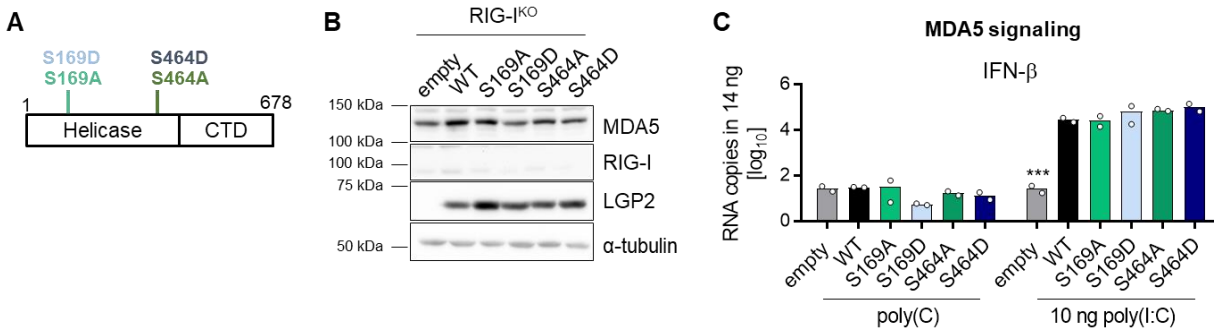

Figure S 29: S169A/D and S464A/D LGP2 phosphomutants function like WT on MDA5 signaling in A549.

(A) Schematic representation of phosphoablative (alanine; A) and -mimetic (aspartic acid; D) S169 and S464 sites within LGP2. **(B)** A549 cells stably expressing N-terminally HA-tagged LGP2 WT, S169A, S169D, S464A, S464D or an empty vector control (empty) were generated in RIG-I^{KO} background by using R2-2-#1 single knock-out clone. RLR expression was measured by Western blot using RIG-I-, MDA5- and LGP2-specific antibodies. α-tubulin served as a loading control. Cells were treated with 200 IU/ml of IFN-α for 24h before harvesting. **(C)** RIG-I^{KO} A549 from (B) were transfected with 10 ng HMW poly(I:C) to stimulate MDA5 signaling. Poly(C) transfected cells served as a negative control. Cells were harvested 12 h post-transfection. n=2. ***, $p \leq 0.001$ (comparison between WT and versions of LGP2 or empty control at the depicted amount of stimulus). This experiment was performed together with Figure 26.

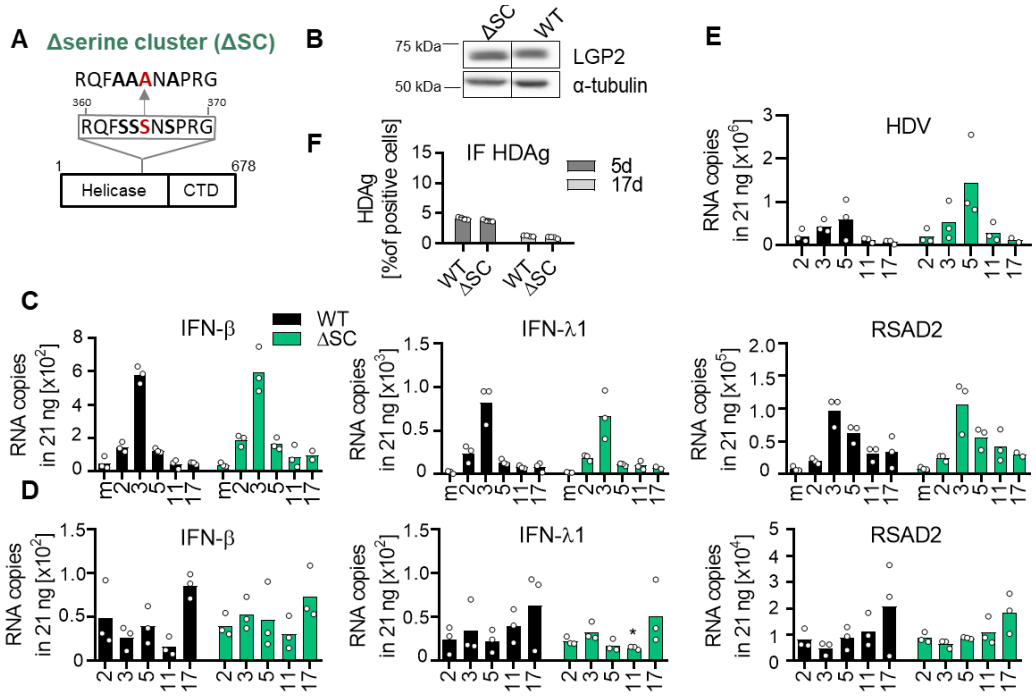

Figure S 30: Serine cluster mutation of LGP2 behaves like WT LGP2 upon HDV infection in HepaRG^{NTCP}.

(A) Schematic representation of phosphoablative (alanine; A) mutations around S365 phosphorylation site of LGP2, including S363, S364, S365, S367. The resulting quadruple mutant S363A S364A S365A S367A is designated as Δserine cluster (ΔSC). Red amino acid emphasizes position 365. Bold amino acids represent the mutation sites. **(B)** LGP2^{KO} HepaRG^{NTCP} cells were reconstituted with either Cas9 cleavage resistant N-terminally HA-tagged WT or ΔSC LGP2. LGP2 expression was measured by Western blot using an LGP2 antibody. α-tubulin served as a loading control. **(C-F)** Cells from (B) were infected with HDV and harvested 2 d, 3 d, 5 d, 11 d, 17 d pi. mRNA levels of IFN-β, IFN-λ1, RSAD2 upon (C) HDV infection or (D) steady-state were measured by qRT-PCR. "m" depicts 2 d mock infected cells. (E) HDV RNA in infected cells was measured as well. (F) At 5 d and 17 d pi percentage of HDV positive cells was analyzed by IF of HDAg and quantified using ImageJ. Data in panels (E) and (F) generated by Dr. Zhenfeng Zhang. Note that this data was part of Figure 14 and Figure S 9 where ΔSC LGP2 results were excluded due to clarity reasons (thus WT LGP2 is shown here as reference). *, $p \leq 0.05$ (comparison between WT and ΔSC LGP2 at the depicted time points). n=3.

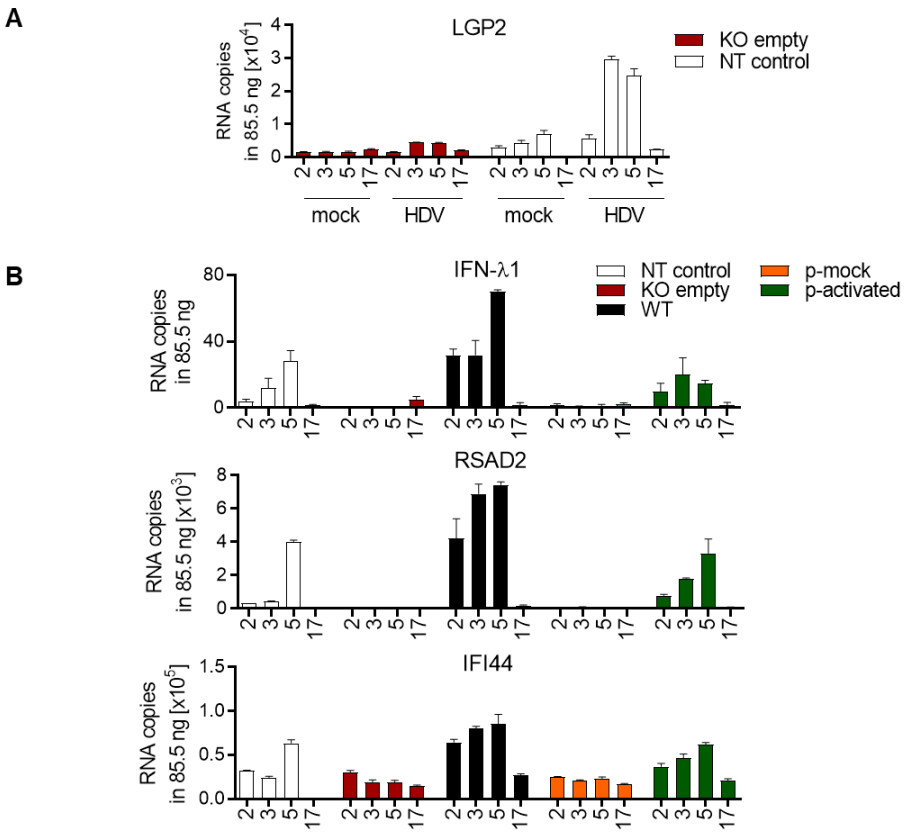

Figure S 31: LGP2 and basal IFN-λ1, RSAD2 and IFI44 mRNA levels (suppl. to Figure 27).
(A) LGP2 levels of HepaRG^{NTCP} LGP2^{KO} and NT-guide RNA expressing control cells were measured 2 d, 3 d, 5 d and 17 d post HDV infection or mock treatment using RNA from Figure 27. n=1. **(B)** Basal gene expression of IFN-λ1, RSAD2 and IFI44 mRNA 2 d, 3 d, 5 d and 17 d post mock treatment of Figure 27 measured by qRT-PCR is shown. n=1. Note that the lower RSAD2 steady-state levels in LGP2 p-mock had been already observed in a previous experiment.

A

Gene	shRNA	TRC number	Source of interaction
DHX30	#1	TRCN0000299893	Li, 2011 [1+2]
	#2	TRCN0000303834	Sanchez David, 2019 [1]
	#3	TRCN0000052031	
EIF2AK2	#4	TRCN0000197012	Li, 2011 [1+2]
	#5	TRCN0000196400	Sanchez David, 2019 [1+2]
	#6	TRCN0000001381	
EIF6	#7	TRCN0000057701	Li, 2011 [1+2]
	#8	TRCN0000057700	
	#9	TRCN0000057699	
STAU2	#10	TRCN0000157149	Li, 2011 [1+2]
	#11	TRCN0000178809	
	#12	TRCN0000152870	
NKRF	#13	TRCN0000016428	Li, 2011 [1+2]
	#14	TRCN0000244908	Snachez David, 2019 [1]
	#15	TRCN0000244909	
USP21	#16	TRCN0000004350	Fan, 2014 [2]
	#17	TRCN0000281897	
	#18	TRCN0000004349	
DDX60	#19	TRCN0000050187	Miyashita, 2011 [2]
	#20	TRCN0000050185	
	#21	TRCN0000050183	
ANKRD17	#22	TRCN0000274424	Wang, 2012 [3]
	#23	TRCN0000274384	
	#24	TRCN0000016952	
TRIM25	#25	TRCN0000272649	Quicke, 2019 [1+2]
	#26	TRCN0000272698	
	#27	TRCN0000003449	
APP	#28	TRCN0000011043	Virok, 2011 [1]
	#29	TRCN0000011042	Olah, 2011 [1]
	#30	TRCN0000006707	
AP2B1	#31	TRCN0000158360	Rual, 2005 [1]
	#32	TRCN0000150775	
	#33	TRCN0000382390	
XRN2	#34	TRCN0000049900	Li, 2011 [1]
	#35	TRCN0000293639	Sanchez David, 2019 [1]
	#36	TRCN0000349677	
CDKN2AIP	#37	TRCN0000154004	Li, 2011 [1]
	#38	TRCN0000154885	
	#49	TRCN0000150334	
STAU1	#40	TRCN0000166217	Li, 2011 [1]
	#41	TRCN0000159875	Sanchez David, 2019 [1]
	#42	TRCN0000164920	

[1] MS (high throughput)
[2] Western blot, reconstituted complex (low throughput)
[3] no direct interaction tested, interaction only analyzed with MDA5, RIG-I, MAVS (low throughput)

B

Gene	Effect published	Source of interaction
DICER1*	yes	Li, 2011 [1+2] Sanchez David, 2019 [1+2]
AGO2*	no	Li, 2011 [1+2]
TRBP	yes	Komuro, 2016 [3+2]
TRAF2	yes	Parisien, 2018 [2]
TRAF3	yes	Parisien, 2018 [2]
TRAF5	yes	Parisien, 2018 [2]
TRAF6	no	Parisien, 2018 [2]
IFI16	no	Hubel, 2019 [1+2]
PACT	yes	Sanchez David, 2019 [1+2]
DDX6	No	Sanchez David, 2019 [1]
ZC3HAV1	No	Sanchez David, 2019 [1]
HUWE1	No	Sanchez David, 2019 [1]
UBR5	No	Sanchez David, 2019 [1]

[1] MS (high throughput)
[2] Western blot, reconstituted complex (low throughput)
[3] Yeast two-hybrid screen (high throughput)
* A549 single knockout clones generated

C

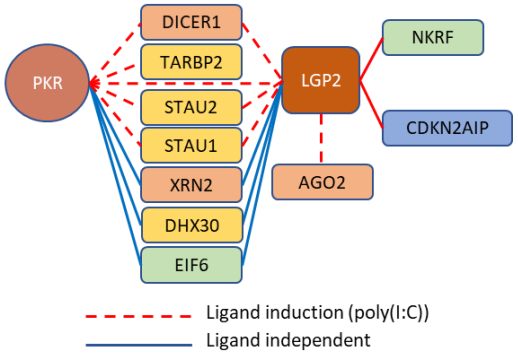

Figure S 32: Published LGP2 interactors.
(A) Table with published LGP2 interactors identified by mass spectrometry (MS) and/or Western blot are shown which were selected for shRNA miniscreen. Potential interaction with ANKRD17 was included. The TRC number of different Mission shRNA bacterial glycerol stocks from Sigma-Aldrich were attached (three per gene). **(B)** Table with additional published LGP2 interactors identified by MS or yeast two-hybrid screen is depicted. **(C)** Map of some LGP2-specific and joint LGP2/PKR interaction partners modified from Li et al. 2011 [130].

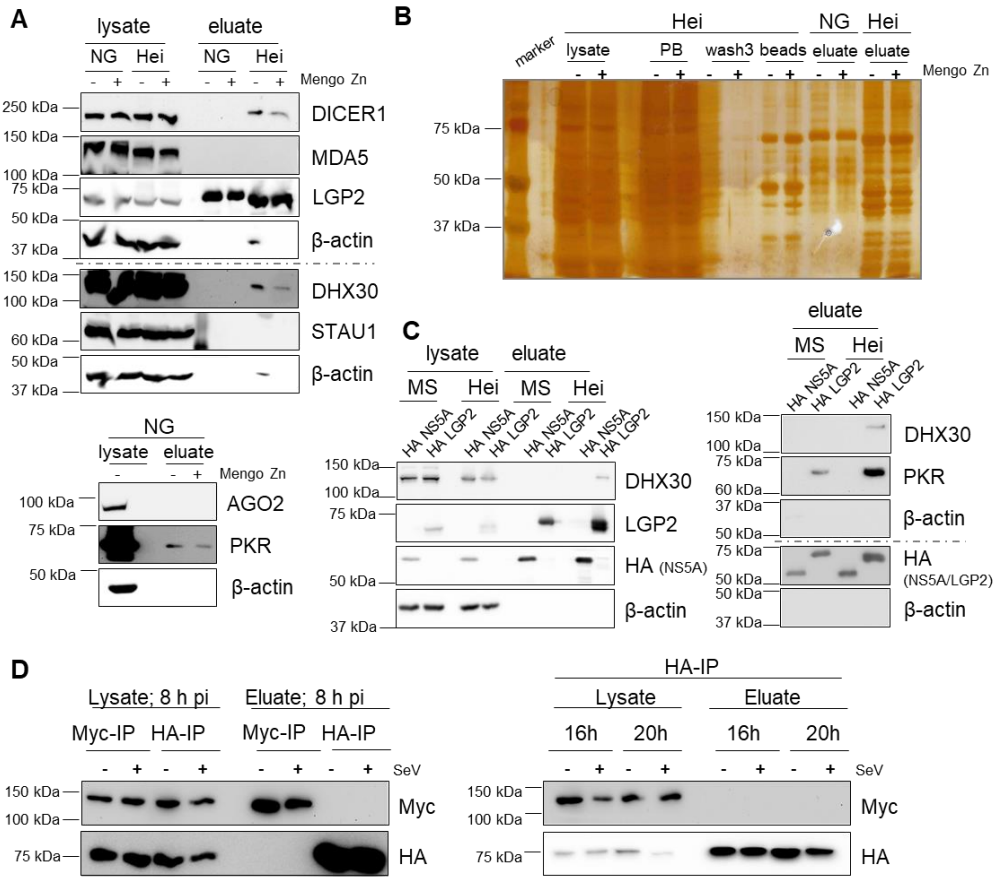

Figure S 33: LGP2 Co-IP reveals interaction with DICER1, DHX30 and PKR in A549 cells.
(A) Lysates and eluates of HA-LGP2 MDA5-Flag-expressing A549 cells after HA-IP are shown on Western blot stained with indicated antibodies. Cells were infected with Mengo Zn virus (MOI=2) or kept uninfected for 24 h before harvesting for IP. NG and Hei buffer conditions were used for lysis and washing of IP. n=1. **(B)** Silver gel of IP steps from (A). Under Hei buffer conditions, lysate, post binding (PB), washing step3 (wash3), left-over on beads (beads) and eluate are shown. Eluate of NG buffer conditions served as a comparison. n=1. **(C)** Equal to (A) HA-LGP2- and HA-NS5A (from HCV)-expressing A549 (in steady-state) were used for HA-IP under Hei and MS buffer conditions. Immunoblot of lysates and/or eluates are shown by using designated antibodies. n=1. **(D)** HA-LGP2 Myc-RIG-I-expressing A549 were used for Myc- and HA-IP under NG buffer conditions. Cells were infected with SeV (MOI=5) or kept uninfected for 8 h, 16 h or 20 h before harvesting for IP. Lysate and eluate of 8 h mock and SeV infected samples after Myc- and HA-IP were immunoblotted using HA and Myc antibodies (left panel). Lysate and eluate of 16 h and 20 h mock and SeV infected samples after HA-IP were stained with HA and Myc antibodies (right panel). n=1.

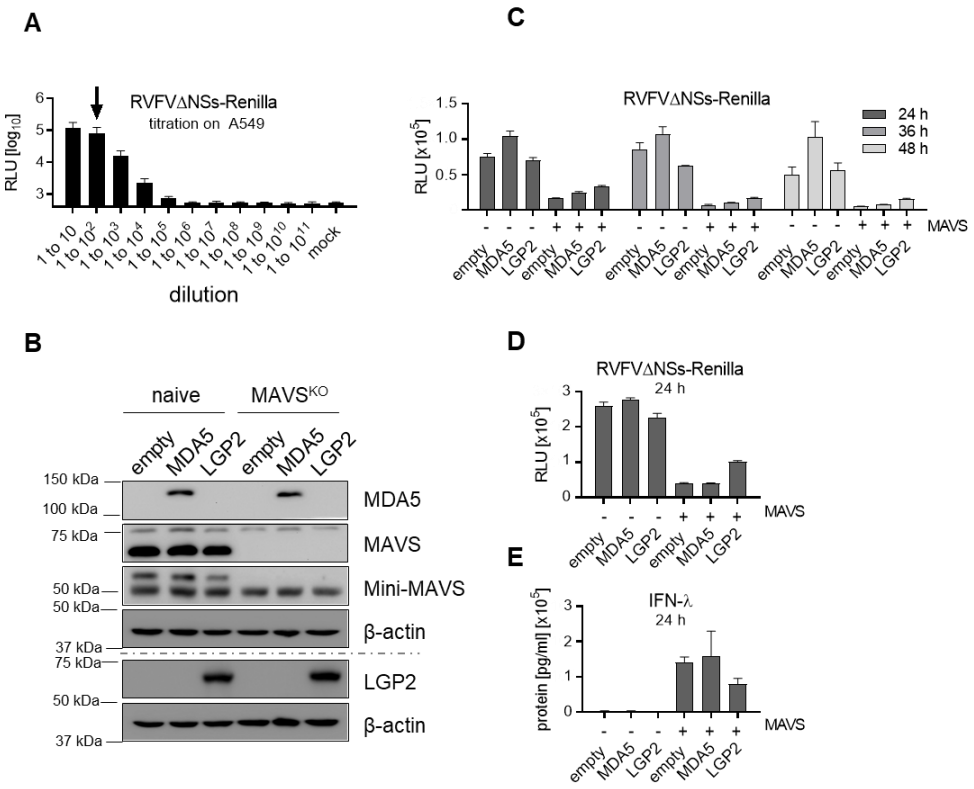

Figure S 34: LGP2 does not expose a direct effector function against RVFV replication.
(A) RVFVΔNss-Renilla was serially diluted on A549 cells to measure respective luciferase counts. 1 to 100 dilution (depicted by arrow) was used for downstream experiments. Error bar indicates SD from three technical replicates. n=1. **(B)** Naïve and MAVS^{KO} clone (MAVS^{KO} 1.77) A549 were stably transduced with lentiviruses harboring an empty vector control (empty) or lentiviruses encoding for MDA5 or LGP2. Cells were immunoblotted to evaluate their protein expression of MDA5, MAVS and LGP2. β-actin served as a loading control. **(C)** Cells (from B) were infected with RVFVΔNSs-Renilla (1:100 dilution) for 24 h, 36 h or 48 h or kept uninfected before harvesting. Renilla luminescence was measured (96 well format) and was undetectable in mock cells (data not shown). Error bar indicates SD from four technical replicates. **(D-E)** Analog to (C) cells were infected with RVFVΔNSs-Renilla (1:100 dilution) for 24 h or kept uninfected before harvesting and measurement of **(D)** virus replication by Renilla luminescence (24 well format) and **(E)** IFN-λ secretion by ELISA. IFN-λ protein levels and Renilla luminescence were undetectable in mock cells (not shown). Error bar indicates SD from three technical replicates. n=1. RLU: relative luminescence unit.

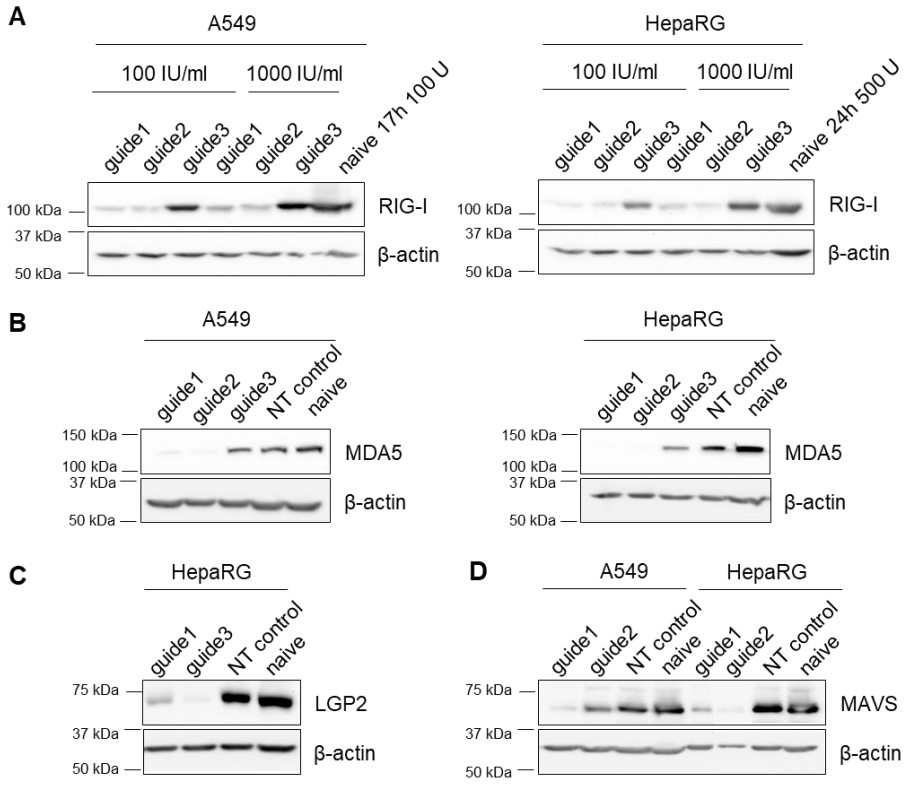

Figure S 35: Evaluation of guide RNA knockout efficiency against RLRs or MAVS in A549 and HepaRG cells.

A549 and HepaRG cells were stably transduced with lentiviruses expressing a guide RNA containing CRISPR-Cas9 vector which targets either RIG-I, MDA5, LGP2 or MAVS, respectively. Stably selected cell pools were harvested for Western blot analysis. Respective guide RNA sequences can be found in Table S 1. **(A)** A549 (left-hand) and HepaRG (right-hand) were transduced with guide RNA-containing lentiviruses against RIG-I (guide1-3) and stimulated with 100 or 1000 IU/ml of IFN-α for 23 h. IFN-α stimulated naive cells served as a positive control for RIG-I expression in Western blot. β-actin served as a loading control. **(B)** A549 (left-hand) and HepaRG (right-hand) were transduced with guide RNA-containing lentiviruses against MDA5 (guide1-3) and stimulated with 500 IU/ml of IFN-α for 26 h. IFN-α stimulated naive cells as well as non-targeting guide RNA (NT control)-expressing cells served as a positive control for MDA5 expression in Western blot. β-actin served as a loading control. **(C)** HepaRG were transduced with guide RNA containing lentiviruses against LGP2 (guide1+3) and stimulated with 500 IU/ml of IFN-α for 26 h. IFN-α stimulated naive cells as well as non-targeting guide RNA (NT control)-expressing cells served as a positive control for LGP2 expression in Western blot. β-actin served as a loading control. **(D)** A549 (left-hand) and HepaRG (right-hand) were transduced with guide RNA-containing lentiviruses against MAVS (guide1+2) and stimulated with 500 IU/ml of IFN-α for 26h. IFN-α stimulated naive cells as well as non-targeting guide RNA (NT control)-expressing cells served as a positive control for MAVS expression in Western blot. β-actin served as a loading control.

Table S 1: RLR and ADAR1 guide RNA and shRNA sequences.

Name	Sequence
MAVS guide RNA-1	tcagccctctgacctccagcg[1]
MAVS guide RNA-2	cgctggaggtcagagggctg[1]
RIG-I guide RNA-1	ctgttggagctccaggagga
RIG-I guide RNA-2	tggagctccaggaggaaggc
RIG-I guide RNA-3	gatatcggttgggataattc
MDA5 guide RNA-1	ggattgtgcagaaagaaaac
MDA5 guide RNA-2	aatcagagcctgttaactct
MDA5 guide RNA-3	gggcatggagaataactcat
LGP2 guide RNA-1	agcttcggtcctaccaatgg
LGP2 guide RNA-3	cggctgcttatgtggccaag
shMDA5a	tgctgttgacagtgagcg**acgagagaagatgatgtataaa**ta*gtgaagccacagatg*t a**tttatacatcatcttctctcgg**tgcctactgcctcgga
shMDA5b	tgctgttgacagtgagcg**accctacaaattaatgacacaa**ta*gtgaagccacagatg*ta **ttgtgtcattaatttgtagggc**tgcctactgcctcgga
shADAR1a	tgctgttgacagtgagcg**cgttgactaagtcacatgtaaa**ta*gtgaagccacagatg*ta**t ttacatgtgacttagtcaact**tgcctactgcctcgga
shADAR1c	tgctgttgacagtgagcg**cgcacatgatctgtctgggaaa**ta*gtgaagccacagatg*ta **tttcccagacagatcatgtgct**tgcctactgcctcgga
[1], taken from Dr. Silke Jung; bold: target sequence, italic: miR-30a loop	